Author:
Beckett, Laura

Title:
Synthesis and Characterisation of Photoresponsive Thermoplastic Liquid Crystal Elastomers

Synthesis and Characterisation of Photoresponsive Thermoplastic Liquid Crystal Elastomers

Laura Elizabeth Beckett

A dissertation submitted to the University of Bristol in accordance with the requirements for award of the degree of Doctor of Philosophy in the Faculty of Engineering

September 2018

Word Count: 55,000

Abstract

Liquid crystal elastomers (LCEs) are polymeric materials capable of rapid, reversible shape change on application of an external stimulus. However, their application as soft actuators has, to date, been limited by the requirement to induce a liquid crystal monodomain, with common alignment methods restricting possible structures to thin films. Thermoplastic LCEs have the potential for processing through large-scale techniques such as extrusion or fibre spinning but have been relatively unexplored, with low-yielding synthetic methods preventing further investigation into their suitability for processing into alternative geometries to films.

For this reason, photoresponsive thermoplastic side-chain LCEs based on a polystyrene-*b*-poly(methylvinylsiloxane)-*b*-polystyrene block copolymer backbone have been synthesised for processing into responsive fibres. A two-step post-polymerisation modification was used to first attach a linking group, followed by the mesogen. A yield of 85% was achieved in the final coupling stage, resulting in polymers with 65-85% of linking groups functionalised with mesogen. Through the choice of linking group or mesogen it was possible to tune the thermal properties of the LCEs to obtain useful transition temperatures for use as room temperature actuators. The presence of a nematic mesophase was shown to have a strong effect on the physical properties of the polymer, resulting in a microphase segregated morphology at temperatures far above the order-disorder transition temperature of the unfunctionalised triblock copolymer. This, combined with the relatively high molecular weight of 150,000 g mol^{-1}, was demonstrated to limit the ability to process the LCE by melt extrusion, with gel-like behaviour observed at temperatures up to 200 °C. However, the high molecular weight of the polymer made it suitable for processing from solution, and preliminary experiments demonstrated for the first time that fibres of a thermoplastic LCE could be produced by electrospinning, with elongation of the jet resulting in the formation of an aligned nematic LC mesophase.

Acknowledgements

The path of this project could optimistically be described as eventful, and so I would like to acknowledge the contributions of those who helped to keep it on course. Firstly, my supervisors Prof. Ian Manners, Dr. Annela Seddon and Dr. Valeksa Ting. In particular, thanks must go to Valeska for coming in towards the end of this project and helping to get everything over the line. I would also like to thank the Manners group for the simple provision of a desk and lab space, something which I would not have had otherwise and which made life a lot easier!

Outside of the lab, the rest of the DTC13 cohort have been through the past 5 years with me, especially Manu and Jamie who have shared in the numerous incidents along the way. I have also been lucky to have Manners group members past and present for company and Friday pub trips, including but not limited to: Alex, Charlotte, Diego G, Horatio, Huda, John, Liam, Sam and Steve, with special mentions to my co-inhabitants of N418, currently: Ali, Becs, Diego, Marius, Nikki, Theresa, and Vince. Without them the past few years would not have been anywhere near as enjoyable.

My parents have been a source of support through the highs and the lows, and I would especially like to thank them for the qualities of resilience and perseverance, which turned out to be quite useful on a regular basis.

Last, but by no means least, I would like to thank Dr. George Whittell for his great contribution from day one. I would have learnt far less without his help, chats and suggestions, and it's fair to say that my time here would have been a lot harder and less productive without having him on side.

Author’s Declaration

I declare that the work in this dissertation was carried out in accordance with the requirements of the University's *Regulations and Code of Practice for Research Degree Programmes* and that it has not been submitted for any other academic award. Except where indicated by specific reference in the text, the work is the candidate's own work. Work done in collaboration with, or with the assistance of, others, is indicated as such. Any views expressed in the dissertation are those of the author.

SIGNED: ..... DATE: .....

Table of Contents

List of Figures ..... **xi**
List of Tables ..... **xxiii**
List of Abbreviations ..... **xxiv**
Chapter 1: Introduction **1**

1.1. Responsive Polymers from Liquid Crystals 1
1.1.1. Liquid Crystals 1
1.1.2. Identification of Liquid Crystal Mesophases 2
1.1.3. Liquid Crystal Elastomers 5
1.2. Processing of Liquid Crystal Elastomers 8
1.2.1. Actuators with Complex Director Profiles 8
1.2.2. Actuators with a Single Director 12
1.2.2.1. Two-Step Crosslinking 12
1.2.2.2. Covalent Adaptable Networks 14
1.2.2.3. Composite Structures 16
1.3. Thermoplastic Liquid Crystal Elastomers 19
1.3.1. Block Copolymers and Microphase Segregation 19
1.3.2. Microphase Segregation in Liquid Crystal Block Copolymers 23
1.3.3. Thermoplastic Elastomers 24
1.4. Processing of Thermoplastic Fibres 26
1.4.1. Melt Processing 26
1.4.2. Solution Processing 32
1.4.3. Electrospinning of Liquid Crystal Polymers 36
1.5. Summary 38
1.6. Thesis Summary 39
1.7. References 40

Chapter 2: Synthesis and Thermal Analysis of Thermoplastic Side-Chain Liquid Crystal Elastomers **47**

2.1. Introduction 47
2.2. Results and Discussion 50
2.2.1. Mesogen Synthesis 50
2.2.1.1. M1, M1-Allyl, M1-Thiol Synthesis 50
2.2.1.2. M2 Synthesis 52
2.2.2. Polymer Backbone Synthesis 54
2.2.2.1. PS-*b*-PMVS-*b*-PS Triblock Copolymer Synthesis 54
2.2.2.2. PMVS Homopolymer 56
2.2.2.3. Repeated PS-*b*-PMVS-*b*-PS Triblock Copolymer Synthesis 58
2.2.3. Linking Group Attachment 58

2.2.3.1. Photoinitiated Thiol-Ene Click Reaction....60
2.2.3.2. Thermally Initiated Thiol-Ene Click Reaction....62
2.2.3.3. Conversion of Carboxylic Acid to NHS Ester....62
2.2.4. Mesogen Attachment Methods....64
2.2.4.1. Displacement of NHS Ester with M2....64
2.2.4.2. Coupling of M1/M2 to P-3/P-5 by a Carbodiimide Mediated Reaction....64
2.2.4.3. Coupling of M1 to PMVS-3 by a Carbodiimide Mediated Reaction....66
2.2.4.4. Larger Scale Functionalisation of P-3 with M1 by a Carbodiimide Mediated Reaction....68
2.2.5. Conversion of Residual Carboxylic Acid Groups to Methyl Esters....69
2.2.5.1. P-3-COOMe....69
2.2.5.2. P*-3(AIBN)-COOMe....70
2.2.5.3. P-3-M1(65)-COOMe(35)....70
2.2.5.4. P*-3(AIBN)-M1-COOMe....70
2.2.6. Thermal Analysis....71
2.2.6.1. Effect of Linking Group....74
2.2.6.2. Effect of Ester/Amide Linkage....76
2.2.6.3. Effect of Converting Carboxylic Acid to Methyl Ester....77
2.2.6.4. PMVS Homopolymer....79
2.2.6.5. Summary of Thermal Analysis....80
2.2.7. UV-Response Test....80
2.3. Conclusions....82
2.4. Experimental....83
2.4.1. Materials and Methods....83
2.4.2. Synthetic Procedures....85
2.4.2.1. Mesogen Synthesis....85
2.4.2.2. Polymer Backbone Synthesis....90
2.4.2.3. Linking Group Attachment....92
2.4.2.4. Mesogen Attachment....96
2.4.3. UV Response....104
2.5. References....105

Chapter 3: Effect of Tensile Strain on the Morphology of Thermoplastic Liquid Crystal Elastomers....107

3.1. Introduction....107
3.2. Results and Discussion....109
3.2.1. Theoretical Volume Fraction....109
3.2.2. Room Temperature Morphology....112
3.2.2.1. P-3....112
3.2.2.2. P-3-M1(82)-COOH(18) and P-3-M2(80)-COOH(20)....114
3.2.2.3. P-3-M1(65)-COOH(35)....117
3.2.2.4. Manually Aligned P-3-M1(82)-COOH(18)....118
3.2.2.5. Manually Aligned P-3-M1(65)-COOH(35)....123

3.2.3. Effect of Isotropic Transition on Polymer Morphology 125
3.2.3.1. Manually Aligned P-3-M1(82)-COOH(18) 125
3.2.3.2. Manually Aligned P-3-M1(65)-COOH(35) 130
3.3. Conclusions 134
3.4. Experimental 134
3.4.1. Sample Preparation 134
3.4.2. SAXS 135
3.4.3. TEM 136
3.5. References 137

Chapter 4: Rheology of Thermoplastic Liquid Crystal Elastomers for Melt Processing 139

4.1. Introduction 139
4.2. Discussion and Results 141
4.2.1. Rheology of Standard Materials 141
4.2.1.1. Amplitude Sweeps 141
4.2.1.2. Frequency Sweeps 143
4.2.2. Rheology of Thermoplastic Liquid Crystal Elastomers 147
4.2.2.1. Amplitude Sweeps 147
4.2.2.2. Frequency Sweeps 149
4.2.2.3. Investigation of T_{ODT} 154
4.2.3. Impact of Polymer Modifications on Melt Behaviour 157
4.2.3.1. Amplitude Sweeps 157
4.2.3.2. Thermally Initiated Thiol-Ene Click Reaction 158
4.2.3.3. Conversion of Carboxylic Acid Groups to Methyl Esters 159
4.2.3.4. Conversion of Residual Carboxylic Acid Groups to Methyl Esters for Liquid Crystal Elastomers 164
4.2.3.5. Comparison of Liquid-Crystal Functionalised PMVS Homopolymer with Triblock Copolymer 169
4.2.3.6. Elastic Behaviour in P-3-M1(65)-COOMe(35) Above T_{ODT} 172
4.3. Conclusions 173
4.4. Experimental 174
4.4.1. Rheology 174
4.4.1.1. Procedure 174
4.4.1.2. Amplitude Sweep 174
4.4.1.3. Frequency Sweep 175
4.4.2. Differential Scanning Calorimetry 175
4.5. References 176

Chapter 5: Suitability of P-3-M1(65)-COOH(35) for Processing by Electrospinning 178

5.1. Introduction 178
5.2. Results and Discussion 179

5.2.1. Microphase Segregated Morphology of Hand-Drawn Fibres 179
5.2.2. Electrospinning Fibres of P-3-M1(65)-COOH(35) 185
5.2.2.1. Determination of Conditions for Electrospinning 185
5.2.2.2. Confirmation of Ordered Nematic Mesophase in Fibres 187
5.2.2.3. Improving Fibre Alignment 188
5.2.3. Responsive Behaviour of Aligned Fibres 195
5.2.3.1. Response to UV Irradiation 195
5.2.3.2. Response to Heating Above T_{iso} 197
5.3. Conclusions 199
5.4. Experimental 199
5.4.1. Hand-Drawn Fibres 199
5.4.2. SAXS 199
5.4.3. Electrospinning 200
5.4.4. Polarised Optical Microscopy 201
5.5. References 202

Chapter 6: Conclusions and Future Work 203
6.1. Conclusions 203
6.1.1. Synthesis of a Thermoplastic Liquid Crystal Elastomer 203
6.1.2. Suitability of Thermoplastic Liquid Crystal Elastomers for Melt Processing 204
6.1.3. Suitability of Thermoplastic Liquid Crystal Elastomers for Processing from Solution 204
6.2. Future Work 205
6.2.1. Extrusion of Thermoplastic Liquid Crystal Elastomers 205
6.2.2. Electrospinning of Thermoplastic Liquid Crystal Elastomers 205
6.2.3. PMVS Homopolymer 206
6.3. References 207

Appendix A: Supporting Information for Chapter 2 208
A.1. Mesogen Synthesis 208
A.2. Polymer Backbone Synthesis 216
A.3. Linking Group Attachment 220
A.4. Mesogen Attachment 226
A.5. Conversion of Carboxylic Acid Groups to Methyl Esters 235
A.6. Thermal Analysis 240

Appendix B: Supporting Information for Chapter 3 241
Appendix C: Supporting Information for Chapter 4 243

List of Figures

Figure 1-1. Mesophases formed by calamitic (or rod-like) liquid crystal mesogens. 1

Figure 1-2. Definition of the angle used for calculation of order in a calamitic liquid crystal material. 2

Figure 1-3. Polarised optical microscopy of a birefringent sample. Reproduced from reference 3 - Nikon. 4

Figure 1-4. Polarised Optical Microscopy image of the Schlieren texture for a nematic mesophase, with black areas indicating isotropic regions. Pictures are taken at 5 second intervals whilst disrupting the mesophase with UV irradiation, resulting in increasing areas of isotropic character. Reproduced with permission from reference 4 – American Chemical Society. 4

Figure 1-5. Mesogens can be attached either end-on (a) or side-on (b) to the polymer backbone to form side-chain liquid crystal polymers or are incorporated into the polymer backbone to give main-chain liquid crystal polymers (c). Reproduced with permission from reference 6 - John Wiley & Sons. 5

Figure 1-6. The formation of a LC monodomain acts to draw polymer chains along the director. On triggering the transition to the isotropic state both the LC and the polymer backbone adopt an isotropic morphology, resulting in a contraction along the director and an expansion perpendicular to it. Adapted with permission from reference 6 - John Wiley & Sons. 6

Figure 1-7. Isomerisation of an azobenzene group from the linear *trans* to the bent *cis* conformation occurs under irradiation with light of λ = 365 nm and can be reversed by exposure to visible light or on heating. 7

Figure 1-8. Light-driven motor designed by Ikeda *et al*. Irradiation of different regions with either UV or visible light resulted in contractions and expansions which drove the rotation of an LCE belt around a pulley. Reproduced with permission from reference 10 - John Wiley & Sons. 7

Figure 1-9. If the director profile is rotated through the thickness of a film, heating above the T_{iso} results in contraction and expansion in different regions and so curvature as the order parameter, *S*, decreases. Reproduced with permission from reference 15 - Elsevier. 9

Figure 1-10. For the spatially patterned LCEs reported in Reference 16, low viscosity LCP precursors were synthesised by mixing the mesogen with a primary amine chain extender. These were oriented in an alignment cell where the step growth polymerisation continued before crosslinking.[16] 9

Figure 1-11. Spatial patterning of complex director profiles such as that in (a) results in three-dimensional deformation on heating (b) with enough force to lift a weight (c). Reproduced with permission from reference 16 - The American Association for the Advancement of Science. 10

Figure 1-12. The photoalignment surface (a) was used to control the orientation of a main-chain LCE. It was shown that the angle between the director and the loading direction (b) had a significant impact on the mechanical properties of the sample (c). This was used to control the local strain environment encountered in soft, stretchable electronics under load. Reproduced with permission from reference 20 under a Creative Commons Licence. 11

Figure 1-13. Layered LCE structure displaying 6 mm stroke when lifting 120x its own weight. Scale bar is 1 cm. Reproduced with permission from reference 21 under a Creative Commons Licence 11

Figure 1-14. Structure of the LCE proposed to perform as artificial muscle by de Gennes. Crosslinking of the triblock copolymer (a) resulted in the lamellar structure (b). Reproduced with permission from reference 31 - John Wiley & Sons.....13

Figure 1-15. Method behind forming LCE actuators through exchangeable disulfide bonds. The stretched geometry can be fixed on heating or application of UV which promotes bond exchange. Reproduced with permission from reference 41 – American Chemical Society. 15

Figure 1-16. Altering the fibre angle in laminate structures (a) results in bends and twists on contraction of a shape memory alloy, which was used to propel a soft turtle robot (b). Reproduced with permission from reference 62 - IOP Publishing.....18

Figure 1-17. Generic phase diagram for an AB block copolymer from the weak (χN=10) to strong (χN=50+) segregation limit. Reproduced with permission from references 67 and 68 - American Chemical Society.....20

Figure 1-18. Definition of scattering angle, 2θ, and azimuthal angle, φ, in 2D SAXS.....22

Figure 1-19. Styrenic TPE. Light regions correspond to spheres formed by PS end blocks which act as physical crosslinks. Dark lines correspond to the continuous phase of the soft midblock. 24

Figure 1-20. Structure of UV-responsive LC-functionalised thermoplastic from Reference 82. The rod-like mesogen was attached to the PS-*b*-PMVS-*b*-PS triblock copolymer backbone *via* a hydrosilylation reaction. 25

Figure 1-21. Operating principle for rotational rheometer with parallel plate geometry.....27

Figure 1-22. Two plates model for rotational rheology. *F* is the force acting on area, *A*. The resulting shear strain is obtained by dividing the deformation, *s*, by the sample thickness, *h*, or by tanφ. Reproduced from reference 85. 28

Figure 1-23*.* Typical flow diagram for thermoplastic polymers with increasing shear rate. γ is the shear rate and η the viscosity. 29

Figure 1-24. Proposed flow diagram for liquid crystalline polymers. γ is the shear rate and η the viscosity.....31

Figure 1-25. Microfluidic setup developed by Ohm *et al*. for formation of a main-chain LCE fibre. Reproduced with permission from reference 93 - John Wiley & Sons. 33

Figure 1-26. Basic schematic of electrospinning setup and Taylor cone. Reproduced with permission from reference 102 - Elsevier. 34

Figure 1-27. Aligned fibres collected between parallel electrodes. Disordered fibres apparent on Si electrodes. Reproduced with permission from reference 105 - American Chemical Society. ...35

Figure 1-28. Fibres obtained by electrospinning of a photocrosslinkable main-chain LCP with (a) 5.0 wt % and (b) 7.2 wt % solutions. Reproduced with permission from reference 116 - John Wiley & Sons.....37

Figure 1-29. Optimisation of SC-LCP fibres. (a) Pure LCP, (b) With addition of 5% small molecule LC, (c) With addition of 0.05 mL of Et_3N and (d) Using LCP:PEO blend of 20:1. Reproduced with permission from reference 118 - Springer Nature. 38

Figure 2-1. Structures of UV-responsive LC-functionalised thermoplastics.[10,11] 48

Figure 2-2. Method of attaching modified mesogen M1 to PMVS block of a PS-*b*-PMVS-*b*-PS thermoplastic elastomer.[10] PDMS block omitted for clarity. DEAD = diethyl azodicarboxylate, TPP = triphenylphosphine. 49

Figure 2-3. Reaction scheme for allylation reaction used to convert **M1** to **M1-Allyl**. 50

Figure 2-4. Reaction scheme for attachment of 1,4-butanedithiol to **M1-Allyl**. AIBN = 2,2′-azobis(2-methylpropionitrile). 51

Figure 2-5. Reaction scheme for Boc-protection and reaction of 3-aminophenol with the diazonium salt to give **I-M2-Boc**. PEG = poly(ethylene glycol) average mol. wt. 200 g mol^{-1}. 52

Figure 2-6. Reaction scheme for conversion of **I-M2-Boc** to **M2**. DCC = *N,N*′-dicyclohexylcarbodiimide, TFA= trifluoroacetic acid. 53

Figure 2-7. Reaction scheme for synthesis of the **PS-*b*-PMVS-*b*-PS** triblock copolymer..... 54

Figure 2-8. GPC data for **PS-*b*-PMVS-*b*-PS** triblock copolymer aliquots. 56

Figure 2-9. Reaction scheme for the synthesis of the **PMVS** homopolymer. 57

Figure 2-10. GPC data for **PMVS** homopolymer. 57

Figure 2-11. General scheme for thiol-ene click reactions. 58

Figure 2-12. Summary of attachment methods. A carboxylic acid-terminated linking group was first attached to the PMVS midblock by a thiol-ene click reaction, before attachment of the mesogen by either displacement of a labile *N*-hydroxysuccinimide (NHS) ester group or by a carbodiimide mediated esterification reaction. Structure of triblock copolymer backbone simplified for clarity. PS = polystyrene. DCC = *N,N*′-dicyclohexylcarbodiimide, DMAP = 4-dimethylaminopyridine. 59

Figure 2-13. Reaction scheme for addition of a carboxylic acid-terminated linking group to the PMVS block of the triblock copolymer. PS = polystyrene. DMPA = 2,2-dimethoxy-2-phenylacetophenone. 60

Figure 2-14. Reaction scheme for addition of the linking group to **PMVS** by the photoinitiated thiol-ene click reaction. DMPA = 2,2-dimethoxy-2-phenylacetophenone. 61

Figure 2-15. Reaction scheme for conversion of **P-3** to **P-3-NHS**. PS = polystyrene. DCC = *N,N*′-dicyclohexylcarbodiimide, DMAP = 4-dimethylaminopyridine. 63

Figure 2-16. GPC data for **P-3** and **P-3-NHS** demonstrating a clear shift to lower retention volume on functionalisation with the NHS ester group..... 63

Figure 2-17. Reaction scheme for coupling of **M1** or **M2** to **P-3** or **P-5** with a DCC mediated coupling reaction to give the LC-functionalised triblock copolymer. DCC = *N,N*′-dicyclohexylcarbodiimide, DMAP = 4-dimethylaminopyridine. General structure, for **P-3**, n=1. For **P-5**, n=3. For **M1**, E= O. For **M2**, E=NH. Backbone simplified for clarity. 66

Figure 2-18. Reaction scheme for coupling of **M1** to **PMVS-3** with a DCC mediated coupling reaction to give **PMVS-3-M1(84)-COOH(16)**. DCC = *N,N*′-dicyclohexylcarbodiimide, DMAP = 4-dimethylaminopyridine. 67

Figure 2-19. GPC data for **PMVS** and **PMVS-3-M1(86)-COOH(14)**..... 68

Figure 2-20. GPC data for **P*-3(AIBN)-M1-COOMe** and **P-3-M1(65)-COOMe(35)** indicating a comparable hydrodynamic radius and so molecular weight. 71

Figure 2-21. TGA thermograms for **PS-*b*-PMVS-*b*-PS**, **P-3**, **P-3-M1(82)-COOH(18)**, **P-3-M2(80)-COOH(20)**, **P-5** and **P-5-M1(86)-COOH(14)**. 72

Figure 2-22. DSC results collected on the second cycle for the **PS-*b*-PMVS-*b*-PS** triblock copolymer, **P-3** and **P-5** on both heating (lower) and cooling (upper). Curves scaled in y-axis for clarity.....75

Figure 2-23. DSC results collected on the second cycle for **P-3-M1(82)-COOH(18)** and **P-5-M1(86)-COOH(14)** on both heating (lower) and cooling (upper).....76

Figure 2-24. DSC results collected on the second cycle for **P-3-M1(82)-COOH(18)** and **P-3-M2(80)-COOH(20)** on both heating (lower) and cooling (upper).....77

Figure 2-25. DSC results collected on the second cycle for **P-3-COOMe** and **P*-3(AIBN)-COOMe** on both heating (lower) and cooling (upper).....77

Figure 2-26. DSC results collected on the second cycle for **P-3-M1(65)-COOH(35)** and **P-3-M1(65)-COOMe(35)** on both heating (lower) and cooling (upper).....78

Figure 2-27. DSC results collected on the second cycle for **P*-3(AIBN)-M1-COOMe** on both heating (lower) and cooling (upper).....79

Figure 2-28. DSC results collected on the second cycle for **PMVS-M1(84)-COOH(16)** on both heating (lower) and cooling (upper).....79

Figure 2-29. Experimental setup for UV-response test. The orange polymer film was adhered between the two green end tabs and loaded into the tensile test machine.....81

Figure 2-30. Force-time curve for aligned **P-3-M1(82)-COOH(18)** during photocontraction test. The shaded regions indicate the time when the UV lamp was on and unshaded regions indicate when the visible light was on. After the initial extension a clear increase in force of around 3 mN was measured on turning on UV. A small relaxation was seen in the period where UV was off. ..81

Figure 2-31. Structure of **I-M1** with labelling used in ^{1}H NMR spectroscopy assignments. 85

Figure 2-32. Structure of **M1** with labelling used in ^{1}H NMR spectroscopy assignments.....86

Figure 2-33. Structure of **M1-Allyl** with labelling used in ^{1}H NMR spectroscopy assignments...86

Figure 2-34. Structure of **M1-Thiol** with labelling used in ^{1}H NMR spectroscopy assignments. 87

Figure 2-35. Structure of **3-aminophenol-Boc** with labelling used in ^{1}H NMR spectroscopy assignments.....88

Figure 2-36. Structure of **I-M2-Boc** with labelling used in ^{1}H NMR spectroscopy assignments..88

Figure 2-37. Structure of **M2-Boc** with labelling used in ^{1}H NMR spectroscopy assignments.....89

Figure 2-38. Structure of **M2-Boc** with labelling used in ^{1}H NMR spectroscopy assignments.....90

Figure 2-39. Structure of **P-3** with labelling used in ^{1}H NMR spectroscopy assignments. 92

Figure 2-40. Structure of **P-5** with labelling used in ^{1}H NMR spectroscopy assignments. 93

Figure 2-41. Structure of **PMVS-3** with labelling used in ^{1}H NMR spectroscopy assignments.....94

Figure 2-42. Structure of **P*-3(AIBN)** with labelling used in ^{1}H NMR spectroscopy assignments. 95

Figure 2-43. Structure of **P-3-M1(82)-COOH(18)** and **P-3-M1(65)-COOH(35)** (E=O). Structure of **P-3-M2(80)-COOH(20)** (E=NH) with labelling used in ^{1}H NMR spectroscopy assignments. ..97

Figure 2-44. Structure of **P-5-M1-(86)-COOH(14)** with labelling used for ^{1}H NMR spectroscopy assignments.....98

Figure 2-45. Structure of **PMVS-3-M1(84)-COOH(16)** with labelling used for ^{1}H NMR spectroscopy assignments. 100

Figure 2-46. Structure of **P-3-COOMe** with labelling used for ^{1}H NMR spectroscopy assignments....101

Figure 2-47. Structure of **P*-3(AIBN)-COOMe** with labelling used for ^{1}H NMR spectroscopy assignments....101

Figure 2-48. Structure of **P-3-M1(65)-COOMe(35)** with labelling used for ^{1}H NMR spectroscopy assignments. 102

Figure 2-49. Structure of **P*-3(AIBN)-M1-COOMe** with labelling used for ^{1}H NMR spectroscopy assignments....103

Figure 2-50. Experimental setup used for UV response test....104

Figure 3-1. Characteristic 2D SAXS scattering pattern for systems with varying levels of orientational order. Reproduced from Reference 13. 108

Figure 3-2. Background subtracted room temperature SAXS data for **P-3** after azimuthal integration showing no clear peaks suggesting a disordered morphology. Inset – 2D SAXS pattern showing no rings indicative of long-range order. 113

Figure 3-3. Representative TEM image for **P-3** showing no microphase separation between the PS and PMVS blocks. The relatively large features suggest that the block copolymer is not homogeneous at room temperature. 113

Figure 3-4. Background subtracted room temperature SAXS data for **P-3-M1(82)-COOH(18)** after azimuthal integration. The q^* peak at 0.174 nm^{-1} corresponds to an average inter-sphere spacing of 36.1 nm, whilst the q_F peak around 0.43 nm^{-1} corresponds to an average sphere radius of 15 nm. Inset – 2D SAXS pattern showing slightly anisotropic scattering. 114

Figure 3-5. Background subtracted room temperature SAXS data for **P-3-M2(80)-COOH(20)** after azimuthal integration. The q^* peak at 0.181 nm^{-1} corresponds to an average inter-sphere spacing of 34.8 nm, whilst the q_F peak around 0.46 nm^{-1} corresponds to an average sphere radius of 14 nm. Inset – 2D SAXS pattern showing isotropic scattering....115

Figure 3-6. Representative TEM image for **P-3-M1(82)-COOH(18)** showing disordered spheres of PS in a darker matrix of the LC-functionalised PMVS....116

Figure 3-7. Representative TEM image for **P-3-M2(80)-COOH(20)** showing disordered spheres of PS in a darker matrix of the LC-functionalised PMVS. 117

Figure 3-8. Background subtracted room temperature SAXS data for **P-3-M1(65)-COOH(35)** after azimuthal integration. The q^* peak at 0.158 nm^{-1} corresponds to an average inter-sphere spacing of 39.8 nm, whilst the q_F peak around 0.31 nm^{-1} corresponds to an average sphere radius of 20 nm. Inset – 2D SAXS pattern showing isotropic scattering....118

Figure 3-9. Definition of 0° and 90° directions used for anisotropic integrations of SAXS results for **P-3-M1(82)-COOH(18)**. 119

Figure 3-10. Distribution of spherical hard domains in a soft phase for (a) undeformed polymer, (b) after deformation of both phases and (c) after deformation of soft phase only. 119

Figure 3-11. Comparison of model results with experimental data for (A) undeformed and (B) deformed films of **P-3-M1(82)-COOH(18)**....120

Figure 3-12. Representative TEM image for aligned **P-3-M1(82)-COOH(18)** showing spheres of PS in a darker matrix of LC-functionalised PMVS. 121

Figure 3-13. Background subtracted room temperature SAXS data for aligned **P-3-M1(82)-COOH(18)** after integrating around the 0° or 90° direction. The q^* peak for the 0° direction at 0.123 nm^{-1} corresponds to an average spacing of 51.9 nm, and that in the 90° direction at 0.217 nm^{-1} corresponds to an average inter-sphere spacing of 29.0 nm. 122

Figure 3-14. Definition of 40° and 130° directions used for anisotropic integrations of SAXS results for **P-3-M1(65)-COOH(35).** 123

Figure 3-15. Background subtracted room temperature SAXS data for aligned **P-3-M1(65)-COOH(35)** after integrating around the 40° or 130° direction. The q^* peak for the 40° direction at 0.150 nm^{-1} corresponds to an average inter-sphere spacing of 42.5 nm, and that in the 130° direction at 0.165 nm^{-1} corresponds to an average inter-sphere spacing of 38.1 nm. The q_F peaks around 0.37 nm^{-1} in the 40° and 0.31 nm^{-1} in the 130° direction indicate an average sphere radius of 17 and 20 nm respectively. 124

Figure 3-16. Background subtracted VT-SAXS data for aligned **P-3-M1(82)-COOH(18)** taken after equilibrating at 80 °C, then heating to 150 °C and cooling to 80 °C for two cycles. The q^* peak retains a shift towards increased spacing after heating through T_{iso}, suggesting that the anisotropic structure obtained by stretching remains to some extent after two heating cycles. 126

Figure 3-17. Background subtracted VT-SAXS data for aligned **P-3-M1(82)-COOH(18)** after integrating around the 0° or 90° direction only. The two peaks remain separated, with the intensity of the 0° direction peak decreasing with increasing numbers of heating/cooling cycles indicating a decrease in the level of long-range order in the sample. 127

Figure 3-18. Background subtracted 2D SAXS results for aligned **P-3-M1(82)-COOH(18)** at 80 °C (left) and 150 °C (right). Dashed line indicates 0° direction used for Herman orientation parameter calculation. 129

Figure 3-19. Calculated values for the Herman orientation parameter for aligned **P-3-M1(82)-COOH(18)** on heating (filled) and cooling (unfilled). A decrease in *f(H)* is seen centred around T_{iso} of 120 °C for heating cycles and an increase on cooling cycles, suggesting the nematic mesophase is lost on heating but reforms to some extent on cooling. 129

Figure 3-20. Background subtracted VT-SAXS data for aligned **P-3-M1(65)-COOH(35)** after integrating around the 130° direction. After heating through T_{iso} the intensity of the q^* peak decreases, and the spacing shifts towards larger values in reciprocal space. The change in spacing then follows the trends expected of an isotropic structure. The arrow indicates the location of spherical form factor peak, which increases in intensity with each cycle. 131

Figure 3-21. Background subtracted VT-SAXS data for aligned **P-3-M1(65)-COOH(35)** after integrating around the 40° direction. After heating through T_{iso} the intensity of the q^* peak decreases, and the spacing shifts towards larger values in reciprocal space. The change in spacing then follows the trends expected of an isotropic material. 132

Figure 3-22. Background subtracted 2D SAXS results for aligned **P-3-M1(65)-COOH(35)** at 80 °C (left) and 150 °C (right). Dashed line indicates 40° direction used for Herman orientation parameter calculation. 132

Figure 3-23. Calculated values for the Herman orientation parameter for aligned **P-3-M1(65)-COOH(35)** on heating (filled) and cooling (unfilled). A decrease in *f(H)* is seen starting from 85 °C and increasing in rate from the T_{iso} of 99 °C for the first heating cycle. After this cycle it was apparent that the material adopted an isotropic structure. 133

Figure 4-1. Structures of the standard 3D printing materials PLA, ABS and TPU. 140

Figure 4-2. Amplitude sweep results for ABS, PLA and TPU for determination of the LVE region. 142

Figure 4-3. Lissajous diagrams generated for ABS, PLA and TPU at strains of 5, 10 and 0.1% respectively, which confirm measurements were taken within the LVE region.....143

Figure 4-4. Frequency sweep results for the change in viscosity of ABS, PLA and TPU with increasing angular frequency. 144

Figure 4-5. Frequency sweep results for the change in shear modulus of ABS, PLA and TPU with increasing angular frequency at selected temperatures. 146

Figure 4-6. Results of amplitude sweeps for **PS-*b*-PMVS-*b*-PS**, **P-3**, **P-3-M1(65)-COOH(35)** and **P-3-M2(80)-COOH(20)**. 148

Figure 4-7. Lissajous diagrams for **PS-*b*-PMVS-*b*-PS**, **P-3**, **P-3-M1(65)-COOH(35)** and **P-3-M2(80)-COOH(20)** at 3, 10, 10 and 10% strain respectively. 149

Figure 4-8. Variation in complex viscosity with angular frequency (left) and temperature (right) for **PS-*b*-PMVS-*b*-PS**.....150

Figure 4-9. Variation in complex viscosity with angular frequency (left) and temperature (right) for **P-3**.....150

Figure 4-10. Variation in complex viscosity with angular frequency (left) and temperature (right) for **P-3-M1(65)-COOH(35)**. 151

Figure 4-11. Variation in complex viscosity with angular frequency (left) and temperature (right) for **P-3-M2(80)-COOH(20)**. 151

Figure 4-12. Frequency sweep results for the change in shear modulus of **PS-*b*-PMVS-*b*-PS** with increasing angular frequency at selected temperatures. 152

Figure 4-13. Frequency sweep results for the change in shear modulus of **P-3**, **P-3-M1(65)-COOH(35)** and **P-3-M2(80)-COOH(20)** with increasing angular frequency at selected temperatures. 153

Figure 4-14. Plot of G' against G'' for ABS. The lack of temperature dependence indicates the polymer is above the T_{ODT}.....154

Figure 4-15. Plot of G' against G'' for **PS-*b*-PMVS-*b*-PS**. The lack of temperature dependence indicates the polymer is above the T_{ODT}. 155

Figure 4-16. G' against G'' for **P-3** and **P-3-M1(65)-COOH(35)**. Both polymers displayed a strong temperature dependence, and so are below the T_{ODT} at all temperatures measured.....156

Figure 4-17. Frequency sweep results for the change in shear modulus of **P*-3(AIBN)** with increasing angular frequency at selected temperatures. 158

Figure 4-18. Plot of G' against G'' for **P*-3(AIBN)**. The strong temperature dependence indicates the polymer is above the T_{ODT} between 120-150 °C, before temperature independence is observed from 150-160 °C suggesting that the PS and PMVS blocks are mixing. Above 160 °C the curve is strongly temperature dependent again, suggesting that the structure is heterogeneous.....159

Figure 4-19. Variation in complex viscosity with temperature for **P-3-COOMe**.....160

Figure 4-20. Variation in complex viscosity with temperature for **P*-3(AIBN)** and **P*-3(AIBN)-COOMe**. 160

Figure 4-21. Plot of G' against G'' for **P-3-COOMe** (left) and **P*-3(AIBN)-COOMe** (right). Both polymers give temperature independent results suggesting that they are above the T_{ODT}.

However, **P*-3(AIBN)-COOMe** appears to return to temperature dependent behaviour from 170 °C. 161

Figure 4-22. Frequency sweep results for the change in shear modulus of **P-3-COOMe** with increasing angular frequency at selected temperatures. 162

Figure 4-23. Frequency sweep results for the change in shear modulus of **P*-3(AIBN)-COOMe** with increasing angular frequency. 163

Figure 4-24. Plot of G' against G'' for **P-3-M1(65)-COOMe(35)**. From 120-140 °C the curves are independent of temperature. However, from 150 °C they become temperature dependent which suggests that a change in the polymer microstructure has occurred, raising the T_{ODT}. Filled symbols indicate an isotropic state whereas unfilled symbols indicate a nematic state. 164

Figure 4-25. Variation in complex viscosity with angular frequency (left) and temperature (right) for **P-3-M1(65)-COOMe(35)**. Filled symbols indicate an isotropic state whereas unfilled symbols indicate a nematic state. 165

Figure 4-26. Frequency sweep results for the change in shear modulus of **P-3-M1(35)-COOMe(65)** with increasing angular frequency. 166

Figure 4-27. Variation in complex viscosity with angular frequency (left) and temperature (right) for **P*-3(AIBN)-M1-COOMe**. Filled symbols indicate an isotropic state whereas unfilled symbols indicate a nematic state. 167

Figure 4-28. Plot of G' against G'' for **P*-3(AIBN)-M1-COOMe**. The strong temperature dependence suggests that the polymer is above T_{ODT} at all temperatures measured. 167

Figure 4-29. Frequency sweep results for the change in shear modulus of **P*-3(AIBN)-M1-COOMe** with increasing angular frequency. 168

Figure 4-30. DSC results for **P-3-M1(65)-COOMe(35)** taken on heating (lower) and cooling (upper). Samples were obtained before (dashed) and after (solid) rheological measurements. Only the sheared rheology sample gave a peak corresponding to the nematic-isotropic transition at 95 °C. 169

Figure 4-31. Frequency sweep results for the change in shear modulus of **PMVS-3-M1(84)-COOH(16)** with increasing angular frequency at selected temperatures. 170

Figure 4-32. Variation in complex viscosity with temperature for **PMVS-3-M1(84)-COOH(16)**. 171

Figure 5-1. Background subtracted room temperature SAXS data for fibres of **P-3-M1(65)-COOH(35)** before and after stretching. The q^* peaks at 0.146 and 0.159 nm^{-1} correspond to an average spacing between PS domains of 39.5 and 43.0 nm for the unstretched and stretched fibre respectively. The broad q_F peak at 0.39 nm^{-1} indicates an average PS domain radius of 16 nm. 180

Figure 5-2. Comparison of model results with experimental data for (A) unstretched and (B) stretched fibres of **P-3-M1(65)-COOH(35)**. 181

Figure 5-3. Definition of 0° and 90° directions used for anisotropic integrations of SAXS results and fibre direction. 182

Figure 5-4. Background subtracted room temperature SAXS data for undeformed fibre of **P-3-M1(65)-COOH(35)**. The q^* peaks at 0.152 and 0.174 nm^{-1} correspond to an average spacing between PS domains of 36.1 and 41.3 nm respectively. Inset – 2D SAXS pattern showing weakly elliptical response. 183

Figure 5-5. Background subtracted room temperature SAXS data for stretched fibre of **P-3-M1(65)-COOH(35)**. The q^* peaks at 0.137 and 0.184 nm^{-1} correspond to an average spacing between PS domains of 45.9 and 34.1 nm respectively. Inset – 2D SAXS pattern showing elliptical, anisotropic response. 184

Figure 5-6. Short fibres obtained with 40 wt% solution of **P-3-M1(65)-COOH(35)** in DMF. ...186

Figure 5-7. Longer fibres obtained from a 32.5 wt% solution of **P-3-M1(65)-COOH(35)** in DMF/THF. 186

Figure 5-8. Images of fibres taken under (a) normal light and (b) crossed polarisers. Bright regions in (b) correspond to areas with LC mesophase present. 187

Figure 5-9. Images of fibres taken under (a) normal light and (b) crossed polarisers. Bright regions in (b) correspond to areas with LC mesophase present. 188

Figure 5-10. Images of fibres obtained at a rotation speed of 800 rpm taken under: (a) and (c) normal light and (b) and (d) crossed polarisers. Bright regions in (b) and (d) correspond to areas with LC mesophase present. Images (c) and (d) were obtained by rotating (a) and (b) through 45°. 190

Figure 5-11. Images of fibres obtained at a rotation speed of 950 rpm under normal light. 191

Figure 5-12. Images of fibres obtained at a rotation speed of 1100 rpm taken under: (a) and (c) normal light and (b) and (d) crossed polarisers. Bright regions in (b) and (d) correspond to areas with LC mesophase present. Images (c) and (d) were obtained by rotating (a) and (b) through 45°. 192

Figure 5-13. Images of fibres taken under (a) normal light and (b) crossed polarisers. Bright regions in (b) correspond to areas with LC mesophase present. 193

Figure 5-14. Images of fibres obtained at a rotation speed of 800 rpm taken under: (a) and (c) normal light and (b) and (d) crossed polarisers. Bright regions in (b) and (d) correspond to areas with LC mesophase present. Images (c) and (d) were obtained by rotating (a) and (b) through 45°. 194

Figure 5-15. Images of fibres collected on a flat surface taken before (a and b) and after (c and d) irradiation with UV light. Images (a) and (c) are taken under normal light, and (b) and (d) taken under crossed polarisers. The level of birefringence observed in the fibre was greatly reduced after irradiation, confirming disruption of the nematic mesophase. 196

Figure 5-16. Images of fibres collected on a rotating wheel taken before (a and b) and after (c and d) irradiation with UV light. Images (a) and (c) are taken under normal light, and (b) and (d) taken under crossed polarisers. The level of birefringence observed in the fibre was greatly reduced after irradiation, confirming disruption of the nematic mesophase. 197

Figure 5-17. Images taken at 90, 100, 110 and 120 °C under crossed polarisers. Red frames are the same size in each image to help visualise decrease in size of the ordered domain. 198

Figure 5-18. Electrospinning setup with narrow wheel collector. 201

Figure A-1. Synthetic route to **M1**. PEG = Poly(ethylene glycol) average mol. wt. 200 g mol^{-1}, DCC = *N,N'*-dicyclohexylcarbodiimide. 208

Figure A-2. ^{1}H NMR spectrum for **I-M1** in $CDCl_3$. 209

Figure A-3. ^{1}H NMR spectrum for **M1** in $CDCl_3$. 209

Figure A-4. ^{1}H NMR spectrum for **M1-Allyl** in $CDCl_3$. 210

Figure A-5. ^{1}H NMR spectrum for **M1-Thiol** in $CDCl_3$. 210

Figure A-6. ESI mass spectrum for **M1-Thiol**. 211

Figure A-7. ^{1}H NMR spectrum for **3-aminophenol-Boc** in $CDCl_3$. 211

Figure A-8. ^{1}H NMR spectrum for **I-M2-Boc** in $CDCl_3$. 212

Figure A-9. Decoupled ^{13}C NMR spectrum for **I-M2-Boc** in $CDCl_3$. 212

Figure A-10. ESI mass spectrum for **I-M2-Boc**. 213

Figure A-11. ^{1}H NMR spectrum for **M2-Boc** in $CDCl_3$. 213

Figure A-12. Decoupled ^{13}C NMR spectrum for **M2-Boc** in $CDCl_3$. 214

Figure A-13. ESI mass spectrum for **M2-Boc**. 214

Figure A-14. ^{1}H NMR spectrum for **M2** in $CDCl_3$. 215

Figure A-15. Decoupled ^{13}C NMR spectrum for **M2** in $CDCl_3$. 215

Figure A-16. ESI mass spectrum for **M2**. 216

Figure A-17. ^{1}H NMR spectrum for Aliquot 1 in $CDCl_3$. 216

Figure A-18. ^{1}H NMR spectrum for Aliquot 2 in $CDCl_3$. 217

Figure A-19. ^{1}H NMR spectrum for Aliquot 3 in $CDCl_3$. 217

Figure A-20. ^{1}H NMR spectrum for **PS-*b*-PMVS-*b*-PS** in $CDCl_3$. 218

Figure A-21. Decoupled ^{13}C NMR spectrum for **PS-*b*-PMVS-*b*-PS** in $CDCl_3$. 218

Figure A-22. ^{1}H NMR spectrum for **PMVS** in $CDCl_3$. 219

Figure A-23. Decoupled ^{13}C NMR spectrum for **PMVS** in $CDCl_3$. 219

Figure A-24. ^{1}H NMR spectrum for **P-3** in acetone-d_6. 220

Figure A-25. Decoupled ^{13}C NMR spectrum for **P-3** in acetone-d_6. 220

Figure A-26. Synthetic scheme for conversion of 5-bromovaleric acid to 5-mercaptopentanoic acid. 221

Figure A-27. ^{1}H NMR spectrum for 5-mercaptopentanoic acid in $CDCl_3$. 221

Figure A-28. ^{1}H NMR spectrum for **P-5** in acetone-d_6. 222

Figure A-29. Decoupled ^{13}C NMR spectrum for **P-5** in acetone-d_6. 222

Figure A-30. GPC data for **P-3** and **P-5**. 223

Figure A-31. ^{1}H NMR spectrum for **PMVS-3** in acetone-d_6. 223

Figure A-32. Decoupled ^{13}C NMR spectrum for **PMVS-3** in acetone-d_6. 224

Figure A-33. DLS of **PMVS-3** in THF, 8 repeats. 224

Figure A-34. ^{1}H NMR spectrum for **P*-3(AIBN)** in acetone-d_6. 225

Figure A-35. Decoupled ^{13}C NMR spectrum for **P*-3(AIBN)** in acetone-d_6. 225

Figure A-36. ^{1}H NMR spectrum for **P-3-NHS** in $CDCl_3$. 226

Figure A-37. ^{1}H NMR spectrum for product of NHS ester coupling reaction in $CDCl_3$. 226

Figure A-38. ^{1}H NMR spectrum for product of reaction of **P-5** with **M2** in $CDCl_3$. 227

Figure A-39. ^{1}H NMR spectrum for **P-3-M1(82)-COOH(18)** in $CDCl_3$. 227

Figure A-40. Decoupled ^{13}C NMR spectrum for **P-3-M1(82)-COOH(18)** in $CDCl_3$. 228

Figure A-41. GPC data for **P-3-M1(82)-COOH(18)** 228

Figure A-42. ^{1}H NMR spectrum for **P-3-M2(80)-COOH(20)** in $CDCl_3$. 229

Figure A-43. Decoupled ^{13}C NMR spectrum for **P-3-M2(80)-COOH(20)** in $CDCl_3$. 229

Figure A-44. GPC data for **P-3-M2(80)-COOH(20)** 230

Figure A-45. ^{1}H NMR spectrum for **P-5-M1(86)-COOH(14)** in $CDCl_3$. 230

Figure A-46. Decoupled ^{13}C NMR spectrum for **P-5-M1(86)-COOH(14)** in $CDCl_3$. 231

Figure A-47. GPC data for **P-5-M1(86)-COOH(14)** 231

Figure A-48. ^{1}H NMR spectrum for **P-3-M1(65)-COOH(35)** in $CDCl_3$. 232

Figure A-49. Decoupled ^{13}C NMR spectrum for **P-3-M1(65)-COOH(35)** in $CDCl_3$. 232

Figure A-50. GPC data for **P-3-M1(65)-COOH(35)** 233

Figure A-51. ^{1}H NMR spectrum for **PMVS-M1(84)-COOH(16)** in $CDCl_3$. 233

Figure A-52. Decoupled ^{13}C NMR spectrum for **PMVS-M1(84)-COOH(16)** in $CDCl_3$. 234

Figure A-53. ^{1}H NMR spectrum for **P-3-COOMe** in $CDCl_3$. 235

Figure A-54. Decoupled ^{13}C NMR spectrum for **P-3-COOMe** in $CDCl_3$. 235

Figure A-55. GPC data for **P-3-COOMe**. 236

Figure A-56. ^{1}H NMR spectrum for **P*-3(AIBN)-COOMe** in $CDCl_3$. 236

Figure A-57. Decoupled ^{13}C NMR spectrum for **P*-3(AIBN)-COOMe** in $CDCl_3$. 237

Figure A-58. GPC data for **P*-3(AIBN)** and **P*-3(AIBN)-COOMe.** 237

Figure A-59. ^{1}H NMR spectrum for **P-3-M1(65)-COOMe(35)** in $CDCl_3$. 238

Figure A-60. Decoupled ^{13}C NMR spectrum for **P-3-M1(65)-COOMe(35)** in $CDCl_3$. 238

Figure A-61. GPC data for **P-3-M1(65)-COOMe(35)**. 239

Figure A-62. ^{1}H NMR spectrum for **P*-3(AIBN)-M1-COOMe** in $CDCl_3$. 239

Figure A-63. GPC data for **P*-3(AIBN)-M1-COOMe**. 240

Figure A-64. TGA thermograms for **P-3-COOMe**, **P*-3(AIBN)**, **P*-3(AIBN)-COOMe**, **P*-3(AIBN)-M1-COOMe** and **P-3-M1(65)-COOMe(35)**. 240

Figure C-1. Amplitude sweep results (left) and corresponding Lissajous diagram (right) at 0.2% strain for **P-3-COOMe**. 243

Figure C-2. Amplitude sweep results (left) and corresponding Lissajous diagram (right) at 1% strain for **P-3-M1(65)-COOMe(35)**. 243

Figure C-3. Amplitude sweep results (left) and corresponding Lissajous diagram (right) at 5% strain for **P*-3(AIBN)**..... 243

Figure C-4. Amplitude sweep results (left) and corresponding Lissajous diagram (right) at 5% strain for **P*-3(AIBN)-COOMe**..... 244

Figure C-5. Amplitude sweep results (left) and corresponding Lissajous diagram (right) at 3% strain for **P*-3(AIBN)-M1-COOMe**. 244

Figure C-6. Amplitude sweep results (left) and corresponding Lissajous diagram (right) at 5% strain for **PMVS-3-M1(86)-COOH(14)**..... 244

List of Tables

Table 2-1. M_n and PDI of aliquots from the **PS-*b*-PMVS-*b*-PS** synthesis 55

Table 2-2. M_n and PDI for **P-3** and **P-5**. 61

Table 2-3. PDI and M_n for **PS-*b*-PMVS-*b*-PS, P-3-M1(82)-COOH(18)**, **P-3-M2(80)-COOH(20)** and **P-5-M1(86)-COOH(14)** 65

Table 2-4. M_n and PDI (where appropriate) of **PMVS**, **PMVS-3** and **PMVS-3-M1(84)-COOH(16).** 68

Table 2-5. M_n and PDI for the polymers before and after conversion of carboxylic acid functionality to methyl ester groups. *M_n calculated from ^{1}H NMR spectroscopy data, PDI obtained from GPC data.* 69

Table 2-6. TGA data for triblock copolymers, including temperature where 3% weight loss was measured and the final weight percentage at 800 °C. 73

Table 2-7. Summary of thermal transitions by DSC. 74

Table 2-8. Yield and % conversion for 0.35 g scale reactions 97

Table 3-1. Calculated molar volume for all repeat units in **PS-*b*-PMVS-*b*-PS**, **P-3**, **P-3-M1(65)-COOH(35)** and **P-3-M1(82)-COOH(18)**. **From reference 15.* 110

Table 3-2. Calculated V_M, f_{PS} and χN for **PS-*b*-PMVS-*b*-PS**, **P-3, P-3-M1(65)-COOH(35)** and **P-3-M1(82)-COOH(18)** and the predicted microphase segregated morphology for each. 111

Table 3-3. Results for model fit and experimental SAXS results for comparison. 120

Table 3-4. Locations of peaks for VT-SAXS on aligned **P-3-M1(82)-COOH(18)** from integrating in the 0° and 90 ° directions, and the corresponding spacing size 128

Table 3-5. Locations of peaks for VT-SAXS on aligned **P-3-M1(65)-COOH(35)** from integrating in the 40° and 130° directions, and the corresponding spacing. 130

Table 3-6. Parameters obtained from fitting of SAXS data for stretched and unstretched **P-3-M1(82)-COOH(18)**. 135

Table 4-1. Amplitude sweep results for standard materials and temperature range for frequency sweeps. 142

Table 4-2. Amplitude sweep results for LCE polymers and temperature ranges for frequency sweeps. 148

Table 4-3. Amplitude sweep results for modified polymers. 157

Table 5-1. Results for model fit and experimental SAXS results for comparison. 181

Table 5-2. Parameters obtained from fitting of SAXS data for stretched and unstretched fibres of **P-3-M1(65)-COOH(35)**. 200

Table B-1. Volume contributions for PMVS repeat unit. 241

Table B-2. Volume contributions for LC end-functionalised PMVS repeat unit. 241

Table B-3. Volume contributions for COOH end-functionalised PMVS repeat unit. 242

List of Abbreviations

$\hat{n}$	Director
ABS	Acrylonitrile-*b*-butadiene-*b*-Styrene
AIBN	2,2′-azobis(2-methylpropionitrile)
-*b*-	Block
Boc	*tert*-butyloxycarbonyl
CAN	Covalent Adaptable Network
D_3	Hexamethylcyclotrisiloxane
DCC	*N,N'*-dicyclohexylcarbodiimide
DLS	Dynamic Light Scattering
DMAP	4-(dimethylamino)pyridine
DMF	Dimethylformamide
DMPA	2,2-dimethoxy-2-phenylacetophenone
DP_n	Degree of Polymerisation
DSC	Differential Scanning Calorimetry
ESI	Electrospray Ionisation
f_i	Volume Fraction
G'	Storage Modulus
G''	Loss Modulus
GPC	Gel Permeation Chromatography
LC	Liquid Crystal
LCE	Liquid Crystal Elastomer
LCP	Liquid Crystal Polymer
LVE	Linear Viscoelastic
MCLCP/MCLCE	Main Chain Liquid Crystal Polymer/Elastomer
M_n	Number Average Molecular Weight
mol. wt.	Molecular Weight
MS	Mass Spectrometry
MST	Microphase Separation Transition
NHS	*N*-hydroxysuccinimide
PDI	Polydispersity
PDMS	Polydimethylsiloxane
PEG	Polyethylene Glycol
PEO	Polyethylene Oxide
PLA	Polylactic Acid
PMMS	Poly(3-mercaptopropylmethylsiloxane)

PMVS	Poly(methylvinylsiloxane)
POM	Polarised Optical Microscopy
PS	Polystyrene
RI	Refractive Index
S/f(H)	Order Parameter
SAOS	Small Amplitude Oscillatory Shear
SAXS	Small-Angle X-ray Scattering
SCLCP/SCLCE	Side Chain Liquid Crystal Polymer/Elastomer
TEM	Transmission Electron Microscopy
T_g	Glass Transition Temperature
TGA	Thermogravimetric Analysis
THF	Tetrahydrofuran
T_{iso}	Isotropic Transition Temperature
T_{ODT}	Order-Disorder Transition Temperature
TPU	Thermoplastic Polyurethane
TTS	Time-Temperature Superposition
v/v	Volume Concentration
V_3	1,3,5-trivinyl-1,3,5-trimethylcyclotrisiloxane
V_M	Molar Volume
VT-SAXS	Variable Temperature Small-Angle X-ray Scattering
WAXS	Wide-Angle X-ray Scattering
wt%	Weight Percent
η	Viscosity
ρ	Density
χ	Flory-Huggins Interaction Parameter

Chapter 1: Introduction

1.1. Responsive Polymers from Liquid Crystals

The work to be presented in this thesis is concerned with the synthesis and characterisation of thermoplastic liquid crystal elastomers (LCEs), with a particular focus on their suitability for processing by common thermoplastic techniques. LCEs are soft materials capable of rapid, reversible shape change, and so have potential applications as soft actuators, but to date have been limited by the processing methods available.

1.1.1. Liquid Crystals

Liquid crystal (LC) mesophases exist between the fully isotropic liquid state of matter and the ordered crystalline solid state, where both orientational and positional order are present in all three dimensions. Mesophases are inherently anisotropic, displaying orientational order along the director (a unit vector denoted by $\hat{n}$) and either no positional order (nematic) or positional order in fewer than three dimensions (smectic) (Figure 1-1). When the liquid crystal molecule (mesogen) is chiral more complex mesophases can also form, including helical chiral nematic mesophases which are utilized in display technology.[1]

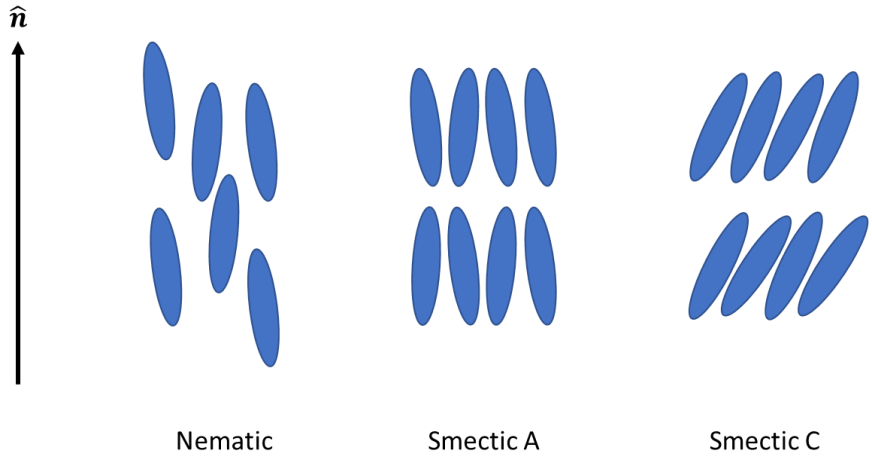

Figure 1-1. Mesophases formed by calamitic (or rod-like) liquid crystal mesogens.

Shape anisotropy of the mesogen (molecule or particle) is a prerequisite for the formation of mesophases. The geometry of mesogens can therefore be divided between calamitic (or rod-like), which form the nematic and smectic mesophases described previously, and discotic (or disk-like), which can form columnar mesophases, where the mesogens stack to form a cylindrical structure. Both these classes of mesogen are thermotropic and so their phase behaviour is dependent on the temperature, with increasing temperature resulting in an increasingly disordered state. The transition from the nematic mesophase to the fully isotropic state occurs at the isotropic transition temperature, T_{iso}, also referred to as the clearing temperature. A second class of LCs also exists, namely lyotropic LCs, where the level of order is dependent on the concentration of a solution. These materials, however, are the not the focus of the current work. The anisotropy of LC mesophases, and the volume change associated with transitioning between them, results in anisotropic elastic, electric, magnetic and optical properties which underly their applications and unique properties.[1]

1.1.2. Identification of Liquid Crystal Mesophases

The level of order within a LC mesophase relative to the director can be quantified by the order parameter, S, using Equation 1.1, where θ is the angle between the director and the local orientation of the mesogen (Figure 1-2). This equation takes the average value over all molecules in the system, therefore, for a perfectly ordered system where θ=0, S=1. If all molecules were oriented at 90° to the director, S=-0.5, and if no orientational order is present, S=0.[1]

$$S = \frac{3\langle \cos^2 \theta \rangle - 1}{2} \qquad 1.1$$

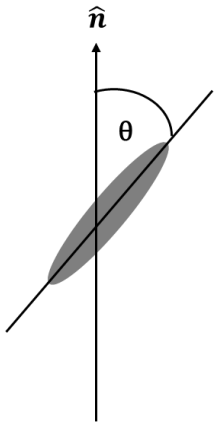

Figure 1-2. Definition of the angle used for calculation of order in a calamitic liquid crystal material.

The presence of an ordered LC mesophase can be identified using complementary experimental techniques. Differential Scanning Calorimetry (DSC) can be used to detect the transition to or from a mesophase through the change in enthalpy associated with increasing or decreasing the level of alignment.[1] This gives an idea of the temperature range over which a mesophase is stable, but does not allow for unambiguous identification of the type of phase present (e.g. nematic or smectic). This requires a technique such as Polarised Optical Microscopy (POM).

POM is the classic technique used for characterisation of LC mesophases and exploits their anisotropic optical properties. In isotropic materials the wavelength and velocity of light propagating through the sample will be decreased according to the refractive index, n. Rod-like mesogens on the other hand have two refractive indices, the ordinary (n_o) and extraordinary (n_e), which will decrease the velocity of propagation by different amounts. This means that light entering a LC mesophase will be split into two directions parallel and perpendicular to the director, with a phase difference between them. This property is known as birefringence and when combined with linearly polarised light allows for the identification of LC mesophases.[2]

In POM a sample is placed between two polarisers which are oriented at 90° to each other, as shown in Figure 1-3. This configuration means that linearly polarised light from the first polariser is not able to pass through the second (also known as the analyser) and is therefore extinguished. For an isotropic material, or a LC mesophase where the director is aligned with one of the polarisers, the light continues to propagate with the initial polarisation having experienced only one refractive index and is extinguished by the analyser. However, for a LC material with the director oriented at some other angle to the polarisers the propagating light is split into two, propagating parallel and perpendicular to the director. This elliptically polarised light is then able to pass through the second polariser to some extent, appearing as a bright region at the objective, with the greatest intensity seen when the director is angled at 45° to the polarisers. If the sample is rotated so that the director aligns with the polariser then the visible region will be extinguished.[2]

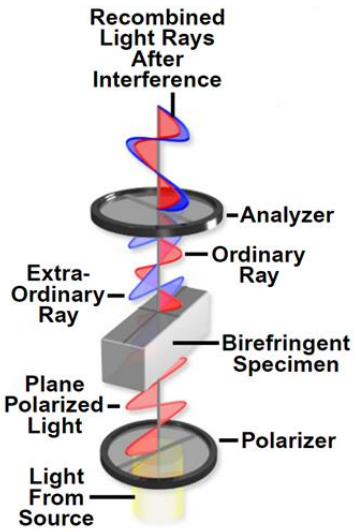

Figure 1-3. Polarised optical microscopy of a birefringent sample. Reproduced from reference 3 - Nikon.

Individual mesophases can then be identified as each displays characteristic patterns and defects known as Schlieren textures.[2] For example, the images shown in Figure 1-4 display the Schlieren texture characteristic of a nematic mesophase, with defects (black) indicating isotropic areas. The sample was irradiated with UV light to promote the transition from a nematic mesophase to an isotropic state, which served to increase the total area of the black regions in the POM images.[4]

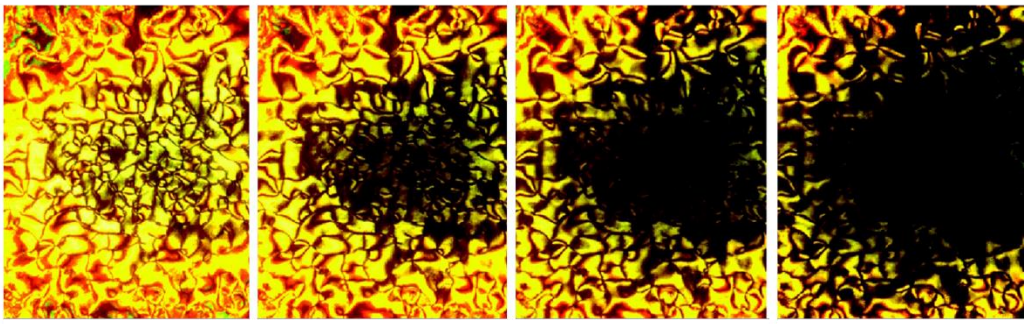

Figure 1-4. Polarised Optical Microscopy image of the Schlieren texture for a nematic mesophase, with black areas indicating isotropic regions. Pictures are taken at 5 second intervals whilst disrupting the mesophase with UV irradiation, resulting in increasing areas of isotropic character. Reproduced with permission from reference 4 – American Chemical Society.

1.1.3. Liquid Crystal Elastomers

Molecular mesogens can be combined with macromolecules to yield liquid crystal polymers (LCPs). The mesogen may be attached to the polymer backbone in one of three configurations, as demonstrated in Figure 1-5. In main-chain LCPs (MCLCPs), the mesogen is incorporated into the polymer backbone, as opposed to side-chain LCPs (SCLCPs), where the mesogen is attached *via* a flexible spacer. SCLCPs can then be further subdivided into either end-on or side-on, dependent on the manner with which the mesogen is attached to the spacer. The role of the flexible spacer is important, as it acts to decouple the thermal motion of the mesogen from that of the polymer backbone. In the absence of an external influence the mesogen will rearrange to form an ordered mesophase whereas the polymer backbone will adopt a random coil-like structure in order to minimise energy. The flexible spacer allows for both components to adopt their preferred conformation to some extent, and allows for the formation of an ordered LC mesophase despite the mesogen being attached to the isotropic polymer backbone.[5]

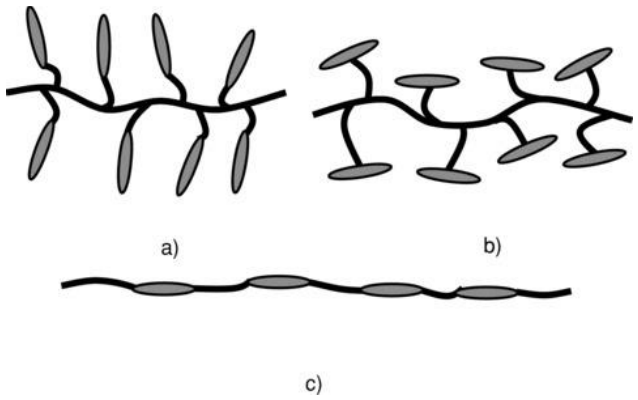

Figure 1-5. Mesogens can be attached either end-on (a) or side-on (b) to the polymer backbone to form side-chain liquid crystal polymers or are incorporated into the polymer backbone to give main-chain liquid crystal polymers (c). Reproduced with permission from reference 6 - John Wiley & Sons.

Liquid crystal elastomers (LCEs) are a subset of LCPs where the polymer chains are lightly crosslinked, typically through covalent bonds. This means that LCEs combine the orientational order associated with an aligned LC mesophase and the elasticity found in lightly-crosslinked polymer networks, which results in soft materials capable of reversible shape change on application of some external stimulus.[7] The anisotropy of a LC monodomain draws out the polymer chains parallel to the director (for main-chain and side-on SCLCEs), preventing them from adopting the preferred random-coil conformation. This deformed state is fixed by the crosslinks, generally introduced in a final synthetic step through photoinitiated reactions.

On triggering the isotropic transition, typically by heating above the T_{iso}, the polymer also adopts a random-coil conformation as the extended chains collapse. This results in a macroscopic shape change; a contraction along the director and a necessary expansion in the perpendicular direction in order to conserve volume (Figure 1-6). This effect is greatest for MCLCEs, where the orientation of the mesophase is strongly coupled to the conformation of the polymer backbone, and weakest for end-on SCLEs.[6]

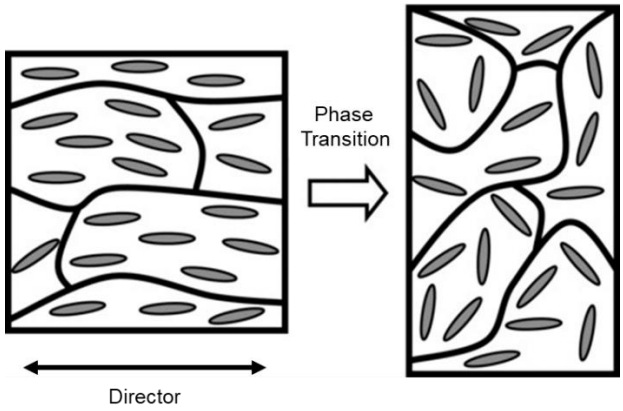

Figure 1-6. The formation of a LC monodomain acts to draw polymer chains along the director. On triggering the transition to the isotropic state both the LC and the polymer backbone adopt an isotropic morphology, resulting in a contraction along the director and an expansion perpendicular to it. Adapted with permission from reference 6 - John Wiley & Sons.

The reversible nature of the actuation has generated interest in the use of LCEs for a variety of applications where soft actuators would be beneficial, as the original conformation can be regained by cooling below the T_{iso} without the need for application of further force. Actuation of LCEs can also be induced in response to a number of stimuli, including light[8] and humidity.[9] Photoresponsive behaviour is commonly achieved by incorporating an azobenzene unit into the mesogen structure, as on irradiation with UV light with a wavelength of 365 nm the azobenzene group isomerises from the linear *trans*-conformation to the bent *cis*-conformation (Figure 1-7). This acts to disrupt the liquid crystal mesophase and yields a disordered isotropic state. Thus, actuation can be achieved at room temperature without the need for heating.

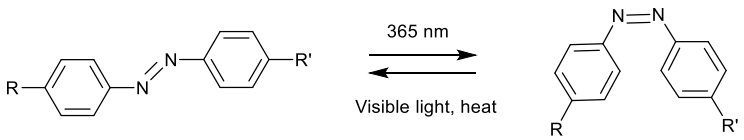

Figure 1-7. Isomerisation of an azobenzene group from the linear *trans* to the bent *cis* conformation occurs under irradiation with light of λ = 365 nm and can be reversed by exposure to visible light or on heating.

The inclusion of azobenzene moieties has been exploited to achieve photomechanical deformation, where light energy is converted to mechanical work. For example, Ikeda *et al*. showed that by attaching the active LCE layer to a passive polyethylene layer for mechanical support and joining the ends of the film together to form a loop, it was possible to create a light driven 'motor' (Figure 1-8).[10]

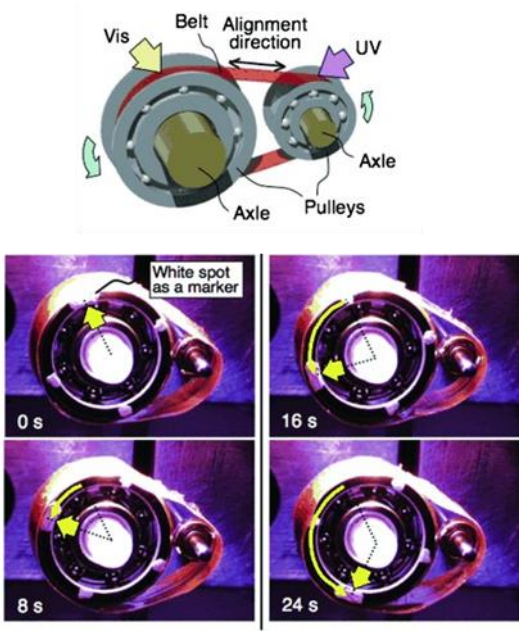

Figure 1-8. Light-driven motor designed by Ikeda *et al*. Irradiation of different regions with either UV or visible light resulted in contractions and expansions which drove the rotation of an LCE belt around a pulley. Reproduced with permission from reference 10 - John Wiley & Sons.

Photomechanical deformation has also been used to replicate the continuous deformation inherent to locomotion in nature, with potential applications in soft robotics proposed.[11,12] A common goal in this field is to replace hard, multi-part actuators with monoliths which more closely mimic the soft structures observed in nature. For example, it was shown that a biomimetic crawling motion could be induced in a LCE film,[11] as well as contraction and expansion in response to light which mimicked the action of the iris.[12] However, despite the potential for reversible, macroscopic shape change, the majority of LCEs reported to date consist of thin films tens of

microns thick which limits their utility. One of the major barriers to increasing the scale of LCE actuators is the limited processing methods available due to the need to induce a liquid crystal monodomain and crosslink the resulting LCP. A great deal of research has therefore been focussed on new methods of processing LCE actuators to give a material with either a uniaxial or complex director profile, as discussed below.

1.2. Processing of Liquid Crystal Elastomers

The responsive properties of LCEs are dependent on the successful formation of a LC monodomain. This can be achieved from either mesogenic monomers or from functionalization of a lightly crosslinked polymer backbone, with different starting materials favouring different alignment methods. The method chosen will determine whether in-plane (contraction and expansion) or out-of-plane (bending and twisting) deformations are possible and may also place a limit on the geometry and thickness of any actuators. To date, the vast majority of LCEs are crosslinked with chemical bonds and so are thermosets, which means that once crosslinked it is not possible to process them any further. However, it has been shown that composite structures can be manufactured which help overcome this limitation to some extent.

1.2.1. Actuators with Complex Director Profiles

LCs for display applications are often oriented through a photoalignment layer, where a preferred direction can be induced through rubbing the surface of a LC alignment cell before the addition of low molecular weight mesogenic groups which then align with the surface. This technique can also be used to pattern the director for the production of LCE films by additionally crosslinking the mesogenic groups *in situ* to give the LCE.

If uniaxial alignment is induced, then uniaxial deformation is seen. If, however, the director is continuously varied either through the thickness or the film or by forming concentric patterns then more complex actuation can be achieved (Figure 1-9). These complex director profiles can be obtained by applying a photomask and rotating the cell while irradiating to create a patterned alignment layer. On filling the cell with the mesogen, those molecules in contact with the surface will orient with the alignment layer and, after crosslinking, create a film that can be switched between a flat and cone-shape by heating through the T_{iso}.[13] This method has also been used to pattern alternating stripes of twisted director profiles, which resulted in accordion-like actuation as the film folded and contracted along its length on triggering the nematic-isotropic transition.[14]

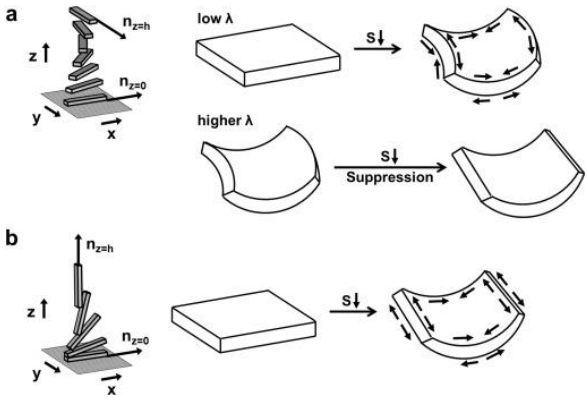

Figure 1-9. If the director profile is rotated through the thickness of a film, heating above the T_{iso} results in contraction and expansion in different regions and so curvature as the order parameter, S, decreases. Reproduced with permission from reference 15 - Elsevier.

An alternative method that allowed for a spatially patterned director in a monolithic material was reported by White *et al*., which was capable of creating patterns made up of volume units, or voxels, with an area as small as 0.01 mm^2, each having its own localised director. This was achieved through the use of a photoalignment material which contained an azobenzene dye. The chromophore in the dye oriented at 90° to the electric field vector of linearly polarised light, and so the domains in the photoalignment layer could be patterned using polarised light from a 445 nm laser. The LC cell was then filled with low viscosity precursors, before undergoing a chain-extension reaction by the Michael addition of a primary amine to a nematic diacrylate to form main-chain nematic oligomers which were then crosslinked (Figure 1-10).[16]

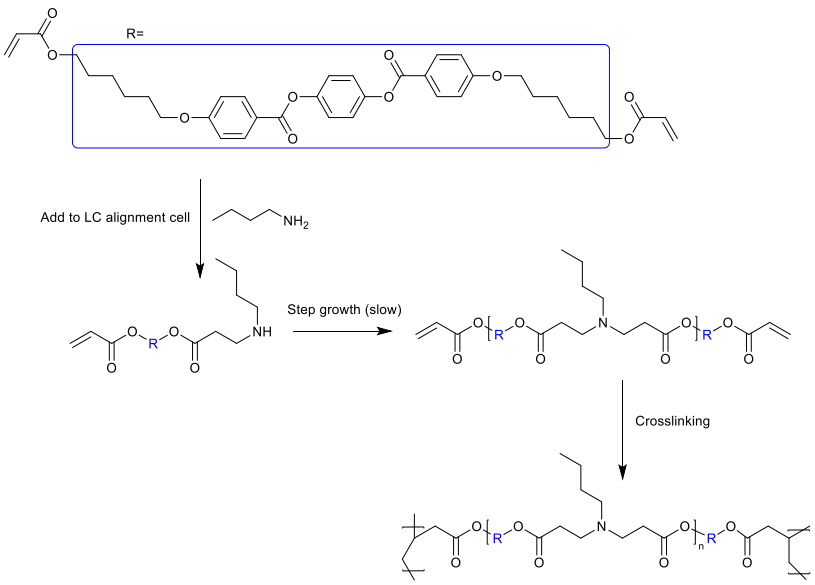

Figure 1-10. For the spatially patterned LCEs reported in Reference 16, low viscosity LCP precursors were synthesised by mixing the mesogen with a primary amine chain extender. These were oriented in an alignment cell where the step growth polymerisation continued before crosslinking.[16]

Using this method allowed for fine resolution in the patterned surface, with 226 distinct directions possible for the director between 0-45°. By programming topological defects it was possible to generate 3D deformation on heating through the T_{iso}. This also acted to amplify the 55% strain measured for a linear contraction to a stroke of 3000% for a film which deformed to produce nine cones through localised stretching and delocalised bending (Figure 1-11). Due to the high energy penalty associated with blocking the resulting Gaussian curvature large deformations were obtained, with the cones able to lift a weight 147 times greater than that of the film, yielding a specific work capacity of 2.6 J/kg.[16]

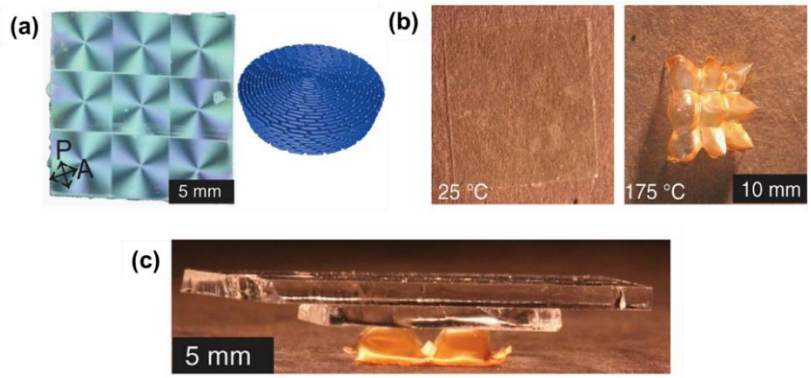

Figure 1-11. Spatial patterning of complex director profiles such as that in (a) results in three-dimensional deformation on heating (b) with enough force to lift a weight (c). Reproduced with permission from reference 16 - The American Association for the Advancement of Science.

This method has since been extended to use thiol-ene chemistry to crosslink the polymer,[17] and to trigger the actuation on irradiation with UV light by modifying the mesogen precursor to contain an azobenzene group.[18] Electromechanical deformation was achieved by the addition of a 0.02 wt% loading of single-walled carbon nanotubes (SWCNTs), which allowed the reversible shape change to be triggered both on heating and on applying a current across the thickness of the film.[19] These structures also display a property known as soft elasticity, where areas with LC alignment occurring perpendicular to the direction of a stretching deformation display non-linear elastic behaviour (Figure 1-12). This property has been proposed to make LCEs patterned in this way useful for soft electronics. Ductile silver nanowires were attached to the surface of a spatially aligned film and on deformation an increase in resistance was measured in the region which displayed soft elastic behaviour. Through the fine control of the alignment, it was possible to incorporate soft elasticity into regions to control the deformation and functionally grade the structure's response to an applied load, without failure occurring in either the polymer or nanowire.[20] These methods allowed for fine control over the deformed structure of films prepared

between two LC cells, but are still limited geometrically by the alignment method to films with a maximum thickness of around 50 μm.

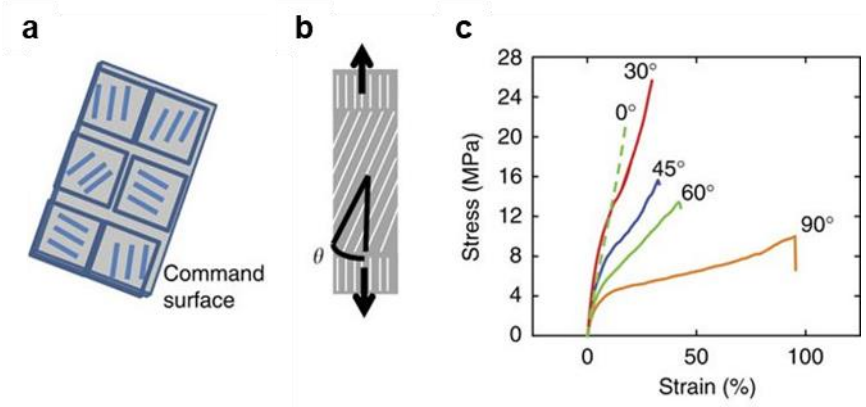

Figure 1-12. The photoalignment surface (a) was used to control the orientation of a main-chain LCE. It was shown that the angle between the director and the loading direction (b) had a significant impact on the mechanical properties of the sample (c). This was used to control the local strain environment encountered in soft, stretchable electronics under load. Reproduced with permission from reference 20 under a Creative Commons Licence.

Attempts to increase the thickness, and so the mechanical properties and work done by LCE films, have been made by adhering two of these aligned LCEs together using the monomer mixture. Using this method, laminates containing 2 or 4 layers of LCE were produced, with each demonstrating a similar level of strain from a thermally induced contraction (50%). The four layer laminate, which had a thickness of 210 μm, lifted a weight 1100 times its own weight, with an output force of 280 mN generated across a 1.6 mm stroke and a specific work of 19 J/kg,[21] in comparison to the 2.6 J/kg measured for the single layer.[16] These four layer laminates could then be layered on top of each other, with glass slides in between each layer, to produce a structure which demonstrated a stroke of 6 mm whilst lifting 120x the weight of the assembly (Figure 1-13).[21]

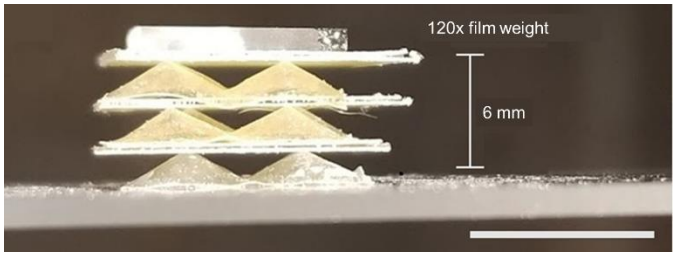

Figure 1-13. Layered LCE structure displaying 6 mm stroke when lifting 120x its own weight. Scale bar is 1 cm. Reproduced with permission from reference 21 under a Creative Commons Licence.

1.2.2. Actuators with a Single Director

Developing artificial materials which replicate the contraction and expansion of muscle is of great interest to a number of areas, including soft robotics.[22,23] Natural muscle consists of a bundle of single-cell fibres, where each fibre contains contractile protein-containing myofilaments. When constrained by joints, the strain observed on contraction is generally less than 20%.[24] LCEs were first proposed as polymeric systems capable of acting as artificial muscle by de Gennes in 1997, who suggested that a main-chain LC polymer backbone would act to drive a contraction on heating above the T_{iso}, whilst flexible spacers between the mesogens would impart flexibility and allow for a return to the undeformed conformation on cooling.[25,26] Since then many examples of LCEs capable of reversible contraction have been reported, produced either from a two-step crosslinking method or by the incorporation of Covalent Adaptable Networks (CANs), but which are all aligned by mechanical deformation of the polymer structure.

1.2.2.1. Two-Step Crosslinking

One of the most common methods for preparing side-chain LCEs was first reported by Finkelmann in 1991. This consists of a two-step process, where a mesogenic core terminated with two vinyl groups was utilised to crosslink the polymer backbone. In the first step a poly(hydrosiloxane) backbone was synthesised and lightly crosslinked, which was necessary for the polymer to have sufficient mechanical strength to be aligned in the second step, where the polymer was stretched and crosslinked further under applied load.[27,28] Since then this method has been extended to different polymer backbones including the preparation of MCLCEs.[29] This method favours the synthesis of LCEs that show uniaxial deformation, as the director will align along the direction of stretch, and so has been used to design polymers that could be developed for use as artificial muscles.

Several LCE systems were reported by Keller and Li aiming to create the artificial muscle structure proposed by de Gennes (Figure 1-14),[25,26] although they utilised side-chain LCPs due to the high polydispersity associated with the synthetic route to main-chain LCPs.[30] They designed a lamella RNR triblock copolymer where the R blocks consisted of an amorphous, crosslinkable polymer and the N block a nematic side-chain polymer. It was expected that the triblock copolymer would be more mechanically robust than a crosslinked N block, and that the monodomain ordering would be better preserved during heating cycles.[31]

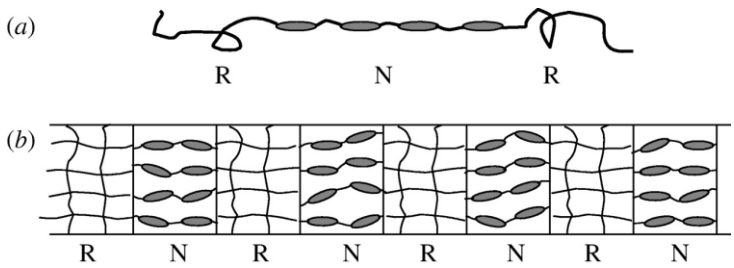

Figure 1-14. Structure of the LCE proposed to perform as artificial muscle by de Gennes. Crosslinking of the triblock copolymer (a) resulted in the lamellar structure (b). Reproduced with permission from reference 31 - John Wiley & Sons.

For the N block a series of LCEs were developed using atom-transfer radical polymerisation (ATRP). A thermoresponsive elastomer was synthesised by first aligning a LC-functionalised acrylate or methacrylate using an alignment layer, before carrying out a UV-initiated crosslinking reaction. Films of this polymer demonstrated a reversible 35-45% change in length on heating through T_{iso} and a stress of 210 kPa.[32] A photoresponsive equivalent was also synthesised, where the monomer was modified to include an azo-benzene group, and which demonstrated a rapid contraction of 12-18% of the original length on irradiation with UV light.[33] The thermoresponsive polymer was chosen for incorporation into the RNR triblock copolymer and was used as a macroinitiator for the statistical copolymer R block, poly(*n*-butylacrylate)-*co*-poly(2-hydroxyethyl acetate), with the polydispersity of the final triblock copolymer measured as 1.3. Hydroxyl groups on the R block were next converted to acrylate groups and the LC component aligned using a 1.7 T magnetic field before crosslinking the acrylates. This polymer was shown to contract by 18% of its original length on heating above the T_{iso} to 140 °C, and returned to its original length on cooling.[30]

Less complex polymers have also been synthesised by Finkelmann's method and these displayed relatively large contractions on exposure to various stimuli. The first example of a photoresponsive LCE actuator was a nematic LCE containing an azobenzene group that contracted by 20% of its initial length on irradiation with UV light.[28] The synthesis of UV-responsive LCEs required the development of new near-IR photoinitiators as the photoresponsive azobenzene group absorbs strongly in the UV range.[33] Electromechanical actuation of smectic LCEs was shown to result in relatively large strains of 4% for ferroelectric LCEs,[34] but was not observed for nematic LCEs until carbon nanotubes were mixed with a side-chain LCP before crosslinking to yield a LCE where a strain of 0.1% was measured.[35] More recently, a main-chain LCE swollen by the liquid crystal 5CB was shown to display a maximum contraction of 19% on application of an electric field.[36]

Fibres of LCEs more closely mimic the structure of bundles of natural muscle fibre than films, and so are a desirable morphology for LCEs. The bulk production of crosslinked fibres will be discussed further in Section 1.4, however, a manually drawn LCE fibre was reported in 2003, whereby a fibre was drawn from a melt mixture of LC acrylate monomers and crosslinker using tweezers. The crosslinking process started in the melt and the action of drawing induced alignment of both the polymer chains and mesophase. The resulting side-chain LCP fibre had a diameter of 300 μm and was shown to contain a nematic mesophase monodomain, with the director oriented along the length of the fibre. A contraction of 30-35% of the original length on heating above T_{iso} was measured, with an increase in length seen on cooling back below the T_{iso}. A contractive stress of 274 kPa was also measured acting against a constant strain of 3%.[37] This method has since been used to draw fibres of photo-responsive main-chain[38] and side-chain[39] LCEs, both with reversible crosslinking arising from hydrogen bonding and thiol-disulfide interconversion respectively. These fibres bent towards a UV light source on irradiation, which generated a stress of between 130-240 kPa depending on the light intensity for the main-chain polymer.[38] In these cases out-of-plane deformation was observed despite the uniaxial director profile, due to irradiation from one side of the fibre triggering the contraction on that side only.

1.2.2.2. Covalent Adaptable Networks

Whilst the method developed by Finkelmann results in active LCEs, the requirement to start with a lightly crosslinked polymer is problematic for creating complex geometries. For this reason, polymers crosslinked with exchangeable bonds may be a promising direction for LCE actuators. CANs have been developed to overcome the processing limitations of thermosets, where thermoplastic-like behaviour can be achieved by heating above a critical temperature to allow for exchange of certain covalent bonds (Figure 1-15). As well as resulting in shape-memory polymer like behaviour, these materials also demonstrate self-healing behaviour where the exchangeable bonds can mix over the interface of a cut and restore the original structure and mechanical properties.[40]

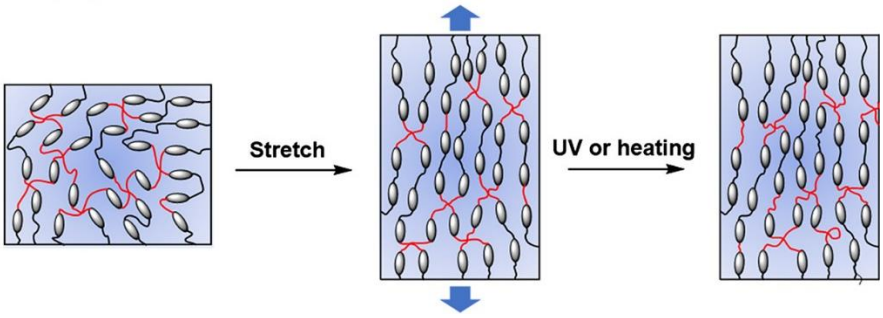

Figure 1-15. Method behind forming LCE actuators through exchangeable disulfide bonds. The stretched geometry can be fixed on heating or application of UV which promotes bond exchange. Reproduced with permission from reference 41 – American Chemical Society.

CANS have been applied to create more readily processible LCEs. Examples of supramolecular LCPs containing intermolecular hydrogen bonds have been reported,[42–44] and in 2008 Ikeda *et al*., proposed that these interactions could be used to create responsive polymer films using mesogens acting as hydrogen bond donors as the linking group.[45] However, each donor could form only one hydrogen bond which limited the mechanical strength and the exchange of bonds between neighbouring acceptor sites. In 2014 Pei *et al.* reported a mouldable LCE based on an epoxy network containing exchangeable covalent crosslinking. This was achieved through transesterification, where ester linkages between ester groups on the spacer and hydroxyl groups on the mesogen were able to exchange when heated above the topology freezing temperature, T_V, the temperature at which the rate of bond exchange became significant. Therefore, the polymer was stretched above the T_V, with this deformed shape frozen in place on cooling, much like the programming method employed for shape memory polymers. At room temperature the transesterification reactions slowed to the extent that the material behaved as a conventional elastomer, and on heating above the T_{iso} the film contracted with a strain of 35%, and returned to the undeformed state on heating above T_V.[46]

In work by Ikeda *et al.* the transesterification reaction was extended to include a photomobile LCE based on a polysiloxane backbone with hydroxylate side chains and mesogen-containing dicarboxylic acid linking groups.[47] Following this work several examples of LCEs containing various exchangeable crosslinks have been reported, in all cases the polymer was readily shaped at high temperature to form either elongated films, curved ribbons or helical structures. The polymers also displayed self-healing behaviour when two pieces of the polymer were held together and heated. Exchangeable bonds used to date include hydrogen bonds where a maximum strain of 150% was measured[48,49] and thiol-acrylate crosslinking,[50,51] where a strain of 60% was achieved using only commercially available starting materials and catalyst.[51]

A downside to the transesterification reactions is that a catalyst is required, which can limit the number of reprocessing cycles. For this reason disulfide linkages have since been incorporated into a LCE, as these bonds can exchange when irradiated with UV or heated with no need for a catalyst.[41,52,53] It was shown by Cai *et al*. that the resulting network could be made exchangeable with both UV and on heating, resulting in LCEs where 20-25% strain was measured during heating/cooling cycles. Their polymer was also processed using an imprint lithography technique to produce a micropillar array in a mould which, after heating at 90 °C, demonstrated a reversible contraction in the height of the pillars and an expansion in the width, indicating that LC alignment occurred along the length of the pillars during the moulding process.[41] A similar structure had been designed previously for a conventional LCE containing CNTs, where contraction of individual pillars could be triggered by a laser diode, with application as a refreshable braille display proposed.[54] Similar structures have also been designed for use as gecko-foot inspired adhesive surfaces.[55]

More complex geometries were obtained by Yang *et al*. from sheets of an LCE containing disulfide crosslinks. They utilised the self-healing properties of the exchangeable crosslinks to combine thin films cut from an alignment-layer oriented LCE into laminates, using a catalyst 'glue' to promote exchange of disulfide bonds across the interface at room temperature. By rotating the director through the thickness of their laminate structure by changing the angle of each ply they were able to achieve curling and bending from a uniaxially aligned film.[53] Most recently polyurethanes with exchangeable carbamate groups with strains of up to 120% have been reported,[56] with exchangeable covalent crosslinking appearing to be an important future research direction for processing LCEs on larger length scales than thin films.

1.2.2.3. Composite Structures

A straightforward method to convert a one-dimensional deformation such as the contraction of a wire into a three-dimensional, out of plane deformation is to incorporate the active material into a composite structure. This is a common strategy to create soft, morphing structures from linear actuators and a passive structural material.[57] Composite LCE structures have been achieved by fracturing a LCE polymer at low temperature to produce monodomain-containing particles with sizes between 1-150 μm, before embedding the particulates in a polydimethylsiloxane (PDMS) matrix. The LCE particles were aligned under a magnetic field during the curing of the PDMS in order to impart thermoresponsive behaviour on the final composite. This method allowed for the production of macroscopic, mouldable structures, which is not possible for pure, crosslinked LCEs. Complex deformations such as saddle-shaped curvature were obtained by forming laminates of polymer-dispersed LCE disks, with strains of 9% measured on heating. This value

was reduced in comparison with the strains measured for the pure LCEs (30-35%),[58] and presents one of the disadvantages of LCE composites as the non-active matrix material acts to limit the deformation of the LC component.

Bilayer structures can also be used to create multi-responsive soft materials, for example by attaching the heat-responsive LCE layer to a water-responsive hydrophilic polymer.[59] LCE films have also been incorporated into composite hinges to promote a bending deformation. An electromechanical response was seen by including a Joule heating layer, consisting of a conductive metal layer. The LCE was then combined with either relatively rigid paper regions to promote hinge-like deformation,[60] or inserted into a soft, 3D printed structure to produce a beam or hinge capable of reversible bending on application of an applied voltage.[61] In both cases the LCE film produced the contractive or extensive force on heating, whilst the surrounding hard regions restricted deformation in certain directions to obtain the desired deformed geometry.

Similar approaches have been used to design actuators for incorporation into larger assemblies, for example to manufacture a biomimetic swimming turtle, where propulsion through water was achieved by a combined bending and twisting of the composite films acting as flippers.[62] The smooth and continuous deformations were driven by an active Shape Memory Alloy (SMA) wire, which demonstrated a reversible contraction under application of a current. The SMA was affixed to soft, 3D printed scaffolds which were designed to have layers with a certain fibre direction, where printing cross- or angle-ply structures resulted in smooth bends or twists that were readily predicted using Classical Laminate Theory. The assembly was then encased in PDMS which resulted in a soft actuator capable of smooth deformations.[62] However, if a polymeric linear actuator such as a LCE was available it may be possible to integrate the passive and active layers by multi-material 3D printing, instead of using the SMA.

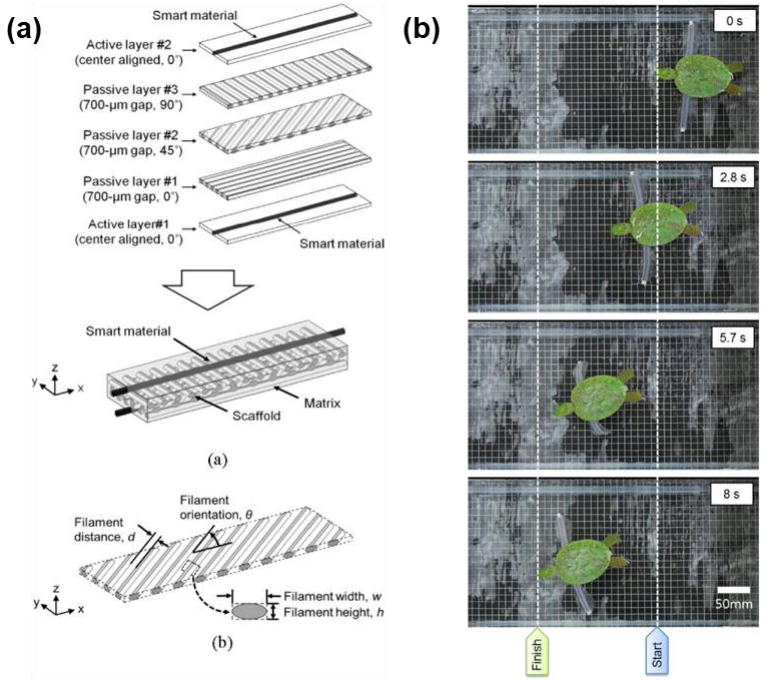

Figure 1-16. Altering the fibre angle in laminate structures (a) results in bends and twists on contraction of a shape memory alloy, which was used to propel a soft turtle robot (b). Reproduced with permission from reference 62 - IOP Publishing.

3D printing of LCEs by direct-write printing has recently been reported.[63–65] In all cases an ink containing a commercially available LC monomer, chain extender and photoinitiator based on the system given in Figure 1-10 was printed. This formed an aligned filament of oligomers which was crosslinked using UV irradiation to form the LCE. The shear encountered by the ink when extruding from the printer nozzle was used to form the LC monodomain, which was demonstrated to align along the direction of the print path and was dependent on the diameter of nozzle used.[63] The resulting printed structures were capable of reversible shape change, including complex out-of-plane deformation, which was achieved by varying the print path so as to change the direction of alignment within each layer. This extrusion method is well suited for spatial patterning on a larger length scale than seen for other alignment techniques, but has to be re-optimised to accommodate the rheological properties of different monomers and crosslinking agents, which limits the ability to alter the mechanical properties of the final polymer system. 3D printing of thermoplastic LCEs would therefore offer an attractive alternative for the manufacturing of soft actuators.

1.3. Thermoplastic Liquid Crystal Elastomers

Whilst it was shown in Section 1.2 that LCEs can be used as actuators, the processing of these materials and formation of aligned mesophases is still difficult for structures on larger length scales. An alternative approach that would make LCEs easier to process and suitable for new techniques, such as 3D printing, is through the development of thermoplastic LCEs. These materials are based on triblock copolymers and require no chemical crosslinks, which means that they should be re-processable without the need for catalysts (unlike CANs).

1.3.1. Block Copolymers and Microphase Segregation

Block copolymers contain two or more non-identical polymer blocks linked together by a covalent bond. This prevents macroscopic separation of the chemically distinct chains, but enables microphase segregation as the chains rearrange in order to minimise the overall free energy, G, which is comprised of an enthalpic and entropic component (Equation 1.2).

$$\Delta G_{mix} = \Delta H_{mix} - T\Delta S_{mix} \qquad 1.2$$

For polymers with a high degree of polymerisation ΔS_{mix} is small and has little effect on the overall free energy. A far greater contribution arises from the unfavourable enthalpy of mixing non-identical blocks, which disfavours mixing and results in microphase segregation of the blocks. This leads to a decrease in entropy of the system as the bonds between blocks become localised at interfaces and polymer chains stretch to maintain a constant density, however, this effect is minimal for polymers at low temperature.[66] The microphase separated morphology depends on the volume fraction (f_i) of one block over the other, where increasing f_i leads to increasing curvature at the interface between blocks in order to minimise interfacial area, and so as f_i moves away from 0.5 the morphology of the microphase segregation transitions from lamellar to gyroidal, cylindrical, then to a spherical morphology (Figure 1-17).

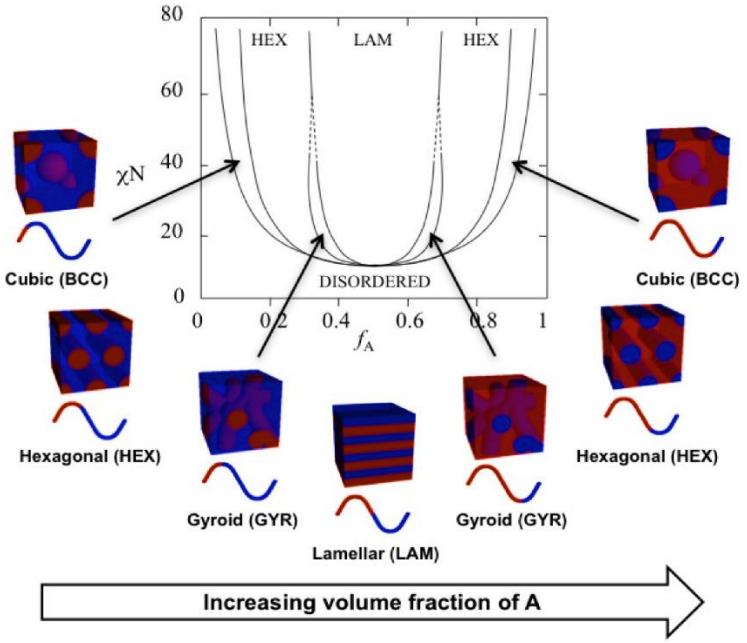

Figure 1-17. Generic phase diagram for an AB block copolymer from the weak (χN=10) to strong (χN=50+) segregation limit. Reproduced with permission from references 67 and 68 - American Chemical Society.

The volume fraction is defined according to Equation 1.3, where the molar volume, $V_{M,i}$, describes the volume occupied by one mole of the given homopolymer, *i*.

$$f_i = \frac{V_{M,i}}{\sum V_{M,i}} \qquad 1.3$$

In addition to the composition (f_i), the polymer-polymer phase behaviour is dependent on the molecular architecture (e.g. diblock, triblock), the choice of monomers, and the degree of polymerisation (N).[66] It has been shown using Self-Consistent Field Theory (SCFT) that symmetrical AB diblock and ABA triblock copolymers will segregate in similar manners (especially in the strong segregation limit),[66,68,69] which allows for the construction of a generic phase diagram such as that given in Figure 1-17. Using this information, the morphology for a block copolymer can be predicted from values for f_i and χN, where χ is the Flory-Huggins interaction parameter.[70,71]

The Flory-Huggins interaction parameter consists of both an enthalpic and entropic component, such that:

$$\chi = \chi_H + \chi_S \qquad 1.4$$

Block copolymers that have χN below 10 are expected to be disordered and homogeneous, with no microphase segregation occurring. Using SCFT it has been shown that regions of the phase diagram can be divided between the weak (χN = 10-12), intermediate (χN = 12-50) and strong segregation limit (χN = 50+), with the gyroidal mesophase becoming less stable as χN increases.[68] Above the weak segregation limit the enthalpic term (χ_H) dominates which leads to microphase separation in order to reduce interactions between the A and B blocks,[66] and so the entropic term (χ_S) can be neglected. The enthalpic component at some temperature, *T*, can be derived from the cohesive energy of the interaction between the two polymer blocks as given in Equation 1.5, where *k* is the Boltzmann constant and ε_{ij} is the interaction energy between blocks of types *i* and *j*.

$$kT\chi_H = \frac{z}{2}(\varepsilon_{AA} - 2\varepsilon_{AB} + \varepsilon_{BB}) \approx \frac{z}{2}\left\{\varepsilon_{AA} - 2(\varepsilon_{AA}\varepsilon_{BB})^{1/2} + \varepsilon_{BB}\right\} \quad 1.5$$

The total cohesive energy, E_{coh}, of a segment surrounded by *z* molecules can be defined according to Equation 1.6:

$$E_{coh} = \frac{z\varepsilon_{ij}}{2} \quad 1.6$$

Dividing E_{coh} by the molar volume, $V_{M,i}$, of the repeat unit gives the cohesive energy density, the square root of which is known as the solubility parameter, δ_i.

$$\delta_i = \left(\frac{E_{coh,i}}{V_{M,i}}\right)^{\frac{1}{2}} = \left(\frac{z\varepsilon_{ij}}{2V_{M,i}}\right)^{\frac{1}{2}} \quad 1.7$$

Substitution of δ_i into Equation 1.5 allows for the equation for χ_H to be rewritten in terms of the molar volume (Equation 1.8) which simplifies to give Equation 1.9.[72]

$$\frac{RT\chi_H}{V_M} = {\delta_{AA}}^2 - 2(\delta_{AA}\delta_{BB}) + {\delta_{BB}}^2 \quad 1.8$$

$$\chi_H = \frac{V_M}{RT}(\delta_{AA} - \delta_{BB})^2 \quad 1.9$$

Therefore, by calculation of the molar volume, and so the volume fraction for the A and B blocks, and with values for δ_A and δ_B that allow for calculation of χ, it is possible to predict the morphology adopted by a given AB or ABA block copolymer. It should also be noted that χ is inversely proportional to the temperature, and so by increasing the temperature it is possible to reduce χ sufficiently that no microphase separation is seen and a homogeneous mixture of the two blocks is obtained. This is known as the order-disorder transition, and occurs at some critical temperature, T_{ODT}.

The microphase segregated morphology can be determined experimentally through a combination of Small Angle X-Ray Scattering (SAXS) and Transmission Electron Microscopy (TEM). In SAXS, X-rays are scattered by the electrons present in the material. Depending on the location of the electrons relative to each other these scattered waves will then interact in either a constructive or destructive manner, before hitting the detector. The intensity will therefore vary depending on the position of the atoms within the material, with the interference pattern defined by the intensity measured at a given scattering angle, θ, and the azimuthal angle, φ (Figure 1-18).

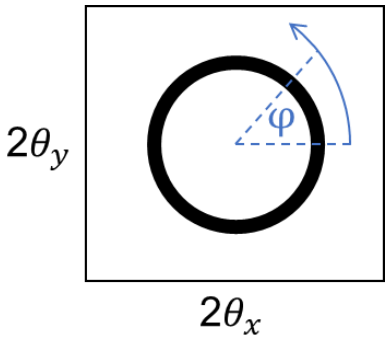

Figure 1-18. Definition of scattering angle, 2θ, and azimuthal angle, φ, in 2D SAXS.

The scattered intensities detected in a 2D plane (if isotropic) can then be reduced to a one-dimensional plot of intensity against a value, q, which is defined in Equation 1.10. This conversion is used as q can be quoted independently of the wavelength of the applied radiation, λ. As q is given as the reciprocal of the wavelength results obtained from these plots and the 2D scattering are in reciprocal space.

$$q = \frac{4\pi}{\lambda} \cdot \sin\theta \qquad 1.10$$

The average internal structure of the material can be deduced from two components of the scattering pattern. Scattering from the atoms that make up one particle results in the form factor, $P(q)$. This is a characteristic scattering pattern which arises due to the shape of the particle, for example spheres, and can be used to determine the average structure of the material. The second feature, the structure factor, $S(q)$, arises due to interference between scattering from different particles, and can therefore be used to determine the spacing between structural features.[73] The values for the spacing, d, in real space can be converted from reciprocal space through Equation 1.11.

$$d = \frac{2\pi}{q} \qquad 1.11$$

As the level of order within a material increases (for example by the development of a microphase segregated structure) peaks arising from the structure factor become more intense and, depending on the lattice symmetry, higher order peaks may be observed. For example, a lamellar microstructure, such as that obtained when $f_i = 0.5$, will have peaks at q, $2q$, $3q$, $4q$, a spherical microstructure will have peaks at q, $\sqrt{2}q$, $\sqrt{3}q$, $2q$ and a hexagonal microstructure will have peaks at q, $\sqrt{3}q$, $2q$, $\sqrt{7}q$.[73] The $P(q)$ and $S(q)$ allow for the determination of the *average* microstructure of a bulk sample of a block copolymer, however, as the data is averaged over the area irradiated with X-rays, a complementary microscopy technique (TEM) is often combined with SAXS, as this enables *individual* particles or domains to be imaged in real space.

1.3.2. Microphase Segregation in Liquid Crystal Block Copolymers

Further contributions to the overall free energy arise from the LC component of LCPs. In a similar manner to how block copolymers microphase separate in order to adopt the most energetically stable configuration by reducing interactions between non-compatible blocks, mesogenic groups will self-assemble to form ordered mesophases. Theoretical phase diagrams calculated for both main-chain and side-chain LC diblock copolymers show similarities with those for conventional block copolymers, with the main difference arising in the boundaries between phases which are asymmetric and favour curved interfaces with the non-LC block on the concave side.[74,75] This difference is driven by the additional stabilisation of the microphase separated state by the ordered nematic mesophase, due to the unfavourable energy penalty associated with mixing with the disordered second block.[75] It was therefore suggested that Equation 1.4 could be extended to give Equation 1.12, where χ_{LC} is an additional interaction parameter introduced by an ordered LC mesophase.[76]

$$\chi_{eff} = \chi + \chi_{LC} \qquad 1.12$$

For low molecular weight LC diblock copolymers, or those with a relatively low volume fraction for the LC block such that a lamellar morphology is adopted, heating above T_{iso} is sufficient to remove the χ_{LC} component and reduce χ_{eff} such that an order-disorder transition occurs and the block copolymer becomes a homogeneous melt.[76,77] For higher molecular weight polymers, or those where the volume fraction of the LC block results in cylinders or spheres of the minority block in a matrix of the LC block, the T_{ODT} is shifted to temperatures greater than the T_{iso}. This was proposed to be driven by the conformational asymmetry between the random-coil forming block and the well-aligned, and so extended, LC block, which leads to unfavourable frustration of the LC component at planar interfaces. This makes the lamellar morphology less stable than cylinders or

spheres, which stabilises the mesophase through curvature of the interface, and so the T_{ODT} is often coincident with the T_{iso} for lamellar systems.[76]

1.3.3. Thermoplastic Elastomers

Microphase segregation allows for the design of thermoplastic elastomers. These polymers display elastomeric properties such as flexibility and softness, but are crosslinked by physical, rather than chemical, interactions. This means that they can be processed by thermoplastic methods, for example from the melt by extrusion. TPEs based on block copolymers are commonly synthesised by two approaches – one gives styrenic TPEs and the second multiblock copolymers. Multiblock copolymers with the structure $(AB)_n$ can be synthesised by polycondensation reactions to give alternating crystalline and amorphous blocks, with an example being thermoplastic polyurethane.[78]

Styrenic TPEs consist of an ABA triblock copolymer structure where the A blocks are glassy polystyrene and the B blocks a soft, elastomeric polymer. Typically, the PS end segments microphase segregate to form spheres within a continuous phase of the B block (Figure 1-19), which act to form a physical network and results in elastomeric properties. These polymers are usually synthesised through living anionic polymerisation, and so the choice of the B block is generally limited to polybutadiene or polyisoprene. When at temperatures above the glass transition temperature (T_g) of the B block, the polymer displays typical elastomeric behaviour, but when heated above the T_g of styrene or dissolved in solvent the hard blocks soften and the polymer can be processed as a conventional thermoplastic melt. On cooling or evaporation of the solvent the hard blocks reform and elastomeric behaviour is recovered.[78]

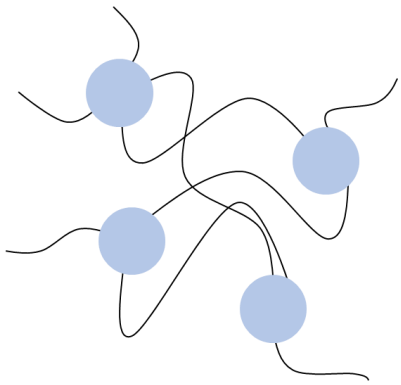

Figure 1-19. Styrenic TPE. Light regions correspond to spheres formed by PS end blocks which act as physical crosslinks. Dark lines correspond to the continuous phase of the soft midblock.

One of the major barriers to the bulk processing of LCEs is the covalent crosslinking required for elastomeric behaviour. For this reason, thermoplastic LCEs may have potential as they could, in theory, be used in more polymer processing techniques than conventional LCEs, including those such as fibre extrusion where incorporation of a crosslinking step would be unpractical due to the rate of fibre drawing. Thermoplastic elastomers commonly consist of ABA triblock copolymers and it is possible to incorporate mesogenic[79,80] or photoresponsive[81] groups into the structure.

Petr *et al*. reported a thermoplastic LCE that was capable of reversible room temperature actuation due to the presence of an azobenzene-containing mesogen.[82] The backbone of this polymer consisted of a polystyrene-*b*-poly(methylvinylsiloxane)-*b*-polystyrene (PS-*b*-PMVS-*b*-PS) triblock copolymer, with the rod-like mesogen attached in a side-on manner to the PMVS block (Figure 1-20).

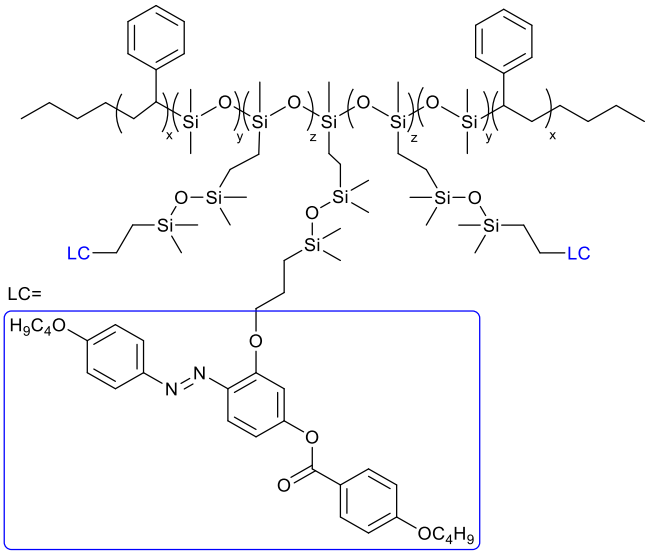

Figure 1-20. Structure of UV-responsive LC-functionalised thermoplastic from Reference 82. The rod-like mesogen was attached to the PS-*b*-PMVS-*b*-PS triblock copolymer backbone *via* a hydrosilylation reaction.

The thermoplastic LCE given in Figure 1-20 was shown to rapidly and reversibly contract with a strain of 3.3% against an applied tensile stress of 25.7 kPa at room temperature,[82] however, the hydrosilylation method used for functionalising the mesogen with a linking group was low yielding (30%).[4]

1.4. Processing of Thermoplastic Fibres

For most LCEs elastomeric behaviour is achieved by lightly crosslinking the aligned polymer to fix in the LC mesophase, typically by the use of a UV-activated process, to form a thermoset polymer.[6] This leads to materials that are capable of significant and complex deformations but which, due to the nature of the alignment and crosslinking steps, are typically limited to very thin films that cannot be processed further. For applications as actuators, fibres are a useful geometry due to the high surface area to volume and so for this reason, applying thermoplastic processing methods to LCEs may be a useful route towards novel structures and applications.

Thermoplastic polymers are processed using a variety of methods, generally either from a melt, or from solution. LC polymers are processed on an industrial scale through both approaches, with nematic thermotropic copolyesters commonly processed using injection moulding. In this process the polymer melt is forced into a shaped mould by a rotating screw which then acts as a plunger to compress the melt and replicate the mould, with solidification occurring on cooling. The low viscosity of nematic LCPs allows for excellent mould replication, even for complex shapes, and the low volume change on transition from a liquid to a solid is also beneficial. Perhaps the most famous LCP to be produced on an industrial scale is Kevlar, which was first produced industrially by DuPont in the 1970s and is a lyotropic aromatic polyamide. The polymer is produced as a fibre from wet-spinning methods, where the drawing of the fibre from solution by precipitation into a poor solvent whilst winding under tension acts to orient the LC part parallel to the fibre direction, which results in high tensile strength in the fibre direction.[83] Similar methods have been applied to LCEs on the laboratory scale in order to produce aligned, responsive fibres. Whether melt or solution processing is better suited will be dependent on a variety of material properties, with the viscoelasticity most important for melt processing and the solubility in appropriate solvents for solution processing.

1.4.1. Melt Processing

It has been shown that the shear encountered during melt extrusion can be used to align a responsive thermoplastic LCE.[84] In this case the midblock consisted of a liquid crystal main-chain polymer, with terphenyl moieties attached on each end by an esterification reaction. The terphenyl end groups self-assembled to form hard domains that acted as physical crosslinks on drawing a fibre from the melt, allowing for reversible actuation on heating and cooling through the isotropic transition temperature (T_{iso}). The liquid crystal block was aligned along the length of the fibre, which allowed for significant changes in length on heating (up to 500%), but also

demonstrated thermoplastic creep at the temperatures required for actuation, which is undesirable for practical applications.

Extrusion from a polymer melt is one of the most convenient and economical processing methods for thermoplastic polymers.[83] The relatively simple process of pushing a polymer melt through a shaped die allows for continuous fibre formation, and can also be used with processes such as 3D printing to create complex, layered structures. The ability for a polymer to be processed from the melt has a strong dependence on its viscoelastic properties, and so understanding the rheology of polymer melts is vital. The flow properties of a thermoplastic polymer melt can be investigated using a rotational rheometer equipped with a parallel plate or cone-plate geometry. Shear is induced through the thickness of the sample by the motion of the rotating top plate relative to the fixed bottom plate (Figure 1-21).

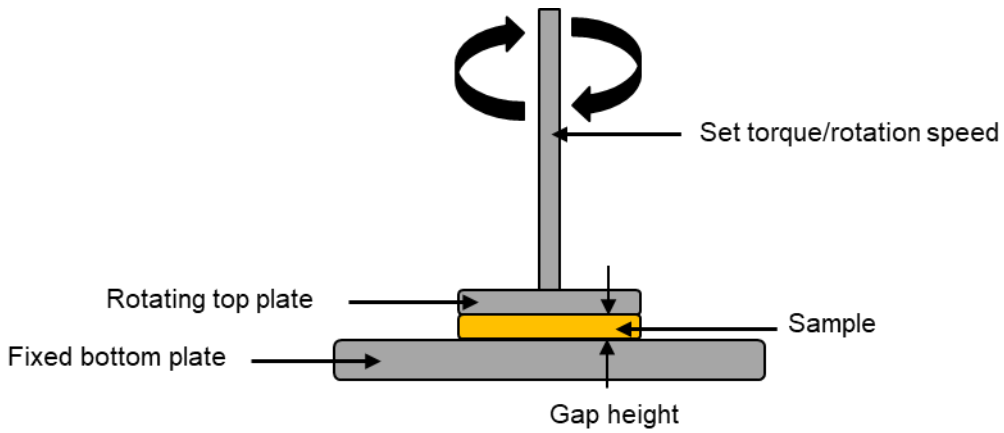

Figure 1-21. Operating principle for rotational rheometer with parallel plate geometry.

This motion generates a force, F, which acts on the sample across the area of the top plate, A, generating a shear stress, τ, where $\tau = \frac{F}{A}$ (Figure 1-22). This stress results in a strain deformation, γ, which is calculated from the deformation, s, relative to the sample thickness, h, by $\gamma = \frac{s}{h}$. On measurement of the appropriate values it is possible to determine the viscosity or shear modulus of the material. Measurements are made assuming that no plastic deformation occurs (and so a homogeneous deformation is applied through the thickness of the sample) and that there is no slip at the sample-plate interface.

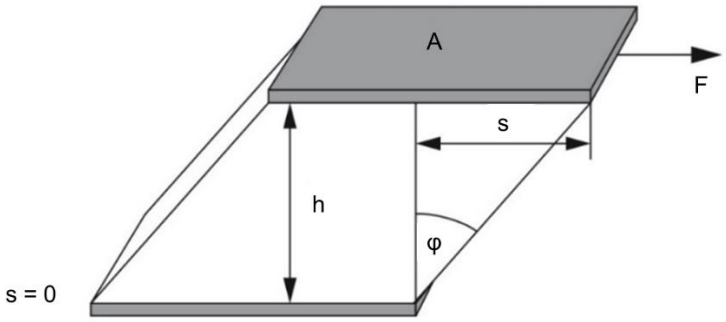

Figure 1-22. Two plates model for rotational rheology. *F* is the force acting on area, *A*. The resulting shear strain is obtained by dividing the deformation, *s*, by the sample thickness, *h*, or by tan φ. Reproduced from reference 85.

By changing the rate of rotation of the top plate it is possible to alter the rate of strain, $\dot{\gamma}$, of the deformation as defined in Equation 1.13, where ν is the velocity and h the gap height.

$$\dot{\gamma} = \frac{\nu}{h} \tag{1.13}$$

The strain rate can then be related to τ by using Newton's law (Equation 1.14) through the viscosity, η, of the material.

$$\tau = \dot{\gamma} \cdot \eta \tag{1.14}$$

The dependence on the shear rate means that viscosity is a time dependent property, and so for a purely viscous material the removal of an applied stress leaves the material in the deformed state, with recovery occurring after some amount of time. As well as the viscosity, rheology can also be used to measure the shear modulus of a polymer, G, which is related to τ and γ for a purely elastic material by Hooke's law (Equation 1.15) when sufficiently low values of γ are used.

$$G = \frac{\tau}{\gamma} \tag{1.15}$$

The shear modulus is not reliant on the shear rate, therefore, once the applied shear stress is removed the internal structure of the material will immediately return to its original state. Polymers, however, form viscoelastic melts, and so a combination of both Newtonian and Hookean behaviour is observed. On removal of an applied stress a partial recovery is seen, which leads to phenomena such as die-swell, whereby after extrusion polymer chains aligned by shear are able to re-coil once the stress is removed, resulting in an expansion relative to the size of the die.[85] Due to their viscoelastic nature there are two components to the shear modulus measured for polymers; G', the storage modulus, and G'', the loss modulus. G' represents energy stored by the material during deformation. Once the applied stress is removed this energy is used to restore the material towards its original state and so describes elastic behaviour. G'' represents

deformation energy lost by the sample during deformation, for example as heat to the surroundings or the sample due to friction forces acting between polymer chains as they slide past each other. This non-reversible energy loss therefore represents the viscous component.

In order to measure the viscosity and shear modulus of polymers across a range of frequencies comparable with those encountered during extrusion, Small Angle Oscillatory Shear (SAOS) tests can be employed. In these experiments the top plate oscillates with a varying frequency to a given amplitude rather than rotate, imparting a sinusoidal strain on the sample (Equation 1.16) where γ_A is the maximum strain amplitude, and ω the angular frequency of the oscillation at time, t.

$$\gamma(t) = \gamma_A \sin \omega t \qquad 1.16$$

The sinusoidal strain results in a sinusoidal shear stress, which is shifted relative to the applied strain by the phase shift angle, δ (Equation 1.17). This value is equal to 0 for a purely elastic response, to 90 for a purely viscous response and is between these two values for viscoelastic materials.

$$\tau(t) = \tau_A \sin(\omega t + \delta) \qquad 1.17$$

Due to the sinusoidal oscillating shear, the shear modulus and viscosity measured by SAOS are given as their complex forms:

$$G^* = \frac{\tau(t)}{\gamma(t)} \text{ and } \eta^* = \frac{\tau(t)}{\dot{\gamma}(t)} \qquad 1.18$$

The typical shear flow diagram seen for homogeneous polymer melts with varying shear rate is given in Figure 1-23, where three characteristic regions have been identified.

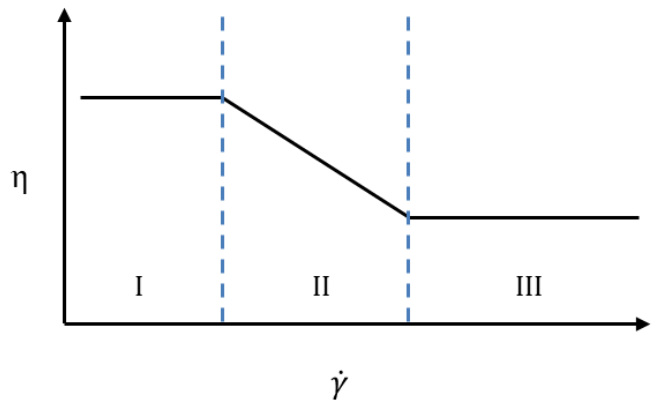

Figure 1-23. Typical flow diagram for thermoplastic polymers with increasing shear rate. $\dot{\gamma}$ is the shear rate and η the viscosity.

In Region I (the first Newtonian range) the viscosity has a plateau value which is equal to the zero-shear viscosity. In this region the shear rate is low enough that polymer chains which have been disentangled are able to re-coil due to their viscoelastic response on the timescale of the measurement to give no net change in viscosity. In Region II the material shows shear-thinning behaviour as a function of $\dot{\gamma}$. In this range the polymer coils are not able to return to their entangled state and so as they align with the increasing shear are capable of moving relative to each other and the overall viscosity decreases until Region III (the second Newtonian range) is reached, which is equal to the infinite-shear viscosity. At this point the resistance to flow is at a minimum and under these high shear conditions it is not possible to decrease the viscosity any further.[85]

For a liquid-like melt, G'' will be greater than G' and viscous behaviour will dominate, whereas for a gel or solid-like material G' is greater than G'' and elastic behaviour dominates (in this regime useful values for η are not obtained as Newton's law is not obeyed). The point where both values are equal is known as the gel-point, with a crossover of curves seen when behaviour shifts from viscous to elastic dominated due to increasing shear. Typically, G' will increase with increasing frequency as the decreasing time period of the measurement results in more elastic-like response from the polymer chains, whilst G'' decreases.

The viscosity and shear moduli of thermoplastic polymers can be modelled assuming that they show thermo-rheologically simple behaviour. This means that the internal structure has no temperature dependence and allows for prediction of behaviour under conditions that are difficult to replicate using a rheometer (i.e. very high or low frequency deformation) by the principle of time-temperature superposition (TTS). Block copolymers can be described as thermo-rheologically simple on the condition that the measurement temperature is greater than the order-disorder transition temperature (T_{ODT}). Under these conditions the microphase separation between the hard and soft blocks in a block copolymer is lost and the polymer exists as a homogeneous, liquid-like melt suitable for extrusion (i.e. the flow curve given in Figure 1-23 applies). Below the T_{ODT} block copolymers behave as filled polymers, and so a solid-like response to applied shear is seen.[86]

Han and Kim demonstrated that a log-log plot of G' and G'' for a polystyrene-*b*-polyisoprene-*b*-polystyrene (SIS) block copolymer could be used to detect T_{ODT}.[86] Oscillatory shear measurements of G' and G'' as a function of angular frequency, ω, were made at 11 temperatures for SIS and for a comparative low-density polyethylene (LDPE). For the LDPE, a plot of log G' against log G'' gave a single curve where the results at each temperature overlapped, indicating that the melt properties had no temperature dependence. They calculated that in the homogeneous state this plot should have a gradient of 2 in the terminal (low frequency) region, giving another characteristic feature

of the transition. Conversely, measurements on SIS resulted in a log G' against log G'' plot that demonstrated a strong temperature dependence as individual curves were observed until reaching the T_{ODT}, whereby they became independent of temperature, overlapped and adopted a terminal gradient of 2, which indicated the loss of a microstructure. The temperature range they obtained for the order-disorder transition was in good agreement with that found by SAXS, and so offers an alternative method for identifying T_{ODT}.[86]

The rheology of LCPs is complex, and they show a number of behaviours that are not seen for conventional polymers. For example, the flow diagram for liquid crystal polymers shows a different trend to that seen in Figure 1-23 with two shear thinning regions and only one plateau as proposed by Onagi and Asada (Figure 1-24).[87] This diagram is not generic however, as the Region II plateau has only been detected for some lyotropic LCPs and some thermotropic LCPs demonstrate only Region I or Region III behaviour depending on their thermal history.[88]

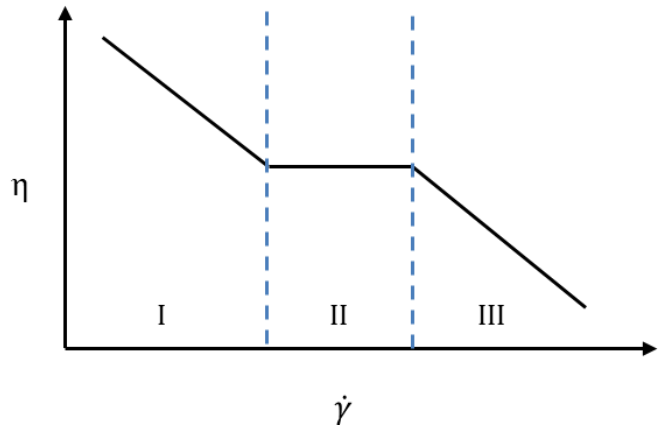

Figure 1-24. Proposed flow diagram for liquid crystalline polymers. $\dot{\gamma}$ is the shear rate and η the viscosity.

In the low shear region (I), the viscosity sharply decreases with shear rate rather than observing zero-shear viscosity. At low $\dot{\gamma}$ the individual nematic domains within the LCP will rotate, however, as in each domain the local director will vary this leads to no net increase in the alignment and so a maximum in the viscosity. As the level of shear increases, increasing numbers of domains will align relative to each other (and the shear direction), resulting in less resistance to flow and so shear-thinning behaviour. By Region II the number of domains has reduced as coalescence increases with shear rate and the larger domains demonstrate more resistance to flow, although this behaviour is rarely seen. At high shear in Region III the LCP chains strongly align with flow and strong shear-thinning behaviour is seen until the polymer behaves as a monodomain.[88]

Another feature of thermotropic LCPs that makes their rheology different from most polymers, and which has led to interest in their use in industrial processes, is that their viscosity can increase with increasing temperature. In the nematic mesophase, polymer chains are aligned relative to each other which reduces their effective hydrodynamic volume and enables them to slide past each other with little resistance, whereas in the isotropic state their orientations are more random with increased entanglements and so increased resistance to flow. Therefore, on heating an ordered nematic mesophase, ordered domains are increasingly converted to the disordered isotropic state, leading to a biphasic structure where viscosity gradually increases.[89–91] This makes main-chain LCPs relatively easy to process at low temperatures (compared with conventional high molecular weight polymers) when in the nematic state, but the strong dependence on temperature makes them thermo-rheologically complex, meaning that concepts such as TTS are not valid.

LCPs based on block copolymers contain a further level of complexity. The nematic state is stabilised by the curvature of spherical or cylindrical morphologies, which can act to raise both the T_{iso} and the T_{ODT} compared with LCPs adopting lamellar morphologies.[76] This effect was also demonstrated for a series of PS-*b*-PI block copolymers that were functionalised with varying amount of a side-chain LC on the PI block, so as to investigate the effect of changing the molecular weight, and so volume fraction, of this block on the order-disorder transition. By this method it was shown that through reducing the liquid crystal loading it was possible to bring the T_{ODT} from above 240 to 140 °C, with the interaction parameter between the side-chain and the PS block strongly dependent on the amount of LC present.[92]

1.4.2. Solution Processing

Whilst melt processing is preferable as no solvent is required, polymer fibres are manufactured on an industrial scale by a number of spinning methods. Solution spinning processes are attractive as continuous fibre formation is possible, so long as there is a constant supply of the polymer solution. A wet-spinning technique for forming LCE fibres was developed by Ohm *et al*. using a microfluidic device consisting of a needle aligned within an outer tube (Figure 1-25). Silicon oil was fed continuously through the outer tube, with a solution of monomers, crosslinker and photoinitiator injected through the needle and aligned along the flow of the silicon oil, whilst crosslinking was carried out with a UV light source to produce a main-chain smectic A elastomer. It was shown that the thickness of the fibre could be controlled by the flow rate of the oil, with faster flow rates resulting in thinner fibres.[93]

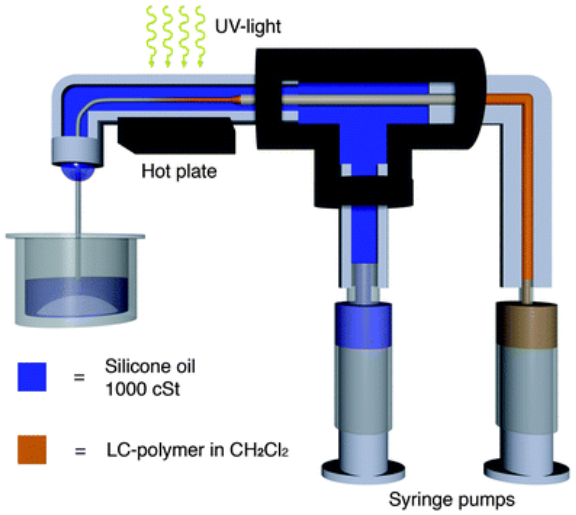

Figure 1-25. Microfluidic setup developed by Ohm *et al*. for formation of a main-chain LCE fibre. Reproduced with permission from reference 93 - John Wiley & Sons.

Fibres were measured to have a diameter of 30-33 μm and to have a smectic mesophase oriented along the fibre length, although the orientation was not strong. A reversible contraction of around 15% was measured on heating the fibres above T_{iso}, but it was necessary to apply a small stress to the fibre to recover the original length.[94]

Electrospinning has gained interest as a method of producing nano-scale fibres for applications where a large surface area is desirable including sensors,[95,96] composite reinforcement[97,98] and tissue engineering.[99,100] One of the advantages of electrospinning is the relatively simple setup required, which combined with the wide variety of materials compatible with the technique, allows for continuous production of fibres with diameters from the micro- to the nanoscale. In a typical laboratory setup, a polymer solution or melt is pumped through a needle from a syringe, with the flow rate controlled by a syringe pump (Figure 1-26). The needle also acts as an electrode, to which a high electric field of 100-500 kV m^{-1} is applied. The fibre collector acts as the counter electrode and is typically located 10-25 cm from the needle tip. Fibres are collected on a conductive surface, at the most simple a piece of aluminium foil, but differing geometries can be chosen in order to promote alignment of fibres.[101]

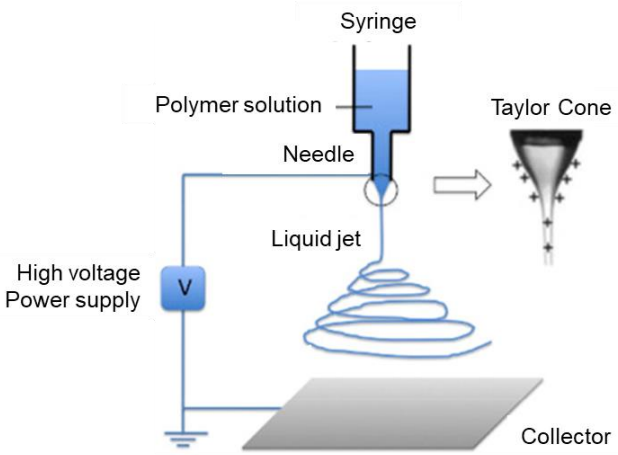

Figure 1-26. Basic schematic of electrospinning setup and Taylor cone. Reproduced with permission from reference 102 - Elsevier.

A drop of the polymer forms at the tip of the needle and with applied voltages between 1-30 kV becomes highly electrified, with charges evenly distributed over the surface.[103] The droplet is deformed by the applied voltage to form a Taylor cone[104] and as the voltage is increased and a critical charge density is reached, the cone becomes unstable as the electrostatic forces overcome the surface tension of the solution and emits a jet of the solution which extends towards the counter electrode.[103] This jet thins as the voltage is increased and instabilities are formed which induce whipping of the fibre. The solvent evaporates and a solid polymer fibre is formed, which is collected at the counter electrode.[102]

Using a flat collector, fibres will be collected as disorganised non-woven mats. Alignment of fibres can be induced by using an alternative collector. It was shown by Li *et al*. in 2003 that two parallel electrodes will modify the local electric field such that fibres stretch across the gap between the two electrodes, resulting in a well-aligned mat that can be removed and used for further characterisation (Figure 1-27). For the polymer solution in their work the gap size could be modified from hundreds of microns to centimetres, with the fibres deposited on the electrodes themselves shown to be highly disordered in contrast to those stretched across the gap.[105] Alignment can also be introduced by the use of a rotating collector. Varying geometries have been shown to work, including drums and thinner wheels,[106] with the thinner width of a wheel resulting in highly aligned fibre arrays.[107–109]

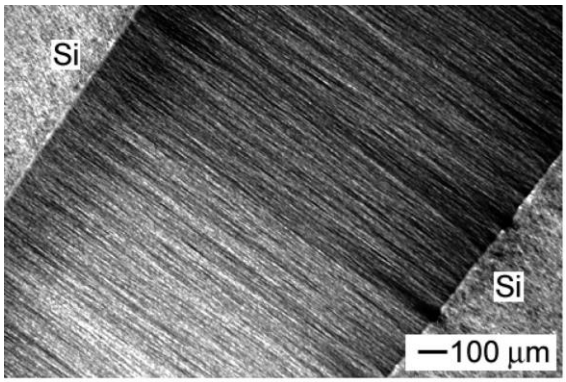

Figure 1-27. Aligned fibres collected between parallel electrodes. Disordered fibres apparent on Si electrodes. Reproduced with permission from reference 105 - American Chemical Society.

The morphology, diameter and alignment of the fibres can be controlled by varying several experimental parameters either for the polymer, the solution or the experimental setup. These include the molecular weight, polydispersity, T_g and solubility of the polymer, the viscosity, viscoelasticity, concentration, surface tension and electrical conductivity of the polymer solution and the vapour pressure of the solvent and humidity. In general, increasing viscosity favours the formation of smooth fibres as a certain level of viscoelasticity is required to overcome instabilities that favour droplet formation. It is necessary to balance the competing effects of the repulsion between electrostatic forces on the Taylor cone (which favour extension of the jet to form a fibre) and the surface tension of the solvent (which favours the formation of droplets).[103] In terms of the electrospinning setup, the fibre diameter can be controlled by the electric field and the feed rate. Fibres become thicker with increasing concentration and feed rate and thinner with increasing electrical conductivity of the solution.[101]

A common defect in electro-spun fibres are droplets which are undesirable as they act as weak points in the fibre structure. The formation of a smooth fibre can be promoted by increasing the surface charge density, the polymer concentration or molecular weight, the solution conductivity or viscosity and the feed rate.[103] The driving force behind all these factors is the minimisation of surface area by surface tension which favours the formation of droplets over a continuous fibre. This must be overcome by the effect of electrostatic repulsions on the droplet surface, which favour increased surface area in order to separate charges.

More complex structures can be obtained by modification of the needle. Coaxial electrospinning is possible by incorporating a second nozzle within the first.[110] This results in core-sheath fibres where the core can consist of a small molecule or low molecular weight polymer that would not ordinarily spin, and the sheath a polymer that will easily form fibres which increases the materials that can be used with electrospinning to include biomolecules[111] and liquid crystals.[112] This

method can also use a sacrificial core to obtain hollow fibres. Li *et al*. developed a setup that used two immiscible liquids in a coaxial spinneret, in this case a mineral oil and an ethanol solution containing poly(vinylpyrrolidone) (PVP) and Ti(O*i*Pr)$_4$. The mineral oil could then be removed by a selective solvent to produce hollow composite fibres, or the as-spun fibres could be converted to hollow, ceramic nanofibers by calcination which removed both the mineral oil and PVP.[113]

1.4.3. Electrospinning of Liquid Crystal Polymers

During electrospinning of LCPs, it is expected that the elongational deformation of the jet by the applied electric field will act to align the LC component along the fibre length. Two approaches to the electrospinning of LCEs have been reported – forming a core-sheath fibre where the LC is confined within a channel of a sheath polymer, or by direct electrospinning of the LCP solution before crosslinking. In the approach developed by Lagerwall *et al*, the coaxial electrospinning method described above was utilised to produce a fibre consisting of a hollow PVP sheath, with the core filled by a commercial nematic liquid crystal. The director was shown to align along the length of the fibre.[112] Later work extended this method to a dual-core fibre, where two different liquid crystals with different clearing temperatures (T_{iso}) were used to fill the channels resulting in a multifunctional fibre.[114] For the formation of coaxial LCEs, rather than a coaxial spinneret, a mixed solution of the PVP or PLA sheath material and the low molecular weight mesogen and photoinitiator were spun, with *in situ* phase separation during evaporation of the solvent shown to result in a core-sheath fibre. Fibres produced in this way were measured to have a diameter of between 2.6-3.2 μm. The LCE was shown to be birefringent, however, the LCE core was not continuous.[115] These fibres were responsive, with a contraction observed on heating above the clearing temperature, but the shape-change was not reversible, potentially due to the high stiffness of the sheath polymer.

For this reason, the second approach of directly spinning the LCE results in fibres better suited for actuation. Few examples exist in the literature, with all utilising photocrosslinkable polymer solutions rather than thermoplastic LCEs. In work reported by Krause *et al*. in 2007 a main-chain LCP with a M_n of 44,000 g mol^{-1} was synthesised by a phase transfer polycondensation reaction. The photocrosslinkable polymer was then dissolved in chloroform, and fibres spun onto glass or silicon substrates, with a UV lamp used to initiate crosslinking of the LCP to produce the LCE. It was shown that by varying the solution concentration it was possible to modify the morphology of the fibres. At 5.0 wt% fibres were obtained that contained several droplets along their length, however, a 7.2 wt% solution of polymer resulted in good quality fibres with no droplets and an average diameter of 1.5 μm (Figure 1-28). By POM it was demonstrated that a uniform director alignment was achieved along the length of the fibre.[116]

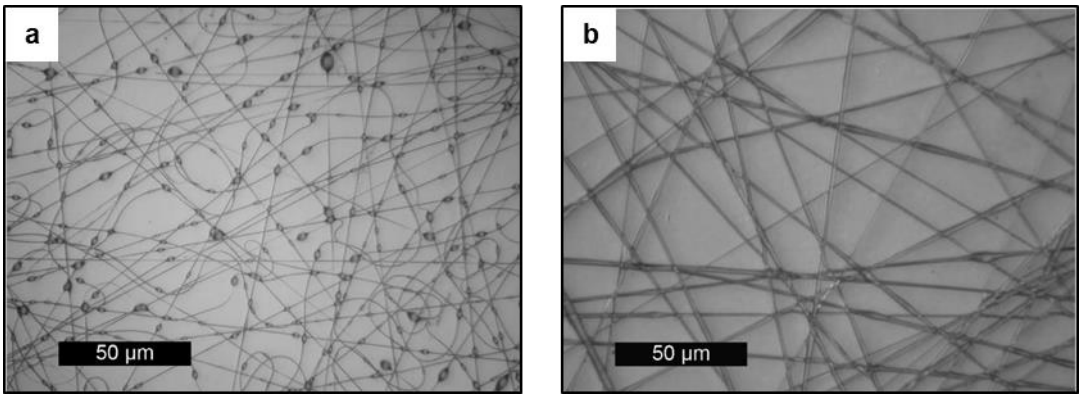

Figure 1-28. Fibres obtained by electrospinning of a photocrosslinkable main-chain LCP with (a) 5.0 wt % and (b) 7.2 wt % solutions. Reproduced with permission from reference 116 - John Wiley & Sons.

A second main-chain polymer based on a polyester backbone with a M_n of 29,000 g mol^{-1} and which formed a smectic mesophase was used in an electrospinning setup, although no crosslinking step was carried out. From this work it was demonstrated that the diameter of the fibre had a strong influence on the level of LC orientation achieved, with thinner diameters giving stronger alignment.[117]

A side-chain LCP fibre consisting of cholesterol units attached end-on to a polysiloxane backbone was used with electrospinning as reported by Wu *et al*. in 2008. The pure SC-LCP solution resulted in fibres with droplets, as seen by Krause *et al*., and it was not possible to obtain smooth fibres by simply varying the polymer solution concentration. This was attributed to the relative stiffness of the polymer, and so three approaches were taken to improve the 'spinnability' of the polymer solution. It was shown previously that important factors in electrospinning are the viscosity of the solution, the charge density and the surface tension. The first modification made was therefore to introduce a LC small molecule, which acted to decrease the viscosity of the solution. This improved the spinnability of the solution, but only decreased the number of droplets rather than remove them entirely. The next approach was to increase the charge density of the solution by including triethylamine, which, due to the presence of trace water, was protonated to form Et_3NH^+. This was shown by POM to improve the birefringence of the resulting fibres; however, large numbers of beads were still present. Finally, a polyethylene oxide (PEO) additive was added. PEO is often used to improve the spinnability of a solution for electrospinning by increasing the viscosity, and resulted in smooth, droplet-free fibres with an average diameter between 0.5-2.0 µm (Figure 1-29).[118] This work therefore demonstrates strategies for improving the spinnability of LCPs by modification of the properties of the polymer solution.

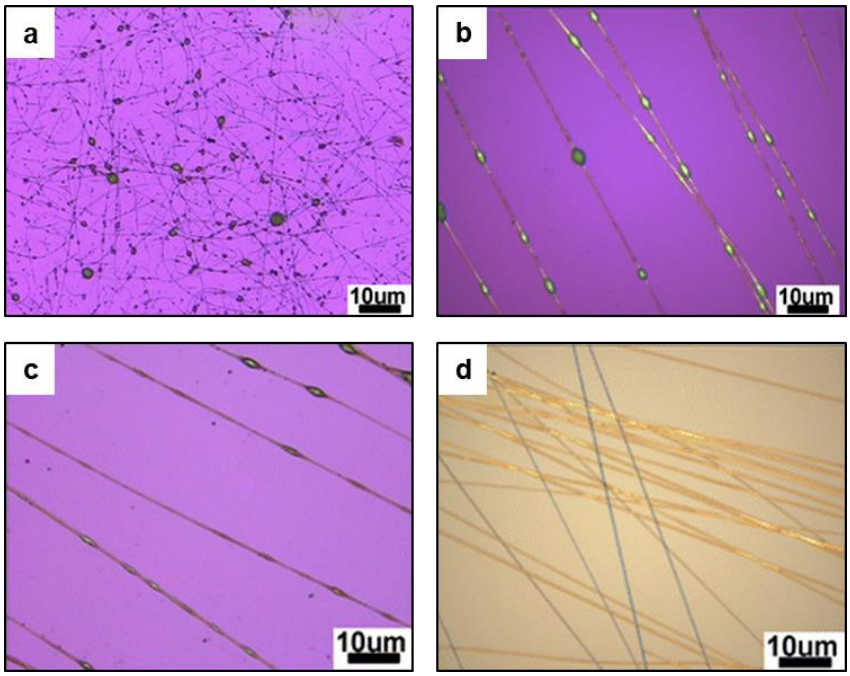

Figure 1-29. Optimisation of SC-LCP fibres. (a) Pure LCP, (b) With addition of 5% small molecule LC, (c) With addition of 0.05 mL of Et_3N and (d) Using LCP:PEO blend of 20:1. Reproduced with permission from reference 118 - Springer Nature.

1.5. Summary

LCEs are polymeric materials capable of rapid, reversible shape change which has resulted in interest for their potential use as soft actuators. For responsive behaviour to be observed it is necessary to first induce a liquid crystal monodomain, which is then generally fixed in place with chemical crosslinking. These factors have limited LCEs to date to thin films with a thickness of tens of micrometres, which in turn limits their potential applications. Research has therefore focussed on new synthetic methods such as introducing exchangeable crosslinking which will allow for mouldable materials still capable of significant deformations. Thermoplastic LCEs have also been proposed as a solution to this problem, which would allow for processing using techniques such as extrusion or from solution without the need for an additional crosslinking step. To date few examples of thermoplastic LCEs exist in the literature, with only one example of an extruded LCE fibre reported and no investigation of their melt properties. Techniques such as solution fibre spinning have been used to produce uncrosslinked fibres, but again this is an area that has not yet been explored. For LCEs to find real applications in the future it is important that the scale of their synthesis be improved and methods to induce alignment simplified, therefore further work on thermoplastic LCEs and their properties would be beneficial in order to determine their potential for use as actuators.

1.6. Thesis Summary

The aim of the work presented in this thesis was therefore to develop a synthetic route to thermoplastic LCEs which had a yield amenable to the multigram scale-synthesis of polymer, and to determine the suitability for processing using thermoplastic methods by further probing the properties of these materials. The results chapters are structured as follows:

Chapter 2 – Identification of a high yielding synthetic route to a UV-responsive thermoplastic LCE, and investigation into the effect of the linking group length and bond type on the thermal transition temperatures related to room temperature actuation.

Work reported in this chapter has been submitted for publication in *Polymer Chemistry*.

Chapter 3 – Characterisation of the microphase segregated structure of the thermoplastic elastomer triblock copolymers reported in Chapter 2, both at room temperature and in response to heating through the T_{iso}.

Analysis of the SAXS data was carried out in collaboration with Professor Robert Richardson. TEM images were taken by Dr Jean-Charles Eloi.

Chapter 4 – Investigation of melt properties by rotational rheometry in order to determine the suitability of the LCEs reported in Chapter 2 for melt processing. These are the first rheological measurements on a side-chain thermoplastic LCE.

Chapter 5 – Determination of the suitability of the thermoplastic LCEs for solution processing by first drawing fibres from a viscous solution, and then attempting to produce fibres by electrospinning. These are the first examples of electrospun side-chain LCEs.

Electrospinning was carried out in collaboration with Martin Pretscher. The analysis of SAXS data was carried out in collaboration with Professor Robert Richardson.

Chapter 6 – Conclusions and future work.

1.7. References

1 P. J. Collings and M. Hird, *Introduction to Liquid Crystals: Chemistry and Physics*, Taylor and Francis, London, 1997.

2 P. J. Collings, *Liquid Crystals: Nature's Delicate Phase of Matter*, Adam Hilger, Bristol, 1990.

3 Polarized Light Microscopy, https://www.microscopyu.com/techniques/polarized-light/polarized-light-microscopy, (accessed 6 August 2018).

4 M. Petr and P. T. Hammond, Room Temperature Rapid Photoresponsive Azobenzene Side Chain Liquid Crystal Polymer, *Macromolecules*, 2011, **44**, 8880–8885.

5 C. B. McArdle, *Side Chain Liquid Crystal Polymers*, Blackie, Glasgow, 1989.

6 C. Ohm, M. Brehmer and R. Zentel, Liquid Crystalline Elastomers as Actuators and Sensors, *Adv. Mater.*, 2010, **22**, 3366–3387.

7 M. Warner and E. M. Terentjev, *Liquid Crystal Elastomers*, Oxford University Press, Oxford, 2003.

8 H. K. Bisoyi and Q. Li, Light-Driven Liquid Crystalline Materials: From Photo-Induced Phase Transitions and Property Modulations to Applications, *Chem. Rev.*, 2016, **116**, 15089–15166.

9 M. Dai, O. T. Picot, J. M. N. Verjans, L. T. De Haan, A. P. H. J. Schenning, T. Peijs and C. W. M. Bastiaansen, Humidity-Responsive Bilayer Actuators Based on a Liquid-Crystalline Polymer Network, *ACS Appl. Mater. Interfaces*, 2013, **5**, 4945–4950.

10 M. Yamada, M. Kondo, J. I. Mamiya, Y. Yu, M. Kinoshita, C. J. Barrett and T. Ikeda, Photomobile Polymer Materials: Towards Light-Driven Plastic Motors, *Angew. Chemie - Int. Ed.*, 2008, **47**, 4986–4988.

11 M. Rogóż, H. Zeng, C. Xuan, D. S. Wiersma and P. Wasylczyk, Light-Driven Soft Robot Mimics Caterpillar Locomotion in Natural Scale, *Adv. Opt. Mater.*, 2016, **4**, 1689–1694.

12 H. Zeng, O. M. Wani, P. Wasylczyk, R. Kaczmarek and A. Priimagi, Self-Regulating Iris Based on Light-Actuated Liquid Crystal Elastomer, *Adv. Mater.*, 2017, **29**, 1701814.

13 L. T. De Haan, C. Sánchez-Somolinos, C. M. W. Bastiaansen, A. P. H. J. Schenning and D. J. Broer, Engineering of Complex Order and the Macroscopic Deformation of Liquid Crystal Polymer Networks, *Angew. Chemie - Int. Ed.*, 2012, **51**, 12469–12472.

14 L. T. De Haan, V. Gimenez-Pinto, A. Konya, T. S. Nguyen, J. M. N. Verjans, C. Sánchez-Somolinos, J. V. Selinger, R. L. B. Selinger, D. J. Broer and A. P. H. J. Schenning, Accordion-like Actuators of Multiple 3D Patterned Liquid Crystal Polymer Films, *Adv. Funct. Mater.*, 2014, **24**, 1251–1258.

15 L. T. de Haan, A. P. H. J. Schenning and D. J. Broer, Programmed Morphing of Liquid Crystal Networks, *Polymer*, 2014, **55**, 5885–5896.

16 T. H. Ware, M. E. McConney, J. J. Wie, V. P. Tondiglia and T. J. White, Voxelated Liquid Crystal Elastomers, *Science*, 2015, **347**, 982–984.

17 T. H. Ware, Z. P. Perry, C. M. Middleton, S. T. Iacono and T. J. White, Programmable Liquid Crystal Elastomers Prepared by Thiol-Ene Photopolymerization, *ACS Macro Lett.*, 2015, **4**, 942–946.

18 S. K. Ahn, T. H. Ware, K. M. Lee, V. P. Tondiglia and T. J. White, Photoinduced Topographical Feature Development in Blueprinted Azobenzene-Functionalized Liquid Crystalline Elastomers, *Adv. Funct. Mater.*, 2016, **26**, 5819–5826.

19 T. Guin, B. A. Kowalski, R. Rao, A. D. Auguste, C. A. Grabowski, P. Lloyd, V. P. Tondiglia, B.

Maruyama, R. A. Vaia and T. J. White, Electrical Control of Shape in Voxelated Liquid Crystalline Polymer Nanocomposites, *ACS Appl. Mater. Interfaces*, 2018, **10**, 1187–1194.

20 T. H. Ware, J. S. Biggins, A. F. Shick, M. Warner and T. J. White, Localized Soft Elasticity in Liquid Crystal Elastomers, *Nat. Commun.*, 2016, **7**, 10781.

21 T. Guin, M. J. Settle, B. A. Kowalski, A. D. Auguste, R. V Beblo, G. W. Reich and T. J. White, Layered Liquid Crystal Elastomer Actuators, *Nat. Commun.*, 2018, **9**, 2531.

22 C. Laschi, M. Cianchetti, B. Mazzolai, L. Margheri, M. Follador and P. Dario, Soft Robot Arm Inspired by the Octopus, *Adv. Robot.*, 2012, **26**, 709–727.

23 L. Hines, K. Petersen, G. Z. Lum and M. Sitti, Soft Actuators for Small-Scale Robotics, *Adv. Mater.*, 2017, **29**, 1603483.

24 S. M. Mirvakili and I. W. Hunter, Artificial Muscles: Mechanisms, Applications, and Challenges, *Adv. Mater.*, 2017, **30**, 1704407.

25 P.-G. de Gennes, A Semi-Fast Artificial Muscle, *Comptes Rendus l'Academie des Sci. Ser. IIb Mec. Phys. Chim. Astron.*, 1997, **324**, 343–348.

26 P. G. De Gennes, M. Hébert and R. Kant, Artificial Muscles Based on Nematic Gels, *Macromol. Symp.*, 1997, **113**, 39–49.

27 J. Kupfec and H. Finkelmann, Nematic Liquid Single Crystal Elastomer, *Makromol. Chemie Rapid Commun.*, 1991, **12**, 717–726.

28 H. Finkelmann, E. Nishikawa, G. G. Pereira and M. Warner, A New Opto-Mechanical Effect in Solids, *Phys. Rev. Lett.*, 2001, **87**, 015501.

29 B. Donnio, H. Wermter and H. Finkelmann, A Simple and Versatile Synthetic Route for the Preparation of Main-Chain, Liquid-Crystalline Elastomers, *Macromolecules*, 2000, **33**, 7724–7729.

30 M. H. Li, P. Keller, J. Yang and P. A. Albouy, An Artificial Muscle with Lamellar Structure Based on a Nematic Triblock Copolymer, *Adv. Mater.*, 2004, **16**, 1922–1925.

31 M. Li and Keller P., Artificial Muscles Based on Liquid Crystal Elastomers., *Philos. Trans. Ser. A, Math. Phys. Eng. Sci.*, 2006, **364**, 2763–2777.

32 D. L. Thomsen, P. Keller, J. Naciri, R. Pink, H. Jeon, D. Shenoy and B. R. Ratna, Liquid Crystal Elastomers with Mechanical Properties of a Muscle, *Macromolecules*, 2001, **34**, 5868–5875.

33 M. H. Li, P. Keller, B. Li, X. G. Wang and M. Brunet, Light-Driven Side-on Nematic Elastomer Actuators, *Adv. Mater.*, 2003, **15**, 569–572.

34 W. Lehman, H. Skupin, C. Tolksdorf, E. Gebhard, R. Zentel, P. Kruger, M. Losche and F. Kremer, Giant Lateral Electrostriction in Ferroelectric Liquid-Crystalline Elastomers, *Nature*, 2001, **410**, 447–50.

35 S. Courty, J. Mine, A. R. Tajbakhsh and E. M. Terentjev, Nematic Elastomers with Aligned Carbon Nanotubes: New Electromechanical Actuators, *Europhys. Lett.*, 2003, **64**, 654–660.

36 S. Hashimoto, Y. Yusuf, S. Krause, H. Finkelmann, P. E. Cladis, H. R. Brand and S. Kai, Multifunctional Liquid Crystal Elastomers: Large Electromechanical and Electro-Optical Effects, *Appl. Phys. Lett.*, 2008, **92**, 181902.

37 J. Naciri, A. Srinivasan, H. Jeon, N. Nikolov, P. Keller and B. R. Ratna, Nematic Elastomer Fiber Actuator, *Macromolecules*, 2003, **36**, 8499–8505.

38 L. Fang, H. Zhang, Z. Li, Y. Zhang, Y. Zhang and H. Zhang, Synthesis of Reactive Azobenzene Main-Chain Liquid Crystalline Polymers via Michael Addition Polymerization and Photomechanical Effects of Their Supramolecular Hydrogen-Bonded Fibers, *Macromolecules*, 2013, **46**, 7650–7660.

39 G. Han, J. Nie and H. Zhang, Facile Preparation of Recyclable Photodeformable Azobenzene Polymer Fibers with Chemically Crosslinked Networks, *Polym. Chem.*, 2016, **7**, 5088–5092.

40 C. J. Kloxin and C. N. Bowman, Covalent Adaptable Networks: Smart, Reconfigurable and Responsive Network Systems, *Chem. Soc. Rev.*, 2013, **42**, 7161–7173.

41 Z. Wang, H. Tian, Q. He and S. Cai, Reprogrammable, Reprocessible, and Self-Healable Liquid Crystal Elastomer with Exchangeable Disulfide Bonds, *ACS Appl. Mater. Interfaces*, 2017, **9**, 33119–33128.

42 T. Kato, Structures and Properties of Supramolecular Liquid-Crystalline Side-Chain Polymers Built through Intermolecular Hydrogen Bonds, *Macromolecules*, 1996, **29**, 8734–8739.

43 X. Li, L. Fang, L. Hou, L. Zhu, Y. Zhang, B. Zhang and H. Zhang, Photoresponsive Side-Chain Liquid Crystalline Polymers with Amide Group-Substituted Azobenzene Mesogens: Effects of Hydrogen Bonding, Flexible Spacers, and Terminal Tails, *Soft Matter*, 2012, **8**, 5532–5542.

44 P. Kandasamy, R. Keerthiga, S. Vijayalakshmi and T. Kaliyappan, Synthesis and Liquid Crystal Properties of Supramolecular Side-Chain Liquid-Crystalline Polymers Containing Poly(Acrylic Acid) Intermolecular Hydrogen Bonds, *Mol. Cryst. Liq. Cryst.*, 2015, **606**, 1–11.

45 J. I. Mamiya, A. Yoshitake, M. Kondo, Y. Yu and T. Ikeda, Is Chemical Crosslinking Necessary for the Photoinduced Bending of Polymer Films?, *J. Mater. Chem.*, 2008, **18**, 63–65.

46 Z. Pei, Y. Yang, Q. Chen, E. M. Terentjev, Y. Wei and Y. Ji, Mouldable Liquid-Crystalline Elastomer Actuators with Exchangeable Covalent Bonds, *Nat. Mater.*, 2014, **13**, 36–41.

47 T. Ube, K. Kawasaki and T. Ikeda, Photomobile Liquid-Crystalline Elastomers with Rearrangeable Networks, *Adv. Mater.*, 2016, **28**, 8212–8217.

48 M. Yan, J. Tang, H.-L. Xie, B. Ni, H.-L. Zhang and E.-Q. Chen, Self-Healing and Phase Behavior of Liquid Crystalline Elastomer Based on a Block Copolymer Constituted of a Side-Chain Liquid Crystalline Polymer and a Hydrogen Bonding Block, *J. Mater. Chem. C*, 2015, **3**, 8526–8534.

49 B. Ni, H. Lou Xie, J. Tang, H. L. Zhang and E. Q. Chen, A Self-Healing Photoinduced-Deformable Material Fabricated by Liquid Crystalline Elastomers Using Multivalent Hydrogen Bonds as Cross-Linkers, *Chem. Commun.*, 2016, **52**, 10257–10260.

50 C. M. Yakacki, M. Saed, D. P. Nair, T. Gong, S. M. Reed and C. N. Bowman, Tailorable and Programmable Liquid-Crystalline Elastomers Using a Two-Stage Thiol-Acrylate Reaction, *RSC Adv.*, 2015, **5**, 18997–19001.

51 D. W. Hanzon, N. A. Traugutt, M. K. McBride, C. N. Bowman, C. M. Yakacki and K. Yu, Adaptable Liquid Crystal Elastomers with Transesterification-Based Bond Exchange Reactions, *Soft Matter*, 2018, **14**, 951–960.

52 Y. Li, Y. Zhang, O. Rios, J. K. Keum and M. R. Kessler, Liquid Crystalline Epoxy Networks with Exchangeable Disulfide Bonds, *Soft Matter*, 2017, **13**, 5021–5027.

53 L. Chen, M. Wang, L.-X. Guo, B.-P. Lin and H. Yang, A Cut-and-Paste Strategy towards Liquid Crystal Elastomers with Complex Shape Morphing, *J. Mater. Chem. C*, 2018, **6**, 8251–8257.

54 C. J. Camargo, H. Campanella, J. E. Marshall, N. Torras, K. Zinoviev, E. M. Terentjev and J. Esteve, Batch Fabrication of Optical Actuators Using Nanotube–elastomer Composites towards Refreshable Braille Displays, *J. Micromechanics Microengineering*, 2012, **22**, 75009.

55 J. Cui, D. M. Drotlef, I. Larraza, J. P. Fernandez-Blazquez, L. F. Boesel, C. Ohm, M. Mezger, R. Zentel and A. del Campo, Bioinspired Actuated Adhesive Patterns of Liquid Crystalline

Elastomers, *Adv Mater*, 2012, **24**, 4601–4604.

56 Z. Wen, M. K. McBride, X. Zhang, X. Han, A. M. Martinez, R. Shao, C. Zhu, R. Visvanathan, N. A. Clark, Y. Wang, K. Yang and C. N. Bowman, Reconfigurable LC Elastomers: Using a Thermally Programmable Monodomain To Access Two-Way Free-Standing Multiple Shape Memory Polymers, *Macromolecules*, 2018, **51**, 5812–5819.

57 W. Wang, H. Rodrigue and S. H. Ahn, Deployable Soft Composite Structures, *Sci. Rep.*, 2016, **6**, 20869.

58 A. Rešetič, J. Milavec, B. Zupančič, V. Domenici and B. Zalar, Polymer-Dispersed Liquid Crystal Elastomers, *Nat. Commun.*, 2016, **7**, 13140.

59 J. M. Boothby and T. H. Ware, Dual-Responsive, Shape-Switching Bilayers Enabled by Liquid Crystal Elastomers, *Soft Matter*, 2017, **13**, 4349–4356.

60 A. Minori, S. Jadhav, Q. He, S. Cai and M. T. Tolley, Reversible Actuation of Origami Inspired Composites Using Liquid Crystal Elastomers, *Proc. Asme Conf. Smart Mater. Adapt. Struct. Intell. Syst. 2017, Vol 1*.

61 C. Yuan, D. J. Roach, C. K. Dunn, Q. Mu, X. Kuang, C. M. Yakacki, T. J. Wang, K. Yu and H. J. Qi, 3D Printed Reversible Shape Changing Soft Actuators Assisted by Liquid Crystal Elastomers, *Soft Matter*, 2017, **13**, 5558–5568.

62 H.-J. Kim, S.-H. Song and S.-H. Ahn, A Turtle-like Swimming Robot Using a Smart Soft Composite (SSC) Structure, *Smart Mater. Struct.*, 2013, **22**, 014007.

63 C. P. Ambulo, J. J. Burroughs, J. M. Boothby, H. Kim, M. Ravi Shankar and T. H. Ware, Four-Dimensional Printing of Liquid Crystal Elastomers, *ACS Appl. Mater. Interfaces*, 2017, **9**, 37332–37339.

64 A. Kotikian, R. L. Truby, J. W. Boley, T. J. White and J. A. Lewis, 3D Printing of Liquid Crystal Elastomeric Actuators with Spatially Programed Nematic Order, *Adv. Mater.*, 2018, **30**, 1–6.

65 M. López-Valdeolivas, D. Liu, D. J. Broer and C. Sánchez-Somolinos, 4D Printed Actuators with Soft-Robotic Functions, *Macromol. Rapid Commun.*, 2018, **39**, 1700710.

66 F. S. Bates, Polymer-Polymer Phase Behavior, *Science*, 1991, **251**, 898–905.

67 J. M. G. Swann and P. D. Topham, Design and Application of Nanoscale Actuators Using Block-Copolymers, *Polymers (Basel).*, 2010, **2**, 454–469.

68 M. W. Matsen and F. S. Bates, Unifying Weak- and Strong-Segregation Block Copolymer Theories, *Macromolecules*, 1996, **29**, 1091–1098.

69 M. W. Matsen and R. B. Thompson, Equilibrium Behavior of Symmetric ABA Triblock Copolymer Melts, *J. Chem. Phys.*, 1999, **111**, 7139–7146.

70 M. L. Huggins, Theory of Solutions of High Polymers, *J. Am. Chem. Soc.*, 1942, **64**, 1712–1719.

71 P. J. Flory, Thermodynamics of High Polymer Solutions, *J. Chem. Phys.*, 1942, **10**, 51–61.

72 D. W. van Krevelen, *Properties of Polymers*, Elsevier, Amsterdam, 3rd edn., 1997.

73 H. Schnablegger and Y. Singh, *The SAXS Guide*, Anton Paar, Graz, 4th edn., 2017.

74 R. A. Sones and R. G. Petschek, Nematic Ordering and Microphase Segregation in a Diblock Polymer Liquid-Crystal-Polymer, *Phys. Rev. E*, 1994, **50**, 2906–2912.

75 M. Anthamatten and P. T. Hammond, Free-Energy Model of Asymmetry in Side-Chain Liquid-Crystalline Diblock Copolymers, *J. Polym. Sci. Part B Polym. Phys.*, 2001, **39**, 2671–2691.

76 M. Anthamatten and P. T. Hammond, A SAXS Study of Microstructure Ordering Transitions

in Liquid Crystalline Side-Chain Diblock Copolymers, *Macromolecules*, 1999, **32**, 8066–8076.

77 M. Yamada, T. Iguchi, A. Hirao, S. Nakahama and J. Watanabe, Side-Chain Liquid Crystal Block Copolymers with Well-Defined Structures Prepared by Living Anionic Polymerization I. Thermotropic Phase Behavior and Structures of Liquid Crystal Segment in Lamellar Type of Microphase Domain, *Polym. J.*, 1998, **30**, 23–30.

78 M. Kutz, Ed., *Applied Plastics Engineering Handbook*, William Andrew, Oxford, 2011.

79 G. Yuan and Y. Zhao, Grafting of Liquid Crystalline Polymers on a Styrene-Butadiene-Styrene Triblock Copolymer and Orientation Induction, *Polymer*, 1997, **38**, 119–125.

80 Y. Yi, X. Fan, X. Wan, L. Li, N. Zhao, X. Chen, J. Xu and Q. F. Zhou, ABA Type Triblock Copolymer Based on Mesogen-Jacketed Liquid Crystalline Polymer: Design, Synthesis, and Potential as Thermoplastic Elastomer, *Macromolecules*, 2004, **37**, 7610–7618.

81 X. T. Li Cui Xiaohu Yan, Guojun Liu, and Yue Zhao, Photoactive Thermoplastic Elastomers of Azobenzene-Containing Triblock Copolymers Prepared through Atom Transfer Radical Polymerization, *Macromolecules*, 2004, **37**, 7097–7104.

82 M. Petr, B. A. Katzman, W. Dinatale and P. T. Hammond, Synthesis of a New, Low-Tg Siloxane Thermoplastic Elastomer with a Functionalizable Backbone and Its Use as a Rapid, Room Temperature Photoactuator, *Macromolecules*, 2013, **46**, 2823–2832.

83 N. R. Council, *Polymer Science and Engineering: The Shifting Research Frontiers*, The National Academies Press, Washington, DC, 1994.

84 S. V. Ahir, A. R. Tajbakhsh and E. M. Terentjev, Self-Assembled Shape-Memory Fibers of Triblock Liquid-Crystal Polymers, *Adv. Funct. Mater.*, 2006, **16**, 556–560.

85 T. G. Mezger, *The Rheology Handbook*, Vincentz Network, Hanover, 4th edn., 2014.

86 C. D. A. E. Han and J. Kim, Rheological Technique for Determining the Order-Disorder Transition Of, *Polymer*, 1987, **25**, 1741–1764.

87 S. Onagi, T. Asada, G. Astarita, G. Marrucci and L. Nicolais, *Rheology*, Plenum Press, New York, 1980, vol. I.

88 M. C. Muir and R. S. Porter, Processing Rheology of Liquid Crystalline Polymers : A Review, *Mol. Cryst. Liq. Cryst.*, 1989, **169**, 83–95.

89 G. Kiss, Anomalous Temperature Dependence of Viscosity of Thermotropic Polyesters, *J. Rheol. (N. Y. N. Y).*, 1986, **30**, 585–599.

90 J. R. Tuttle, H. E. Bartony and R. W. Lenz, The Rheological Characterization of a Series of Thermotropic Liquid Crystalline Polymers, *Polym. Eng. Sci.*, 1987, **27**, 1156–1163.

91 Y. Fan, S. Dai and R. I. Tanner, Rheological Properties of Some Thermotropic Liquid Crystalline Polymers, *Korea-Australia Rheol. J.*, 2003, **15**, 109–115.

92 K. M. Lee and C. D. Han, Microphase Separation Transition and Rheology of Side-Chain Liquid-Crystalline Block Copolymers, *Macromolecules*, 2002, **35**, 3145–3156.

93 C. Ohm, M. Morys, F. R. Forst, L. Braun, A. Eremin, C. Serra, R. Stannarius and R. Zentel, Preparation of Actuating Fibres of Oriented Main-Chain Liquid Crystalline Elastomers by a Wetspinning Process, *Soft Matter*, 2011, **7**, 3730.

94 R. Stannarius, A. Eremin, K. Harth, M. Morys, A. Demiglio, C. Ohm and R. Zentel, Mechanical and Optical Properties of Continuously Spun Fibres of a Main-Chain Smectic A Elastomer, *Soft Matter*, 2012, **8**, 1858–1864.

95 X. Wang, C. Drew, S.-H. Lee, K. J. Senecal, J. Kumar and L. A. Samuelson, Electrospun Nanofibrous Membranes for Highly Sensitive Optical Sensors, *Nano Lett.*, 2002, **2**, 1273–

1275.

96 H. Liu, J. Kameoka, D. A. Czaplewski and H. G. Craighead, Polymeric Nanowire Chemical Sensor, *Nano Lett.*, 2004, **4**, 671–675.

97 J. S. Kim and D. H. Reneker, Mechanical Properties of Composites Using Ultra-Fine Electrospun Fibers, *Polym. Compos.*, 1999, **20**, 124–131.

98 M. M. Bergshoef and G. J. Vancso, Transparent Nanocomposites with Ultrathin, Electrospun Nylon-4,6 Fiber Reinforcement, *Adv. Mater.*, 1999, **11**, 1362–1365.

99 W. J. Li, C. T. Laurencin, E. J. Caterson, R. S. Tuan and F. K. Ko, Electrospun Nanofibrous Structure: A Novel Scaffold for Tissue Engineering., *J. Biomed. Mater. Res. Part A*, 2002, **60**, 613–621.

100 H. Yoshimoto, Y. M. Shin, H. Terai and J. P. Vacanti, A Biodegradable Nanofiber Scaffold by Electrospinning and Its Potential for Bone Tissue Engineering, *Biomaterials*, 2003, **24**, 2077–2082.

101 A. Greiner and J. H. Wendorff, Electrospinning: A Fascinating Method for the Preparation of Ultrathin Fibers, *Angew. Chemie - Int. Ed.*, 2007, **46**, 5670–5703.

102 G. C. Rutledge and S. V. Fridrikh, Formation of Fibers by Electrospinning, *Adv. Drug Deliv. Rev.*, 2007, **59**, 1384–1391.

103 D. Li and Y. Xia, Electrospinning of Nanofibers: Reinventing the Wheel?, *Adv. Mater.*, 2004, **16**, 1151–1170.

104 G. Taylor, Disintegration of Water Drops in an Electric Field, *Proc. R. Soc. A Math. Phys. Eng. Sci.*, 1964, **280**, 383–397.

105 D. Li, Y. Wang and Y. Xia, Electrospinning of Polymeric and Ceramic Nanofibers as Uniaxially Aligned Arrays, *Nano Lett.*, 2003, **3**, 1167–1171.

106 W. E. Teo and S. Ramakrishna, A Review on Electrospinning Design and Nanofibre Assemblies, *Nanotechnology*, 2006, **17**, R89–R106.

107 A. Theron, E. Zussman and A. L. Yarin, Electrostatic Field-Assisted Alignment of Electrospun Nanofibres, *Nanotechnology*, 2001, **12**, 384–390.

108 C. Y. Xu, R. Inai, M. Kotaki and S. Ramakrishna, Aligned Biodegradable Nanofibrous Structure: A Potential Scaffold for Blood Vessel Engineering, *Biomaterials*, 2004, **25**, 877–886.

109 R. Inai, M. Kotaki and S. Ramakrishna, Structure and Properties of Electrospun PLLA Single Nanofibres, *Nanotechnology*, 2005, **16**, 208–213.

110 Z. Sun, E. Zussman, A. L. Yarin, J. H. Wendorff and A. Greiner, Compound Core-Shell Polymer Nanofibers by Co-Electrospinning, *Adv. Mater.*, 2003, **15**, 1929–1932.

111 Y. Lu, J. Huang, G. Yu, R. Cardenas, S. Wei, E. K. Wujcik and Z. Guo, Coaxial Electrospun Fibers: Applications in Drug Delivery and Tissue Engineering, *WIREs Nanomedicine and Nanobiotechnology*, 2016, **8**, 654–677.

112 J. P. F. Lagerwall, J. T. McCann, E. Formo, G. Scalia and Y. Xia, Coaxial Electrospinning of Microfibres with Liquid Crystal in the Core, *Chem. Commun.*, 2008, 5420–5422.

113 D. Li and Y. N. Xia, Direct Fabrication of Composite and Ceramic Hollow Nanofibers by Electrospinning, *Nano Lett.*, 2004, **4**, 933–938.

114 Y. Kye, C. Kim and J. Lagerwall, Multifunctional Responsive Fibers Produced by Dual Liquid Crystal Core Electrospinning, *J. Mater. Chem. C*, 2015, **3**, 8979–8985.

115 A. Sharma and J. P. F. Lagerwall, Electrospun Composite Liquid Crystal Elastomer Fibers,

Materials (Basel)., 2018, **11**, 393.

116 S. Krause, R. Dersch, J. H. Wendorff and H. Finkelmann, Photocrosslinkable Liquid Crystal Main-Chain Polymers: Thin Films and Electrospinning, *Macromol. Rapid Commun.*, 2007, **28**, 2062–2068.

117 K. Nakashima, K. Tsuboi, H. Matsumoto, R. Ishige, M. Tokita, J. Watanabe and A. Tanioka, Control over Internal Structure of Liquid Crystal Polymer Nanofibers by Electrospinning, *Macromol. Rapid Commun.*, 2010, **31**, 1641–1645.

118 Y. Wu, Q. An, J. Yin, T. Hua, H. Xie, G. Li and H. Tang, Liquid Crystal Fibers Produced by Using Electrospinning Technique, *Colloid. Polym. Sci.*, 2008, **286**, 897–905.

Chapter 2: Synthesis and Thermal Analysis of Thermoplastic Side-Chain Liquid Crystal Elastomers

2.1. Introduction

Liquid crystal elastomers (LCEs) are polymeric materials capable of programmed shape change in response to a variety of external stimuli, including temperature and light, which has made them of great interest for use as soft actuators.[1–3] In order for actuation to occur it is necessary to first align the LC component to form a monodomain using techniques including surface alignment,[4,5] mechanical deformation,[6] and optical patterning.[7] Actuation then occurs by switching between an ordered mesophase and the disordered isotropic state, with contraction occurring along the direction of alignment and expansion perpendicular to it. Elastomeric behaviour is achieved by lightly crosslinking the aligned polymer to fix in the LC mesophase, typically by the use of a UV-activated process, to form a thermoset polymer.[3] This leads to materials that are capable of significant and complex deformations but which, due to the nature of the alignment and crosslinking steps, are typically limited to very thin films that cannot be processed further.

One of the major barriers to the bulk processing of LCEs is the covalent crosslinking required for elastomeric behaviour. For this reason, thermoplastic LCEs may have potential as they could, in theory, be utilised in more polymer processing techniques than conventional LCEs, including those such as melt extrusion where incorporating a crosslinking step would be unpractical due to the rate of fibre drawing. Thermoplastic elastomers commonly consist of ABA triblock copolymers, where microphase separation between the hard A and soft B blocks acts to form physical, rather than chemical, crosslinks.[8,9] Petr *et al*. reported a thermoplastic LCE that was capable of reversible room temperature actuation due to the presence of an azobenzene-containing mesogen.[10] The backbone of this polymer consisted of a polystyrene-*b*-poly(methylvinylsiloxane)-*b*-polystyrene (PS-*b*-PMVS-*b*-PS) triblock copolymer, with the rod-like mesogen attached in a side-on manner to the PMVS block (Figure 2-1a).

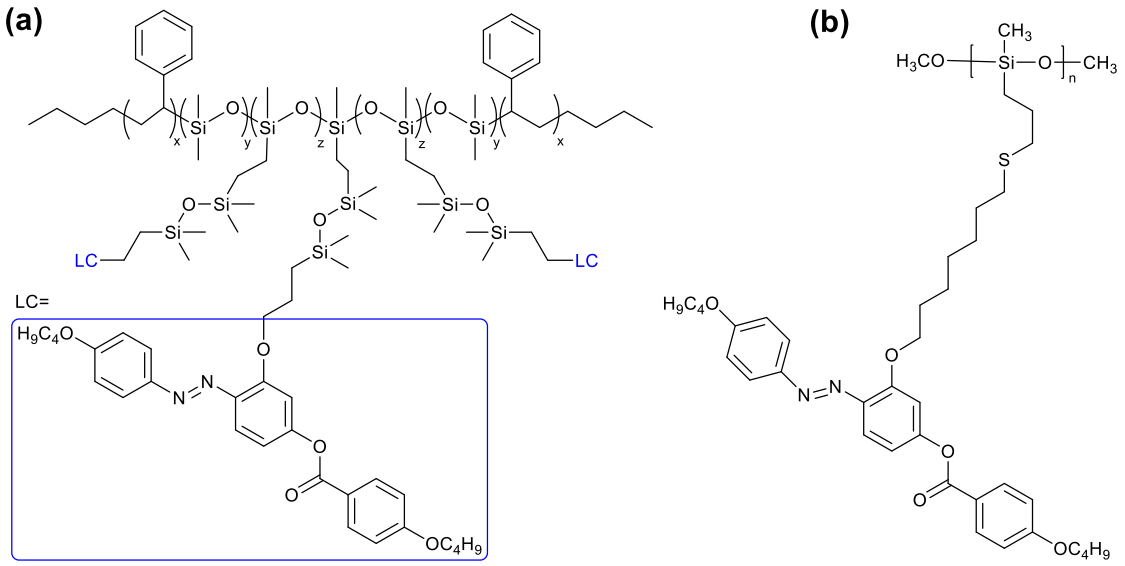

Figure 2-1. Structures of UV-responsive LC-functionalised thermoplastics.[10,11]

Polysiloxanes are regularly used for liquid crystalline polymer synthesis due to the low glass transition temperature (T_g),[12] which allows for high chain mobility even at room temperature. The physical crosslinks responsible for elastomeric behaviour can then be formed by a high T_g polymer, such as PS in this instance. The mesogen, first described by Li *et al.*,[13] is photoresponsive, as on irradiation with UV light with a wavelength of 365 nm the azobenzene group isomerises from the linear *trans*-conformation to the bent *cis*-conformation. This acts to disrupt the liquid crystal mesophase and yields a disordered isotropic state. Thus, actuation can be achieved at room temperature without the need for heating to the measured T_{iso} of 95 °C,[13] which avoids creep occurring at temperatures approaching the T_g of the glassy domain.

The thermoplastic LCE given in Figure 2-1a was shown to rapidly and reversibly contract with a strain of 3.3% against an applied tensile stress of 25.7 kPa at room temperature,[10] however the hydrosilylation method used for functionalising the mesogen with a linking group outlined in Figure 2-2 was low yielding (30%).[14] This currently serves as a barrier to larger scale processing of thermoplastic LCEs using higher throughput methods than those available to crosslinked LCEs, and therefore a higher yielding method of functionalising the backbone would be beneficial.

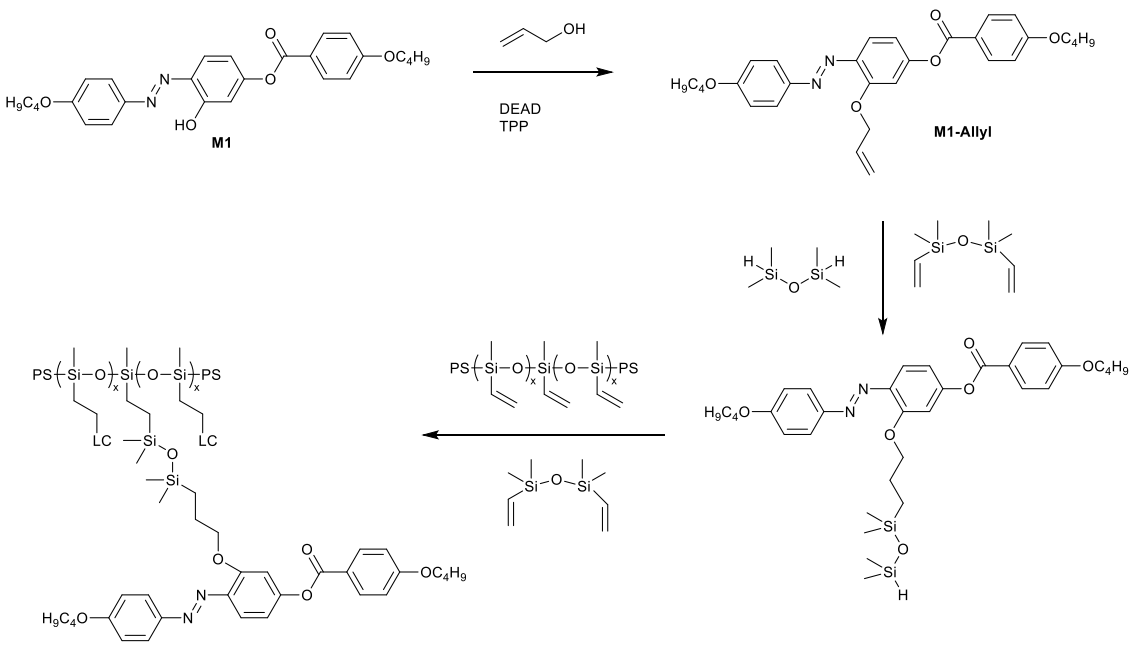

Figure 2-2. Method of attaching modified mesogen M1 to PMVS block of a PS-*b*-PMVS-*b*-PS thermoplastic elastomer.[10] PDMS block omitted for clarity. DEAD = diethyl azodicarboxylate, TPP = triphenylphosphine.

Thiol-ene click chemistry describes a series of reactions where a thiol is added across a vinyl group that are characteristically high yielding.[15] This method has been successfully used to functionalise a commercially available poly(3-mercaptopropylmethylsiloxane) (PMMS) backbone with the photoresponsive mesogen designed by Li *et al*. to give complete attachment of the thiol groups on PMMS to the mesogen (Figure 2-1b).[11] The triblock copolymer reported by Petr *et al*. contains vinyl functionality on the PMVS block which is suitable for functionalisation by thiol-ene click chemistry, and advantageously can be synthesised by living anionic polymerisation techniques. This allows for fine control over the degree of polymerisation in each block, the relative molecular weights of the blocks, and consequently the phase behaviour and mechanical properties of the material. This, combined with an alternative to hydrosilylation tolerant of a variety of linking or mesogenic groups for mesogen attachment, would allow for the synthesis of a thermoplastic LCE whilst retaining control over its properties, and so the ability to optimise performance both as a photoactuator and for ease of processing.

The aim of this work was to develop a new synthetic route for attaching the UV-responsive mesogen **M1** to the PS-*b*-PMVS-*b*-PS triblock copolymer described above that would result in improved yields and allow for control over the properties of the final polymer. This was attempted by using a combination of thiol-ene click reactions and mild coupling reactions which tolerate both the polysiloxane backbone and the mesogen functionality. An amine-functionalised equivalent of the mesogen described by Li *et al.* was also synthesised and the number of alkyl units

in the linking group between the mesogen and polymer backbone varied to obtain a range of copolymers. In order to understand how the structure affects the thermal transitions, Differential Scanning Calorimetry (DSC) was used to identify the most promising combination of linking group and mesogen for use as a room temperature photoactuator.

2.2. Results and Discussion

2.2.1. Mesogen Synthesis

2.2.1.1. M1, M1-Allyl, M1-Thiol Synthesis

The synthesis of mesogen **M1** was carried out according to a literature method (Section A.1.).[13] This molecule, first reported by Li *et al.,* has been used extensively in the synthesis of photo-responsive liquid crystal polymers due to the light-induced *cis-trans* isomerisation of the azobenzene group and the straightforward method of synthesis.[10,11,14] In all cases the mesogen was attached to the polymer backbone through the hydroxyl group on the central ring to give a side-on arrangement of the mesogen relative to the polymer. This was previously achieved by conversion of **M1** to **M1-Allyl** using allyl alcohol and either diethyl azodicarboxylate (DEAD)[14] or diisopropyl azodicarboxylate (DIAD)[11] as shown in Figure 2-2. This new functionality was then reacted with difunctional 1,1,3,3-tetramethyldisiloxane *via* a low yielding hydrosilylation reaction before coupling to the triblock copolymer backbone.[14] In this work **M1-Allyl** was prepared by a different route, employing a nucleophilic substitution at allyl bromide, using K_2CO_3 in acetone (Figure 2-3). The reaction proceeded with a yield of 68%, which is comparable to that using allyl alcohol (74% with DEAD, 69% with DIAD). The spectrum obtained by ^{1}H NMR spectroscopy (Figure A-4) had peak locations and integrals which matched those given in the literature,[14] confirming the successful synthesis of **M1-Allyl**.

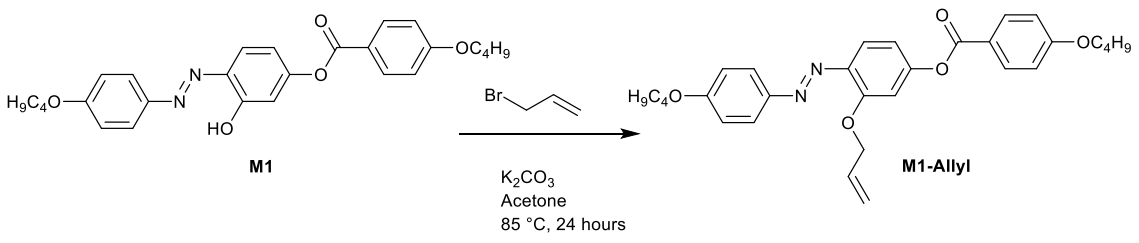

Figure 2-3. Reaction scheme for allylation reaction used to convert **M1** to **M1-Allyl**.

For attachment of **M1-Allyl** to the triblock copolymer backbone a higher yielding method than hydrosilylation was desired. The thermally activated initiator 2,2′-azobis(2-methylpropionitrile) (AIBN) was successfully used in the functionalisation of poly(3-mercaptopropylmethylsiloxane) (PMMS) with **M1-Allyl** by a thiol-ene click reaction,[11] and so was incorporated into a method whereby 1,4-butanedithiol was chosen as a difunctional linking group in an analogous role to 1,1,3,3-tetramethyldisiloxane in Figure 2-2. The thiol was added first to the mesogen rather than the triblock copolymer backbone so as to avoid intra- or inter-chain coupling which would be likely due to the large numbers of vinyl groups present in the PMVS block.

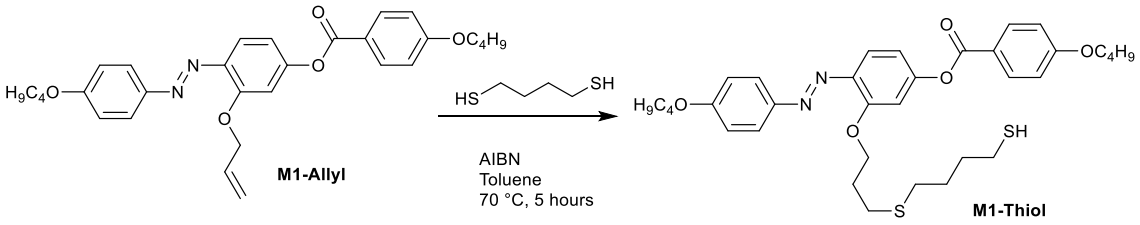

Figure 2-4. Reaction scheme for attachment of 1,4-butanedithiol to **M1-Allyl**. AIBN = 2,2′-azobis(2-methylpropionitrile).

After heating **M1-Allyl** with 1,4-butanedithiol and AIBN in toluene at 70 °C for 5 hours the solvent was removed, resulting in a dark red, highly viscous residue. In order to obtain a sample for characterisation the residue was first purified by chromatography (silica gel, eluting with 4:6 ratio of ethyl acetate:hexane), before attempting recrystallisation from CH_2Cl_2 and cyclohexane. This afforded a highly viscous liquid which was analysed by ^{1}H NMR spectroscopy (Figure A-5). Peaks characteristic of the allyl group on **M1-Allyl** between 5.31-6.18 ppm were not observed, whilst new peaks were present between 2.42-3.55 ppm, and a relatively broad peak at 3.4 ppm. No peaks were seen between 7.05-7.87 ppm, which were present for both **M1** and **M1-Allyl**. The broad peak was found at a chemical shift characteristic for an aniline, whilst the missing aromatic peaks correspond to the protons introduced on conversion of the intermediate **I-M1** to **M1**. From this information, it would therefore appear that despite the introduction of new alkyl groups, which suggests successful attachment of the dithiol, the target product **M1-Thiol** was not obtained due to cleavage of the azo-bond. Electrospray ionisation mass spectrometry (ESI-MS) was carried out on the product, where no peak was observed at the expected molecular weight of 624.9 g mol^{-1} (Figure A-6). However, a peak was present at 462.2 g mol^{-1} which corresponds to **M1-Thiol** after the loss of 4-butoxyaniline by cleavage of the azo bond. It can therefore be concluded that these reaction conditions are not appropriate, due to the apparent decomposition of the mesogen.

2.2.1.2. M2 Synthesis

To increase the scope of the coupling chemistry with the copolymer and potentially modulate the thermal properties of the resulting material, an amine functionalised equivalent of **M1** was also synthesised, namely **M2,** which had not been previously prepared. No further functionalisation of **M2** was carried out, for example to attach a linking group, due to the decomposition of **M1** during the thiol-ene click reaction described in Section 2.2.1.1. As for the synthesis of **M1**, a diazonium salt was first generated from 4-butoxyaniline, however, in the next step protected amine functionality was introduced at position 3 (where the hydroxyl group was found for the literature example).[13] This was achieved through the reaction of the diazonium salt with 3-aminophenol, which was first protected using a *tert*-butyloxycarbonyl (Boc) group, to give the intermediate, **I-M2**, with a yield of 87% as outlined in Figure 2-5.

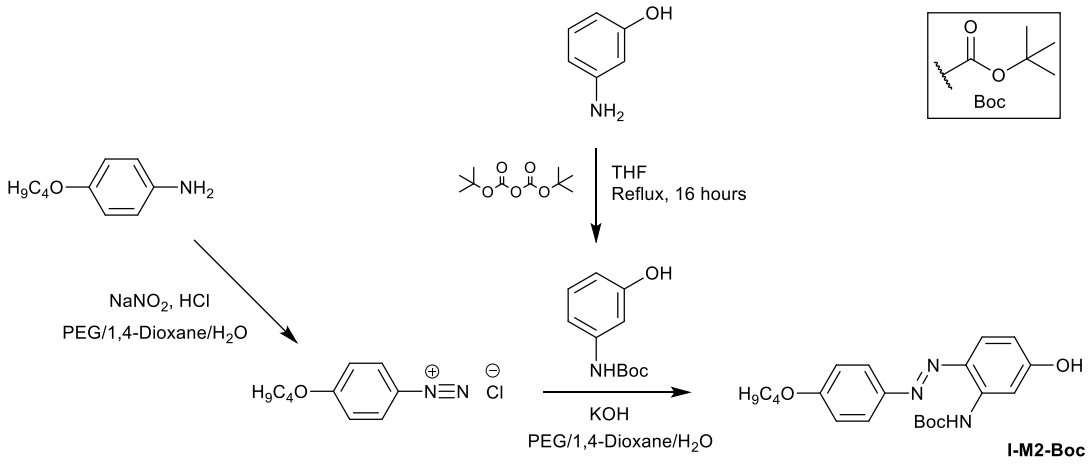

Figure 2-5. Reaction scheme for Boc-protection and reaction of 3-aminophenol with the diazonium salt to give **I-M2-Boc**. PEG = poly(ethylene glycol) average mol. wt. 200 g mol^{-1}.

The protection of 3-aminophenol was established by ^{1}H NMR spectroscopy (Figure A-7), with the amide proton resulting in a peak at 8.27 ppm that integrated 1:1 with the peak at 8.27 ppm corresponding to the phenol group. This protection was necessary to ensure that the diazonium salt reacted at position 4 on the 3-aminophenol as both primary amines and phenols are strong electron donating groups, which direct electrophilic attack at the *para* position. By decreasing the electron donating ability of the amine group by converting it to an amide, the diazonium salt should therefore be directed to the correct position on the ring by the phenol. This was confirmed by ^{1}H NMR spectroscopy (Figure A-8), with four distinct aromatic proton environments observed for **I-M2-Boc.** The peak at 7.88 ppm represented the one proton *ortho* to both the amide and

phenol, the overlapping multiplets at 7.71-7.82 ppm corresponded to the three protons on positions either side of the azo-bond, whilst those at 6.95-7.02 corresponded to the two protons at the remaining positions on the di-substituted ring. Finally, the peak at 6.57 ppm represented the proton located *para* to the amide.

In the second step of the synthesis an ester bond was formed between **I-M2-Boc** and 4-butoxybenzoic acid, mediated by *N,N'*-dicyclohexylcarbodiimide (DCC) with 4-pyrrolidinopyridine as a catalyst, to give **M2-Boc** with a yield of 72%. Deprotection of the amine group was then achieved by stirring a solution of **M2-Boc** in CH_2Cl_2 and trifluoroacetic acid for 1 hour at room temperature (Figure 2-6).

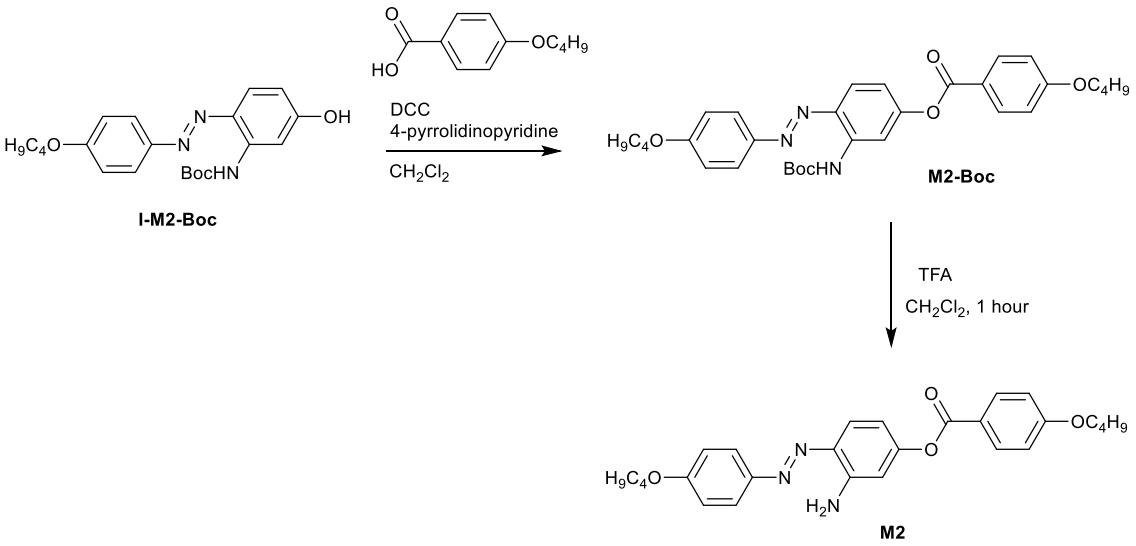

Figure 2-6. Reaction scheme for conversion of **I-M2-Boc** to **M2**. DCC = *N,N'*-dicyclohexylcarbo-diimide, TFA= trifluoroacetic acid.

The formation of **M2-Boc** was confirmed by ^{1}H NMR spectroscopy (Figure A-11) by the loss of the peak at 6.32 ppm and the persistence of the peak at 9.39 ppm seen in the spectrum for **I-M2-Boc**, corresponding to the phenol and amide protons, respectively. On deprotection to give **M2** the peak at 6.32 ppm shifted to 5.88 ppm and integrated to two protons relative to the alkyl protons (Figure A-14), confirming successful regeneration of the amine functionality.

2.2.2. Polymer Backbone Synthesis

2.2.2.1. PS-*b*-PMVS-*b*-PS Triblock Copolymer Synthesis

The PS-*b*-PMVS-*b*-PS triblock copolymer backbone was synthesised by the sequential living anionic polymerisation of styrene, hexamethylcyclotrisiloxane (D_3) and 1,3,5-trivinyl-1,3,5-trimethylcyclotrisiloxane (V_3) as outlined in Figure 2-7. The first step of the reaction was the initiation of styrene with *sec*-BuLi at -50 °C. Following complete consumption of the monomer, a small amount of D_3 was added, which reduces the nucleophilicity of the propagation site to avoid side reactions with the vinyl groups of the V_3 monomer. The final triblock copolymer was formed by coupling two chains of PS-*b*-PMVS using a precise amount of dichloromethylvinylsilane to ensure that the chains couple together rather than form end-functionalised diblock copolymers.

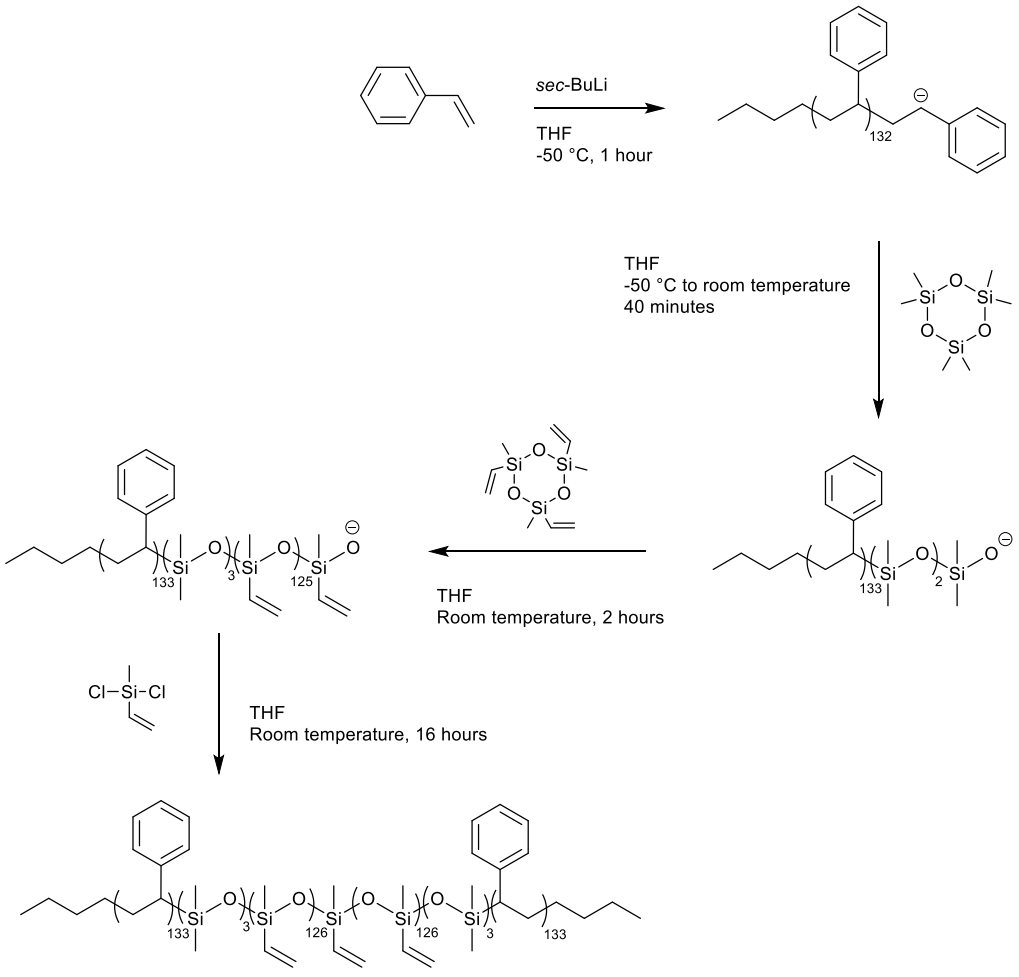

Figure 2-7. Reaction scheme for synthesis of the **PS-*b*-PMVS-*b*-PS** triblock copolymer.

Aliquots were taken at each stage of the synthesis to determine the molecular weight and polydispersity index (PDI) of the developing block copolymer, and these data are included in Table 2-1. The molecular weight for the PS block in the first step was determined in absolute terms using multi-detection GPC. This technique afforded a number-average molecular weight (M_n) of 13,800 g mol^{-1} for the PS block, which corresponds to a number-average degree of polymerisation (DP_n) of 133. A relatively high PDI of 2.25 was determined, which is significantly higher than that previously reported for this synthetic route (1.15).[10] This is most likely an effect of the scale of the reaction leading to insufficient cooling of the solvent during the polymerisation of styrene. By comparison of the M_n determined experimentally with that expected from the stoichiometry of the reaction (Table 2-1), it can be seen that the synthetic method resulted in values close to those targeted (within 10%).

Table 2-1. M_n and PDI of aliquots from the **PS-*b*-PMVS-*b*-PS** synthesis

Polymer	PDI	M_n (g mol^{-1}) [a]	M_n (g mol^{-1})
PS	2.25	12,800	13,800[b]
PS-*b*-PDMS	2.36	13,000	14,100[c]
PS-*b*-PDMS-*b*-PMVS	1.75	26,700	27,000[c]
PS-*b*-PMVS-*b*-PS	1.90	53,500	50,000[c]

[a] Predicted from stoichiometry, [b] Obtained by GPC, [c] Obtained by ^{1}H NMR spectroscopy.

Whilst GPC can be used to determine the absolute molecular weight of homopolymers, assumptions about polymer chain coiling and so hydrodynamic radius are not valid for block copolymers. Therefore, in order to determine the size of the subsequent blocks, ^{1}H NMR spectroscopy (Figure A-17 to A-20) was used to calculate the ratio of characteristic groups associated with each block relative to those for PS, and this information in conjunction with the GPC data for PS allowed for calculation of overall molecular weight.

For the **PS-*b*-PDMS** aliquot the relative ratio of the peaks for the five aromatic styrene protons at 6.45-7.07 ppm was integrated with respect to the two methyl groups of PDMS at 0.13 ppm to give a ratio of 98:2, corresponding to a PDMS block of three $SiMe_2O$ units. The addition of the PDMS block therefore adds approximately 300 g mol^{-1} to the molecular weight of the polymer, and makes little contribution to the mass of the final material. The low intensity arising from the methyl peaks of the PDMS block makes their unambiguous identification problematic once the PMVS block has been added, and consequently a DP_n of 3 is propagated through the subsequent calculations. After addition of the PMVS block and coupling to form the triblock copolymer the

ratio of the five aromatic PS protons was again calculated, this time against the peaks for the three PMVS vinyl protons from 5.75-6.03 ppm. This gave a ratio of PS:PMVS of 52:48, corresponding to a DP_n of 255 for the PMVS block. A formula of PS_{133}-*b*-$PDMS_3$-*b*-$PMVS_{253}$-*b*-$PDMS_3$-*b*-PS_{133} was therefore calculated, where subscripts indicate the DP_n of each block, and a M_n of 50,000 g mol^{-1}. The relatively small amount of PDMS block and its compatibility with the PMVS block means that it is likely to have little effect on the copolymer, and henceforth we will omit the PDMS component from the formula, referring to this product as **PS-*b*-PMVS-*b*-PS**.

The PDI for the final triblock copolymer was 1.90, which had decreased compared with the original PS homopolymer. This reduction suggests that no significant back-biting of the propagating PMVS chains or oxidative coupling of the living PS chains occurred during the polymerisation, which would be expected to result in a broader molecular weight distribution. This is consistent with the GPC data (Figure 2-8) whereby each aliquot gave a monomodal peak which was generally symmetric about the maximum. The peaks also shift to lower retention volumes as each block is added, in keeping with increasing the molecular weight, with the difference between **PS-*b*-PDMS-*b*-PMVS** and **PS-*b*-PMVS-*b*-PS** indicating successful coupling of the diblock copolymers.

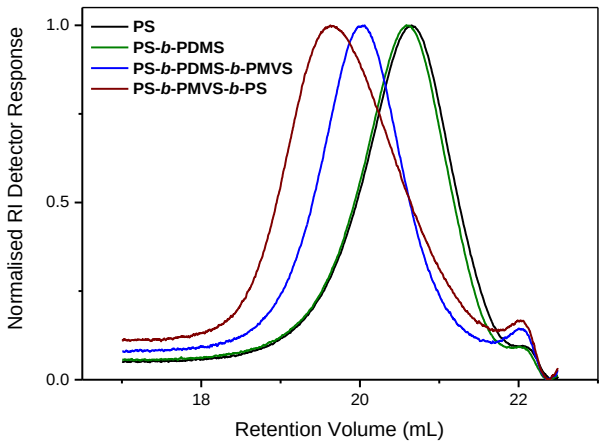

Figure 2-8. GPC data for **PS-*b*-PMVS-*b*-PS** triblock copolymer aliquots.

2.2.2.2. PMVS Homopolymer

To isolate the properties of the liquid crystalline PMVS block from the influence of the styrene end blocks, a PMVS homopolymer was prepared by living anionic polymerisation. D_3 was first initiated with *n*-BuLi at room temperature to give a less nucleophilic propagating site and stirred for 3 hours to ensure complete consumption of the monomer before the addition of V_3, after which the reaction was again allowed to stir for 3 hours. The polymerisation was terminated with

chloro(dimethyl)vinylsilane (Figure 2-9) and the product **PMVS** isolated by precipitation from THF into methanol.

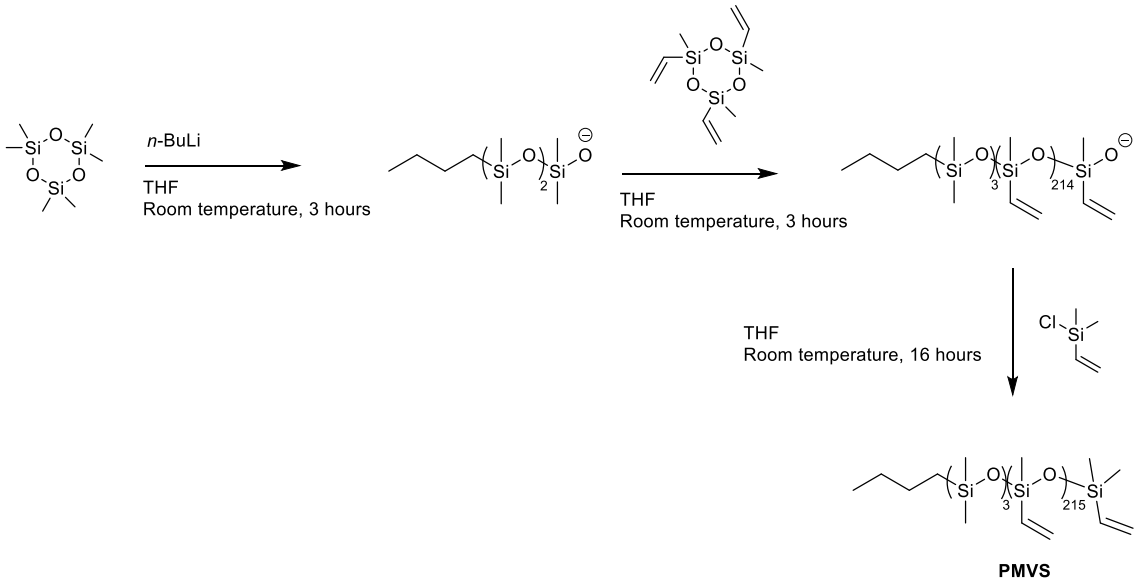

Figure 2-9. Reaction scheme for the synthesis of the **PMVS** homopolymer.

The polymerisation resulted in a highly viscous product with a M_n of 18,500 g mol^{-1} and PDI of 1.37 as measured by multi-detection GPC. This corresponds to a DP_n of 217, comparable to that of the midblock in **PS-*b*-PMVS-*b*-PS** (DP_n = 253), and thus suitable for a comparison of polymer behaviour with and without the glassy PS segments. Again, the narrow, monomodal peak in the chromatogram indicated that any backbiting of the propagating PMVS chain was minimal and is consistent with the formation of a linear homopolymer (Figure 2-10).

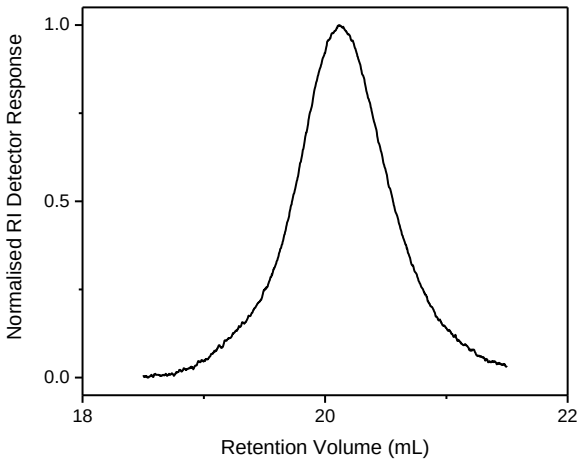

Figure 2-10. GPC data for **PMVS** homopolymer.

2.2.2.3. Repeated PS-*b*-PMVS-*b*-PS Triblock Copolymer Synthesis

For experiments using AIBN (to be discussed in Section 2.2.3.2), a repeat synthesis of the triblock copolymer was carried out using the conditions and methods discussed in Section 2.2.2.1. This resulted in a polymer with a formula of PS_{121}-*b*-$PDMS_3$-*b*-$PMVS_{253}$-*b*-$PDMS_3$-*b*-PS_{121} and M_n of 47,300 g mol^{-1}. This difference is not expected to result in significantly different properties, however, this polymer will be referred to as **PS-*b*-PMVS-*b*-PS***.

2.2.3. Linking Group Attachment

The target material of this synthesis is a side-on LCE, where the rod-like mesogen is attached through a linking group to the deformable PMVS midblock of the triblock copolymer backbone. In literature examples of the attachment of **M1-Allyl** to a PMVS block, hydrosilylation was used to attach 1,1,3,3-tetramethyldisiloxane first to the mesogen, with a yield of 30%, before repeating the reaction with the PMVS block (Figure 2-2).[14] For materials applications, however, multigram quantities are required, and these are most efficiently achieved by high yielding reactions. Therefore, an alternative method of attachment with a greater yield was desired. It was shown in Section 2.2.1.1. that attachment of the linking group to the mesogen by a thiol-ene click reaction was not a viable strategy, and so synthetic routes that allowed for modification of the vinyl group on the PMVS block were developed.

In this work, attachment of the linking group was achieved post-polymerisation *via* thiol-ene click reactions using either a UV or thermally activated initiator (Figure 2-11), a method that is commonly used to add functionality to vinyl groups in high yields and is effective for modifying polymers.[15–18]

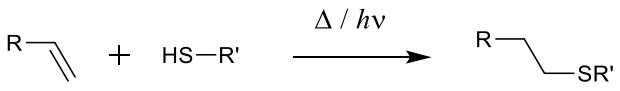

Figure 2-11. General scheme for thiol-ene click reactions.

Thiol-ene click reactions have previously been used to functionalise a PMMS backbone with a vinyl-terminated mesogen.[11] This method has also been used by our group to add a carboxylic acid group to the PMVS blocks of copolymers,[19] which as a consequence of the limited range of commercially available thiols were further functionalised by reaction with various amines.[20] This method of attaching a carboxylic acid-terminated linking group to the PMVS block *via* a thiol-ene

click reaction would therefore be suitable for coupling the mesogen with the triblock copolymer backbone, and would be appropriate here as it is expected to proceed with high yields.

Two attachment strategies were investigated to attach the photoresponsive mesogen to the **PS-*b*-PMVS-*b*-PS** block copolymer backbone as outlined in Figure 2-12. In both cases a thiol-ene click reaction (initiated by either irradiation with UV light or by heating) was used to add a carboxylic acid-terminated thiol to the PMVS block. Attachment of the mesogen was then attempted by either converting the carboxylic acid to a more labile ester group before reacting with **M2**, or by directly coupling either **M1** or **M2** to the carboxylic acid functionality by a carbodiimide-mediated esterification/amidation reaction.

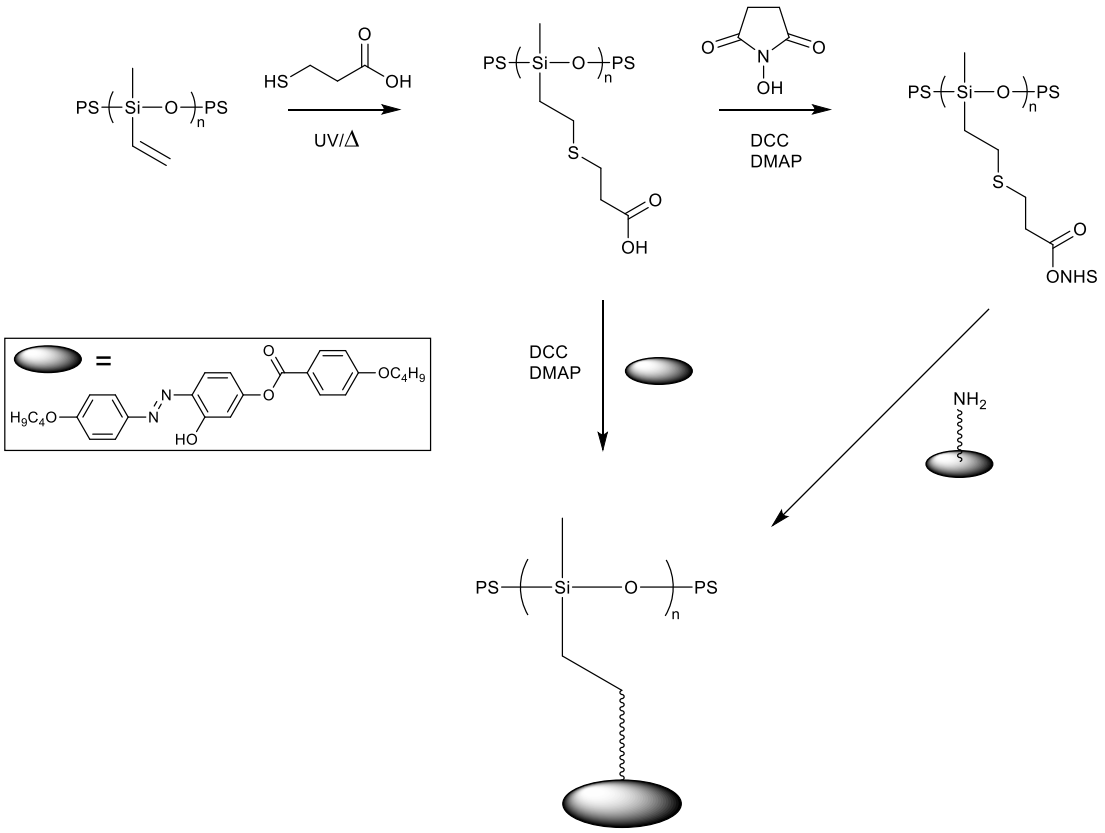

Figure 2-12. Summary of attachment methods. A carboxylic acid-terminated linking group was first attached to the PMVS midblock by a thiol-ene click reaction, before attachment of the mesogen by either displacement of a labile *N*-hydroxysuccinimide (NHS) ester group or by a carbodiimide mediated esterification reaction. Structure of triblock copolymer backbone simplified for clarity. PS = polystyrene. DCC = *N,N'*-dicyclohexylcarbodiimide, DMAP = 4-dimethylaminopyridine.

2.2.3.1. Photoinitiated Thiol-Ene Click Reaction

The photoinitiator 2,2-dimethoxy-2-phenylacetophenone (DMPA) was used to attach the carboxylic acid-terminated linking group to the vinyl groups of the PMVS block for both the triblock copolymer and the homopolymer. In both cases, the polymer was dissolved in dry THF before addition of the DMPA and 10 equivalents of the thiol and irradiation with UV light for 2.5 hours at room temperature. This approach allowed for variation in the number of carbons in the linking group alkyl chain by using either 3-mercaptopropionic acid or 5-mercaptopentanoic acid, a feature that was expected to be useful for tuning the properties of the final LCE as the linking group acts to decouple the motion of the backbone from that of the mesogen, and has been shown to play a vital role in the formation of a LC mesophase.[21]

Attachment of Linking Group to PS-*b*-PMVS-*b*-PS

The attachment of the carboxylic acid to the triblock copolymer polymer backbone was carried out using both 3-mercaptopropionic acid to obtain **P-3** and 5-mercaptopentanoic acid to obtain **P-5**, as outlined in Figure 2-13. Both products were isolated in high yields (86 and 95% respectively), with the level of linking group attachment calculated from the ^{1}H NMR spectroscopy data (Figure A-24 and Figure A-28). For both **P-3** and **P-5** the disappearance of the vinyl peaks at 5.75-6.02 ppm in the ^{1}H NMR spectrum indicated full conversion of the PMVS vinyl groups to the carboxylic acid-terminated side-chains. This was confirmed by comparing the integration of peaks for the alkyl-groups in the linking group (2.62-2.84 ppm) with the methyl resonance for the PMVS group (0.28 ppm), which integrated in a 1:1 ratio and so confirm the presence of one carboxylic acid-terminated linking group per silicon in the PMVS block. With this information, and using the PMVS DP_n of 253 calculated earlier, the molecular weight for each polymer can be calculated, and these are given in Table 2-2, along with values for the PDI obtained by GPC.

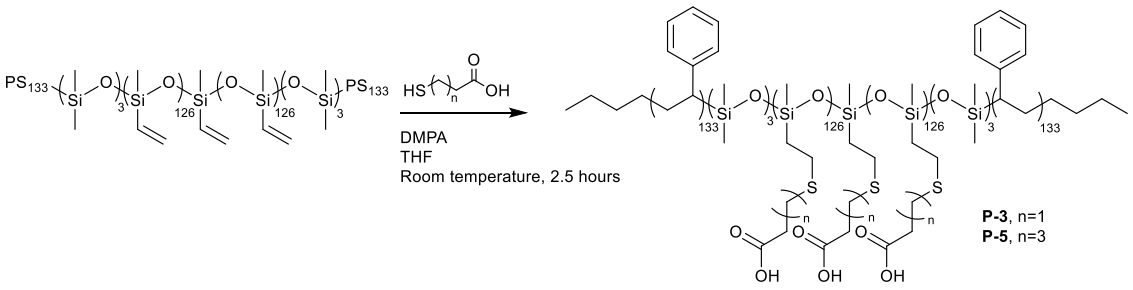

Figure 2-13. Reaction scheme for addition of a carboxylic acid-terminated linking group to the PMVS block of the triblock copolymer. PS = polystyrene. DMPA = 2,2-dimethoxy-2-phenylacetophenone.

Table 2-2. M_n and PDI for **P-3** and **P-5**.

Polymer	PDI	M_n (g mol^{-1})
PS-*b*-PMVS-*b*-PS	1.90	50,000
P-3	1.75	77,000
P-5	1.79	84,000

As expected, the addition of the thiol across the vinyl group does not significantly affect the PDI compared with the **PS-*b*-PMVS-*b*-PS** triblock copolymer and is high yielding for both alkyl chain lengths. This route therefore offers a simple method for attaching variable length side-chains to the PMVS block, which can then be coupled to the mesogen in order to impart responsive behaviour.

Attachment of Linking Group to PMVS Homopolymer

The photoinitiated thiol-ene click reaction was repeated for the **PMVS** homopolymer, as shown in Figure 2-14, with 10 equivalents of 3-mercaptopropionic acid. As for the triblock copolymer, the percentage of attachment of the linking group was calculated from ^{1}H NMR spectroscopic data (Figure A-31). For the product, **PMVS-3**, no vinyl peaks were observed at 5.76-6.04 ppm, and the alkyl peaks at 2.59-2.81 and 0.97-1.02 ppm integrated in a 1:1 ratio with the methyl resonance from PMVS at 0.25 ppm, confirming one linking group was attached per silicon. This resulted in a polymer with a M_n of 44,200 g mol^{-1}. It was not possible to characterise the product by GPC due to strong interactions between the carboxylic acid groups and the column material, but dynamic light scattering experiments on a solution of the polymer in THF resulted in a single peak indicating that a monomodal product was obtained (Figure A-33).

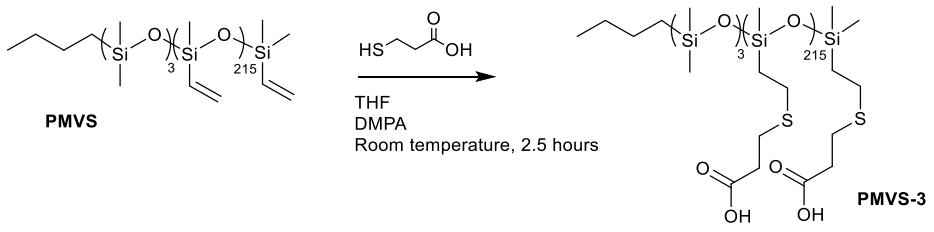

Figure 2-14. Reaction scheme for addition of the linking group to **PMVS** by the photoinitiated thiol-ene click reaction. DMPA = 2,2-dimethoxy-2-phenylacetophenone.

2.2.3.2. Thermally Initiated Thiol-Ene Click Reaction

The photoinitiated thiol-ene reaction has been shown to be rapid and highly efficient,[22] but it may be beneficial in this case to carry out the reaction at a slower rate to minimise any side reactions between vinyl groups on the PMVS blocks which could lead to undesired crosslinking. Thiol-ene reactions using 2,2′-azobis(2-methylpropionitrile) (AIBN) as the initiator have been shown, for some reactions, to give a lower conversion of vinyl groups, and proceed at a slower rate than those initiated with DMPA.[22] For this reason, the addition of the linking group 3-merpcaptopropionic acid to **PS-*b*-PMVS-*b*-PS*** was carried out using AIBN as the initiator to obtain **P*-3(AIBN)**, to determine whether or not any difference in the product was evident when compared with **P-3**.

PS-*b*-PMVS-*b*-PS* and 5 equivalents of 3-mercaptopropionic acid were dissolved in toluene, before freshly recrystallised AIBN was added and the solution heated at 70 °C for 5 hours. After precipitation of the product the level of functionalisation of the PMVS block was calculated from ^{1}H NMR spectroscopic data (Figure A-34). The ratio of peaks and their chemical shifts seen for **P*-3(AIBN)** were in good agreement with that observed for **P-3**, suggesting no obvious structural difference between the two products. The alkyl groups integrated in a 1:1 ratio with the PMVS alkyl resonances at 1.04 ppm which indicated a polymer with one linking group per silicon in the PMVS block, and a M_n of 62,800 g mol^{-1}. GPC afforded a chromatogram with a broad, monomodal peak (Figure A-58) which had a PDI of 2.48, significantly higher than that obtained for the triblock copolymer. This is likely due to interactions between the carboxylic acid functionality and the GPC column material as broad, low intensity peaks were also obtained for **P-3** and **P-5**.

2.2.3.3. Conversion of Carboxylic Acid to NHS Ester

In order for the mesogen to be added to the linking group, the carboxylic acid functionality on **P-3** was first converted to a more labile *N*-hydroxysuccinimidyl (NHS) ester to yield **P-3-NHS** (Figure 2-15). This was expected to be readily displaced by a primary amine under mild conditions, which had previously been shown to work for a comparable PMVS containing block copolymer where quantitative conversion to the amide product was achieved.[20] The esterification reaction was performed at room temperature in dry CH_2Cl_2 with DCC and a catalytic amount of 4-dimethylaminopyridine (DMAP), with the product isolated by first filtering off solid impurities before precipitation from THF into hexane.

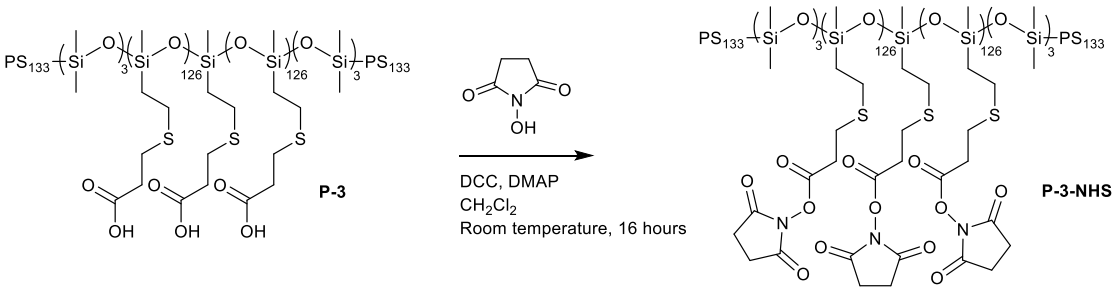

Figure 2-15. Reaction scheme for conversion of **P-3** to **P-3-NHS**. PS = polystyrene. DCC = *N,N'*-dicyclohexylcarbodiimide, DMAP = 4-dimethylaminopyridine.

The attachment of NHS to the carboxylate groups was confirmed by ^{1}H NMR spectroscopy and GPC. In the ^{1}H NMR spectrum (Figure A-36) a new peak appeared at 2.66 ppm which corresponded to the four chemically equivalent protons on the NHS ring. The expected singlet, however, overlapped with multiplets from the by-product, dicyclohexylurea, making analysis of the percentage conversion of carboxylic acid groups problematic. By GPC the peak shifted from a maximum at retention volume of 19.9 mL for **P-3** to 18.3 mL for **P-3-NHS**, indicating a significant increase in hydrodynamic volume, consistent with increased molecular weight and so attachment of NHS (Figure 2-16). The peak for **P-3-NHS** was broad with a shoulder at lower molecular weight which suggests that not all the carboxylic acid groups had reacted, however, the value for the retention volume combined with the ^{1}H NMR spectrum indicated a high level of attachment was likely.

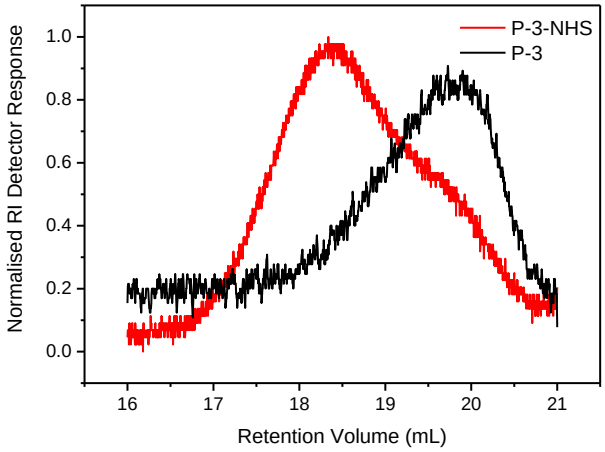

Figure 2-16. GPC data for **P-3** and **P-3-NHS** demonstrating a clear shift to lower retention volume on functionalisation with the NHS ester group.

2.2.4. Mesogen Attachment Methods

2.2.4.1. Displacement of NHS Ester with M2

The displacement of the NHS-ester group by a primary amine was shown to proceed at room temperature for a variety of amines,[20] and so this reaction was attempted using **M2.** To carry out the coupling between the block copolymer and mesogen, **P-3-NHS** was dissolved in THF with **M2** and stirred at room temperature overnight, in accordance with a literature procedure.[20] The product was then precipitated from THF into methanol. ^{1}H NMR spectroscopy of the isolated product showed peaks characteristic of unreacted **M2**, including sharp peaks in the aromatic region from 6.48-8.14 ppm and a multiplet at 4.04 ppm. The peak arising from the NHS group at 2.64 ppm was reduced in intensity with respect to **P-3-NHS** but still present, suggesting that not all of the NHS groups had been displaced. A new peak was observed at 3.48 ppm, which can be attributed to a methyl ester group (Figure A-37). It was therefore likely that **M2** did not attach to the linking group on **P-3-NHS** in significant amounts, but rather that during the precipitation step methanol displaced a portion of the NHS groups to form a methyl ester-terminated linking group. It is expected that **M2** will be a stronger nucleophile than **M1**, and so an alternative mesogen attachment method was attempted.

2.2.4.2. Coupling of M1/M2 to P-3/P-5 by a Carbodiimide Mediated Reaction

The DCC coupling reaction used in both the mesogen synthesis and to form the NHS ester is a mild reaction which is often used for the formation of peptides.[23,24] It is therefore compatible with both the polysiloxane block of the thermoplastic elastomer backbone, which is susceptible to cleavage under strongly acidic or basic conditions, and the functionality present in **M1** and **M2**. Attachment would be expected to occur by formation of an ester or amide bond between the hydroxyl or amine group on **M1** or **M2**, respectively, and the carboxylic acid group that was attached to the triblock copolymer backbone by the thiol-ene click reaction. This allows for a number of polymers to be formed with varying linking groups (ester or amide) and alkyl chain lengths.

To carry out the attachment, either **P-3** or **P-5** was dissolved in dry CH_2Cl_2 with 1.5 equivalents of either **M1** or **M2** and the solution stirred at room temperature for 60 hours. On removal of solid impurities by filtration, the polymer was isolated from excess unattached mesogen by repeated precipitations from toluene into methanol to give a soft, orange solid. This suggested successful attachment of the mesogen, as opposed to reaction with methanol during the precipitation step, which was confirmed by ^{1}H NMR spectroscopy (Figure A-39, A-42 and A-45). The yields and level of attachment varied with the different starting materials, with the results given in Table 2-3. Polymers are named by the convention **P-x-y(a)-COOH(b)**, where x indicates the number of

carbons in the linking group, y the mesogen, (a) the percentage of linking groups with mesogen attached and (b) the percentage of linking groups that were unreacted.

Table 2-3. PDI and M_n for **PS-*b*-PMVS-*b*-PS, P-3-M1(82)-COOH(18)**, **P-3-M2(80)-COOH(20)** and **P-5-M1(86)-COOH(14)**.

Polymer	PDI	M_n (g mol^{-1})[a]	M_n (g mol^{-1})[b]	% Attachment to PMVS block[b]
PS-*b*-PMVS-*b*-PS	1.90	25,565	50,000	N/A
P-3-M1(82)-COOH(18)	1.89	36,468	170,000	82%
P-3-M2(80)-COOH(20)	1.77	32,858	167,500	80%
P-5-M1(86)-COOH(14)	1.94	30,951	181,700	86%

[a]Obtained by GPC, [b]Obtained by ^{1}H NMR spectroscopy.

The successful attachment of mesogen to the polymer for the systems given in Table 2-3 can be inferred from the decrease in retention volume, indicative of an increase in hydrodynamic radius and so molecular weight, compared with that obtained for **PS-*b*-PMVS-*b*-PS** by GPC (Table 2-3). This is further supported by the broadening of peaks in the ^{1}H NMR spectra compared with those for the free mesogen, which contrasts with the spectrum obtained for the product of the reaction between **P-5** and **M2** (Figure A-38). In this case several sharp peaks were observed, indicating that the unreacted mesogen was not separated fully from the polymer and that the level of attachment was very low, if it occurred at all. The attachment percentage was calculated by comparing the relative integrals for the six alkyl protons on the linking group (2.5-2.9 ppm) with the four associated with the OCH_2 group on the mesogen (4.0 ppm). These peaks were chosen for the calculation as neither overlaps with signals from other parts of the polymer. Full conversion of carboxylic acid groups to either ester or amide was not achieved for any polymer, with 14-20% of PMVS units remaining unreacted, depending on the system. Whilst it is not possible to detect the carboxylic acid proton in the spectrum, it is assumed that the non-converted linking groups have not reacted further, i.e. to form methyl esters.

The level of attachment was found to be between 80-86% for both **M1** and **M2**, suggesting that the attachment method proceeded equally well for ester or amide formation. The PDI as determined by GPC increased slightly compared with **P-3** or **P-5** in all cases, which would be a result of the non-complete addition of mesogen to the linking groups. The PMVS midblock of the copolymer should therefore be considered as a random block copolymer of the COOH and mesogen functionalised units as shown in Figure 2-17.

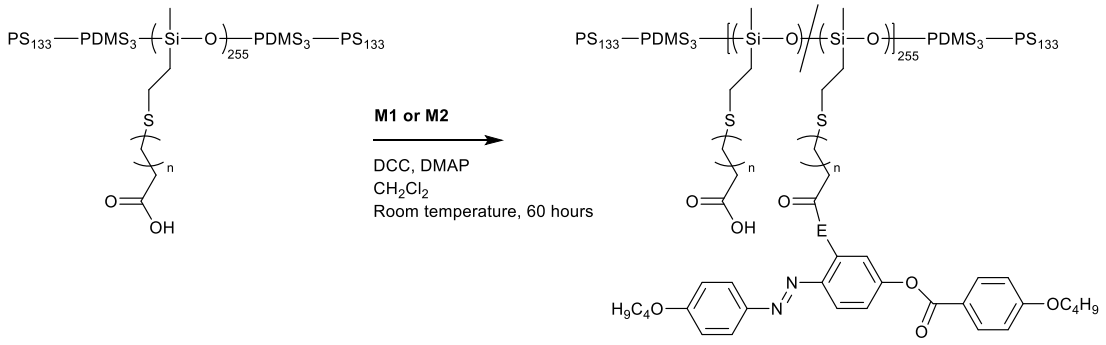

Figure 2-17. Reaction scheme for coupling of **M1** or **M2** to **P-3** or **P-5** with a DCC mediated coupling reaction to give the LC-functionalised triblock copolymer. DCC = *N,N'*-dicyclohexylcarbodiimide, DMAP = 4-dimethylaminopyridine. General structure, for **P-3**, n=1. For **P-5**, n=3. For **M1**, E= O. For **M2**, E=NH. Backbone simplified for clarity.

There was a significant decrease in the yield of LC-functionalised polymers based on **P-5** compared with **P-3**. The polymer isolated for both the ester and amide was less soluble than the corresponding **P-3** product, suggesting that the increased length of the linking group has a considerable effect on the solution properties of the polymer and this, combined with the non-attachment of **M2** to **P-5**, suggests that the 3-mercaptopropionic acid linking group is preferable for high yielding syntheses of the LCEs. Nevertheless, the lowest yielding polymer isolated (**P-5-M1(86)-COOH(14)**) was still obtained in a higher percentage yield than the literature method (30%).[14] By requiring significantly less mesogen this method should allow for scaling up the synthesis of the thermoplastic LCE for larger scale processing methods.

2.2.4.3. Coupling of M1 to PMVS-3 by a Carbodiimide Mediated Reaction

The LC-functionalised homopolymer, **PMVS-3-M1(84)-COOH(16)** was obtained by coupling of **M1** to **PMVS-3** *via* the DCC mediated esterification reaction described in Section 2.2.3.2, however, the reaction was carried out in dry THF due to **PMVS-3** being insoluble in CH_2Cl_2 (Figure 2-18). The product was obtained as a soft solid, which was in contrast to the oil obtained for a PMVS homopolymer of similar molecular weight functionalised with **M1** through the hydrosilylation reaction.[14]

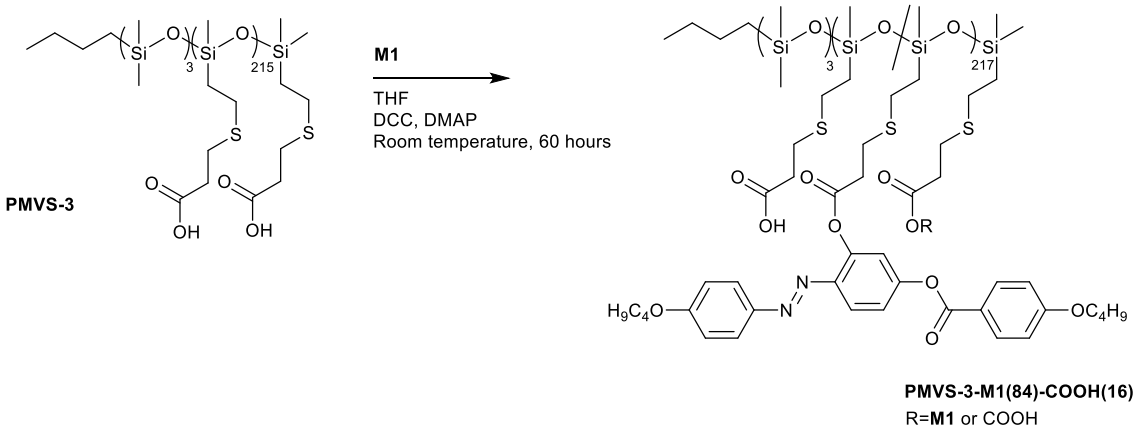

Figure 2-18. Reaction scheme for coupling of **M1** to **PMVS-3** with a DCC mediated coupling reaction to give **PMVS-3-M1(84)-COOH(16)**. DCC = *N,N'*-dicyclohexylcarbodiimide, DMAP = 4-dimethylaminopyridine.

The product **PVMS-3-M1(84)-COOH(16)** was characterised by ^{1}H NMR spectroscopy (Figure A-51) and GPC, with the percentage of linking groups functionalised with **M1** calculated from ^{1}H NMR spectroscopic data. By integration of the peak at 3.79-3.85 ppm, characteristic of the four OCH_2 protons on the mesogen, with the peak at 2.57-2.83 ppm, characteristic of six alkyl protons on the linking group, it was found that 84% of linking groups were functionalised with **M1**. A relatively high PDI of 2.68 was determined by GPC (Figure 2-19), which represents a large increase in the breadth of the molecular weight distribution when compared with that of the starting **PMVS** (Table 2-4). The molecular weight of the functionalised homopolymer is dominated by the contribution from the mesogen rather than the polysiloxane backbone, and so small differences in the level of attachment of **M1** will have a significant effect and result in a broad range of molecular weights. This will increase the disparity between the number and weight average molecular weights, as evidenced by the tail towards higher retention volume in the GPC data, resulting in the increased PDI.

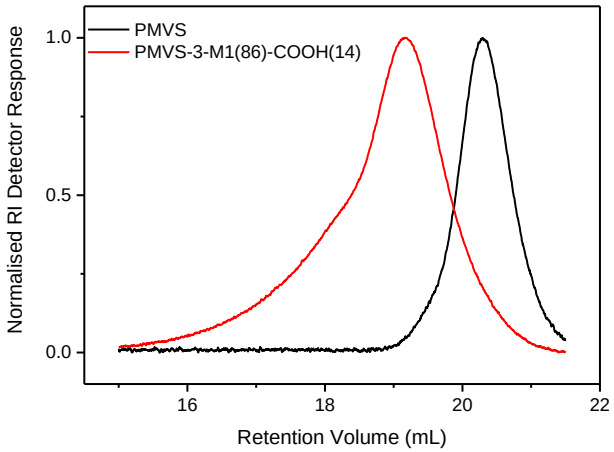

Figure 2-19. GPC data for **PMVS** and **PMVS-3-M1(86)-COOH(14)**.

Table 2-4. M_n and PDI (where appropriate) of **PMVS**, **PMVS-3** and **PMVS-3-M1(84)-COOH(16).**

Polymer	M_n (g mol^{-1})	PDI
PMVS	18,500[a]	1.37
PMVS-3	44,200[b]	N/A
PMVS-3-M1(84)-COOH(16)	133,500[b]	2.68

*[a]Determined by GPC. It was not possible to obtain GPC data for **PMVS-3** due to interactions with column material. [b] Obtained from ^{1}H NMR spectroscopy.*

2.2.4.4. Larger Scale Functionalisation of P-3 with M1 by a Carbodiimide Mediated Reaction

The synthetic method described for the synthesis of **P-3-M1(82)-COOH(18)** in Section 2.2.4.2. was repeated starting with 2.35 g of **P-3** and scaling up the quantities of **M1,** DCC and DMAP accordingly. The reaction resulted in a soft, orange polymer as before, with the percentage attachment of the mesogen determined by comparison of the integral for the six alkyl protons on the linking group at 2.41-3.00 ppm with that for the four protons associated with the OCH_2 group on the mesogen at 3.91 ppm (Figure A-48). In this case, the level of attachment was found to be lower than for the 0.35 g scale reaction, with approximately 65% of the linking groups functionalised with **M1**. GPC afforded a chromatogram displaying a monomodal peak with a PDI of 1.62 (Figure A-50), which is comparable with the results given in Table 2-3 for the products of the 0.35 g scale reactions. The resulting polymer **P-3-M1(65)-COOH(35)** was therefore calculated to have a M_n of 150,750 g mol^{-1}.

2.2.5. Conversion of Residual Carboxylic Acid Groups to Methyl Esters

It was expected that the unreacted carboxylic acid groups on the LCEs would have a significant impact on the thermal properties of the polymer. The DCC-mediated esterification reaction was therefore used to convert residual carboxylic acid groups on **P-3**, **P*-3(AIBN)** and **P-3-M1(65)-COOH(35)** to methyl esters by coupling the linking groups with methanol. A polymer described as **P*-3(AIBN)-M1-COOMe** was also prepared, but full characterisation was not possible due to the low solubility of the PMVS block (discussed below). In each case, the starting polymer was dissolved in dry CH_2Cl_2 with 10 equivalents of methanol, DCC and a catalytic amount of DMAP. The solution was stirred at room temperature for 60 hours before the removal of solid impurities by filtration. The products were isolated by precipitation, with the M_n and PDI of each polymer both before and after conversion to the methyl ester equivalent given in Table 2-5.

Table 2-5. M_n and PDI for the polymers before and after conversion of carboxylic acid functionality to methyl ester groups. *M_n calculated from ^{1}H NMR spectroscopy data, PDI obtained from GPC data.*

Polymer	M_n (g mol^{-1})	PDI
P-3	77,000	1.75
P-3-COOMe	80,600	1.62
P*-3(AIBN)	62,800	2.48
P*-3(AIBN)-COOMe	65,500	1.76
P-3-M1(65)-COOH(35)	150,750	1.98
P-3-M1(65)-COOMe(35)	152,000	2.07
P*-3(AIBN)-M1-COOMe	-	1.76

2.2.5.1. P-3-COOMe

The product of the esterification of the carboxylic acid groups on **P-3**, namely **P-3-COOMe,** was characterised using ^{1}H NMR spectroscopy (Figure A-53) and GPC (Figure A-55). In the ^{1}H NMR spectrum, a new peak was observed at 3.69 ppm which was identified as arising from the methyl ester group. The level of conversion of carboxylic acid groups to methyl esters was confirmed through the comparison of the peaks characteristic of two alkyl protons on the linking group at 0.80-0.95 ppm with the methyl ester resonance, with the two signals integrating in a 1:1 ratio. This confirmed full conversion of the carboxylic acid to a methyl ester group, which allows for the M_n to be calculated as 80,600 g mol^{-1}. GPC afforded a chromatogram with a monomodal peak, and a slightly reduced PDI of 1.62 when compared with **P-3** (PDI = 1.75).

2.2.5.2. P*-3(AIBN)-COOMe

The product of the esterification of the carboxylic acid groups on **P*-3(AIBN)**, namely **P-3*(AIBN)-COOMe,** was characterised using ^{1}H NMR spectroscopy (Figure A-56) and GPC (Figure A-58). In the ^{1}H NMR spectrum, a new peak was observed at 3.69 ppm which was identified as arising from the methyl ester group. The level of conversion of carboxylic acid groups to methyl esters was confirmed through comparison of the peaks characteristic of two alkyl protons on the linking group at 0.88-0.92 ppm with the methyl ester resonance, with the two signals integrating in a 1:1 ratio. This confirmed full conversion of the carboxylic acid to a methyl ester group, which allows for the M_n to be calculated as 65,840 g mol^{-1}. GPC afforded a chromatogram with a monomodal peak, and a reduced PDI of 1.76 when compared with **P*-3(AIBN)**.

2.2.5.3. P-3-M1(65)-COOMe(35)

The product of the esterification of the carboxylic acid groups on **P-3-M1(65)-COOH(35)**, namely **P-3-M1(65)-COOMe(35),** was characterised using ^{1}H NMR spectroscopy (Figure A-59) and GPC (Figure A-61). In the ^{1}H NMR spectrum a new peak was observed at 3.58 ppm which was identified as arising from the methyl ester group. The level of conversion of carboxylic acid groups to methyl ester was confirmed through the comparison of the peaks characteristic of the four OCH_2 protons on the mesogen at 3.91 ppm with the three protons from the methyl ester group. This confirmed full conversion of the carboxylic acid to a methyl ester group, with these peaks found in a ratio of 65:35. Integration of the ^{1}H NMR peak at 3.91 ppm compared with the alkyl resonances from PMVS confirmed that 65% of the PMVS blocks remained functionalised with **M1** and no mesogen had been displaced by a methyl ester group, which allowed for the M_n to be calculated as 152,000 g mol^{-1}. GPC afforded a chromatogram with a monomodal peak, and a PDI of 2.07.

2.2.5.4. P*-3(AIBN)-M1-COOMe

A sample of **P*-3(AIBN)** was functionalised with **M1** using the DCC mediated esterification reaction described in Section 2.2.4.2. Attachment of the mesogen to the PMVS block was confirmed by ^{1}H NMR spectroscopy, however, it was not possible to obtain a pure sample using the precipitation method that had previously been used to successfully separate the polymer from excess mesogen. The mixture of polymer and unreacted **M1** was therefore used in the next reaction to convert any remaining carboxylic acid functionality to methyl ester groups. This resulted in a polymer that was easily precipitated from toluene into methanol and was separated from unreacted **M1** to give a soft, orange solid. The polymer was not fully soluble in any ^{1}H NMR solvent tested, with all appearing to be selective for the PS block over the PMVS block. This gave

spectra from which it was not possible to calculate the percentage attachment of **M1** or methyl ester groups, but which confirmed the presence of both by the broadening of their respective peaks when compared to the unattached state (Figure A-62). GPC afforded a chromatogram with a monomodal peak (Figure A-63) with a lower retention volume than measured for **P*-3(AIBN)**, consistent with an increased in the molecular weight, and which demonstrated a hydrodynamic radius comparable with that for **P-3-M1(65)-COOMe(35)** (Figure 2-20), suggesting that a similar level of mesogen loading was achieved. A PDI of 1.76 was measured, again suggesting that the distribution of groups in the product was comparable with previous examples. However, this product will be referred to as **P*-3(AIBN)-M1-COOMe** as the LC loading cannot be quantified.

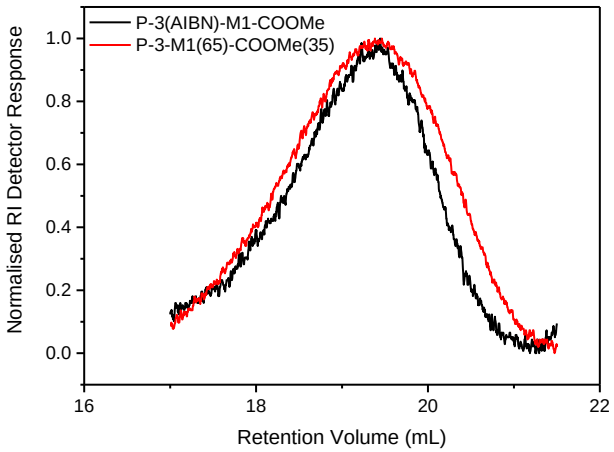

Figure 2-20. GPC data for **P*-3(AIBN)-M1-COOMe** and **P-3-M1(65)-COOMe(35)** indicating a comparable hydrodynamic radius and so molecular weight.

2.2.6. Thermal Analysis

Previous studies of thermoplastic liquid crystal elastomers (LCEs) identified two important transition temperatures to consider in the design of a photoactuator based on the PS-*b*-PMVS-*b*-PS triblock copolymer, namely the glass transition temperature (T_g) for the liquid crystal-functionalised PMVS block, and the isotropic transition or clearing temperature (T_{iso}) where the nematic mesophase transitions to the disordered isotropic state. The T_g of the PMVS block should be at or below room temperature to ensure sufficient chain mobility to accommodate the change in order, and the T_{iso} should not be so high that the PMVS block is too viscous for rapid switching between states to occur.[25]

The synthetic route developed in this work allows for variation in the number of methylene units in the linking group and in the bond type between it and the mesogen. This can be used to tune the thermal properties of the polymer, as the linking group acts to decouple the motion of the polymer backbone from that of the mesogen. This is necessary for mesophase formation to occur, as the polymer backbone will otherwise spontaneously form random coils, which inhibit liquid crystal ordering.[21] It is expected that increasing the distance between these two components will therefore decrease transition temperatures by reducing the influence of the backbone on the mesogen and *vice versa*. Secondly, through the attachment of either **M1** or **M2**, an ester or amide bond will be formed, with the increased hydrogen bonding due to the amide expected to increase interactions between chains, and so raise both the T_g and T_{iso}. Thermal analysis should also identify any differences arising between polymers converted to methyl esters or synthesised using AIBN.

To determine the stable temperature range of the polymers prior to DSC measurements, thermogravimetric analysis (TGA) was carried out (Figure 2-21 and Figure A-64). The thermograms obtained are presented in Table 2-6, and indicated that a 3% weight loss occurred from around 200 °C for the liquid-crystal functionalised polymers (which is taken as being the onset of thermal degradation). It was noted that **P-3-M2(80)-COOH(20)** had a higher weight percentage remaining at 800 °C than the other polymers, which may have been as a result of the greater degree of hydrogen bonding possible due to the presence of amide bonds.

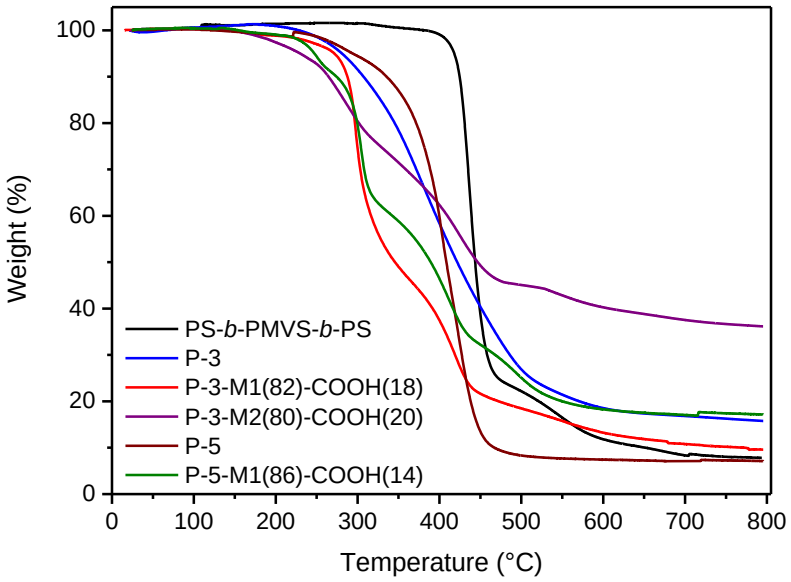

Figure 2-21. TGA thermograms for **PS-*b*-PMVS-*b*-PS**, **P-3**, **P-3-M1(82)-COOH(18)**, **P-3-M2(80)-COOH(20)**, **P-5** and **P-5-M1(86)-COOH(14)**.

Table 2-6. TGA data for triblock copolymers, including temperature where 3% weight loss was measured and the final weight percentage at 800 °C.

Polymer	Temperature where 3% weight loss measured (°C)	Final weight % at 800 °C
PS-*b*-PMVS-*b*-PS	413	8
P-3	266	16
P-3-COOMe	292	15
P*-3(AIBN)	247	13
P*-3(AIBN)-COOMe	300	19
P-5	273	7
P-3-M1(82)-COOH(18)	250	10
P-3-M2(80)-COOH(20)	206	36
P-5-M1(86)-COOH(14)	236	17
P-3-M1(65)-COOH(35)	261	8
P-3-M1(65)-COOMe(35)	265	18
P*-3(AIBN)-M1-COOMe	234	17

To ensure that no thermal degradation occurred during DSC measurements, cyclic experiments were carried out between -50 and 150 °C. Measurements were repeated three times, with the first cycle expected to remove the thermal history of the sample, and the subsequent cycles used for measurement of the T_g and T_{iso}. Values for the T_g of the PMVS block and the T_{iso} (where appropriate) are listed in Table 2-7 for all stages of the LCE synthesis. Using this data, it was possible to identify the effect of varying the number of alkyl units in the linking group and of the presence of hydrogen bonding on the thermal properties of the LCEs.

Table 2-7. Summary of thermal transitions by DSC.

Polymer	T_g (PMVS) (°C)	T_{iso} (°C)
PS-*b*-PMVS-*b*-PS	< -50	N/A
P-3	-24	N/A
P-3-COOMe	< -50	N/A
P*-3(AIBN)	-38	N/A
P*-3(AIBN)-COOMe	< -50	N/A
P-5	-35	N/A
P-3-M1(82)-COOH(18)	20	118
P-3-M2(80)-COOH(20)	45	> 200
P-5-M1(86)-COOH(14)	13	92
P-3-M1(65)-COOH(35)	16	99
P-3-M1(65)-COOMe(35)	3	Not detected
P*-3(AIBN)-M1-COOMe	-18	Not detected
PMVS-M1(84)-COOH(16)	23	129

2.2.6.1. Effect of Linking Group

The addition of the carboxylic acid-terminated thiols to the PMVS block was expected to raise the T_g, and this was confirmed by comparison of the DSC results for the **PS-*b*-PMVS-*b*-PS** triblock copolymer with both **P-3** and **P-5** (Figure 2-22). For the triblock copolymer the only transition that was apparent within the temperature range of the experiment was the T_g for the PS block at 98 °C, which was expected as the T_g of unfunctionalised PMVS has been measured at -110 °C,[26] outside the range of the instrument used here. On addition of the linking groups a second T_g was visible at -24 °C for **P-3** and -35 °C for **P-5,** which can be attributed to the functionalised PMVS block.

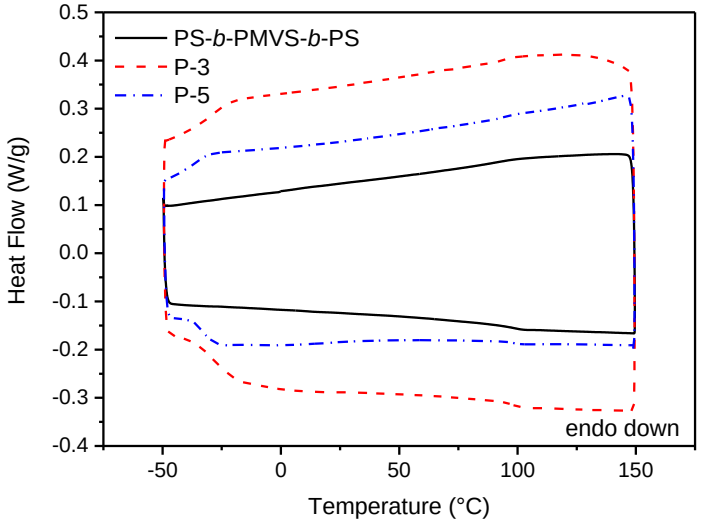

Figure 2-22. DSC results collected on the second cycle for the **PS-*b*-PMVS-*b*-PS** triblock copolymer, **P-3** and **P-5** on both heating (lower) and cooling (upper). Curves scaled in y-axis for clarity.

The effect of increasing the number of alkyl units in the linking group can be identified by first comparing **P-3** with **P-5.** The lower T_g for **P-5** compared with **P-3** suggests that the increased flexibility of the linking group aides the decoupling of the motion of the polymer chain from the mesogen, and in doing so reduces the energetic barrier to a more mobile state. This trend has been described for a variety of side-chain liquid crystal polymers, where a decrease in T_g was measured for increasing number of alkyl units in the linking group due to a plasticising effect.[27–29] This effect outweighed that of increasing the molecular weight of the linking group, which would be expected to raise the T_g, and can be confirmed by comparing the DSC results for **P-3-M1(82)-COOH(18)** and **P-5-M1(86)-COOH(14)** as given in Figure 2-23. With the mesogen attached the polymer is capable of forming a liquid crystal mesophase, and so a peak for the T_{iso} was seen on both heating and cooling in addition to the T_g for the PMVS block. This first order transition dominated the T_g for the PS block in the DSC curve, which is a typical result for a liquid crystal polymer.[30] On moving from **P-3-M1(82)-COOH(18)** to **P-5-M1(86)-COOH(14)** there was a decrease in the T_g of 8 °C and in the T_{iso} of 26 °C. Considering both polymers have a similar loading of mesogen, this difference can therefore be attributed to the increased alkyl chain length in the linking group, and the subsequent plasticising effect. In both cases the T_g of the functionalised PMVS block was below room temperature and the T_{iso} around 100 °C, making these promising candidates for further investigation as room temperature actuators.

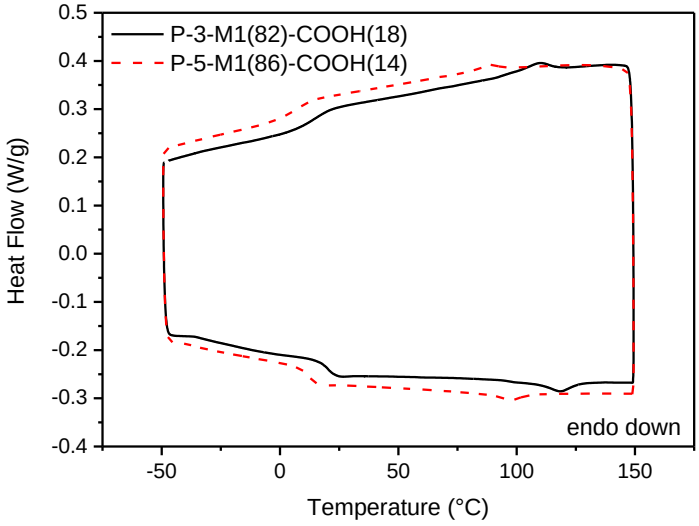

Figure 2-23. DSC results collected on the second cycle for **P-3-M1(82)-COOH(18)** and **P-5-M1(86)-COOH(14)** on both heating (lower) and cooling (upper).

2.2.6.2. Effect of Ester/Amide Linkage

Through the choice of mesogen introduced during the attachment step it was possible to form either an ester (**M1**) or amide bond (**M2**) with the linking group. The ability of the amide to form hydrogen bonds was expected to increase the temperature of the thermal transitions of the polymer, and its effect was clearly evident on comparison of the DSC results for **P-3-M1(82)-COOH(18)** and **P-3-M2(80)-COOH(20)** (Figure 2-24). The T_g for the PMVS block was considerably higher for **P-3-M2(80)-COOH(20)**, occurring at 45 °C compared with 20 °C for **P-3-M1(82)-COOH(18)**. This suggests that the hydrogen bonding from the amide groups has a significant effect on the final properties of the polymer. No T_{iso} was detected for **P-3-M2(80)-COOH(20)** in the temperature range measured, which was increased to 200 °C for this sample, indicating that it occurred outside the range of thermal stability for the polymer. This, combined with the relatively high T_g of the PMVS block, indicates that the LCEs functionalised with **M2** are not suitable for use as room temperature actuators.

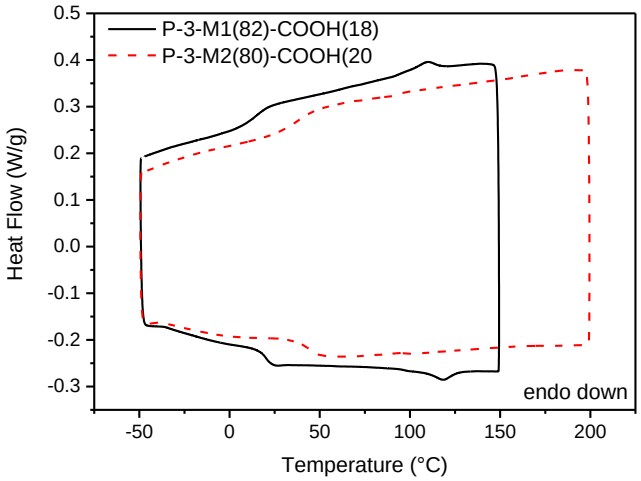

Figure 2-24. DSC results collected on the second cycle for **P-3-M1(82)-COOH(18)** and **P-3-M2(80)-COOH(20)** on both heating (lower) and cooling (upper).

2.2.6.3. Effect of Converting Carboxylic Acid to Methyl Ester

The significant influence of the carboxylic acid groups on the T_g of the PMVS block and the T_{iso} was further confirmed by measurements on **P-3-COOMe** and **P*-3(AIBN)-COOMe**. For these polymers no T_g was detected for the PMVS block (Figure 2-25), suggesting that on removing the hydrogen bonding capability the T_g was reduced to a temperature below -50 °C.

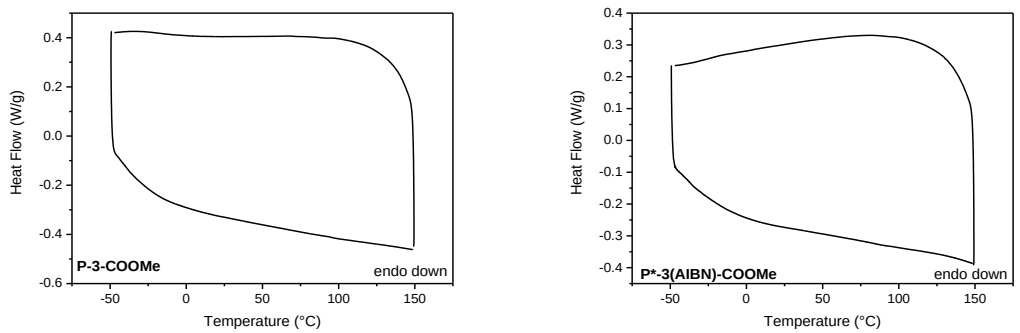

Figure 2-25. DSC results collected on the second cycle for **P-3-COOMe** and **P*-3(AIBN)-COOMe** on both heating (lower) and cooling (upper).

The effect of converting carboxylic acid groups to methyl esters can also be seen when comparing the results for **P-3-M1(65)-COOH(35)** with **P-3-M1(65)-COOMe(35)** (Figure 2-26). In this case, the modification resulted in a decrease in the T_g from 16 to 3 °C. Surprisingly, a second difference was observed in that no T_{iso} was detected between -50 and 150 °C for the methyl ester polymer**.** It is expected that by removing hydrogen bonding the temperature of this transition would be lowered from the value of 99 °C measured for **P-3-M1(65)-COOH(35)** due to the reduction in interaction between side chains in the PMVS block, and so should be comfortably found within the temperature range of the experiment. However, the disappearance of this peak suggests that no nematic mesophase was formed in the as-prepared polymer. It may be that the significantly reduced T_g of the PMVS block resulted in a structure where the polymer chains were too disordered and mobile to maintain a well-ordered and aligned nematic mesophase, resulting in the apparently isotropic behaviour. This will be discussed further in Chapter 4.

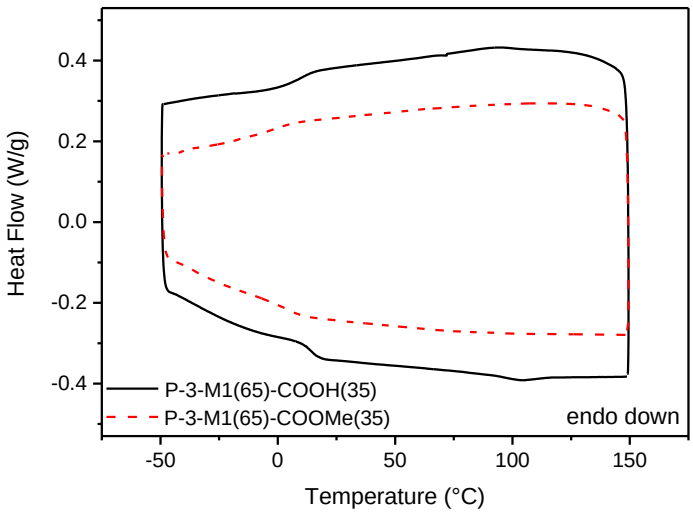

Figure 2-26. DSC results collected on the second cycle for **P-3-M1(65)-COOH(35)** and **P-3-M1(65)-COOMe(35)** on both heating (lower) and cooling (upper).

The theory that the low T_g of the PMVS block prevents the formation of an ordered mesophase is supported by the DSC results for **P*-3(AIBN)-M1-COOMe**, which again demonstrated a low T_g of -18 °C and no T_{iso} in the temperature range of the experiment. However, in this case it was not possible to isolate a pure sample of **P*-3(AIBN)-M1-COOH** in order to make a comparison.

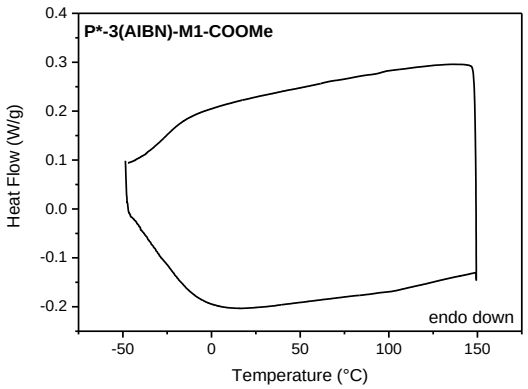

Figure 2-27. DSC results collected on the second cycle for **P*-3(AIBN)-M1-COOMe** on both heating (lower) and cooling (upper).

2.2.6.4. PMVS Homopolymer

P-3-M1(82)-COOH(18) was shown to have a T_g of 15 °C and a T_{iso} of 99 °C, with both peaks apparent on both heating and cooling cycles (Figure 2-28). These are comparable with the values obtained for the PMVS blocks in **P-3-M1(65)-COOH(35)** and **P-3-M1(82)-COOH(18)**, and so confirms that the composition of the homopolymer is appropriate for comparison of melt properties with the triblock copolymers.

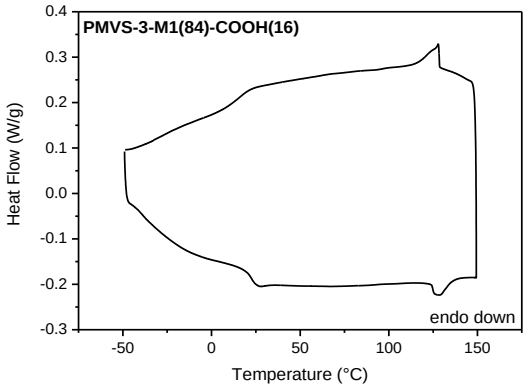

Figure 2-28. DSC results collected on the second cycle for **PMVS-M1(84)-COOH(16)** on both heating (lower) and cooling (upper).

2.2.6.5. Summary of Thermal Analysis

For application as a room temperature photoactuator, it is necessary that the LCE has a T_{iso} around 100 °C, and that the PMVS block has a T_g close to room temperature. By these standards, the best suited LCEs are the ester-linked materials **P-3-M1(82)-COOH(18)**, **P-3-M1(65)-COOH(35)** and **P-5-M1(80)-COOH(20)**. For synthetic reasons, the polymers based on **P-3** are preferable as the linking group is available commercially and attachment of the mesogen to the linking group proceeded with a higher yield than for **P-5**. For this reason, **P-5-M2(80)-COOH(20)** will not be considered further, despite having transition temperatures in a useful range. To confirm that attachment of **M1** to **P-3** resulted in a responsive LCE, a test was carried out to measure its response to UV irradiation at room temperature.

2.2.7. UV-Response Test

P-3-M1(82)-COOH(18) is capable of room temperature actuation due to the presence of the azobenzene group in the mesogen which switches between the linear *trans* conformation and bent *cis* conformation on irradiation with UV light of wavelength 365 nm. This isomerisation is reversed when exposed to visible light or if allowed to thermally equilibrate, and as the PS domains remain glassy the microphase segregation maintains the induced alignment of the polymer backbone.

To identify if the polymer was UV-responsive, a stretched film of **P-3-M1(82)-COOH(18)** was prepared by casting from toluene and deforming under tension whilst heated above the T_{iso}. This method had previously been shown to result in sufficient alignment of the LC component for reversible actuation to occur.[10] The film was adhered between two end tabs in a single-fibre tensile test machine and held under tension to minimise any wrinkling that would contribute to the change in length (Figure 2-29). A UV lamp was fixed approximately 3 cm above the polymer film and a visible light source placed adjacent to the UV lamp before covering the entire assembly with an opaque box.

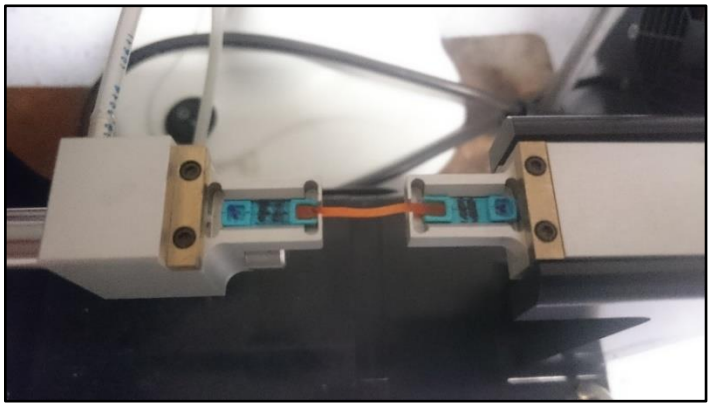

Figure 2-29. Experimental setup for UV-response test. The orange polymer film was adhered between the two green end tabs and loaded into the tensile test machine.

The test machine was set to maintain a constant tensile stress of 25.7 kPa on the film, and so on switching between UV and visible light sources it was possible to measure the change in force required by the test machine to counter any shape change. UV-on time was limited to one minute to prevent heating of the sample which could cause softening of the PS domains and affect the results. The resulting force-time curve is shown in Figure 2-30, where shaded regions represent the one-minute intervals where the UV lamp was switched on and unshaded regions represent the two-minute intervals where the visible light source was switched on. The large spikes in the force between 0-30 seconds are a result of the test machine fully extending the film after loading the sample and reaching equilibrium.

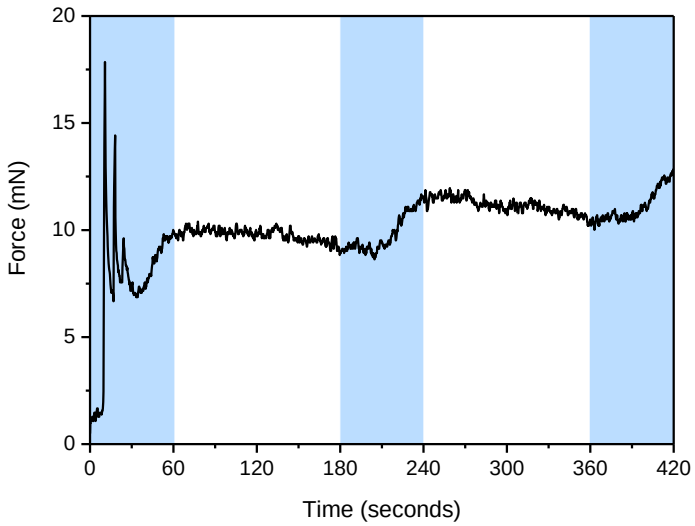

Figure 2-30. Force-time curve for aligned **P-3-M1(82)-COOH(18)** during photocontraction test. The shaded regions indicate the time when the UV lamp was on and unshaded regions indicate when the visible light was on. After the initial extension a clear increase in force of around 3 mN was measured on turning on UV. A small relaxation was seen in the period where UV was off.

From Figure 2-30 it was apparent that there was a clear increase in force measured during UV-on time, after an initial delay. This delay may be due to the lamp taking time to reach its full intensity, where initially it was not able to penetrate the relatively thick film and trigger a significant degree of isomerisation. The increase in force of approximately 3 mN suggests that a small contraction of the film had occurred during the UV-on period as the test machine increased the force required to maintain a constant tensile stress on the sample. It is more likely that this effect was caused by isomerisation of the mesogen rather than heating of the film as softening of the PS domains would lead to the polymer being easier to deform, and so require less force to maintain a constant tensile stress. After turning off the UV light and approximately 60 seconds of exposure to the visible light source the force started to decrease, but full relaxation to the equilibrium state was not seen. This may be due to the relatively low intensity of the visible light source, which may not have been sufficient for the thickness of the polymer film, or the limited time frame available for relaxation to occur. The relaxation trends towards smaller values of the force, and so leaving the experiment for longer may result in complete recovery of the structure.

The force of 3 mN acting against the contraction indicates that the shape change was small, and it was not possible to measure the strain in order to compare with other LCE actuators. However, it was demonstrated that the polymer **P-3-M1(82)-COOH(18)** was responsive to UV irradiation at room temperature, and so appropriate for further investigation of its properties with respect to actuation and processing.

2.3. Conclusions

A two-step method for functionalising a PS-*b*-PMVS-*b*-PS triblock copolymer backbone with a photoresponsive mesogen was developed, where the backbone can be synthesised using conventional living anionic polymerisation to give excellent control over the M_n and so give the desired physical properties. Post-polymerisation modification was then carried out by first attaching a linking group using a thiol-ene click reaction, before coupling the mesogen through a mild ester or amide forming reaction to introduce stimuli responsive properties. This method allowed for variation in the number of alkyl units in the linking group as well as the bond type with the mesogen. Polymers based on **P-5**, containing the longer linking group, were isolated in lower yields than those based on **P-3**. This, combined with the fact that 5-mercaptopentanoic acid is not available commercially, made them unsuitable for meeting the target of increasing the yield of polymer for gram-scale processing.

Modifications of the linking group did not appear to have a significant effect on the thermal stability of the polymers, with all variations starting to show degradation around 200 °C by TGA. It was, however, shown by DSC to modify both the T_g and T_{iso} of the resulting LCEs, with the increased hydrogen bonding from amide bonds demonstrated to result in a significant increase in both transition temperatures. Conversion of residual carboxylic acid groups to methyl esters acted to reduce the T_g of the PMVS block, but also resulted in LCEs where no isotropic transition was observed, suggesting that the presence of some hydrogen bonding is beneficial for the responsive properties of the final LCEs. The structure of the LCE therefore has a direct influence on its suitability for use as a room temperature actuator, with esters giving superior results to amides.

A film of **P-3-M1(82)-COOH(18)** was aligned manually, and shown to contract in responsive to UV light, with a force of 3.3 mN required to maintain a constant tensile stress of 25.7 kPa on the film. This result confirms that the developed synthetic route was suitable for obtaining a responsive LCE, with yields at each stage of the mesogen attachment greater than 80%. This represents a significant improvement on the limiting value of 30% reported previously.[14]

2.4. Experimental

2.4.1. Materials and Methods

Hexamethylcyclotrisiloxane (D_3) and 1,3,5-trimethylcyclotrisiloxane (V_3) were purchased from abcr, 4-butoxyaniline (97%) was purchased from Santa Cruz Biotechnology, 3-aminophenol (98%) and thiourea (99%) were purchased from Acros and di-*tert*-butyl dicarbonate (97+%) was purchased from Alfa Aesar. All other reagents were purchased from Sigma.

Styrene, V_3, dichloromethylvinylsilane and chloro(dimethyl)vinylsilane were dried with CaH_2 under nitrogen overnight, and then vacuum distilled. D_3 was dissolved in hexane and dried with CaH_2 under nitrogen overnight, before recrystallisation at -65 °C. The obtained crystals were further purified by sublimation. Tetrahydrofuran (THF) for anionic polymerisation and thiol-ene reactions was purified by distillation from sodium/benzophenone. THF and CH_2Cl_2 used in mesogen coupling reactions were purified using a Grubbs-type solvent purification system. 2,2′-azobis(2-methylpropionitrile) (AIBN) was recrystallised from methanol prior to use. All other reagents were used as received.

Photoirradiation experiments were carried out with a 125W mercury lamp (Photochemical Reactors Ltd.) in an ethylene glycol/water bath at room temperature.

^{1}H NMR spectra were recorded using a Jeol Eclipse 400 MHz or Varian VNMR 400 MHz spectrometer. ^{13}C NMR spectra were recorded using a Varian VNMR 400 MHz or Bruker Avance III HD 500 MHz Cryo spectrometer.

Molecular weights of homopolymers and polydispersity index (PDI) of all polymers were obtained by gel permeation chromatography (GPC) using a Viscotek VE 2001 Triple-Detector GPC equipped with an automatic sampler, a pump, an injector, an inline degasser, a column oven (30 °C), styrene/divinylbenzene columns, a VE 3580 refractometer, a four-capillary differential viscometer and a 90° angle laser and low angle laser (7°) light scattering detector (VE 3210 & VE 270). THF, stabilised with 0.025% butylated hydroxytoluene (Fisher), was used as the eluent at a flow rate of 1.0 mL min−1. Conventional calibration GPC was performed on a Viscotek RI Max, using a flow rate of 1.0 mL min^{-1} of THF with 0.1 wt% [*n*-Bu_4N]Br and calibrated monodisperse polystyrene standards from Aldrich. Molecular weights of block copolymers were calculated from the absolute molecular weight of the first block, as determined by multi-detection GPC, and the block ratio as determined by ^{1}H NMR spectroscopy.

Accurate mass of **M2** and its intermediates was obtained by electrospray ionisation mass spectrometry using a Bruker Daltronics MicrO TOF II spectrometer.

Differential Scanning Calorimetry (DSC) experiments were carried out with a TA Instruments Q100. Samples were weighed into an aluminium pan and cycled three times between -50 and 150 °C under a nitrogen atmosphere, with measurements taken on both the heating and cooling cycles using a heating/cooling rate of 10 °C per minute.

Thermogravimetric analysis (TGA) was carried out using a TA Q500 under a nitrogen atmosphere. Samples were heated from room temperature to 800 °C with a ramp rate of 10 °C per minute.

Dynamic Light Scattering (DLS) experiments were carried out using a Malvern Zetasizer Nano. A 2 mg ml^{-1} solution of the polymer was made in THF, and 10 runs of 8 measurements each were made at 25 °C using a glass cuvette.

2.4.2. Synthetic Procedures

2.4.2.1. Mesogen Synthesis

M1: The synthetic route to **M1** was modified from the literature.[13] A solvent mixture of poly(ethylene glycol), average mol. wt. 200 g mol^{-1} (PEG 200)/1,4-dioxane/deionised water (90/45/15 mL) was cooled in an ice bath before addition of 5.2 mL HCl (37%) and 5.0 g (0.0303 mol) of 4-butoxyaniline. A solution of 2.30 g (0.0333 mol) $NaNO_2$ (98%) in 10 mL water was then added dropwise and the solution stirred at 5 °C for 1 hour.

A further 150 mL of the PEG 200/1,4-dioxane/deionised water solvent was prepared and to this was added 10.0 g (0.0909 mol) of resorcinol (99%) and 1.33 g (0.0333 mol) of NaOH. The second solution was combined with the first and stirred for a further 15 minutes at 5 °C before allowing to reach room temperature. 350 mL deionised water was then added, and the solution made slightly acidic by the dropwise addition of HCl (37%), which led to precipitation of a brown solid. This solid was collected by filtration and washed with deionised water, before drying under vacuum with P_2O_5 for 16 hours to yield **I-M1** (7.13 g, 0.025 mol, 82%).

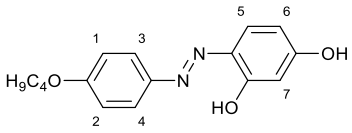

Figure 2-31. Structure of **I-M1** with labelling used in ^{1}H NMR spectroscopy assignments.

I-M1: ^{1}H NMR (400 MHz, chloroform-*d*) δ 13.68 (s, 1H, O*H*), 7.74 (dd, *J* = 18.6, 8.8 Hz, 3H, Ar 3+4+5), 6.98 (d, *J* = 8.9 Hz, 2H, Ar 1+2), 6.52 (dd, *J* = 8.7, 2.5 Hz, 1H, Ar 6), 6.41 (d, *J* = 2.5 Hz, 1H, Ar 7), 4.03 (t, *J* = 6.5 Hz, 2H, OC*H*$_2$), 1.80 (q overlapping, *J* = 14.6, 6.5 Hz, 2H, *n*-butyl), 1.51 (h overlapping, *J* = 7.5 Hz, 2H, *n*-butyl), 0.99 (t, *J* = 7.4 Hz, 3H, *n*-butyl).

I-M1 (6.90 g, 0.0241 mol) was dissolved in a Schlenk flask with 165 mL of dry CH_2Cl_2 under nitrogen, to which 5.97 g (0.0289 mol) of *N,N'*-dicyclohexylcarbodiimide (DCC, 99%), 0.43 g (0.0029 mol) of 4-pyrrolidinopyridine (98%) and 4.68 g (0.0241 mol) of 4-butoxybenzoic acid (98%) were added. The flask was sealed and left to stir at room temperature for 36 hours. The solution was washed with 200 mL water, 200 mL 5% v/v acetic acid and a further 200 mL water before separating the organic phase and drying with Na_2SO_4. The solvent was then removed by rotary evaporation and the product recrystallised from toluene/ethanol. The recrystallisation was repeated once more and the product **M1** collected by filtration as an orange powder (7.15 g, 0.0155 mol, 64%).

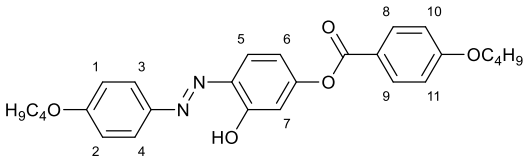

Figure 2-32. Structure of **M1** with labelling used in ^{1}H NMR spectroscopy assignments.

M1: ^{1}H NMR (400 MHz, chloroform-*d*) δ 13.26 (s, 1H, O*H*), 8.19 – 8.05 (m, 2H, Ar 8+9), 7.91 (d, *J* = 8.6 Hz, 1H, Ar 5), 7.87 – 7.79 (m, 2H, Ar 3+4), 7.05 – 6.95 (m, 4H, Ar 1+2+10+11), 6.93 (dd, *J* = 8.6, 2.4 Hz, 1H, Ar 6), 6.88 (d, *J* = 2.4 Hz, 1H, Ar 7), 4.06 (td, *J* = 6.5, 2.5 Hz, 4H, OC*H*$_2$), 1.81 (p, *J* = 14.4, 6.6 Hz, 4H, *n*-butyl), 1.60 – 1.45 (m overlapping, 4H, *n*-butyl), 1.00 (t, *J* = 7.4 Hz, 6H, *n*-butyl).

M1-Allyl: To add an allyl group to **M1**, 0.75 g (0.0016 mol) was added to a round bottomed flask and dissolved in 15 mL of acetone. To this was added 0.45 g (0.0033 mol) of K_2CO_3 and 0.42 mL (0.0049 mol) of allyl bromide (97%). The flask was equipped with a condenser and the solution heated to reflux for 24 hours, when the solution was allowed to cool to room temperature before filtering off insoluble impurities and removal of the solvent. The product was recrystallised from a mixture of toluene and ethanol and dried at 40 °C under vacuum to yield 0.553 g (68%) of orange crystals.

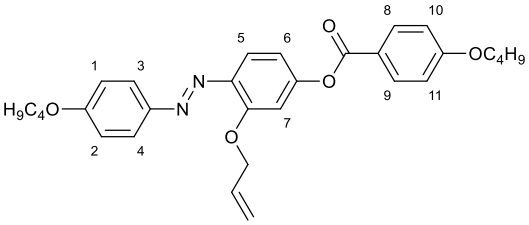

Figure 2-33. Structure of **M1-Allyl** with labelling used in ^{1}H NMR spectroscopy assignments.

M1-Allyl: ^{1}H NMR (400 MHz, Chloroform-*d*) δ 8.21 – 8.07 (m, 2H, Ar 8+9), 7.96 – 7.86 (m, 2H, Ar 3+4), 7.74 (d, *J* = 8.8 Hz, 1H, Ar 5), 7.05 – 6.93 (m, 5H, Ar 1+2+10+11+6), 6.88 (dd, *J* = 8.8, 2.3 Hz, 1H, Ar 7), 6.14 (ddd, *J* = 17.1, 10.4, 5.2 Hz, 1H, Vinyl C*H*), 5.51 (dd, *J* = 17.3, 1.5 Hz, 1H, Vinyl C*H*$_2$), 5.33 (dd, *J* = 10.5, 1.4 Hz, 1H, Vinyl C*H*$_2$), 4.90 – 4.66 (m, 2H, CH-C*H*$_2$), 4.05 (q, *J* = 6.5 Hz, 4H, OC*H*$_2$), 1.81 (ddq, *J* = 12.2, 6.5, 3.4, 2.9 Hz, 4H, *n*-butyl), 1.60 – 1.42 (m, 4H, *n*-butyl), 1.00 (td, *J* = 7.4, 1.1 Hz, 6H, *n*-butyl).

M1-Thiol: 0.5 g (0.001 mol) of **M1-Allyl** was dissolved in 25 mL dry toluene with 1.2 mL (0.010 mol) 1,4-butanedithiol (97%) and 0.082 g (0.0005 mol) of AIBN. The solution was degassed by three freeze-pump-thaw cycles before heating at 70 °C for 5 hours. The solvent was removed and the residue was purified by silica gel column chromatography, first washing with a 1:9 mixture of ethyl acetate:hexane, before collecting the product which eluted with a 4:6 mixture of the same solvents. After removal of solvent, the viscous liquid was dried under vacuum and recrystallisation attempted from CH_2Cl_2 and cyclohexane. The product was obtained as a dark red, viscous liquid, which from ^{1}H NMR spectroscopy appears to have undergone cleavage of the azo-group.

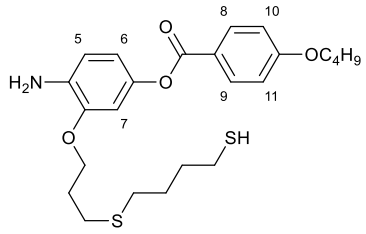

Figure 2-34. Structure of **M1-Thiol** with labelling used in ^{1}H NMR spectroscopy assignments.

M1-Thiol: ^{1}H NMR (400 MHz, Chloroform-*d*) δ 8.10 (d, *J* = 9.0 Hz, 2H, aromatic 8+9), 6.95 (d, *J* = 9.0 Hz, 2H, aromatic 10+11), 6.64 (dd, *J* = 13.7, 1.5 Hz, 3H, aromatic 5+6+7), 4.10 – 3.82 (m, 4H, O*CH*$_2$), 3.55 – 3.41 (m, 2H, N*H*$_2$), 2.64 – 2.42 (m, 2H), 1.91 – 1.60 (m, 8H, alkyl), 1.51 (dq, *J* = 14.9, 7.5 Hz, 4H, alkyl), 1.10 – 0.85 (m, 5H, alkyl).

M2: An amine functionalised analogue of **M1**, namely **M2**, was synthesised using a modified literature method.[13] 3-aminophenol was first protected by dissolving 11.00 g (0.101 mol) in 210 mL THF with 26.45 g (0.121 mol) of di-*tert*-butyl dicarbonate. The solution was heated at reflux for 15 hours before removal of the solvent under vacuum to give a yellow oil. The oil was diluted with ethyl acetate and washed three times with 200 mL deionised water, before separating the organic phase and drying with Na_2SO_4. The solid product was recrystallised from hexane by the addition of 25 mL CH_2Cl_2 and storing at -20 °C for 16 hours. After filtration and washing with cold hexane the product was recrystallised once more to yield white crystals (17.00 g, 0.081 mol, 80%).

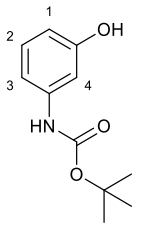

Figure 2-35. Structure of **3-aminophenol-Boc** with labelling used in ^{1}H NMR spectroscopy assignments.

3-aminophenol-Boc: ^{1}H NMR (400 MHz, acetone-d_6) δ 8.27 (s, 1H, N*H*), 8.21 (s, 1H, O*H*), 7.20 (s, 1H, Ar 4), 7.06 (t, *J* = 8.0 Hz, 1H, Ar 2), 6.96 (d, *J* = 7.4 Hz, 1H, Ar 3), 6.47 (dd, *J* = 8.0, 2.3 Hz, 1H, Ar 1), 1.47 (s, 9H, butyl).

A solvent mixture of 150 mL of PEG 200/1,4-dioxane/deionised water (90/45/15 mL) was cooled in an ice bath before addition of 5.2 mL (0.0607 mol) HCl (37%) and 5.0 g (0.0303 mol) of 4-butoxyaniline. A solution of 2.30 g (0.0333 mol) $NaNO_2$ in 10 mL of water was then added dropwise and the solution stirred at 5 °C for 1 hour.

A further 150 mL of the PEG 200/1,4-dioxane/deionised water solvent was prepared and to this was added 17.0 g (0.081 mol) of **3-aminophenol-Boc** and 1.87 g (0.0333 mol) of KOH. The second solution was combined with the first and stirred for a further 15 minutes before being allowed to reach room temperature. Next, 350 mL deionised water was added, and the solution made slightly acidic by the dropwise addition of HCl (37%), which led to precipitation of a brown solid. This was collected by filtration and washed with deionised water, then dried under vacuum with P_2O_5 for 16 hours to give the product **I-M2-Boc** as a dark yellow powder (10.12 g, 0.0262 mol, 87%).

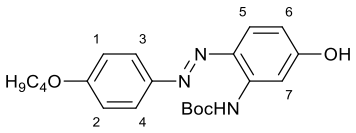

Figure 2-36. Structure of **I-M2-Boc** with labelling used in ^{1}H NMR spectroscopy assignments.

I-M2-Boc: ^{1}H NMR (400 MHz, chloroform-*d*) δ 9.70 (s, 1H, N*H*), 7.88 (d, *J* = 2.7 Hz, 1H, Ar 7), 7.82 – 7.71 (m, 3H, Ar 3+4+5), 7.02 – 6.95 (m, 2H, Ar 1+2), 6.57 (dd, *J* = 8.8, 2.7 Hz, 1H, Ar 6), 6.32 (s, 1H, O*H*), 4.03 (t, *J* = 6.5 Hz, 2H, O*CH*$_2$), 1.89 – 1.68 (m overlapping, 2H, *n*-butyl), 1.59 – 1.44 (m overlapping, 11H, *n*-butyl + Boc butyl), 0.98 (t, *J* = 7.4 Hz, 3H).

$^{13}C\{^{1}H\}$ NMR (101 MHz, chloroform-*d*) δ 161.20, 159.36, 152.88, 146.49, 137.56, 133.46, 124.01, 123.78, 114.80, 109.95, 104.57, 80.99, 68.06, 31.22, 28.35, 19.21, 13.83.

Accurate mass ESI: 408.1898 g mol^{-1} $(M^{+}Na)^{+}$, calculated 408.1899 g mol^{-1}.

10.12 g (0.0262 mol) of **I-M2-Boc** was dissolved in a Schlenk flask with 200 mL dry CH_2Cl_2 under nitrogen, and 6.50 g (0.0315 mol) of DCC, 0.47 g (0.0032 mol) of 4-pyrrolidinopyridine and 5.10 g (0.0262 mol) of 4-butoxybenzoic acid were added. The flask was sealed and left to stir at room temperature for 36 hours. The solution was washed with 200 mL water, 200 mL 5% v/v acetic acid and a further 200 mL water before drying the organic phase with Na_2SO_4. The solvent was then removed by rotary evaporation and the product recrystallised from toluene/ethanol. The recrystallisation was repeated once more and the product **M2-Boc** collected as a yellow powder by filtration (10.56 g, 0.0188 mol, 72%).

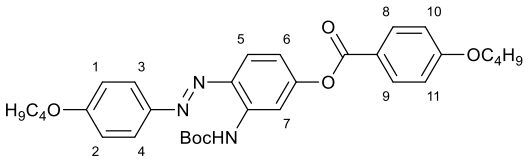

Figure 2-37. Structure of **M2-Boc** with labelling used in ^{1}H NMR spectroscopy assignments.

M2-Boc: ^{1}H NMR (400 MHz, chloroform-*d*) δ 9.39 (s, 1H, N*H*), 8.30 (d, *J* = 2.2 Hz, 1H, Ar 7), 8.13 (d, *J* = 8.9 Hz, 2H, Ar 10+11), 7.85 (dd, *J* = 8.9, 5.3 Hz, 3H, Ar 3+4+5), 7.02 (d, *J* = 9.0 Hz, 2H, Ar 1+2), 6.96 (dd, *J* = 8.8, 2.9 Hz, 3H, Ar 6+8+9), 4.06 (td, *J* = 6.5, 2.6 Hz, 4H, OC*H*$_2$), 1.89 – 1.74 (m, 4H, *n*-butyl), 1.59 – 1.45 (m overlapping, 13H, *n*-butyl + Boc butyl), 1.00 (t, *J* = 7.4 Hz, 6H, *n*-butyl).

$^{13}C\{^{1}H\}$ NMR (101 MHz, chloroform-*d*) δ 164.58, 163.58, 160.93, 153.51, 146.95, 143.91, 135.11, 132.29, 127.98, 123.82, 121.42, 114.70, 114.29, 111.15, 109.26, 77.31, 76.99, 68.00, 31.25, 31.12, 19.22, 19.18, 13.84, 13.81.

Accurate mass ESI: 562.2912 g mol^{-1} $(M^{+}H)^{+}$, calculated 562.2917 g mol^{-1}.

To remove the protecting group, 4.0 g (0.00712 mol) of **M2-Boc** was dissolved in 20 mL CH_2Cl_2 and then cooled in an ice bath, before dropwise addition of 10 mL trifluoroacetic acid (TFA). The solution was allowed to reach room temperature whilst stirring for 1 hour, before dilution with chloroform and removal of solvent and TFA under vacuum. The remaining solid was dissolved in CH_2Cl_2 and washed twice with a saturated aqueous $NaHCO_3$ solution, and once with deionised

water, then dried with Na_2SO_4. The product **M2** was recrystallised from toluene/ethanol and dried under vacuum at 40 °C to give a yellow powder (2.50 g, 0.0054 mol, 77%).

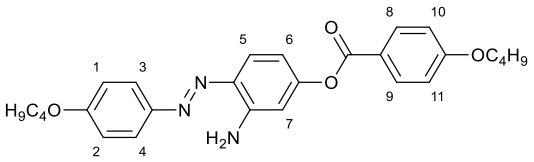

Figure 2-38. Structure of **M2-Boc** with labelling used in ^{1}H NMR spectroscopy assignments.

M2: ^{1}H NMR (400 MHz, chloroform-*d*) δ 8.13 (d, *J* = 8.8 Hz, 2H, Ar 10+11), 7.81 (dd, *J* = 8.8, 4.9 Hz, 3H, Ar 3+4+5), 6.98 (dd, *J* = 8.9, 4.5 Hz, 4H, Ar 6+7+8+9), 6.65 (d, *J* = 8.3 Hz, 2H, Ar 1+2), 5.88 (s, 2H, N*H*$_2$), 4.05 (q, *J* = 6.3 Hz, 4H, OC*H*$_2$), 1.89 – 1.74 (m, 4H, *n*-butyl), 1.62 – 1.45 (m overlapping, 4H, *n*-butyl), 1.00 (t, *J* = 7.4 Hz, 6H, *n*-butyl).

^{13}C{^{1}H} NMR (101 MHz, chloroform-*d*) δ 164.54, 163.56, 161.83, 153.82, 152.40, 146.56, 137.37, 136.48, 132.34, 124.58, 121.40, 121.31, 115.73, 114.84, 114.25, 111.84, 80.90, 77.31, 76.99, 68.12, 67.98, 31.20, 31.14, 28.32, 19.21, 19.19, 13.83.

Accurate mass ESI: 462.23873 g mol^{-1} $(M^+H)^+$, calculated 462.2393 g mol^{-1}.

2.4.2.2. Polymer Backbone Synthesis

PS-*b*-PMVS-*b*-PS: The polystyrene-*b*-poly(methylvinylsiloxane)-*b*-polystyrene (PS-*b*-PMVS-*b*-PS) triblock copolymer was synthesised using living anionic polymerisation by a method adapted from the literature.[10] In this procedure a small amount of hexamethylcyclotrisiloxane (D_3) was added after the styrene polymerisation step and before the 1,3,5-trivinyl-1,3,5-trimethylcyclotrisiloxane (V_3) monomer. All glassware was dried at 200 °C prior to use, and all manipulations carried out under a nitrogen atmosphere in a glovebox, with the exception of the final termination step with dichloromethylvinylsilane which was carried out under nitrogen on a Schlenk line. Aliquots were taken before the addition of D_3, V_3 and the termination step for analysis by GPC and NMR spectroscopy.

A round bottom flask was equipped with a magnetic stirrer bar and 4.50 g (0.043 mol) styrene was added with 150 mL of dry THF. The solution was stirred in a cold well immersed in a dry ice/ethanol bath. The polymerisation was initiated by the addition of 0.25 mL (0.00035 mol) *sec*-BuLi (1.4M in hexanes), which resulted in the colourless solution becoming orange. After 1 hour of stirring, 0.11 g (0.0005 mol) of D_3 in 1.1 mL dry THF was added and after a further 10 minutes

the flask was removed from the cold well and allowed to reach room temperature over 35 minutes, resulting in fading of the orange colouration. On the addition of 4.77 g (0.0185 mol) of V_3 the solution became colourless and was stirred for a further 2 hours before transferring to a Schlenk tube which was sealed and removed from the glove box. The polymerisation was terminated under nitrogen with 17.4 μL (0.00013 mol) of dichloromethylvinylsilane and left to stir for 16 hours. The solution was concentrated by removal of THF under vacuum and the polymer precipitated into methanol. Two further precipitations were carried out before drying the product under vacuum at 40 °C to give a white powder (7.72 g).

Aliquot 1, PS: ^{1}H NMR (400 MHz, chloroform-*d*) δ 7.04 (s, 3H, Ar styrene), 6.56 (s, 2H, Ar styrene), 1.83 (s, 1H, C*H* styrene), 1.41 (s, 2 H, CH_2 styrene).

GPC Analysis: M_n = 13,776 g mol^{-1} (PDI = 2.25).

Aliquot 2, PS-*b*-PDMS: ^{1}H NMR (400 MHz, chloroform-*d*) δ 7.07 (s, 3H, Ar styrene), 6.56 (s, 2H, Ar styrene), 1.83 (s, 1H, C*H* styrene), 1.41 (s, 2H, CH_2 styrene), 0.13 (s, 6H, CH_3 PDMS).

GPC Analysis: M_n = 13,006 g mol^{-1} (PDI = 2.36). NMR Integration: M_n = 14,100 g mol^{-1}.

Aliquot 3, PS-*b*-PDMS-*b*-PMVS: ^{1}H NMR (400 MHz, chloroform-*d*) δ 7.08 (s, 3H, Ar styrene), 6.57 (s, 2H, Ar styrene), 5.75-6.03 (m, 3H, vinyl PMVS), 1.83 (s, 1H, C*H* styrene), 1.42 (s, 2H, CH_2 styrene), 0.18 (s, 3H, CH_3 PMVS), 0.07 (s, 6H, CH_3 PDMS).

GPC Analysis: M_n = 20,722 g mol^{-1} (PDI = 1.75). NMR Integration: M_n = 27,000 g mol^{-1}.

Aliquot 4, PS-*b*-PMVS-*b*-PS: ^{1}H NMR (400 MHz, chloroform-*d*) δ 7.07 (s, 3H, Ar styrene), 6.56 (s, 2H, Ar styrene), 5.75-6.02 (m, 3H, vinyl PMVS), 1.85 (s, 1H, C*H* styrene), 1.41 (s, 2H, CH_2 styrene), 0.14 (s, 3H, CH_3 PMVS), 0.06 (s, 6H, CH_3 PDMS).

^{13}C{^{1}H} NMR (126 MHz, chloroform-*d*) δ 136.73, 133.09, 127.96, 127.86, 127.42, 125.64, 40.43, 40.36, -0.57.

GPC Analysis: M_n = 25,565 g mol^{-1} (PDI = 1.90). NMR Integration: M_n = 50,000 g mol^{-1}.

PMVS: 0.021 g of D_3 (0.000094 mol) in 0.2 mL dry THF was added to a greaseless Schlenk tube, before the addition of 30 mL of dry THF. The polymerisation was initiated by the addition of 28.7 μL (0.000045 mol) of *n*-BuLi (1.6 M in hexanes) at room temperature. The solution was stirred for 3 hours before the addition of 1 g (0.0039 mol) of V_3. The reaction was stirred for a further 3 hours before termination with 0.06 mL (0.00045 mol) of dichloromethylvinylsilane, which was allowed

to stir for 16 hours. The solution was then concentrated, and the product obtained by precipitation from THF into methanol two times. The product **PMVS** was obtained as a viscous liquid (0.444 g).

PMVS: ^{1}H NMR (400 MHz, Chloroform-*d*) δ 6.07 – 5.69 (m, 3H, vinyl), 0.14 (s, 3H, C*H*$_3$ PMVS), 0.08 – 0.03 (m, 6H, C*H*$_3$ PDMS).

^{13}C{^{1}H} NMR (101 MHz, chloroform-*d*) δ 136.71, 133.07, -0.60.

GPC Analysis: M_n = 18,500 g mol^{-1} (PDI = 1.37).

2.4.2.3. Linking Group Attachment

Photoinitiated thiol-ene click reaction

P-3: A carboxylic acid terminated side chain was added to the vinyl group of PMVS using a UV-initiated thiol-ene click reaction (Figure 2-13). In a typical experiment, 0.50 g of **PS-*b*-PMVS-*b*-PS** (2.5 mmol vinyl) was added to 5 mL of dry THF in a greaseless Schlenk tube with the photoinitiator 2,2-dimethoxy-2-phenylacetophenone (DMPA, 99%). An excess of 3-mercaptopropionic acid (99%) (0.67 mL, 7.65 mmol) was added and the flask sealed under nitrogen. The tube was then fixed approximately 3 cm from the UV lamp and irradiated at room temperature for 2.5 hours. The polymer was precipitated three times from THF into hexane and dried at 40 °C under vacuum to give the product as a soft, white solid (0.66 g, 86%).

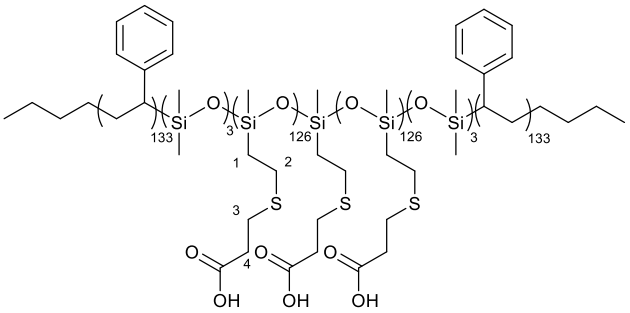

Figure 2-39. Structure of **P-3** with labelling used in ^{1}H NMR spectroscopy assignments.

P-3: ^{1}H NMR (400 MHz, acetone-d_6) δ = 7.2 (s, 3H, Ar styrene), 6.5 (s, 2H, Ar styrene), 2.75 (m, 6H, side chain 2+3+4), 1.95 (s, 1H, C*H* styrene), 1.60 (s, 2H, C*H*$_2$ styrene), 1.0 (t, *J* = 16.0, 8.2 Hz, 2H, side chain 1), 0.25 (s, 3H, *CH*$_3$ PMVS). Peak for methyl groups on PDMS not observed.

^{13}C{^{1}H} NMR (126 MHz, acetone-d_6) δ 172.99, 128.04, 127.67, 125.68, 40.55, 34.24, 26.58, 26.18, 18.21, -0.44.

GPC Analysis: M_n = 18,300 g mol^{-1} (PDI = 1.75). NMR Integration: M_n = 77,000 g mol^{-1}.

P-5: Using a procedure adapted from the literature,[31] 1.75 g (0.00987 mol) of 5-bromovaleric acid (97%) was added to 1.10 g (0.0145 mol) of thiourea in 20 mL ethanol and heated to reflux with stirring for 16 hours under nitrogen. The solution was allowed to cool, and the solvent removed by rotary evaporation, before addition of 20 mL of 7.5 M NaOH in deionised water. The solution was heated at 90 °C under nitrogen for 16 hours, and then allowed to cool to room temperature before cooling further in an ice bath. 2M H_2SO_4 was slowly added with stirring until a pH of around 1 was obtained. The product was extracted from the solution by washing twice with 150 mL CH_2Cl_2 and the organic phase dried using Na_2SO_4. The solution was filtered, and the solvent was removed to give the product as a pale-yellow oil. No further purification was carried out prior to the thiol-ene click reaction.

5-mercaptopentanoic acid: ^{1}H NMR (400 MHz, chloroform-*d*) δ 2.53 (q, *J* = 7.1 Hz, 2H, SH-C*H*$_2$), 2.36 (t, *J* = 7.2 Hz, 2H, C*H*$_2$-COOH), 1.80 – 1.57 (m, 4H, C*H*$_2$), 1.34 (t, *J* = 7.9 Hz, 1H, S*H*).

0.50 g of **PS-*b*-PMVS-*b*-PS** (2.5 mmol vinyl) was added to 5 mL of dry THF in a greaseless Schlenk tube with the photoinitiator DMPA. An excess of 5-mercaptopentanoic acid (0.70 mL, 5.7 mmol) was added and the flask sealed under nitrogen. The tube was then fixed approximately 3 cm from the UV lamp and irradiated at room temperature for 2.5 hours. The polymer was precipitated three times from THF into hexane, then dried at 40 °C under vacuum to give the product as a soft, white solid (0.77 g, 95%).

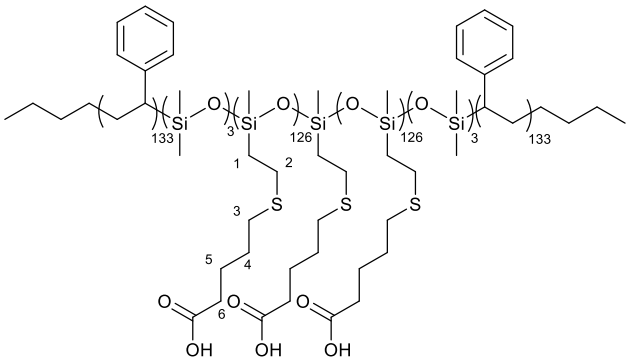

Figure 2-40. Structure of **P-5** with labelling used in ^{1}H NMR spectroscopy assignments.

P-5: ^{1}H NMR (400 MHz, acetone-d_6) δ 7.11 (s, 3H, Ar styrene) 6.68 (s, 2H, Ar styrene), 2.65 (dt, *J* = 25.7, 7.6 Hz, 4H, side chain 2+3), 2.36 (t, *J* = 7.1 Hz, 2H, side chain 6), 1.93 (s, 1H, C*H* styrene), 1.71 (ddt, *J* = 21.8, 15.4, 6.9 Hz, 4H, side chain 4+5), 1.01 (m, 2H, side chain 1), 0.27 (s, 3H, *CH*$_3$ PMVS). Peak for methyl groups on PDMS not observed.

$^{13}C\{^{1}H\}$ NMR (126 MHz, acetone-d_6) δ 174.56, 128.03, 127.62, 127.48, 125.71, 125.56, 40.49, 33.17, 31.30, 26.15, 24.17, 18.33, -0.38.

GPC Analysis: M_n = 15,628 g mol^{-1} (PDI = 1.79). NMR Integration: M_n = 84,000 g mol^{-1}.

PMVS-3: To add the linking group, 0.357 g (0.004 mol vinyl) of **PMVS** was dissolved in 4 mL of dry THF in a glovebox before addition of DMPA and 1.3 mL (0.0149 mol) of 3-mercaptopropionic acid. The tube was sealed and fixed approximately 3 cm from the UV lamp and irradiated for 2.5 hours before precipitation of the product from THF into hexane three times to yield 0.734 g (86%) of **PMVS-3** as a viscous, yellow liquid.

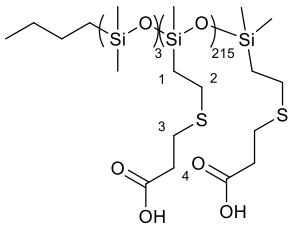

Figure 2-41. Structure of **PMVS-3** with labelling used in ^{1}H NMR spectroscopy assignments.

PMVS-3: ^{1}H NMR (400 MHz, Acetone-d_6) δ 2.98 – 2.48 (m, 6H, side chain 2+3+4), 1.12 – 0.86 (m, 2H, side chain 1), 0.25 (s, 1H, CH_3 PMVS). Peak for methyl groups on PDMS not observed.

$^{13}C\{^{1}H\}$ NMR (126 MHz, acetone-d_6) δ 173.01, 34.26, 26.58, 26.17, 18.20, -0.44.

GPC Analysis: *Not detectable by GPC. Monomodal by DLS.* NMR Integration: M_n = 44,200 g mol^{-1}.

Temperature initiated thiol-ene click reaction

P*-3(AIBN): 0.6 g (0.00276 mol of vinyl) of **PS-*b*-PMVS-*b*-PS*** was dissolved in 30 mL dry toluene. To this was added 1.2 mL (0.0138 mol) of 3-mercaptopropionic acid and 0.225 g (0.00137 mol) of AIBN. The solution was degassed with three freeze-pump-thaw cycles before heating to 70 °C for 5 hours. The solvent was removed by rotary evaporation before redissolving the residue in THF and precipitating into hexane twice, methanol once and then once more into hexane. The product was obtained as a soft white solid and dried under vacuum at 40 °C to give 0.603 g (68%).

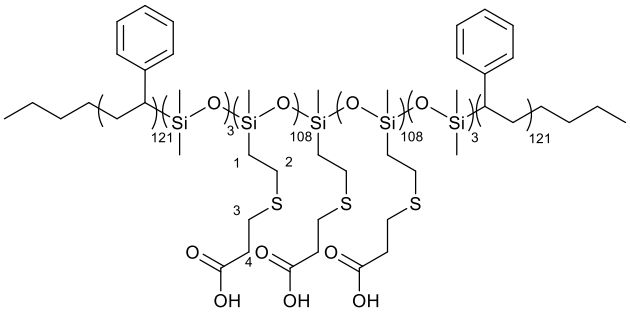

Figure 2-42. Structure of **P*-3(AIBN)** with labelling used in ^{1}H NMR spectroscopy assignments.

P*-3(AIBN): ^{1}H NMR (400 MHz, Acetone-d_6) δ 7.03 (s, 3H, Ar styrene), 6.62 (s, 2H, Ar styrene), 2.90 – 2.58 (m, 6H, side chain 2+3+4), 1.97 (s, 1H, C*H* styrene), 1.61 (s, 2H, CH_2 styrene), 1.09 – 0.96 (m, 2H, side chain 1), 0.28 (s, 3H, methyl). Peak for methyl groups on PDMS not observed.

^{13}C{^{1}H} NMR (126 MHz, acetone-d_6) δ 173.15, 128.16, 128.03, 125.68, 40.22, 34.32, 26.60, 26.17, 18.21, -0.43.

GPC Analysis: M_n = 46,180 g mol^{-1} (PDI = 1.01). NMR Integration: M_n = 62,800 g mol^{-1}.

Conversion of carboxylic acid to NHS ester

P-3-NHS: 0.238 g (0.00079 mol vinyl groups) of **P-3** was dissolved in 15 mL of THF under nitrogen. To this solution, 0.289 g (0.00251 mol) of *N*-hydroxysuccinimide (NHS, 98%), 0.061 g (0.00050 mol) of DMAP (99%) and 0.518 g (0.00251 mol) of DCC was added and the flask sealed before allowing to stir for 60 hours at room temperature. The product was obtained by precipitating three times from THF into hexane, before drying under vacuum at 40 °C (0.178 g, 57%).

P-3-NHS: ^{1}H NMR (400 MHz, Chloroform-*d*) δ 8.38 (d, 2H, DMAP), 7.05 (s, 3H, Ar styrene), 6.72 (d, 2H, DMAP), 6.58 (s, 1H, Ar styrene), 3.20 (s, 3H, DMAP), 3.00 – 2.72 (m, 6H, alkyl linking group overlapping), 2.66 (s, 4H, NHS overlapping), 1.85 (s, 1H, styrene overlapping), 1.50 – 1.13 (m, 2H, styrene overlapping), 1.02 – 0.77 (m, 2H, linking group overlapping), 0.17 (s, 3H, CH_3 PMVS). Peaks from DCC and DCU overlap in the region 1-3 ppm.

GPC Analysis: M_n = 45,884 g mol^{-1} (PDI = 1.73). NMR Integration: No clear separation of peaks for calculation.

2.4.2.4. Mesogen Attachment

Displacement of NHS Ester with M2

0.416 g (0.00070 mol vinyl) of **P-3-NHS** was dissolved in 80 mL THF with 0.956 g (0.0021 mol) of **M2** and stirred at room temperature for 16 hours. The solution was concentrated before precipitation of the product into methanol. The precipitation was repeated two times, and the resulting orange solid dried under vacuum at 40 °C. From the ^{1}H NMR spectroscopy it was apparent the NHS group was displaced by methanol on precipitation, and so that no mesogen attachment had occurred.

^{1}H NMR (400 MHz, Chloroform-*d*) δ 8.13 (d, *J* = 8.9 Hz, 2H, Ar M2), 7.81 (dd, *J* = 9.0, 4.3 Hz, 3H, Ar M2), 7.07 (s, 3H, Ar styrene), 6.97 (dd, *J* = 8.9, 4.5 Hz, 5H, Ar M2), 6.69 – 6.61 (m, 1H, Ar M2), 6.53 (s, 1H, Ar styrene), 4.14 – 3.97 (m, 4H, OCH_2), 3.48 (s, 3H, OCH_3), 3.01 – 2.74 (m, 6H, linking group), 2.72 – 2.52 (m, 4H, NHS), 2.02 (s, 1H, styrene overlapping), 1.87 – 1.74 (m, 4H, alkyl M2), 1.52 (dq, *J* = 14.8, 7.4 Hz, 4H, alkyl M2), 1.43 (s, 2H, styrene overlapping), 0.99 (t, *J* = 7.4 Hz, 6H, alkyl M2), 0.92 (d, *J* = 10.0 Hz, 2H, linking group), 0.17 (s, 3H, CH_3 PMVS).

Coupling of M1/M2 to P-3/P-5 by a Carbodiimide Mediated Reaction

In a typical reaction, 0.35g of **P-3** or **P-5** (1.16 mmol vinyl) was dissolved in 35 mL of dry CH_2Cl_2 under nitrogen. To this solution, 0.80g (1.74 mmol) of **M1** or 0.83g (1.74 mmol) of **M2** was added, followed by 0.29 g *N,N′*-dicyclohexylcarbodiimide (DCC) (1.39 mmol) and 0.017g (0.14 mmol) DMAP. The flask was sealed and allowed to stir for 60 hours at room temperature.

The polymer was isolated by first filtering off insoluble impurities and washing with cold CH_2Cl_2, before removal of the solvent under vacuum and precipitating five times from toluene into methanol. The product was obtained as a soft, orange/brown solid and dried under vacuum at 40 °C. The yield and percentage conversion of carboxylic acid to mesogen varied depending on the length of the side chain and the choice of mesogen - these results are summarised in Table 2-8. It was not possible to obtain a pure sample of the product of the reaction between **P-5** and **M2** by this method, with ^{1}H NMR suggesting very low (if any) coupling of the mesogen to the carboxylic acid. The solid that was obtained was insoluble, and so further characterisation was not possible.

Table 2-8. Yield and % conversion for 0.35 g scale reactions.

Polymer	Mass (g)	Yield (%)	% Conversion COOH*
P-3-M1(82)-COOH(18)	0.66	85	82
P-3-M2(80)-COOH(20)	0.60	78	80
P-5-M1(86)-COOH(14)	0.59	46	86

**Calculated from relative ratio of peaks for OCH_2 from mesogen and alkyl protons from linking group in ^1H NMR spectra*

P-3-M1(65)-COOH(35): 2.35 g of **P-3** (0.00767 mol vinyl) was dissolved in 135 mL dry CH_2Cl_2, before the addition of 5.334 g (0.0115 mol) of **M1**, 1.905 g (0.00923 mol) of DCC and 0.113 g (0.000925 mol) of DMAP. The procedure used for the 0.35 g scale reaction was followed, with the product obtained as a soft, orange/brown solid and dried under vacuum at 40 °C to give 3.691 g (80%).

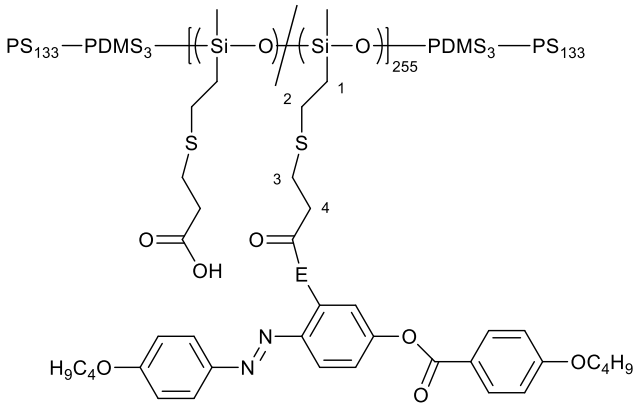

Figure 2-43. Structure of **P-3-M1(82)-COOH(18)** and **P-3-M1(65)-COOH(35)** (E=O). Structure of **P-3-M2(80)-COOH(20)** (E=NH) with labelling used in ^1H NMR spectroscopy assignments.

P-3-M1(82)-COOH(18): ^1H NMR (400 MHz, chloroform-*d*) δ 7.97-6.81 (m, 11H, Ar mesogen), 7.07 (s, 3H, Ar styrene), 6.58 (s, 2H, Ar styrene), 3.86 (s, 4H, O*C*H_2 mesogen), 2.85-2.59 (m, 6H, side chain 2+3+4), 1.67 (s, 5H, *n*-butyl + C*H* styrene), 1.41 (s, 6H, *n*-butyl + CH_2 styrene), 0.90 (s, 8H, *n*-butyl + side chain 1), 0.06 (s, 6H, CH_3 PMVS). Peak for methyl groups on PDMS not observed.

$^{13}C\{^1H\}$ NMR (126 MHz, chloroform-*d*) δ 170.16, 164.38, 163.72, 161.87, 154.03, 153.79, 152.89, 148.87, 146.86, 144.33, 141.54, 135.38, 133.50, 132.39, 128.04, 127.96, 127.91, 125.65, 125.61, 124.96, 123.99, 121.19, 120.93, 119.83, 117.88, 116.89, 115.07, 114.69, 114.37, 113.74, 111.18, 68.05, 40.70, 40.40, 40.25, 34.53, 31.14, 29.71, 26.77, 26.63, 19.21, 18.21, 13.84, 1.03, -0.00.

GPC Analysis: M_n = 36,468 g mol^{-1} (PDI = 1.89). NMR Integration: M_n = 170,000 g mol^{-1}.

P-3-M1(65)-COOH(35): ^{1}H NMR (400 MHz, chloroform-*d*) δ 7.99-6.48 (m, 11H, Ar mesogen), 6.85 (s, 3H, Ar styrene), 6.57 (s, 2H, Ar styrene), 4.06 (s, 4H, OC*H*$_2$), 2.87 – 2.36 (m, 6H, side chain 2+3+4), 1.69 (s, 5H, *n*-butyl and styrene), 1.42 (s, 4H, *n*-butyl and styrene), 0.90 (s, 8H, *n*-butyl and side chain 1), 0.10 (s, 6H, CH3 PMVS). Peak for methyl groups on PDMS not observed.

^{13}C{^{1}H} NMR (126 MHz, chloroform-*d*) δ 170.30, 164.38, 163.72, 161.87, 154.04, 153.79, 152.90, 148.88, 146.93, 144.33, 135.38, 133.50, 132.39, 128.23, 128.02, 127.96, 127.67, 127.42, 125.64, 125.48, 124.98, 123.99, 121.19, 117.92, 116.93, 115.07, 114.37, 113.74, 111.18, 68.16, 68.05, 40.59, 40.36, 34.53, 31.21, 31.14, 26.80, 26.63, 26.46, 19.21, 18.16, 13.84, 1.03, 0.01.

GPC Analysis: M_n = 43,271 g mol^{-1} (PDI = 1.98). NMR Integration: M_n = 150,750 g mol^{-1}.

P-3-M2(80)-COOH(20): ^{1}H NMR (400 MHz, chloroform-*d*) δ 9.96 (s, 1H, N*H*), 8.40-6.55 (m, 11H, Ar mesogen), 7.08 (s, 3H, Ar styrene), 6.55 (s, 2H, Ar styrene), 3.92 (m, 4H, OC*H*$_2$ mesogen), 2.84-2.61 (m, 6H, side chain 2+3+4), 1.85-1.26 (m, 11H, *n*-butyl + C*H*-C*H*$_2$ styrene), 0.94 (m, 8H, *n*-butyl + side chain 1), 0.07 (s, 6H, C*H*$_3$ PMVS). Peak for methyl groups on PDMS not observed.

^{13}C{^{1}H} (126 MHz, chloroform-*d*) δ 136.45, 132.31, 128.04, 125.53, 124.67, 114.73, 114.16, 67.98, 40.30, 31.15, 30.32, 29.33, 27.22, 25.62, 19.18, 18.25, 13.86, 1.03, -0.05.

GPC Analysis: M_n = 32,858 g mol^{-1} (PDI = 1.77). NMR Integration: M_n = 167,500 g mol^{-1}.

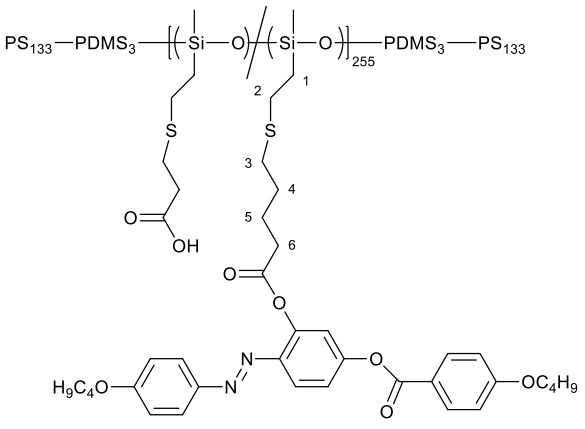

Figure 2-44. Structure of **P-5-M1-(86)-COOH(14)** with labelling used for ^{1}H NMR spectroscopy assignments.

P-5-M1(86)-COOH(14): ^{1}H NMR (400 MHz, chloroform-*d*) δ 8.01-6.56 (m, 11H, Ar mesogen), 7.08 (s, 3H, Ar styrene), 6.56 (s, 2H, Ar styrene), 3.91 (s, 4H, OC*H*$_2$ mesogen), 2.52 (s, 6H, side chain 2+3+6), 1.80-1.42 (m, 9H, *n*-butyl + C*H* styrene + side chain 4+5), 0.90 (m, 8H, *n*-butyl + side chain 1), 0.10 (s, 6H, C*H*$_3$ PMVS). Peak for methyl groups on PDMS not observed.

^{13}C{^{1}H} NMR (126 MHz, chloroform-*d*) δ 171.61, 164.38, 163.71, 161.87, 154.03, 153.79, 152.93, 149.05, 146.96, 144.33, 141.78, 135.38, 133.50, 132.39, 128.02, 127.64, 127.52, 125.63, 124.93, 121.19, 120.98, 119.81, 116.90, 115.06, 114.36, 113.74, 111.18, 68.16, 68.05, 40.56, 40.35, 33.60, 31.74, 31.14, 29.79, 29.66, 28.93, 28.79, 26.57, 24.22, 24.01, 19.21, 18.32, 13.84, 1.03, -0.03.

GPC Analysis: M_n = 30,951 g mol^{-1} (PDI = 1.94). NMR Integration: M_n = 181,700 g mol^{-1}.

P-5 with M2: ^{1}H NMR (400 MHz, chloroform-*d*) δ 8.13 (d, *J* = 9.1 Hz, 2H, Ar mesogen 10+11), 7.85 – 7.77 (m, 3H, Ar mesogen 3+4+5), 6.97 (dd, *J* = 7.6, 5.9 Hz, 4H, Ar mesogen 6+7+8+9), 6.65 (d, *J* = 9.9 Hz, 2H, Ar mesogen 1+2), 5.88 (s, 1H, N*H*), *4*.05 (q, *J* = 6.4 Hz, 4H, OC*H*$_2$), 1.86 – 1.75 (m, 4H, *n*-butyl), 1.55 – 1.48 (m, 4H, *n*-butyl), 1.04 – 0.95 (m, 6H, *n*-butyl), 0.07 (s, 6H, C*H*$_3$ PMVS). Peak for methyl groups on PDMS not observed.

These peaks corresponded to a mixture of unreacted **P-5** and **M2**.

Coupling of M1 to PMVS-3 by a Carbodiimide Mediated Reaction

PMVS-3-M1(84)-COOH(16): 0.32 g (0.00168 mol of vinyl) of **PMVS-3** was dissolved in 15 mL of dry THF before the addition of 1.159 g (0.00251 mol) of **M1**, 0.414 g (0.00201 mol) of DCC and 0.025 g (0.000205 mol) of DMAP. The solution was sealed under nitrogen and allowed to stir for 60 hours at room temperature. Solid impurities were then removed by filtration and the product obtained by successive precipitations from toluene into methanol before drying under vacuum at 40 °C to give 0.320 g (33 %).

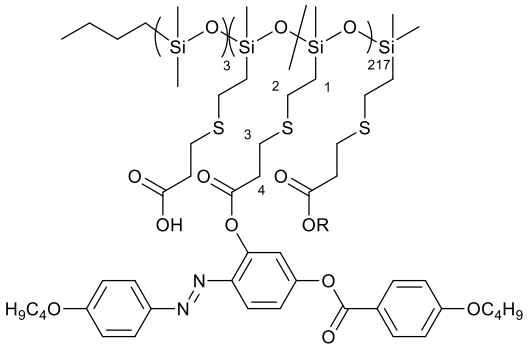

Figure 2-45. Structure of **PMVS-3-M1(84)-COOH(16)** with labelling used for ^{1}H NMR spectroscopy assignments.

PMVS-3-M1(84)-COOH(16): ^{1}H NMR (400 MHz, Chloroform-*d*) δ 7.94 (s, 2H, Ar mesogen), 7.66 (s, 3H, Ar mesogen), 7.04 (s, 2H, Ar mesogen), 6.78 (s, 4H, Ar mesogen), 3.82 (s, 4H, OC*H*$_2$), 2.97 – 2.42 (m, 6H, side chain 2+3+4), 1.79 – 1.48 (m, 4H, alkyl mesogen), 1.37 (m, 4H, alkyl mesogen), 1.01 – 0.73 (m, 6H, alkyl mesogen), 0.06 (s, 6H, C*H*$_3$ PMVS). Peak for methyl groups on PDMS not observed.

^{13}C{^{1}H} NMR (126 MHz, chloroform-*d*) δ 170.08, 163.90, 163.53, 161.90, 154.03, 153.79, 152.86, 148.91, 146.80, 141.50, 135.38, 133.50, 132.39, 132.25, 124.91, 123.99, 120.95, 119.74, 117.75, 116.82, 115.07, 114.60, 114.24, 113.74, 111.18, 67.91, 34.51, 31.10, 26.76, 26.62, 19.15, 18.17, 13.83, 1.03, -0.02.

GPC Analysis: M_n = 43,509 g mol^{-1} (PDI = 2.68). NMR Integration: M_n = 133,500 g mol^{-1}.

Conversion of Carboxylic Acid Groups to Methyl Esters

P-3-COOMe: 0.3 g (0.000992 mol of vinyl) of **P-3** was dissolved in 15 mL of dry CH_2Cl_2 before the addition of 0.016 g (0.000123 mol) of DMAP, 0.12 mL (0.00296 mol) of methanol and 0.246 g (0.00119 mol) of DCC. The flask was sealed and the solution stirred under nitrogen for 60 hours before filtering off solid impurities and washing with CH_2Cl_2. The polymer was precipitated three times from THF into methanol and once from THF into hexane, before the white solid was dried under vacuum at 40 °C (0.152 g, 48%).

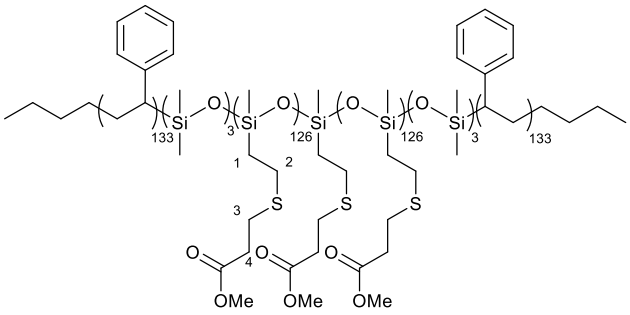

Figure 2-46. Structure of **P-3-COOMe** with labelling used for ^{1}H NMR spectroscopy assignments.

P-3-COOMe: ^{1}H NMR (400 MHz, Chloroform-*d*) δ 7.05 (s, 3H, Ar styrene), 6.57 (s, 1H, Ar styrene), 3.69 (s, 3H, OC*H*$_3$), 2.79 (t, *J* = 7.4 Hz, 2H, side chain 4), 2.59 (q, *J* = 9.5, 8.4 Hz, 4H, side chain 2 and 3), 1.85 (s, 1H, C*H* styrene), 1.36 (s, 2H, C*H*$_2$ styrene), 0.95 – 0.80 (m, 2H, side chain 1), 0.15 (s, 3H, C*H*$_3$ methyl). Peak for methyl groups on PDMS not observed.

^{13}C{^{1}H} NMR (126 MHz, chloroform-*d*) δ 172.31, 128.03, 127.64, 125.64, 51.77, 40.57, 40.35, 34.55, 26.88, 26.49, 18.19, -0.01.

GPC Analysis: M_n = 38,788 g mol^{-1} (PDI = 1.64). NMR Integration: M_n = 80,600 g mol^{-1}.

P*-3(AIBN)-COOMe: 0.3 g (0.000942 mol of vinyl) of **P*-3(AIBN)** was dissolved in 20 mL of dry CH_2Cl_2 before the addition of 0.1 mL (0.00247 mol) of methanol, 0.233 g (0.00113 mol) of DCC and 0.014 g (0.000115 mol) of DMAP. The solution was sealed under nitrogen and allowed to stir for 60 hours. Solid impurities were removed by filtration and the product obtained by precipitation from THF into methanol and then hexane, to obtain a soft, white solid which was dried under vacuum at 40 °C to give 0.216 g (69%).

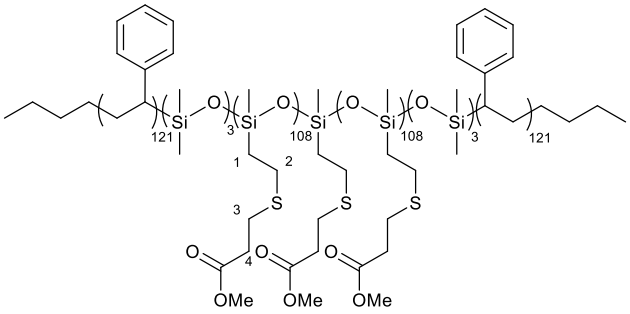

Figure 2-47. Structure of **P*-3(AIBN)-COOMe** with labelling used for ^{1}H NMR spectroscopy assignments.

P*-3(AIBN)-COOMe: ^{1}H NMR (400 MHz, Chloroform-*d*) δ 7.22 – 6.81 (s, 3H, Ar styrene), 6.52 (s, 2H, Ar styrene), 3.69 (s, 3H, OC*H*$_3$), 2.79 (t, *J* = 7.0 Hz, 1H, side chain 4), 2.60 (q, *J* = 9.4, 8.4 Hz, 4H, side chain 2+3), 1.88 (s, 1H, C*H* styrene), 1.41 (s, 2H, C*H*$_2$ styrene), 1.02 – 0.74 (m, 2H, side chain 1), 0.15 (s, 3H, methyl). Peak for methyl groups on PDMS not observed.

^{13}C{^{1}H} NMR (126 MHz, chloroform-*d*) δ 172.31, 128.04, 127.65, 125.65, 51.77, 40.37, 34.54, 26.88, 26.48, 18.20, 1.03, -0.02.

GPC Analysis: M_n = 33,476 g mol^{-1} (PDI = 1.76). NMR Integration: M_n = 65,500 g mol^{-1}.

P-3-M1(65)-COOMe(35): 0.9 g of **P-3-M1(65)-COOH(35)** was dissolved in 50 mL of dry CH_2Cl_2, before the addition of 0.411 g (0.00199 mol) of DCC, 0.1 mL (0.00247 mol) of methanol and 0.024 g (0.000196 mol) of DMAP. The solution was sealed under nitrogen and allowed to stir at room temperature for 60 hours. Solid impurities were removed by filtration before precipitation of the polymer from toluene into methanol three times. The product was dried under vacuum at 40 °C to give 0.760 g (80%) of the orange polymer.

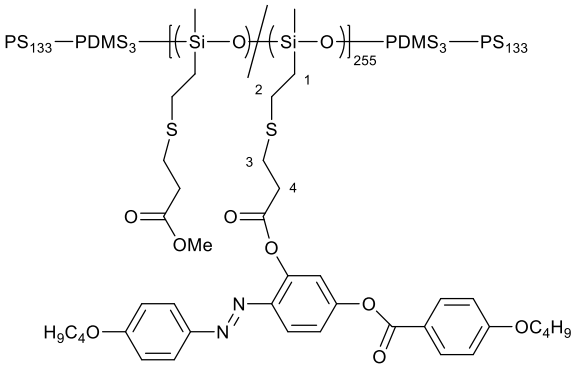

Figure 2-48. Structure of **P-3-M1(65)-COOMe(35)** with labelling used for ^{1}H NMR spectroscopy assignments.

P-3-M1(65)-COOMe(35): ^{1}H NMR (400 MHz, Chloroform-*d*) δ 8.02-6.85 (11H, Ar mesogen), 7.07 (s, 3H, Ar styrene), 6.57 (s, 2H, Ar styrene), 3.91 (s, 4H, OC*H*$_2$), 3.58 (s, 3H, OC*H*$_3$), 3.00 – 2.41 (m, 6H, side chain 2+3+4), 1.71 (s, 5H, *n*-butyl and styrene), 1.43 (6, 4H, *n*-butyl and styrene), 0.92 (s, 8H, *n*-butyl and side chain 1), 0.12 (s, 6H, C*H*$_3$ PMVS). Peak for methyl groups on PDMS not observed.

^{13}C{^{1}H} NMR (126 MHz, chloroform-*d*) δ 172.27, 170.10, 164.01, 163.72, 161.99, 152.92, 148.91, 146.86, 145.35, 141.54, 132.50, 132.30, 128.27, 128.04, 127.95, 127.67, 127.42, 127.30, 125.65,

125.47, 124.94, 120.97, 119.85, 117.90, 116.89, 115.07, 114.68, 114.32, 67.97, 51.68, 40.62, 40.60, 40.35, 34.54, 31.11, 26.80, 26.65, 26.43, 25.33, 19.18, 18.19, 13.84, 1.33, 0.74, -0.01.

GPC Analysis: M_n = 33,476 g mol^{-1} (PDI = 2.07). NMR Integration: M_n = 152,000 g mol^{-1}.

P*-3(AIBN)-M1-COOMe: 2.31 g (0.00679 mol of vinyl) of **P*-3(AIBN)** was dissolved in 125 mL of dry CH_2Cl_2 with 4.084 g (0.00883 mol) of **M1**, 1.682 g (0.00815 mol) of DCC and 0.099 g (0.000810 mol) of DMAP. The solution was sealed under nitrogen and stirred at room temperature for 60 hours. Solid impurities were removed by filtration and precipitation of the product was attempted from toluene into methanol. Precipitation did not lead to effective separation of the product and **M1**, and so the unpurified solid was used for the subsequent synthetic step.

3.526 g of the mixture of polymeric product and **M1** was dissolved in 125 mL of dry CH_2Cl_2, before the addition of 0.35 mL (0.0087 mol) of methanol, 1.404 g (0.0068 mol) of DCC and 0.083 g (0.00068 mol) of DMAP. The solution was sealed under nitrogen and stirred at room temperature for 60 hours. The resulting solution did not filter, and so solid impurities were removed by centrifuge before removal of the solvent by rotary evaporation. The product was precipitated from toluene into methanol five times to remove excess **M1**, with the resulting polymer obtained as a soft, orange solid before drying under vacuum at 40 °C to give 0.838 g.

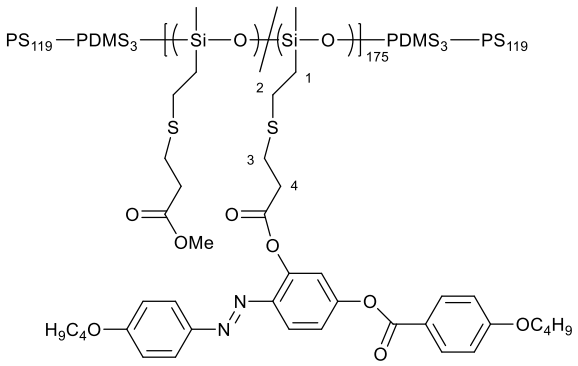

Figure 2-49. Structure of **P*-3(AIBN)-M1-COOMe** with labelling used for ^{1}H NMR spectroscopy assignments.

P*-3(AIBN)-M1-COOMe: ^{1}H NMR (400 MHz, Chloroform-*d*) δ 13.26 (s, unattached **M1**), 8.22 – 8.09 (m, unattached (sharp) and attached (broad, low intensity) **M1**), 7.97 – 7.72 (m, unattached (sharp) and attached (broad, low intensity) **M1**), 7.17 – 6.85 (m, 3H, Ar styrene + attached mesogen), 6.58 (s, 2H, Ar styrene), 4.12 – 3.90 (m, unattached (sharp) and attached (broad, low

intensity) **M1**), 3.81 – 3.61 (m, OCH_3), 3.48 (s, 0H), 3.23 – 2.39 (m, linking group alkyls), 2.04 – 1.65 (m, styrene alkyls, mesogen alkyls), 1.63 – 1.19 (m, styrene+mesogen+linking group alkyls), 1.09 – 0.78 (m, 3H, CH_3 PMVS).

GPC Analysis: M_n = 40,620 g mol^{-1} (PDI = 1.76). NMR Integration: *Weak peaks from PMVS block prevent calculation of mesogen loading and so molecular weight.*

2.4.3. UV Response

A thin film of **P-3-M1(82)-COOH(18)** was prepared by solvent casting from toluene before annealing at 120°C for 2 hours. The film was then stretched uniaxially at 120 °C before allowing to cool to promote alignment of the LC component. A strip was cut from the film with the direction of alignment along its long axis, then adhered to two end tabs to give a sample with gauge length of 13.6 mm and a thickness of 0.1 mm.

The end tabs were loaded in a Diastron LEX820 tensile tester with 20 N load cell. The test machine was set to maintain a target stress of 25.7 kPa by controlling the tensile force exerted on the film. The end tabs pulled apart at a rate of 0.2 mm s^{-1} to meet this condition and the data collected at 220 ms interval for the 420 second duration of the experiment. A 100W UV lamp (Hoenle UVACube 100 with mercury bulb, main peak 365 nm) was fixed 3 cm above the film and switched on for 60 second intervals and off for 120 second intervals. When the UV lamp was switched off a visible light source was turned on to promote isomerisation of the mesogen. The force required to maintain a constant stress was recorded and plotted against time. The experimental setup is shown in Figure 2-50. During experiments this was covered with an opaque box to block the UV light.

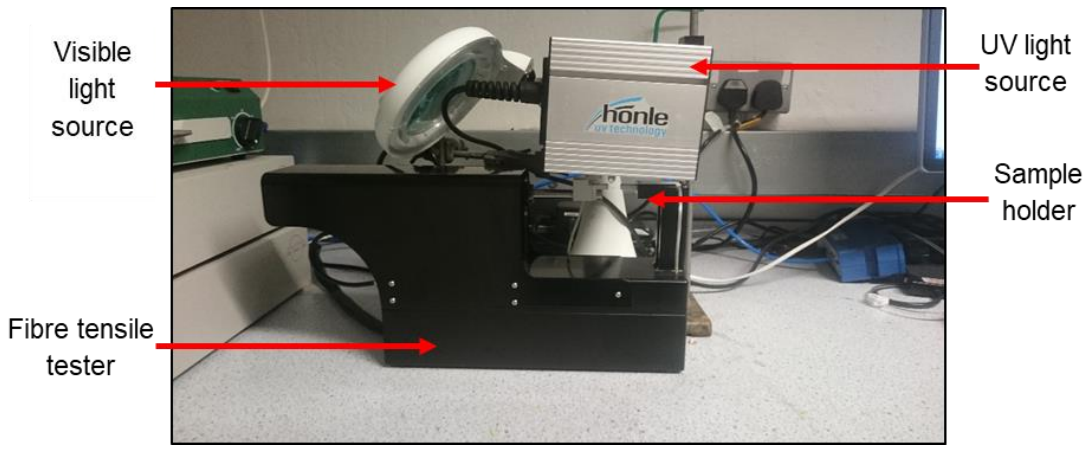

Figure 2-50. Experimental setup used for UV response test.

2.5. References

1 H. Yu and T. Ikeda, Photocontrollable Liquid-Crystalline Actuators, *Adv. Mater.*, 2011, **23**, 2149–2180.

2 H. Jiang, C. Li and X. Huang, Actuators Based on Liquid Crystalline Elastomer Materials, *Nanoscale*, 2013, **5**, 5225.

3 C. Ohm, M. Brehmer and R. Zentel, Liquid Crystalline Elastomers as Actuators and Sensors, *Adv. Mater.*, 2010, **22**, 3366–3387.

4 D. L. Thomsen, P. Keller, J. Naciri, R. Pink, H. Jeon, D. Shenoy and B. R. Ratna, Liquid Crystal Elastomers with Mechanical Properties of a Muscle, *Macromolecules*, 2001, **34**, 5868–5875.

5 T. Ikeda, M. Nakano, Y. Yu, O. Tsutsumi and A. Kanazawa, Anisotropic Bending and Unbending Behavior of Azobenzene Liquid-Crystalline Gels by Light Exposure, *Adv. Mater.*, 2003, **15**, 201–205.

6 J. Kupfec and H. Finkelmann, Nematic Liquid Single Crystal Elastomer, *Makromol. Chemie Rapid Commun.*, 1991, **12**, 717–726.

7 T. H. Ware, M. E. McConney, J. J. Wie, V. P. Tondiglia and T. J. White, Voxelated Liquid Crystal Elastomers, *Science*, 2015, **347**, 982–984.

8 R. J. Spontak and N. P. Patel, Thermoplastic Elastomers: Fundamentals and Applications, *Curr. Opin. Colloid Interface Sci.*, 2000, **5**, 334–341.

9 N. Mischenko, K. Reynders, K. Mortensen, R. Scherrenberg, F. Fontaine, R. Graulus and H. Reynaers, Structural Studies of Thermoplastic Triblock Copolymer Gels, *Macromolecules*, 1994, **27**, 2345–2347.

10 M. Petr, B. A. Katzman, W. Dinatale and P. T. Hammond, Synthesis of a New, Low-Tg Siloxane Thermoplastic Elastomer with a Functionalizable Backbone and Its Use as a Rapid, Room Temperature Photoactuator, *Macromolecules*, 2013, **46**, 2823–2832.

11 M. Wang, L.-X. Guo, B.-P. Lin, X.-Q. Zhang, Y. Sun and H. Yang, Photo-Responsive Polysiloxane-Based Azobenzene Liquid Crystalline Polymers Prepared by Thiol-Ene Click Chemistry, *Liq. Cryst.*, 2016, **43**, 1626–1635.

12 E. Verploegen, T. Zhang, N. Murlo and P. T. Hammond, Influence of Variations in Liquid-Crystalline Content upon the Self-Assembly Behavior of Siloxane-Based Block Copolymers, *Soft Matter*, 2008, **4**, 1279.

13 M. H. Li, P. Auroy and P. Keller, An Azobenzene-Containing Side-on Liquid Crystal Polymer, *Liq. Cryst.*, 2000, **27**, 1497–1502.

14 M. Petr and P. T. Hammond, Room Temperature Rapid Photoresponsive Azobenzene Side Chain Liquid Crystal Polymer, *Macromolecules*, 2011, **44**, 8880–8885.

15 C. E. Hoyle and C. N. Bowman, Thiol-Ene Click Chemistry, *Angew. Chemie - Int. Ed.*, 2010, **49**, 1540–1573.

16 M. J. Kade, D. J. Burke and C. J. Hawker, The Power of Thiol-Ene Chemistry, *J. Polym. Sci. Part A Polym. Chem.*, 2010, **48**, 743–750.

17 A. B. Lowe, Thiol-Ene "Click" Reactions and Recent Applications in Polymer and Materials Synthesis, *Polym. Chem.*, 2010, **1**, 17–36.

18 A. B. Lowe, Thiol-Ene 'Click' Reactions and Recent Applications in Polymer and Materials Synthesis: A First Update, *Polym. Chem.*, 2014, **1**, 4820–4870.

19 D. J. Lunn, C. E. Boott, K. E. Bass, T. A. Shuttleworth, N. G. McCreanor, S. Papadouli and I. Manners, Controlled Thiol-Ene Functionalization of Polyferrocenylsilane-Block-Polyvinylsiloxane Copolymers, *Macromol. Chem. Phys.*, 2013, **214**, 2813–2820.

20 C. E. Boott, D. J. Lunn and I. Manners, Versatile and Controlled Functionalization of Polyferrocenylsilane-b-Polyvinylsiloxane Block Copolymers Using a N-Hydroxysuccinimidyl Ester Strategy, *J. Polym. Sci. Part A Polym. Chem.*, 2016, **54**, 245–252.

21 C. B. McArdle, *Side Chain Liquid Crystal Polymers*, Blackie, Glasgow, 1989.

22 L. M. Campos, K. L. Killops, R. Sakai, J. M. J. Paulusse, D. Damiron, E. Drockenmuller, B. W. Messmore and C. J. Hawker, Development of Thermal and Photochemical Strategies for Thiol-Ene Click Polymer Functionalization, *Macromolecules*, 2008, **41**, 7063–7070.

23 B. Neises and W. Steglich, Simple Method for the Esterification of Carboxylic Acids, *Angew. Chemie Int. Ed.*, 1978, **17**, 522–524.

24 A. El-Faham, Peptide Coupling Reagents, More than a Letter Soup, *Chem. Rev.*, 2011, **111**, 6557–6602.

25 M. Petr, M. E. Helgeson, J. Soulages, G. H. McKinley and P. T. Hammond, Rapid Viscoelastic Switching of an Ambient Temperature Range Photo-Responsive Azobenzene Side Chain Liquid Crystal Polymer, *Polymer*, 2013, **54**, 2850–2856.

26 J. Brandrup, E. Immergut and E. A. Grulke, Eds., *Polymer Handbook*, John Wiley & Sons, New York, 3rd edn., 1990.

27 A. A. Craig and C. T. Imrie, Effect of Spacer Length on the Thermal Properties of Side-Chain Liquid Crystal Polymethacrylates. 2. Synthesis and Characterization of the Poly[Cu-(4'-Cyanobiphenyl-4-Yloxy)Alkyl Methacrylates, *Macromolecules*, 1995, **28**, 3617–3624.

28 J.-S. Hu, B. Zhang, L.-M. Liu and F.-B. Meng, Synthesis, Structures and Properties of Side-Chain Cholesteric Liquid Crystalline Polysiloxanes, *J. Appl. Polym. Sci.*, 2003, **89**, 3944–3950.

29 X. Li, L. Fang, L. Hou, L. Zhu, Y. Zhang, B. Zhang and H. Zhang, Photoresponsive Side-Chain Liquid Crystalline Polymers with Amide Group-Substituted Azobenzene Mesogens: Effects of Hydrogen Bonding, Flexible Spacers, and Terminal Tails, *Soft Matter*, 2012, **8**, 5532–5542.

30 D. Acierno and C. A. A., *Rheology and Processing of Liquid Crystal Polymers*, Chapman & Hall, London, 1996.

31 C. M. Jung, W. Kraus, P. Leibnitz, H.-J. Pietzsch, J. Kropp and H. Spies, Syntheses and First Crystal Structures of Rhenium Complexes Derived from ω-Functionalized Fatty Acids as Model Compounds of Technetium Tracers for Myocardial Metabolism Imaging, *Eur. J. Inorg. Chem.*, 2002, 1219.

Chapter 3: Effect of Tensile Strain on the Morphology of Thermoplastic Liquid Crystal Elastomers

3.1. Introduction

In Chapter 2 it was shown that the liquid crystal (LC) functionalised triblock copolymers **P-3-M1(82)-COOH(18)** and **P-3-M1(65)-COOH(35)** had glass and isotropic transition temperatures (T_g and T_{iso}, respectively) appropriate for use as UV-responsive room temperature actuators. Whilst the thermal properties are important in determining their suitability as actuators, there are other structural factors to consider. Typically, liquid crystal elastomers (LCEs) require covalent crosslinking for reversible actuation, so as to recover the initial, undeformed state on removal of an applied stress.[1] However, in the case of the **P-3-M1(x)-COOH(y)** polymers the triblock copolymer backbone is designed to act as a thermoplastic elastomer, which means that the reversible actuation is reliant on the microphase separated morphology adopted by the polystyrene (PS) and poly(methylvinylsiloxane) (PMVS) blocks at room temperature. Generally, a spherical arrangement of the hard blocks (PS in this case) in a matrix of the soft block (PMVS) is required to physically crosslink the chains and for elastomeric behaviour to be observed.[2] Therefore, if the **M1** functionalised polymers have a volume fraction and interaction parameter that favours this morphology they are highly likely to demonstrate elastomeric behaviour.

As well as forming a thermoplastic elastomer, it is also necessary to induce a LC monodomain for macroscopic shape change to occur. It was demonstrated by Petr *et al*. that stretching a film of their thermoplastic LCE whilst heated above the T_{iso} was sufficient to obtain a reversible contraction of 3.3% when irradiated with UV light at room temperature.[3] However, no further insight was presented as to the nanoscale origin of the actuation, which was triggered on isomerisation of the azobenzene group present in the mesogen. The level of order within a LC mesophase can be identified for smectic mesophases using Wide-Angle X-ray Scattering (WAXS) to obtain peaks characteristic of the spacing between layers.[4–6] Nematic mesophases such as those found in **P-3-M1(x)-COOH(y)**, however, demonstrate a much lower level of long-range order than smectics and so it is not possible to directly probe the LC mesophase for the thermoplastic LCEs synthesised in Chapter 2 by this method.

Similar methods of inducing alignment in LCEs to that utilised by Petr *et al*. have been adopted for Covalent Adaptable Networks (CANs), where the polymer was first heated to a temperature where covalent bonds could exchange before stretching and cooling to freeze-in the deformed state.[7–9] It has been shown that for side-chain LCPs the rod-like mesogen preferentially orients parallel to

the polymer backbone due to the flexible, side-on linking group.[10] For the triblock copolymers reported in Chapter 2, it is likely that manually deforming the film whilst heated above the glass transition temperature of both blocks will lead to changes in the microphase separated morphology. Therefore, whilst it is not possible to directly probe the level of order within the nematic mesophase, it is possible to observe the effect of an applied tensile force on the morphology of the triblock copolymer backbone through SAXS.

It has been shown that for sphere-forming block copolymer systems shear forces, such as those encountered by applying uniaxial tension, increase the level of orientational order between spherical domains.[11,12] This can be determined from the 2D scattering pattern, with isotropic samples resulting in a circular pattern with equal intensity at all points on the circle and anisotropic structures resulting in areas of higher or lower intensity (Figure 3-1).[13] SAXS would therefore be useful not only to determine whether a thermoplastic elastomer has been synthesised, but also for characterisation of the level of alignment of the domains achieved by stretching the polymer film. This could then be extended to different processing methods which apply tensile strain to the polymer, for example melt extrusion (to be discussed in Chapter 4) and electrospinning (to be discussed in Chapter 5).

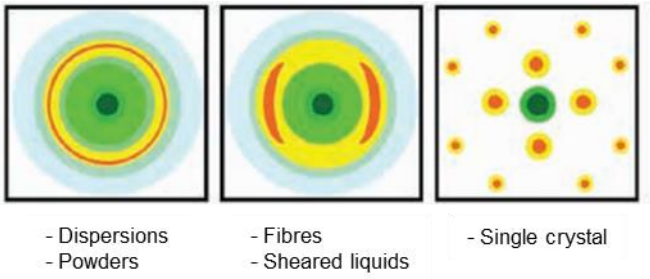

Figure 3-1. Characteristic 2D SAXS scattering pattern for systems with varying levels of orientational order. Reproduced from Reference 13.

High temperature SAXS would offer further insight. The presence of a nematic mesophase can be inferred from its effect on the microphase separated morphology of block copolymers. The unfavourable increase in free energy associated with mixing an ordered LC mesophase with a random-coil polymer chain can result in phase transitions shifting to higher temperatures, including the order-disorder transition (T_{ODT}).[14] Evidence of a microphase separated morphology at high temperatures is therefore consistent with the presence of a nematic mesophase. If a change in morphology can be detected at temperatures above the T_{iso}, it would also be a good indication that the thermoplastic LCEs have the desired responsive properties for use as actuators.

The aim of the following work was therefore to understand the morphology adopted by the LCEs described in Chapter 2 at room temperature and to determine what effect, if any, the application of a tensile force had. The room temperature morphology was predicted and characterised for films of **P-3**, **P-3-M1(65)-COOH(35)**, **P-3-M1(82)-COOH(18)** and **P-3-M2(80)-COOH(20)** using a combination of SAXS and Transmission Electron Microscopy (TEM). TEM was used to confirm the presence of the predicted morphology and approximate dimensions of individual domains, whilst SAXS was utilised to determine the bulk morphology, including the average size and spacing between domains.

The effect of stretching the polymer film on the morphology was then investigated, both at room temperature and on heating above the T_{iso} using variable temperature SAXS (VT-SAXS), to determine whether a detectable change in the domains could be observed. Finally, mechanical measurements were made on a film of the stretched polymer whilst irradiating using UV to determine whether the change in morphology of the triblock copolymer backbone could be linked to photoactuation of the film.

3.2. Results and Discussion

3.2.1. Theoretical Volume Fraction

In order to predict the microphase segregated morphology adopted by the thermoplastic LCEs, a value for the Flory-Huggins Interaction Parameter, χ, was calculated using Equation 3.1 (where δ_i is the solubility parameter of block i). It was also necessary to calculate the molar volume ($V_{M,i}$) for the PS and PMVS blocks both before and after functionalisation. This was carried out for **PS-*b*-PMVS-*b*-PS**, **P-3**, **P-3-M1(65)-COOH(35)** and **P-3-M1(82)-COOH(18)**. No further calculations were made for **P-3-M2(80)-COOH(20)** as the level of LC loading is expected to have a greater impact on the properties than the identity of the mesogen (**M1** or **M2**), which would have a marginal effect on the V_M.

$$\chi_H = \frac{V_M}{RT}(\delta_{AA} - \delta_{BB})^2 \qquad 3.1$$

It has been shown that $V_{M,i}$ can be calculated from the sum of the contributions from each atom in the polymer repeat unit, with results obtained in this manner showing good agreement with those found experimentally at a given temperature.[15] The molar volume for each homopolymer can therefore be calculated according to Equation 3.2, Where V_x is the volume contribution per atom, x.

$$V_{M,i}(298K) = \sum_i V_x(298K) \quad 3.2$$

To account for contraction the in atomic volume due to bonding interactions, the van der Waals volume ($V_{W,A}$) is used. For amorphous polymers this value has a linear relationship with the molar volume, where $V_M = 1.6V_{W,A}$, which allows for estimation of the molar volume of structural subunits from experimentally derived values of $V_{W,A}$.[15] For a block copolymer comprised of blocks *i* and *j*, a total molar volume, V_M, that accounts for the molar volume of each block can be expressed according to Equation 3.3, assuming that each block has an approximately equal degree of polymerisation.

$$V_M = \left(V_{M,i}V_{M,j}\right)^{\frac{1}{2}} \quad 3.3$$

For the triblock copolymers described in Chapter 2, the molar volume of the repeat unit can be calculated using data tabulated by van Krevelen for common organic structural groups, as no experimental values are quoted in the literature.[15] To account for the mixture of linking groups terminated with either a mesogen or carboxylic acid group in **P-3-M1(82)-COOH(18)** and **P-3-M1(65)-COOH(35),** the molar volume was first calculated for both PMVS repeat units either fully terminated with carboxylic acid (PMVS-COOH) or with **M1** (PMVS-M1), and then weighted according to the percentage of each in the final polymer. The resulting values for V_M are given in Table 3-1, with the structural groups used and their individual contributions listed in Appendix B.

Table 3-1. Calculated molar volume for all repeat units in **PS-*b*-PMVS-*b*-PS**, **P-3**, **P-3-M1(65)-COOH(35)** and **P-3-M1(82)-COOH(18)**. **From reference 15.*

Repeat Unit	$V_{M,i}$ (cm^3 mol^{-1})
PMVS-M1	570.5
PMVS-COOH	162.5
PMVS-M1(82)-COOH(18)	497.1
PMVS-M1(65)-COOH(35)	427.1
PMVS	83.9
PS	99.0*

The molar volume of the polystyrene repeat unit was obtained from the literature as 99.0 cm^3 mol^{-1}.[15] This allowed for calculation of V_M for the block copolymers using Equation 3.3, and also the f_{PS} for each polymer using Equation 3.4. The microphase segregated morphology adopted by the triblock copolymers could then be predicted after calculating χN using Equation 3.1. The degree of polymerisation for a triblock copolymer is equivalent to $2N$,[16] therefore a value of N=262 was used for all polymers based on the backbone described in Section 2.2.2.1. Values for the solubility parameter for polystyrene and polydimethylsiloxane (PDMS) are given in the literature as 17.8 and 15.3 $MPa^{1/2}$ respectively.[17] Calculated values of V_M, f_{PS}, χN and the corresponding predicted morphologies are listed in Table 3-2.

$$f_i = \frac{V_{M,i}}{\sum V_{M,i}} \qquad 3.4$$

Table 3-2. Calculated V_M, f_{PS} and χN for **PS-*b*-PMVS-*b*-PS**, **P-3, P-3-M1(65)-COOH(35)** and **P-3-M1(82)-COOH(18)** and the predicted microphase segregated morphology for each.

Polymer	V_M (cm^3 mol^{-1})	f_{PS}	χN	Predicted Morphology
PS-*b*-PMVS-*b*-PS	91.2	0.55	60	Lamellar
P-3	126.9	0.38	84	Lamellar
P-3-M1(82)-COOH(18)	221.8	0.17	151	Spherical/Cylindrical*
P-3-M1(65)-COOH(35)	205.6	0.20	121	Spherical/Cylindrical*

*****_Values for f_{PS} in strong segregation limit on borderline between spherical and cylindrical regions._

The calculated values listed in Table 3-2 can only be considered as estimates, as in the calculation of χ the solubility parameter for PDMS was used to represent the midblock, but this will not account for any difference in the interaction parameter caused by functionalisation with the linking group or the mesogen. Secondly, the relationship given in Equation 3.1 holds only for polymers in which dispersive (van der Waals) interactions dominate, however, it is expected that hydrogen bonding will have a significant effect that is not accounted for in this model.[18] This will have an impact on values for χN calculated for the LC-functionalised polymers, and in particular for **P-3** which contains a large number of carboxylic acid groups. Hydrogen bonding can act to decrease χ to the extent that negative values are measured,[18] and so the values in Table 3-2 may over-estimate the actual value of χN. However, despite these limitations the lamellar morphology predicted for **PS-*b*-PMVS-*b*-PS** was confirmed experimentally by Petr *et al.*[3], suggesting that the results of the calculations are valid. The morphologies predicted for **P-3-M1(82)-COOH(18)** and **P-3-M1(65)-COOH(35)** suggested that they have a suitable composition for forming a

thermoplastic elastomer, and so samples were prepared for TEM and SAXS to confirm which was present.

3.2.2. Room Temperature Morphology

Films of the polymers **P-3**, **P-3-M1(82)-COOH(18)**, **P-3-M1(65)-COOH(35)** and **P-3-M2(80)-COOH(20)** were cast from a toluene solution and annealed for 2 hours at 120 °C. For **P-3-M1(82)-COOH(18)** and **P-3-M1(65)-COOH(35)**, one of the films was also uniaxially stretched whilst heated above the T_{iso} to promote the formation of a LC monodomain. Thin sections were cut from the films using a microtome and collected on copper grids for TEM.

3.2.2.1. P-3

The azimuthal integration of the SAXS data obtained for **P-3** (Figure 3-2) showed no discernible peaks, which indicated an amorphous morphology with no long-range order present. It was shown by Petr *et al*. that the unfunctionalised **PS-*b*-PMVS-*b*-PS** triblock copolymer adopted a lamellar morphology,[3] and this structure was predicted for **P-3** from volume fraction calculations. It can therefore be proposed that the introduction of hydrogen bonding due to the addition of the carboxylic acid-terminated linking group to the PMVS block has decreased χ to the extent that at room temperature the polymer was below the critical value for microphase segregation to occur,[18] and so in the disordered region of the phase diagram. However, the structure seen by TEM in Figure 3-3 does not suggest the expected homogeneous mixed phase of PS and PMVS was present. This, combined with the predicted lamellar microstructure from the molar volume of the PS block suggests incomplete annealing of the film had occurred. This would mean that at the time annealing was stopped, the domains were still evolving with long-range order yet to be established.

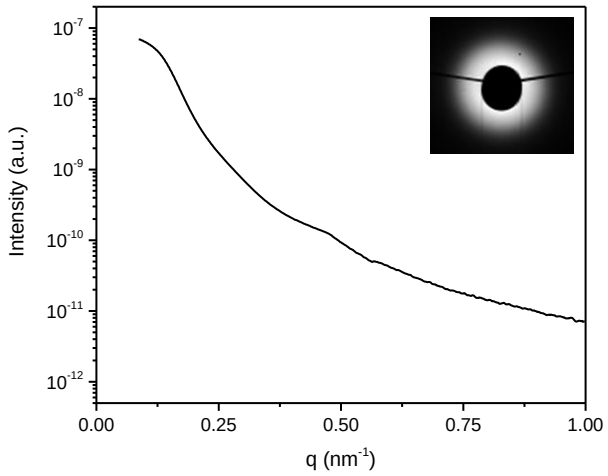

Figure 3-2. Background subtracted room temperature SAXS data for **P-3** after azimuthal integration showing no clear peaks suggesting a disordered morphology. Inset – 2D SAXS pattern showing no rings indicative of long-range order.

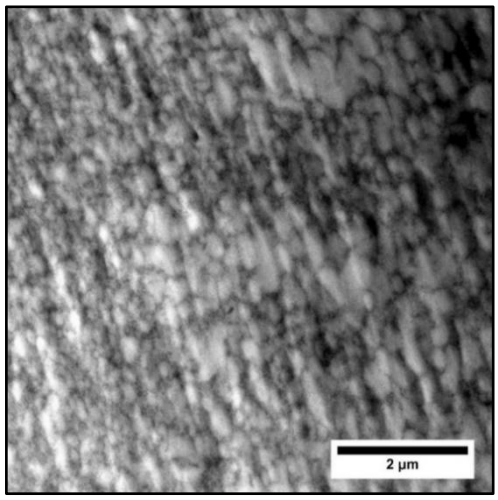

Figure 3-3. Representative TEM image for **P-3** showing no microphase separation between the PS and PMVS blocks. The relatively large features suggest that the block copolymer is not homogeneous at room temperature.

3.2.2.2. P-3-M1(82)-COOH(18) and P-3-M2(80)-COOH(20)

On the attachment of the mesogen (either **M1** or **M2**) to the linking group on **P-3**, and with no further alignment processes carried out, both the SAXS and TEM results indicated that microphase separation of the PS and PMVS blocks had occurred. The 2D scattering patterns obtained suggested that the film of **P-3-M1(82)-COOH(18)** (Figure 3-4) had some level of anisotropy present, evident from the increased regions of intensity in the equatorial direction and slight elliptical nature. In contrast, **P-3-M2(80)-COOH(20)** (Figure 3-5) resulted in an isotropic, circular scattering pattern which displayed equal intensity at all points. Neither film was stretched or deformed in order to promote an anisotropic structure, and so the increased anisotropy observed for **P-3-M1(82)-COOH(18)** most likely arose as a result of drying effects during the film preparation, or from sample loading for the SAXS measurement. For both polymers the azimuthal integration resulted in a plot with two peaks: a broad peak at higher q values arising from the form factor, $F(q)$, denoted by q_F, and a more defined peak at lower q values, characteristic of the structure factor, $S(q)$, denoted by q^*.

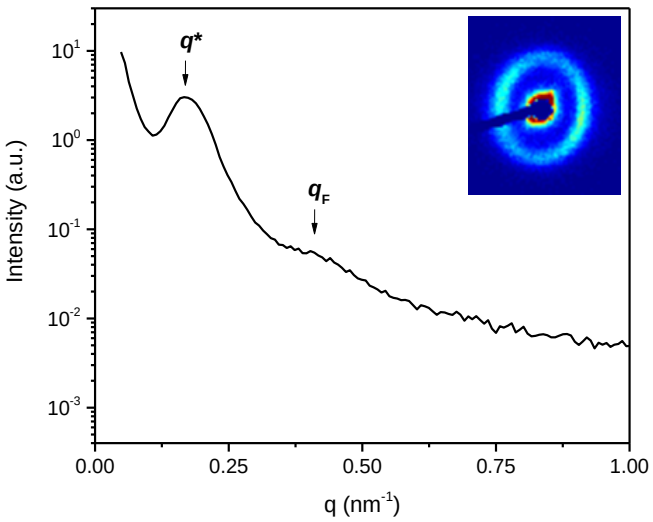

Figure 3-4. Background subtracted room temperature SAXS data for **P-3-M1(82)-COOH(18)** after azimuthal integration. The q^* peak at 0.174 nm^{-1} corresponds to an average inter-sphere spacing of 36.1 nm, whilst the q_F peak around 0.43 nm^{-1} corresponds to an average sphere radius of 15 nm. Inset – 2D SAXS pattern showing slightly anisotropic scattering.

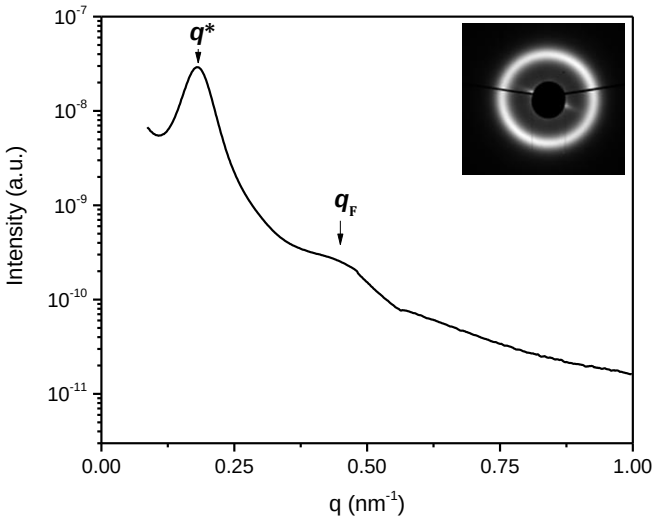

Figure 3-5. Background subtracted room temperature SAXS data for **P-3-M2(80)-COOH(20)** after azimuthal integration. The q^* peak at 0.181 nm^{-1} corresponds to an average inter-sphere spacing of 34.8 nm, whilst the q_F peak around 0.46 nm^{-1} corresponds to an average sphere radius of 14 nm. Inset – 2D SAXS pattern showing isotropic scattering.

The broad q_F peaks are characteristic of the spherical form factor[19,20] and arise due to *intra*-sphere interference from atoms within the domains.[21] This peak indicated that a spherical morphology was present for both materials, where the spheres had an average radius of 15 nm for **P-3-M1(82)-COOH(18)** and 14 nm for **P-3-M2(80)-COOH(20)** (due to the broad nature of the spherical form factor peak the value of the average radius of the spheres was calculated to two significant figures). The sharper q^* peak arises due to *inter*-sphere interference,[19,21] which allows for determination of the average spacing between the centres of two neighbouring domains. The peak maximum in reciprocal space was measured to four decimal places, and then converted to a value in real space using Equation 3.5. This gave values of 36.1 nm for **P-3-M1(82)-COOH(18)** and 34.8 nm for **P-3-M2(80)-COOH(20)**, confirming that the identity of the mesogen had negligible effect on the microphase separation of the PS and PMVS blocks.

$$d = \frac{2\pi}{q} \qquad 3.5$$

Neither peak in the two sets of SAXS data had a shoulder or higher order reflection, which suggests that a relatively disordered arrangement of domains was adopted as opposed to a well-ordered lattice (*i.e.* body centred or face centred cubic) or a hexagonally close packed (HCP) cylindrical morphology. Without higher order reflections it is not possible to distinguish between spherical and cylindrical morphologies from the SAXS data only, however, it can be suggested that for both

polymers the PS chains form spheres with an average radius around 14-15 nm, which are arranged with an average separation of 35-36 nm between their centres in a matrix of the PMVS chains.

The spherical morphology suggested by SAXS was confirmed by TEM, with representative images for **P-3-M1(82)-COOH(18)** and **P-3-M2(80)-COOH(20)** given in Figure 3-6 and Figure 3-7, respectively. In both cases the lighter regions correspond to the PS block and the darker regions to the more electron-rich, LC-functionalised PMVS block. Measurement of the radius of the PS spheres from these images gave values close to the 14 nm determined by SAXS, although the action of microtoming the films acted to distort the domains from perfect spheres. The sample preparation also led to wrinkles in the surface of the film which caused regions of increased or decreased brightness due to the non-uniform height of the sample which, when combined with the soft edges to the PS domains, made measurement of the inter-sphere spacing from these images problematic. Nevertheless, values around 35 nm between the centres of adjacent spheres could be measured throughout the image. The spherical domains were seen for all samples with no apparent evidence of cylinders, for example areas of HCP packing or side-on cylinders, which is in agreement with the lack of higher order reflections in the SAXS data.

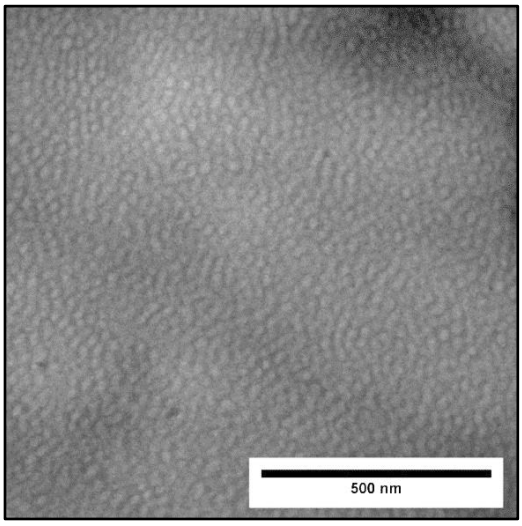

Figure 3-6. Representative TEM image for **P-3-M1(82)-COOH(18)** showing disordered spheres of PS in a darker matrix of the LC-functionalised PMVS.

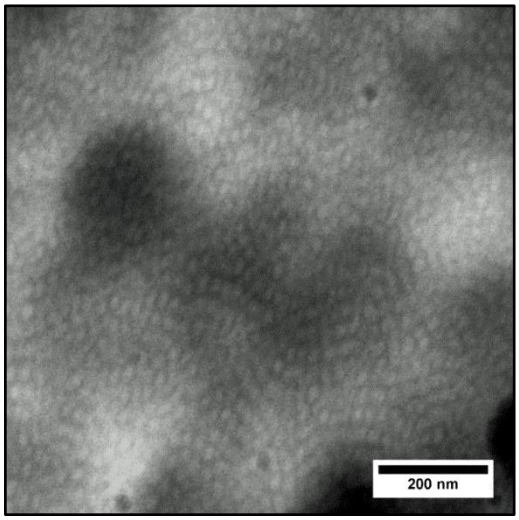

Figure 3-7. Representative TEM image for **P-3-M2(80)-COOH(20)** showing disordered spheres of PS in a darker matrix of the LC-functionalised PMVS.

3.2.2.3. P-3-M1(65)-COOH(35)

A scaled-up functionalisation of **P-3** with **M1** was carried out which afforded **P-3-M1(65)-COOH(35)** (Section 2.2.4.4.). Whilst the lower level of mesogen loading was not predicted to result in a different morphology to that seen for **P-3-M1(82)-COOH(18)**, further SAXS experiments were carried out on a film of this polymer as the microphase separated morphology is critical to the elastomeric properties of the LCE. As expected, the undeformed sample gave results indicative of an isotropic structure, with the azimuthal integration of the SAXS data given in Figure 3-8. As before, two peaks were seen. However, in this case they were located at values equivalent to q^* and $2q^*$. This ratio can be characteristic of a lamellar microstructure, although the calculated volume fraction for the PS block of 0.20 is too low for this morphology to be expected. A reflection at $2q^*$ can also arise due to a cylindrical microstructure, however, further peaks would again be expected, with the HCP structure expected to result in a peak at $\sqrt{3}q^*$.[13] The fact that no further reflections are seen in the SAXS data, combined with the values for the volume fraction of the PS block, suggests that the second peak instead arises due to the spherical form factor, with the radius of the spheres increasing relative to **P-3-M1(82)-COOH(18)** due to the increased volume fraction of the PS block. It is therefore most likely that **P-3-M1(65)-COOH(35)** consists of spheres of PS in a matrix of PMVS with an average radius of 20 nm and an average inter-sphere distance of 39.8 nm. Without TEM images this remains a suggested structure, but from the data available and the TEM images for **P-3-M1(82)-COOH(18)**, is the most likely scenario.

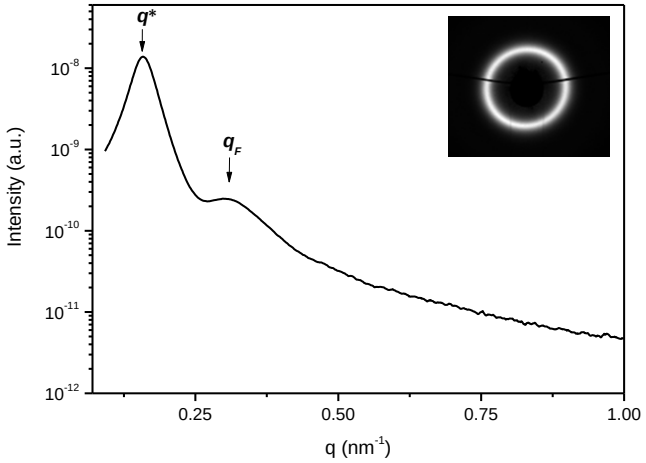

Figure 3-8. Background subtracted room temperature SAXS data for **P-3-M1(65)-COOH(35)** after azimuthal integration. The q^* peak at 0.158 nm^{-1} corresponds to an average inter-sphere spacing of 39.8 nm, whilst the q_F peak around 0.31 nm^{-1} corresponds to an average sphere radius of 20 nm. Inset – 2D SAXS pattern showing isotropic scattering.

Using the calculated interaction parameter and volume fraction it was predicted that these LC-functionalised polymers would microphase segregate to form either body-centred-cubic (BCC) spheres or a hexagonally packed cylindrical morphology. The above results confirm that **P-3-M1(82)-COOH(18)** and **P-3-M1(65)-COOH(35)** adopt the spherical morphology required for thermoplastic elastomers, as well as having values for the T_g and T_{iso} in the appropriate range for room temperature actuation. Stretching of LCE films has been demonstrated to align the LC component to afford responsive materials,[3,7] and so the effect of tensile forces on the microphase morphology was investigated for these polymers to identify whether processing using shear is a viable method for obtaining actuating structures.

3.2.2.4. Manually Aligned P-3-M1(82)-COOH(18)

To determine what effect, if any, mechanical alignment of the polymer had on its morphology, a film of **P-3-M1(82)-COOH(18)** was annealed at 120 °C for two hours before manually stretching along its length and allowing to cool. In all SAXS experiments the aligned film was fixed such that its long axis (and so the alignment) was oriented along the 0° direction as defined in Figure 3-9. The elliptical nature of the 2D SAXS result suggests that the sample has an anisotropic structure, with a reduction in inter-sphere spacing occurring in the 90° direction and an increase in the 0° direction, whilst the broad regions of increased intensity suggest that the PS domains are polydisperse and not strongly oriented.

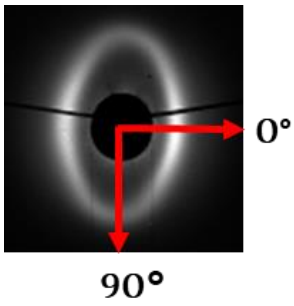

Figure 3-9. Definition of 0° and 90° directions used for anisotropic integrations of SAXS results for **P-3-M1(82)-COOH(18)**.

A strongly elliptical response, with a significant contraction in reciprocal space along the direction of the tensile stretch, has been reported previously for a thermoplastic polyurethane elastomer.[22] When uniaxial tension is applied to a block copolymer with a spherical morphology there are two potential deformations that can occur, as illustrated in Figure 3-10. In the first, both the hard and soft domains deform equally (affine deformation). In this scenario, an elliptical scattering pattern with equal intensity in all directions is expected. In the second case, the spherical domains change their position relative to each other, but their shapes remain undeformed. A model which combined the anisotropic scattering from the positions of the spheres in the lattice and the isotropic scattering arising from the undeformed spheres was reported by Blundell *et al*. and was shown to replicate the elliptical scattering with increased intensity in the meridional direction.[22] This deformation would be expected to occur for **P-3-M1(82)-COOH(18)** as the hard PS spheres will have a greater resistance to deformation than the soft PMVS block. The aligned films of LC-functionalised **PS-*b*-PMVS-*b*-PS** can therefore be treated as a continuous soft phase of PMVS containing hard, undeformed PS particulates.

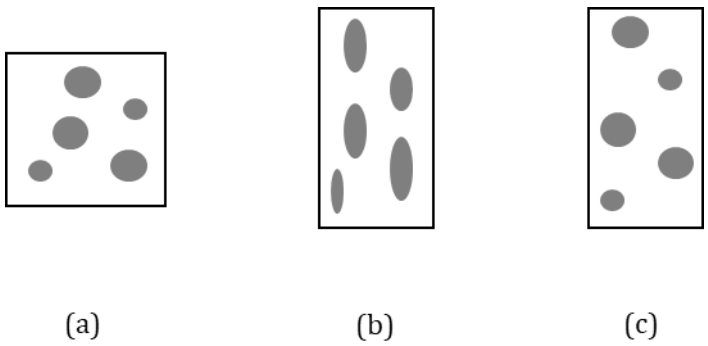

Figure 3-10. Distribution of spherical hard domains in a soft phase for (a) undeformed polymer, (b) after deformation of both phases and (c) after deformation of soft phase only.

A model for the affine deformation of the PMVS block with hard PS particles based on that reported by Blundell *et al*. was created and used to fit the experimental data collected for **P-3-M1(82)-COOH(18)**, with the results for the radius of the PS domains and the inter-sphere spacing presented in Table 3-3. It was also possible to calculate the strain applied to the film, presented as the draw ratio, with an increase from 1.10 for the unstretched film to 1.41 for the stretched film observed. The increased level of deformation in the stretched film was confirmed by the increase in the d-spacing.

Table 3-3. Results for model fit and experimental SAXS results for comparison.

Sample	PS Radius (nm)	d-spacing (nm)	Draw Ratio
Unstretched P-3-M1(82)-COOH(18)	12.70 ± 0.02	31.40 ± 0.02	1.10
SAXS	*15*	*36.1*	
Stretched P-3-M1(82)-COOH(18)	12.06 ± 0.02	32.39 ± 0.06	1.41
SAXS	*14*	*32-47*	

The model replicated the 2D scattering result both in terms of the shape (spherical or elliptical) and also the intensity for both samples (Figure 3-11), suggesting that it captured the internal structure of the two films, although the intensity in the vertical direction was greater for the experimental data than the results of the model.

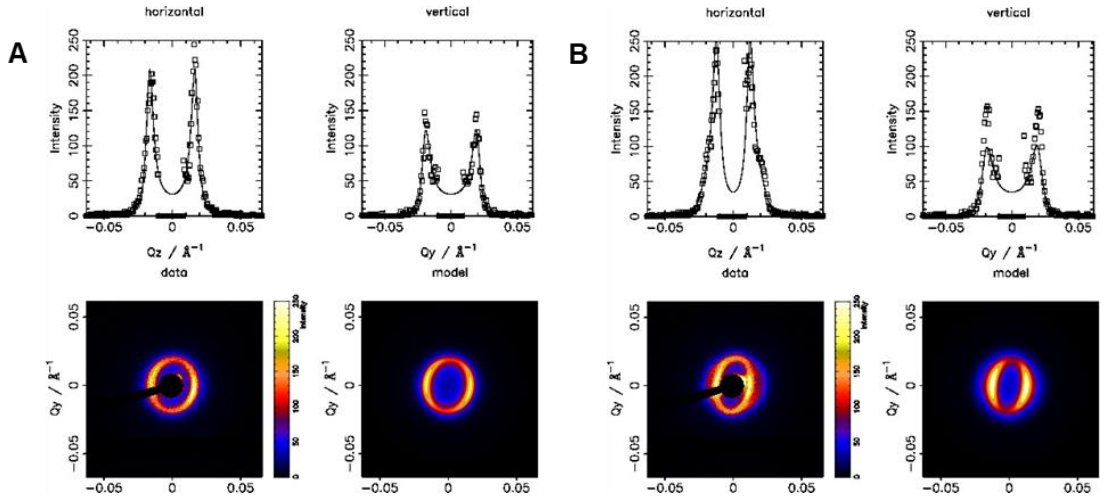

Figure 3-11. Comparison of model results with experimental data for (A) undeformed and (B) deformed films of **P-3-M1(82)-COOH(18)**.

The proposed deformation mechanism was also supported by TEM, with a representative image given in Figure 3-12. The PS domains, although faint, appear to be circular and not elongated (some deformation is expected from microtoming). Regions of linearly-aligned domains are also apparent, suggesting that the spheres had rearranged relative to one another in the soft PMVS phase. This alignment was not strong, with the trend limited to relatively small regions before the preferred direction appeared to change.

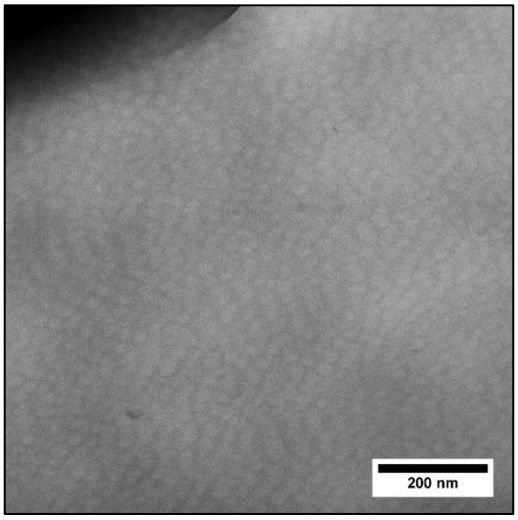

Figure 3-12. Representative TEM image for aligned **P-3-M1(82)-COOH(18)** showing spheres of PS in a darker matrix of LC-functionalised PMVS.

Given the anisotropy of the scattering, it was not appropriate to average the data over the full azimuthal range. The film was stretched uniaxially above the T_g of both the PMVS and PS blocks and the T_{iso}, which would be expected to increase the average centre-to-centre spacing between spherical domains along the direction of stretch, with a corresponding contraction occurring perpendicular to it. The SAXS data was therefore re-integrated first in the 0 ° (-5 to 5°) and then the 90° (85 to 95°) direction (as defined in Figure 3-9), with the results given in Figure 3-13.

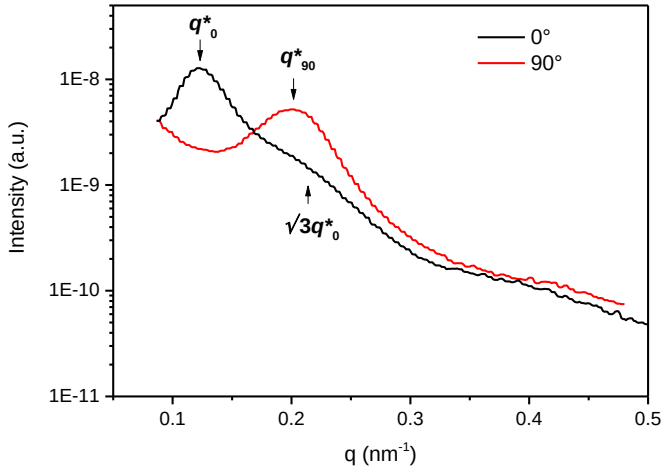

Figure 3-13. Background subtracted room temperature SAXS data for aligned **P-3-M1(82)-COOH(18)** after integrating around the 0° or 90° direction. The q^* peak for the 0° direction at 0.123 nm^{-1} corresponds to an average spacing of 51.9 nm, and that in the 90° direction at 0.217 nm^{-1} corresponds to an average inter-sphere spacing of 29.0 nm.

The film was aligned such that the direction of stretch was along the 0° direction, with the plot obtained by integrating in this direction featuring a peak that corresponded to a spacing of 51.9 nm. In the 90° direction an average spacing of 29.0 nm was measured which, when compared with the equilibrium spacing of 36 nm, indicated that the stretching process acted to reduce the spacing between deformed spheres perpendicular to the stretch and increase it along the stretch direction. A broad shoulder was observed on the q^* peak in the 0° direction around 0.2 nm^{-1}, which is the value expected for the $\sqrt{3}q^*$ peak seen for an HCP arrangement. This suggests that the overall level of order of the spherical PS domains had increased in the direction of the stretch. With this information it is expected that the stretched film should demonstrate responsive behaviour, whether to irradiation with UV or by heating through T_{iso}, the action of drawing out the PS spheres should also act to align the PMVS chains and so increase the anisotropy of the nematic mesophase (which will align parallel to the PMVS chain)[10] such that switching between the nematic and isotropic states should have a non-negligible impact on the conformation of the surrounding polymer chains.

3.2.2.5. Manually Aligned P-3-M1(65)-COOH(35)

As with **P-3-M1(82)-COOH(18)**, a film of **P-3-M1(65)-COOH(35)** was stretched along its length whilst heated above the T_{iso} in order to promote alignment of the LC mesophase. This resulted in a slightly elliptical detector image, with increased intensity in the 130° direction, as seen in Figure 3-14. From this image it would appear that the level of alignment achieved in this film was lower than that seen for **P-3-M1(82)-COOH(18)** due to the relatively wide ellipse.

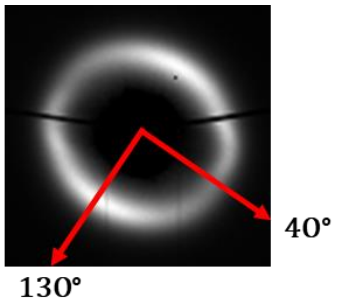

Figure 3-14. Definition of 40° and 130° directions used for anisotropic integrations of SAXS results for **P-3-M1(65)-COOH(35).**

The broad nature of the features on the azimuthal plot, combined with the elliptical detector image, suggests an anisotropic structure was obtained and so the data was integrated over the apparent direction of alignment (130° as determined by the detector image, integrated from 125-130°) and in the perpendicular direction (40°, integrated from 35-45°). This resulted in two plots which were not as strongly separated as those seen for **P-3-M1(82)-COOH(18)**, confirming the lower level of alignment achieved, but which still demonstrated a clear difference in the inter-sphere spacings in the two perpendicular directions (Figure 3-15).

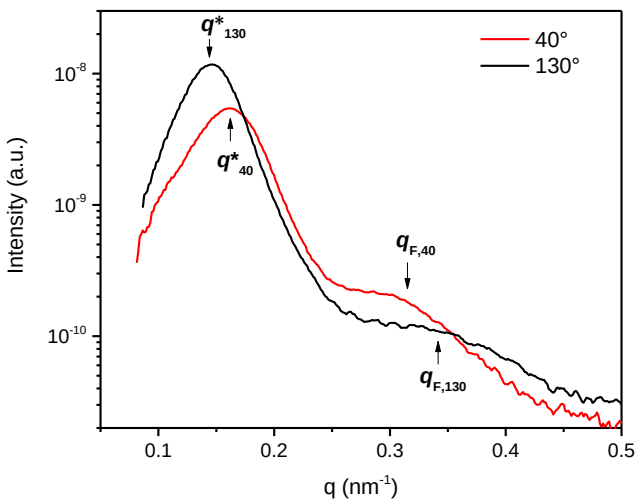

Figure 3-15. Background subtracted room temperature SAXS data for aligned **P-3-M1(65)-COOH(35)** after integrating around the 40° or 130° direction. The q^* peak for the 40° direction at 0.150 nm^{-1} corresponds to an average inter-sphere spacing of 42.5 nm, and that in the 130° direction at 0.165 nm^{-1} corresponds to an average inter-sphere spacing of 38.1 nm. The q_F peaks around 0.37 nm^{-1} in the 40° and 0.31 nm^{-1} in the 130° direction indicate an average sphere radius of 17 and 20 nm respectively.

In the 130° direction the q^* peak had shifted to give an inter-sphere spacing of 42.5 nm, which was greater than that measured for the as-cast film. The spherical form factor peak showed a reduced intensity and was shifted towards higher q values, indicating an average sphere radius around 17 nm. This was smaller than that seen for the as-cast film, which would not be expected along the direction of stretch. However, it has been shown that the level of alignment was relatively low in this sample, and so the spheres are only weakly oriented along a common direction. Integrating over just 10° of the 2D SAXS scattering result will therefore capture contributions from a small sample size, with the weak nature of this peak confirming a broad distribution of values for the radius.

In the 40° direction the average inter-sphere spacing had shifted to 38.1 nm, slightly smaller than for the as-cast film. The spherical form factor peak was again broad and centred around values of q indicative of a 20 nm radius. The deformation therefore had little effect on the shape of the PS domains in this direction. This result confirmed that both **P-3-M1(82)-COOH(18)** and **P-3-M1(65)-COOH(35)** adopt the spherical morphology required for elastomeric behaviour, although it was shown that the manual alignment technique did not result in reproducible levels of alignment. The microphase separated morphology adopted by both polymers was next investigated on heating through the T_{iso} in order to identify whether either demonstrated a shape-change on switching between the nematic and isotropic states.

3.2.3. Effect of Isotropic Transition on Polymer Morphology

Actuation in this polymeric system arises on switching between the ordered nematic mesophase and disordered isotropic state of the mesogenic groups attached to the PMVS block. This can be achieved through either irradiation with UV light with a wavelength of 365 nm, or by heating through the T_{iso} (measured to be 118 °C for **P-3-M1(82)-COOH(18)** and 99 °C for **P-3-M1(65)-COOH(35)** by DSC). This process would be expected to affect the morphology of the polymer by changing the packing of polymer chains within the PMVS domains and may potentially trigger an order-disorder transition on attainment of an isotropic state.[23,24] The microphase separation above the T_{iso} was therefore probed using VT-SAXS. In these experiments a film of the aligned polymer was heated to 80 °C and allowed to equilibrate before cycling twice between 80 and 150 °C, with measurements taken on both the heating and cooling cycles. A heating rate of 10 °C per minute was used, with one heating cycle taking 7 minutes. The kinetics of switching for a comparable thermoplastic LCE at room temperature were shown to be fast, with a total of 6 seconds required for contraction to occur on irradiation with UV light and 2 seconds for recovery back to the nematic state.[3] It is therefore expected that any change in morphology should be captured within the experimental timeframe.

3.2.3.1. Manually Aligned P-3-M1(82)-COOH(18)

The reduced data obtained from an azimuthal integration of the 2D SAXS result at the beginning and end of the two experimental cycles for **P-3-M1(82)-COOH(18)** are shown in Figure 3-16. At 80 °C the shoulder on the q^* peak was still resolved as at room temperature, but on heating through T_{iso} for the first time the intensity of this peak decreased, indicating a decreased level of long-range order present in the polymer. However, the intensity of this peak remained significant on each cycle, which suggests that the microphase segregated morphology was maintained. This implies that the T_{ODT} for this polymer is higher than 150 °C, although the overall low level of order adopted by the PS spheres would make unambiguous identification of the order-disorder transition by SAXS difficult.

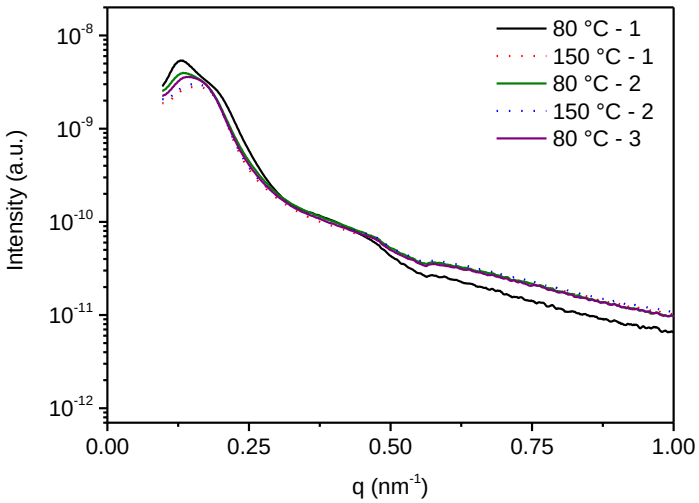

Figure 3-16. Background subtracted VT-SAXS data for aligned **P-3-M1(82)-COOH(18)** taken after equilibrating at 80 °C, then heating to 150 °C and cooling to 80 °C for two cycles. The q^* peak retains a shift towards increased spacing after heating through T_{iso}, suggesting that the anisotropic structure obtained by stretching remains to some extent after two heating cycles.

The broad nature of the q^* peak for each measurement after the first heating cycle, particularly in the case of the measurements taken at 80 °C, suggests an anisotropic morphology still existed at all temperatures and so the data was re-integrated along the 0° and 90° directions as in Section 3.2.2.4. These results are given in Figure 3-17, focussing only on the q^* peak for clarity as no change was evident in the spherical form factor peak, as shown in Figure 3-16. When integrating in the 0° direction the intensity of the q^* peak decreased on heating through T_{iso} and then increased slightly on cooling back to 80 °C. This suggested that the alignment achieved by the stretching process was gradually reduced once the isotropic state was reached, with the nematic mesophase reforming to some extent on cooling back below T_{iso}. The spacing between PS spheres remained greater than that seen for the as-cast film, suggesting that the anisotropy had not been fully lost, but the spacing and intensity decreased towards the equilibrium value with each heating cycle. This behaviour is expected for high molecular weight LCPs adopting a spherical morphology,[23] and it would therefore be expected that the undeformed morphology would be regained by heating the sample to a higher temperature or for a longer period of time than that encountered during this experiment.

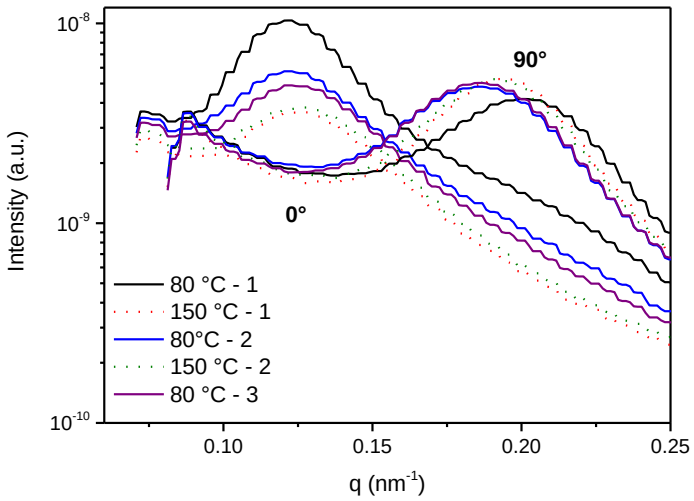

Figure 3-17. Background subtracted VT-SAXS data for aligned **P-3-M1(82)-COOH(18)** after integrating around the 0° or 90° direction only. The two peaks remain separated, with the intensity of the 0° direction peak decreasing with increasing numbers of heating/cooling cycles indicating a decrease in the level of long-range order in the sample.

The values for the peaks in reciprocal space in both directions and their corresponding d-spacings are listed in Table 3-4, from which it is apparent that on heating from 80 to 150 °C for the first time the spacing along the 0° direction decreased (as did the intensity) and in the 90° direction it increased (with a slight increase in intensity). This suggests that on heating above the T_{iso} the mesogenic groups become more disordered as expected, and so distorted the alignment of the surrounding PMVS chains. This resulted in a contraction along the direction of the stretch as the aligned chains adopted a more coil-like structure, and a resulting expansion in the perpendicular direction to conserve volume.

The trend in the 0° direction repeated with each cycle, with the inter-sphere spacing decreasing on heating and increasing on cooling. This suggests that a significant level of the induced anisotropy remained despite twice heating above T_{iso}. In the 90° direction, however, after heating through T_{iso} once the spacing also decreased on heating and increased on cooling. This is opposite to the expected trend, and instead suggests that on reforming the nematic mesophase after the first heating/cooling cycle, a portion of the LC domains re-oriented along the 90° direction.

Table 3-4. Locations of peaks for VT-SAXS on aligned **P-3-M1(82)-COOH(18)** from integrating in the 0° and 90 ° directions, and the corresponding spacing size.

	0°		90°	
	q (nm^{-1})	d-spacing (nm)	q (nm^{-1})	d-spacing (nm)
80 °C – 1	0.121	51.9	0.206	31.5
150 °C – 1	0.127	49.5	0.192	32.7
80 °C – 2	0.122	51.5	0.184	34.1
150 °C – 2	0.127	49.5	0.192	32.7
80 °C – 3	0.126	49.9	0.184	34.1

For both peaks the measured changes in spacings were small, suggesting that the film was only weakly aligned, which is in agreement with the low order indicated by TEM. The level of alignment was quantified by calculating the Herman orientation parameter, *f(H)*, for the PS domains in each frame captured during the variable temperature experiment. This figure indicates the degree of orientation with respect to some starting angle by integrating the intensity, *I*, at azimuthal angle, ϕ, over $\pi/2$ radians and is calculated using Equation 3.6:

$$f(H) = \frac{3\langle cos^2\phi\rangle - 1}{2} \qquad 3.6$$

where $\langle cos^2\phi\rangle = \frac{\sum_{i=o}^{i=\pi/2} I_i cos^2\phi_i \, sin\phi_i}{\sum_{i=o}^{i=\pi/2} I_i sin\phi_i}$

An orientation parameter of 1 would therefore indicate perfect alignment along the starting angle, whilst one of 0 would indicate an isotropic structure and a value of -0.5 indicates perfect alignment perpendicular to the starting direction. Example 2D SAXS results used for the analysis and the starting direction for the integration are shown in Figure 3-18. The integration measured the intensity, *I*, recorded at each azimuthal angle, ϕ, and therefore the orientation parameter was obtained for the alignment of the PS domains relative to the 0° direction. The orientation parameter will therefore not measure the alignment within the nematic mesophase directly, but it is expected that the mesophase will align parallel to the PMVS chains and so the direction of stretch. It was shown in Section 3.2.2.4. that the PS domains align along the direction of the stretch, and so the orientation parameter offers some insight into the overall order of the system.

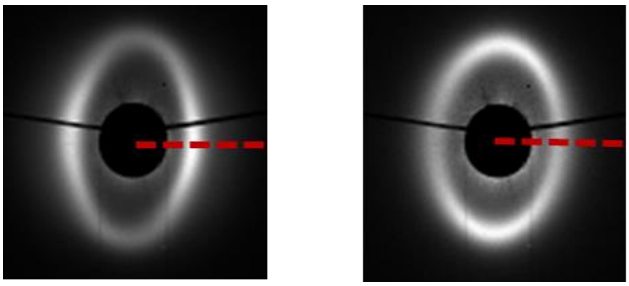

Figure 3-18. Background subtracted 2D SAXS results for aligned **P-3-M1(82)-COOH(18)** at 80 °C (left) and 150 °C (right). Dashed line indicates 0° direction used for Herman orientation parameter calculation.

For the aligned film of **P-3-M1(82)-COOH(18)** the orientation parameter was calculated starting from the direction with the most intense scattering, 0°. From Figure 3-19 it can be seen that *f(H)* was relatively constant from 80 to 100 °C, where it started to decrease as the temperature passed through T_{iso} at 120 °C and then reached a minimum around 140 °C. On cooling back to 80 °C, *f(H)* increased again on passing through T_{iso} and the trend repeated on the second heating/cooling cycle.

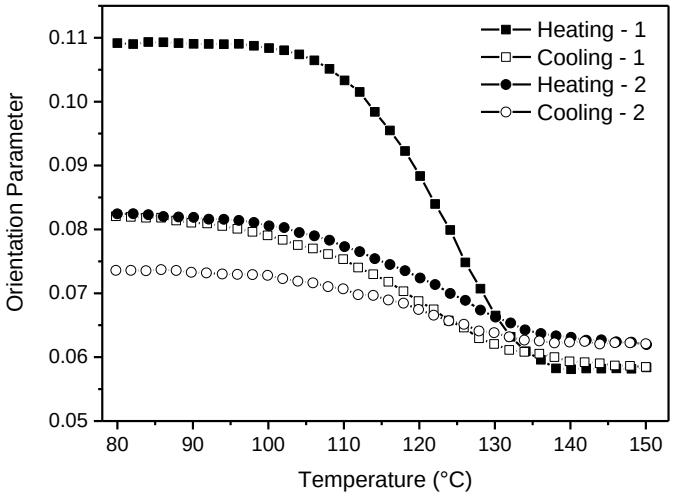

Figure 3-19. Calculated values for the Herman orientation parameter for aligned **P-3-M1(82)-COOH(18)** on heating (filled) and cooling (unfilled). A decrease in *f(H)* is seen centred around T_{iso} of 120 °C for heating cycles and an increase on cooling cycles, suggesting the nematic mesophase is lost on heating but reforms to some extent on cooling.

As with the intensity of the 0° peak in the VT-SAXS data, it was clear that after heating through T_{iso} for the first time the original level of order was not regained, with the value of *f(H)* dropping from 0.11 to around 0.08 as no deformation was applied at elevated temperatures in order to reproduce the more aligned starting state. Another important contributor to the loss of order was that the PS domains were repeatedly heated above the measured T_g of 96 °C, and so at 150 °C would not be acting as the 'hard' block of glassy domains required to fix the order of the softer PMVS block, which increased the overall mobility of the polymer chains. The low magnitude of *f(H)* is expected as from the SAXS results it was apparent that the triblock copolymer remained microphase separated at 150 °C, therefore, when the film was stretched the polymer chains were being aligned in a relatively inflexible matrix reinforced by the PS domains which would not allow for significant deformations to occur.

3.2.3.2. Manually Aligned P-3-M1(65)-COOH(35)

By inspection of the 2D SAXS results and the results of the integration in the 40 and 130° directions (Figure 3-15) it was concluded that the level of order achieved in the film of **P-3-M1(65)-COOH(35)** was lower than that seen for **P-3-M1(82)-COOH(18)**. On integrating the 2D results of the VT-SAXS experiments in these directions only, the peaks representative of the inter-sphere spacing did not show a large decrease in intensity on heating above T_{iso}, which suggests that the polymer was below the T_{ODT} at 150 °C. The two peaks measured for the inter-sphere spacing did not demonstrate a clear separation, with the locations of the peaks in reciprocal space and their corresponding spacing values given in Table 3-5.

Table 3-5. Locations of peaks for VT-SAXS on aligned **P-3-M1(65)-COOH(35)** from integrating in the 40° and 130° directions, and the corresponding spacing.

	40°		**130°**	
	q (nm^{-1})	**d-spacing (nm)**	**q (nm^{-1})**	**d-spacing (nm)**
80 °C – 1	0.161	39.1	0.145	42.5
150 °C – 1	0.160	39.4	0.152	41.4
80 °C – 2	0.162	38.8	0.154	40.7
150 °C – 2	0.159	39.4	0.152	41.4
80 °C – 3	0.162	38.8	0.153	40.7

In the 130° direction there was a clear decrease in intensity of the q^* peak on heating through T_{iso} as the spacing in this direction returned towards that seen in the as-cast state (Figure 3-20). The spacing decreased further on cooling back through the T_{iso}, and from then on the spacing increased on heating and decreased on cooling. This trend indicated that the low level of order was lost after heating through T_{iso} once, as the polymer then demonstrated an isotropic response to heating and cooling. These results provide a contrast to those seen for **P-3-M1(82)-COOH(18)**, where the increased level of alignment meant that the anisotropic response of the LCE was retained (albeit to a considerably lesser extent) after two heating cycles.

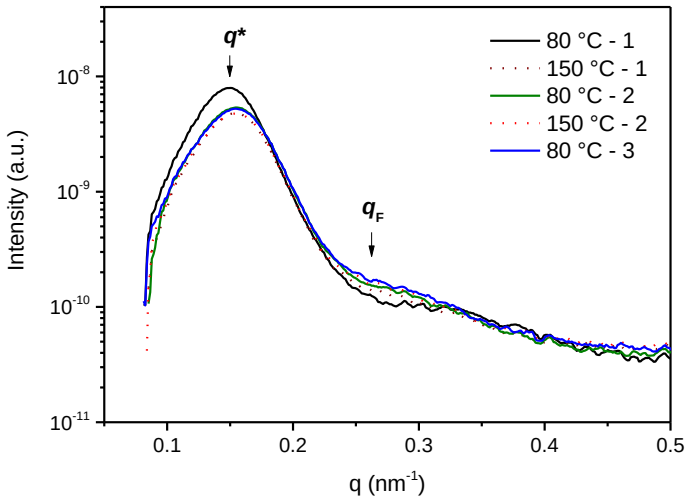

Figure 3-20. Background subtracted VT-SAXS data for aligned **P-3-M1(65)-COOH(35)** after integrating around the 130° direction. After heating through T_{iso} the intensity of the q^* peak decreases, and the spacing shifts towards larger values in reciprocal space. The change in spacing then follows the trends expected of an isotropic structure. The arrow indicates the location of spherical form factor peak, which increases in intensity with each cycle.

In the 40° direction there was an initial increase in the spacing between spheres on heating from 80-150 °C (Figure 3-21). On cooling the intensity of the q^* peak increased and the spacing shifted to slightly smaller values. From then on, the spacing increased on heating and reduced on cooling, with values approaching that of the equilibrium state. The fact that this response was seen in both directions after heating through T_{iso} for the first time confirms that the level of long-range order in the sample was reduced to the extent that the material displayed essentially isotropic behaviour.

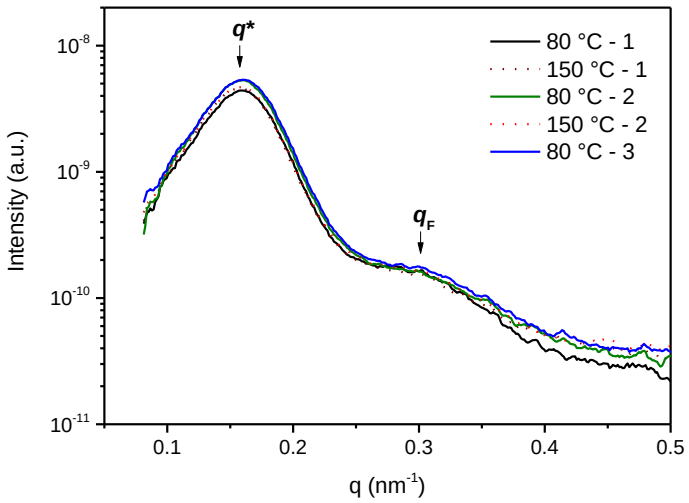

Figure 3-21. Background subtracted VT-SAXS data for aligned **P-3-M1(65)-COOH(35)** after integrating around the 40° direction. After heating through T_{iso} the intensity of the q^* peak decreases, and the spacing shifts towards larger values in reciprocal space. The change in spacing then follows the trends expected of an isotropic material.

The Herman orientation parameter was calculated for **P-3-M1(65)-COOH(35)** over π/2 radians using Equation 3.6. This measurement was only made for the results of the first heating and cooling cycle, as after this isotropic behaviour was observed. The integration was started from the low intensity 40° direction in order to avoid interference by scattering from the beamstop, with the starting direction and example 2D SAXS results given in Figure 3-22.

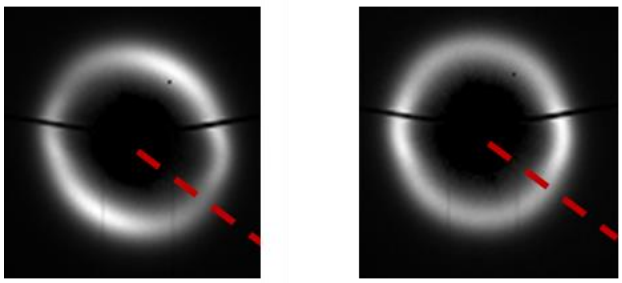

Figure 3-22. Background subtracted 2D SAXS results for aligned **P-3-M1(65)-COOH(35)** at 80 °C (left) and 150 °C (right). Dashed line indicates 40° direction used for Herman orientation parameter calculation.

The resulting plot of *f(H)* with temperature is given in Figure 3-23, where the trend in calculated orientation parameter with temperature was inverted with respect to that seen in Figure 3-19 as the alignment occurred perpendicular to the starting direction. On the first heating cycle a decrease in the orientation parameter was clear, however, the values of *f(H)* obtained after the first heating cycle did not trend towards zero, suggesting that they were offset, potentially due to the overall low level of alignment in the sample. For this reason, the trend presented by the results should remain valid, but the overall low order of PS spheres mean it is not meaningful to quote a value for the orientation parameter.

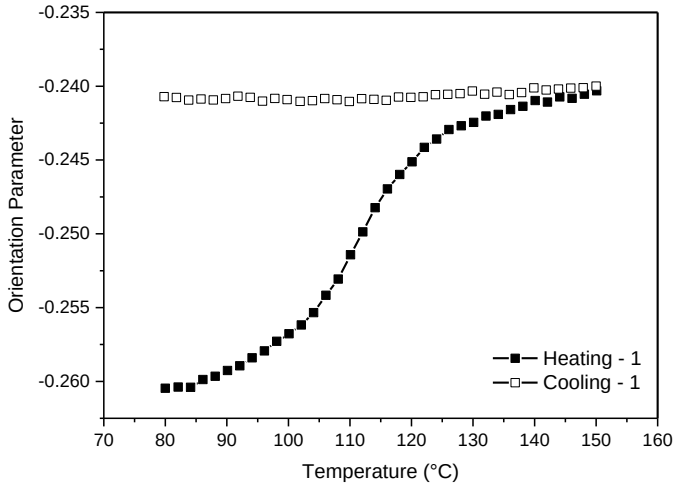

Figure 3-23. Calculated values for the Herman orientation parameter for aligned **P-3-M1(65)-COOH(35)** on heating (filled) and cooling (unfilled). A decrease in *f(H)* is seen starting from 85 °C and increasing in rate from the T_{iso} of 99 °C for the first heating cycle. After this cycle it was apparent that the material adopted an isotropic structure.

Importantly, the decrease in *f(H)* started at a lower temperature than that seen for **P-3-M1(82)-COOH(18)**, with the onset occurring around 85 °C, compared with 100 °C. Both polymers are based on the same **PS-*b*-PMVS-*b*-PS** triblock copolymer backbone, and so if the change in orientation parameter was due to heating above the T_g of the PS block it would be expected that the transition would occur over the same temperature range. The fact that it appears to shift with the T_{iso} suggests that it is the nematic-isotropic transition driving the change in order, and so confirms the responsive nature of these LCEs.

3.3. Conclusions

Using a combination of SAXS and TEM it was shown that the LC-functionalised triblock copolymers adopt the predicted spherical morphology required for use as thermoplastic elastomers. In all cases the PS spheres demonstrated low long-range order, even for the manually aligned samples, and this was confirmed by the relatively low orientation parameter calculated for the stretched film of **P-3-M1(82)-COOH(18)** of 0.11. The anisotropic microphase structure of the deformed films was confirmed by integrating the 2D SAXS results in the direction of the stretch and perpendicular to it, with the tensile deformation demonstrated to increase the inter-sphere spacing along the stretch direction and to reduce it in the perpendicular direction. The SAXS data could be fit using a model combining an affine deformation of the PMVS block with hard, undeformed spheres of PS. Much weaker alignment was seen for **P-3-M1(65)-COOH(35)** than for **P-3-M1(82)-COOH(18)**, which demonstrates the limitations of the crude manual alignment method employed, which is inherently incapable of producing reproducible levels of alignment.

Despite the weak long-range order present for the PS domains, it was demonstrated that films of **P-3-M1(82)-COOH(18)** showed a measurable response to both heating through the T_{iso} and triggering the transition to the disordered isotropic LC state by irradiation with UV light (Chapter 2). This confirmed that measurement of the level of order present between the PS domains could be used to approximate the level of order within the nematic mesophase. It is expected that the stronger the alignment, the stronger its response to UV irradiation or heating would be, and so in order to produce a more effective actuator alternative processing methods that induce high shear forces on the material in a liquid-like state would be highly beneficial in order to maximise the shape-changing response. For this reason, the suitability of these polymers for processing by melt extrusion (Chapter 4) and from solution by electrospinning (Chapter 5) will be determined.

3.4. Experimental

3.4.1. Sample Preparation

Thin films of **P-3**, **P-3-M1(82)-COOH(18)**, **P-3-M1(65)-COOH(35)** and **P-3-M2(80)-COOH(20)** were prepared by solvent casting from toluene before annealing at 120°C for 2 hours. A second film of **P-3-M1(82)-COOH(18)** and **P-3-M1(65)-COOH(35)** was also stretched uniaxially whilst at 120 °C before allowing to cool to promote alignment of the LC component.

3.4.2. SAXS

Room temperature SAXS experiments for **P-3-M1(82)-COOH(18)** without alignment were carried out using a Ganesha SAXS/WAXS instrument (Xenocs) at room temperature, using a Cu Kα source (1.5406Å) over a Q-range of 0.001 < Q < 0.7 $Å^{-1}$ and an exposure time of 1800 seconds. Data were visualized and reduced using SAXSGUI. Scattering patterns were normalised against the transmitted beam intensity and corrected for background scattering.

All other polymers, and the VT-SAXS experiments, were carried out at beamline I22 at the Diamond Light Source with a wavelength of 1 Å and using a Pilatus P3-2M detector with a Linkam DSC heating stage. Sample films were sandwiched between Kapton in a DSC pan. Room temperature experiments were carried out at 30 °C. One frame was captured after 200 milliseconds wait time with an exposure time of 1 second. For variable temperature experiments the film was first heated to 80 °C and allowed to equilibrate, before ramping between 80-150 °C at a rate of 10 °C per minute for two full heating/cooling cycles. For all data collected, results were processed using DAWN to generate the reduced data. First the background frame collected for a pan containing only Kapton was subtracted followed by an azimuthal integration. The reduced data was then normalised against the transmitted beam intensity and multiplied by the scaling factor to give results as absolute intensity. For samples showing anisotropy, the data was also integrated over 10° centred on the alignment direction of the sample and the direction perpendicular to alignment.

Peak values in reciprocal space were calculated to four decimal places from the reduced data as local maxima using Origin 9.1 and rounded to 3 significant figures. For broad form factor peaks with no clear maximum the value was quoted to 2 significant figures.

Data were fit to a model describing affine deformation with hard particles by Professor Robert Richardson at the University of Bristol. Data was fitted with Porod constant = 0 and an interface thickness of 1, with further parameters given in Table 3-6.

Table 3-6. Parameters obtained from fitting of SAXS data for stretched and unstretched **P-3-M1(82)-COOH(18)**.

Sample	Number of points	Standard Deviation (nm^{-1})	PDI of Radius	Tilt Direction (°)	Reduced χ^2
P-3-M1(82)-COOH(18) Stretch	31,725	10.3	1.02	-8.7	1.27
P-3-M1(82)-COOH(18) No stretch	31,725	8.3	1.03	-10.8	0.77

3.4.3. TEM

TEM images were taken by Dr Jean-Charles Eloi at the University of Bristol.

Annealed films as prepared for SAXS measurements were adhered to epoxy stubs before sectioning using a microtome. The sections were floated on water and collected on copper grids (Agar Scientific, mesh 400). Films were imaged using a Jeol 1400 TEM operating at 120 kV and equipped with a Gatan digital camera. Radius of spheres and spacings were measured using ImageJ.

3.5. References

1 T. J. White and D. J. Broer, Programmable and Adaptive Mechanics with Liquid Crystal Polymer Networks and Elastomers, *Nat. Mater.*, 2015, **14**, 1087–1098.

2 R. J. Spontak and N. P. Patel, Thermoplastic Elastomers: Fundamentals and Applications, *Curr. Opin. Colloid Interface Sci.*, 2000, **5**, 334–341.

3 M. Petr, B. A. Katzman, W. Dinatale and P. T. Hammond, Synthesis of a New, Low-Tg Siloxane Thermoplastic Elastomer with a Functionalizable Backbone and Its Use as a Rapid, Room Temperature Photoactuator, *Macromolecules*, 2013, **46**, 2823–2832.

4 H. Mensinger, A. Biswas and H. Poths, Small-Angle X-Ray Scattering Investigations of Novel Superstructures in Combined Chiral Liquid Crystalline Polymers, *Macromolecules*, 1992, **25**, 3156–3163.

5 S. K. Ahn, P. Deshmukh, M. Gopinadhan, C. O. Osuji and R. M. Kasi, Side-Chain Liquid Crystalline Polymer Networks: Exploiting Nanoscale Smectic Polymorphism to Design Shape-Memory Polymers, *ACS Nano*, 2011, **5**, 3085–3095.

6 S. Dey, D. Agra-Kooijman, W. Ren, P. J. McMullan, A. C. Griffin and S. Kumar, Soft Elasticity in Main Chain Liquid Crystal Elastomers, *Crystals*, 2013, **3**, 363–390.

7 Z. Pei, Y. Yang, Q. Chen, E. M. Terentjev, Y. Wei and Y. Ji, Mouldable Liquid-Crystalline Elastomer Actuators with Exchangeable Covalent Bonds, *Nat. Mater.*, 2014, **13**, 36–41.

8 T. Ube, K. Kawasaki and T. Ikeda, Photomobile Liquid-Crystalline Elastomers with Rearrangeable Networks, *Adv. Mater.*, 2016, **28**, 8212–8217.

9 B. Ni, H. Lou Xie, J. Tang, H. L. Zhang and E. Q. Chen, A Self-Healing Photoinduced-Deformable Material Fabricated by Liquid Crystalline Elastomers Using Multivalent Hydrogen Bonds as Cross-Linkers, *Chem. Commun.*, 2016, **52**, 10257–10260.

10 G. R. Mitchell, F. J. Davis, W. Guo and R. Cywinski, Coupling between Mesogenic Units and Polymer Backbone in Side-Chain Liquid Crystal Polymers and Elastomers, *Polymer*, 1991, **32**, 1347–1353.

11 T. Kota, K. Imaizumi, S. Sasaki and S. Sakurai, Spontaneous Enhancement of Packing Regularity of Spherical Microdomains in the Body-Centered Cubic Lattice upon Uniaxial Stretching of Elastomeric Triblock Copolymers, *Polymers (Basel).*, 2011, **3**, 36–50.

12 S. Tomita, I. Wataoka, N. Igarashi, N. Shimizu, H. Takagi, S. Sasaki and S. Sakurai, Strain-Induced Deformation of Glassy Spherical Microdomains in Elastomeric Triblock Copolymer Films: Time-Resolved 2D-SAXS Measurements under Stretched State, *Macromolecules*, 2017, **50**, 3404–3410.

13 H. Schnablegger and Y. Singh, *The SAXS Guide*, Anton Paar, Graz, 4th edn., 2017.

14 M. Anthamatten and P. T. Hammond, Free-Energy Model of Asymmetry in Side-Chain Liquid-Crystalline Diblock Copolymers, *J. Polym. Sci. Part B Polym. Phys.*, 2001, **39**, 2671–2691.

15 D. W. van Krevelen, *Properties of Polymers*, Elsevier, Amsterdam, 3rd edn., 1997.

16 M. W. Matsen and R. B. Thompson, Equilibrium Behavior of Symmetric ABA Triblock Copolymer Melts, *J. Chem. Phys.*, 1999, **111**, 7139–7146.

17 J. Brandrup, E. Immergut and E. A. Grulke, Eds., *Polymer Handbook*, John Wiley & Sons, New York, 3rd edn., 1990.

18 F. S. Bates, Polymer-Polymer Phase Behavior, *Science*, 1991, **251**, 898–905.

19 D. J. Kinning and E. L. Thomas, Hard-Sphere Interactions between Spherical Domains in Diblock Copolymers, *Macromolecules*, 1984, **17**, 1712–1718.

20 D. A. Rider, K. A. Cavicchi, K. N. Power-Billard, T. P. Russell and I. Manners, Diblock Copolymers with Amorphous Atactic Polyferrocenylsilane Blocks: Synthesis, Characterization, and Self-Assembly of Polystyrene-Block-Poly(Ferrocenylethylmethylsilane) in the Bulk State, *Macromolecules*, 2005, **38**, 6931–6938.

21 G. Shin, N. Sakamoto, K. Saijo, S. Suehiro, T. Hashimoto, K. Ito and Y. Amemiya, Time-Resolved SAXS Studies of a Sphere-Forming Block Copolymer under Large Oscillatory Shear Deformation, *Macromolecules*, 2000, **33**, 9002–9014.

22 D. J. Blundell, G. Eeckhaut, W. Fuller, A. Mahendrasingam and C. Martin, Real Time SAXS / Stress – Strain Studies of Thermoplastic Polyurethanes at Large Strains, *Polymer*, 2002, **43**, 5197–5207.

23 M. Anthamatten and P. T. Hammond, A SAXS Study of Microstructure Ordering Transitions in Liquid Crystalline Side-Chain Diblock Copolymers, *Macromolecules*, 1999, **32**, 8066–8076.

24 M. Yamada, T. Iguchi, A. Hirao, S. Nakahama and J. Watanabe, Side-Chain Liquid Crystal Block Copolymers with Well-Defined Structures Prepared by Living Anionic Polymerization I. Thermotropic Phase Behavior and Structures of Liquid Crystal Segment in Lamellar Type of Microphase Domain, *Polym. J.*, 1998, **30**, 23–30.

Chapter 4: Rheology of Thermoplastic Liquid Crystal Elastomers for Melt Processing

4.1. Introduction

Extrusion is a common processing technique for thermoplastic polymers, in which the material is heated to form a homogeneous melt and then forced through a shaped die in order to obtain the desired cross section. For the liquid crystal elastomers (LCEs) synthesised in Chapter 2, the high shear encountered during extrusion would be expected not only to shape the polymer, but also to align the liquid crystal (LC) component and form a nematic monodomain, and in doing so remove the need for a separate alignment step. Extrusion has previously been used to align a thermoplastic LCE which consisted of a soft and deformable main-chain liquid crystal polymer (LCP) midblock capped by two terphenyl moieties. After extrusion, an aligned fibre of the polymer was capable of a reversible contraction on heating through the isotropic transition temperature, T_{iso}, with a maximum strain of 500% being measured.[1] In order for melt extrusion to be a viable processing method, it is necessary that the polymer forms a liquid-like melt below the onset of thermal decomposition. For thermoplastic LCEs it is also necessary to consider the two key transition temperatures that determine the melt behaviour of the polymer, namely the order-disorder transition temperature (T_{ODT}) and the T_{iso}.

Block copolymers are processable by melt extrusion when heated above the T_{ODT}, when the microphase segregation between blocks is lost and the polymer exists as a homogeneous, liquid-like melt. Below the T_{ODT} block copolymers behave as filled polymers (systems mixed with hard particles), and so an elastic-like response to applied shear is seen.[2] The T_{ODT} can be determined experimentally by Variable Temperature Small Angle X-Ray Scattering (VT-SAXS), where the homogeneous state can be detected by the decrease in intensity and broadening of any peak characteristic of the self-assembled morphology, as well through the reduction in intensity of any higher order reflections.[3–5] Whilst this technique can be effective for highly ordered systems, it was shown in Chapter 3 that the LCEs in this work adopt a disordered spherical morphology, and so no higher order reflections were present in the SAXS data. This makes unambiguous identification of the T_{ODT} problematic, and so an alternative method using Small Amplitude Oscillatory Shear (SAOS) rheology was employed. Han and Kim demonstrated that a log-log plot of the storage modulus (G') against the loss modulus (G'') could be used to detect the T_{ODT} by identifying the point at which the material's response to applied shear becomes independent of temperature.[2] They also calculated that in the homogeneous state the plot should have a gradient

of 2 in the terminal (low frequency) region, giving another characteristic feature of the transition that is identifiable by SAOS.

The T_{iso} is also important, as below this temperature LCEs are expected to demonstrate behaviour similar to filled polymers, with aligned domains acting like nanoscale reinforcing components. On heating to the isotropic phase the polymer behaves as a liquid-like, random-coil polymer, and so this transition can be identified using the SAOS technique developed by Han and Kim for detecting T_{ODT}.[6] The VT-SAXS results from Chapter 3 suggested that a microphase segregated structure was still present at temperatures above the T_{iso} due to stabilisation of the nematic mesophase by the curvature of the spherical PS domains, which acted to raise the T_{ODT} above the T_{iso}. This effect was reported for literature examples of stabilised side-chain LC block copolymers, where it was shown that for block ratios resulting in spherical morphologies the T_{ODT} was shifted to values greater than the $T_{iso.}$ However, neither paper investigated the rheological behaviour of these materials in order to confirm whether a liquid-like response was eventually obtained above the T_{ODT}.[7,8]

Therefore, in order to determine the suitability of the LCEs described in Chapter 2 for processing by extrusion from a melt, SAOS measurements were carried out to measure the complex viscosity (η^*) and shear modulus (G^*) at several temperatures and across a range of frequencies. The rheological behaviour of side-chain thermoplastic LCEs has not been reported, and so experiments were conducted to isolate the effects of the microphase segregation of the triblock copolymer from those of the nematic mesophase. These results were compared against the standard 3D printing materials acrylonitrile-butadiene-styrene (ABS), polylactic acid (PLA) and thermoplastic polyurethane (TPU) (Figure 4-1) in order to identify the desired characteristics for effective processing.

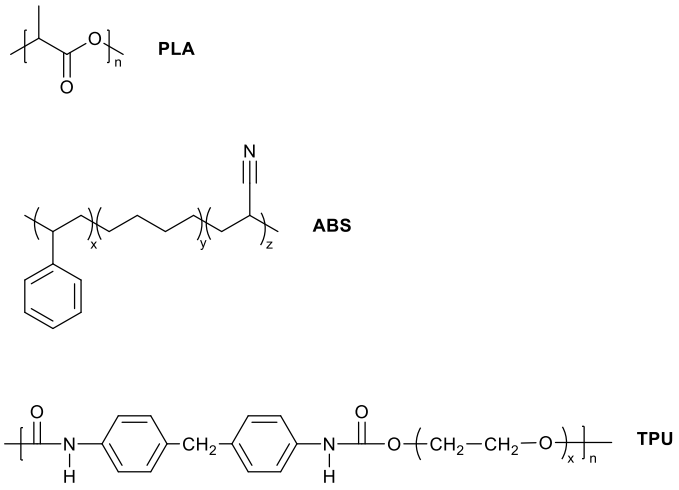

Figure 4-1. Structures of the standard 3D printing materials PLA, ABS and TPU.

4.2. Discussion and Results

4.2.1. Rheology of Standard Materials

To determine if the LCEs were suitable for processing by melt extrusion, measurements of the viscosity and shear moduli by SAOS were carried out for **PS-*b*-PMVS-*b*-PS**, **P-3**, **P-3-M1(65)-COOH(35)** and **P-3-M2(80)-COOH(20)**. These results were compared with those measured for the standard 3D printing materials PLA, ABS and TPU in order to identify characteristics of materials suitable for processing in this manner. For the standard materials, disks with a diameter of 15 mm and a thickness of 1 mm were prepared by 3D printing, whilst for the experimental polymers disks with a diameter of 15 mm and a thickness of approximately 1 mm were prepared in a polydimethylsiloxane (PDMS) mould from toluene solution.

To ensure that no plastic deformation occurs when measuring G^* and η^* it is necessary to take measurements with a strain small enough that it does not lead to permanent deformation of the polymer structure. This strain range is known as the linear viscoelastic (LVE) region and is detected by first carrying out an amplitude sweep at a constant temperature and frequency, with the limiting strain value occurring when values for G', G'' or η^* leave a plateau region and show a dependence on strain amplitude. Amplitude sweep experiments were carried out for all materials between strains of 0.01-100% (except for TPU where a range of 0.01-1% was used). The limiting value of the strain was then used in the frequency sweep experiments, where the frequency of the oscillation was varied between 1-100 radians per second for isothermal measurements.

4.2.1.1. Amplitude Sweeps

The recommended extrusion temperatures for printing the standard 3D printing materials were given as 190-230 °C (PLA),[9] 240 °C (ABS)[10] and 225-235 °C (TPU).[11] These materials were chosen in order to provide a comparison with the experimental polymers, and so to determine whether they demonstrated suitable melt behaviour for extrusion. Therefore, these temperature ranges were used to determine the experimental temperature range. The LVE region was identified from plots of strain against the storage and loss modulus (Figure 4-2). The limiting value was taken as the largest strain where G' was independent of applied strain, with the results listed in Table 4-1.

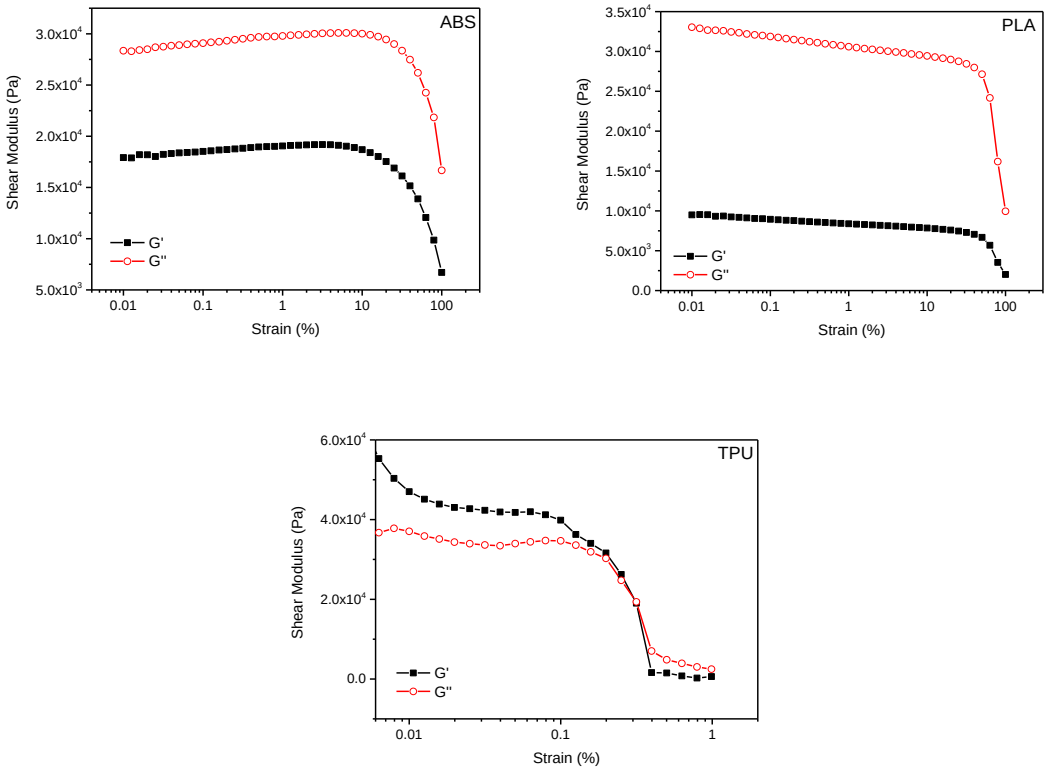

Figure 4-2. Amplitude sweep results for ABS, PLA and TPU for determination of the LVE region.

Table 4-1. Amplitude sweep results for standard materials and temperature range for frequency sweeps.

Polymer	Amplitude Sweep Temperature (°C)	Limiting LVE Region Strain (%)	Frequency Sweep Temperature Range (°C)
ABS	200	5	200-250
PLA	170	10	170-220
TPU	200	0.1	200-250

Inspection of the plots of the amplitude sweeps exposed a difference between the properties of the conventional thermoplastics, ABS and PLA, and those of the thermoplastic elastomer, TPU. For a non-crosslinked polymer in a liquid like melt, as encountered under extrusion conditions, it is expected that *G''* would be greater than *G'*. This was the case for both ABS and PLA, however, for the TPU in the LVE region the inverse relationship was seen. It is known that the material will extrude, as the disk itself was prepared by 3D printing from a melt, and so this trend may be a feature of thermoplastic elastomers under these experimental conditions that has no bearing on the suitability for melt processing.

Confirmation that the chosen strain values were within the LVE region was obtained by generating Lissajous plots of stress against strain (Figure 4-3) for each material. The strictly sinusoidal response obtained at the chosen strain is demonstrated by the elliptical shape of these plots, with the area enclosed by the ellipse characteristic of the energy dissipated by the material during the experiment. A purely elastic response would therefore generate a straight line with an area equal to zero, and a purely viscous response a circle, with viscoelastic materials giving ellipses angled at 45°, as observed.

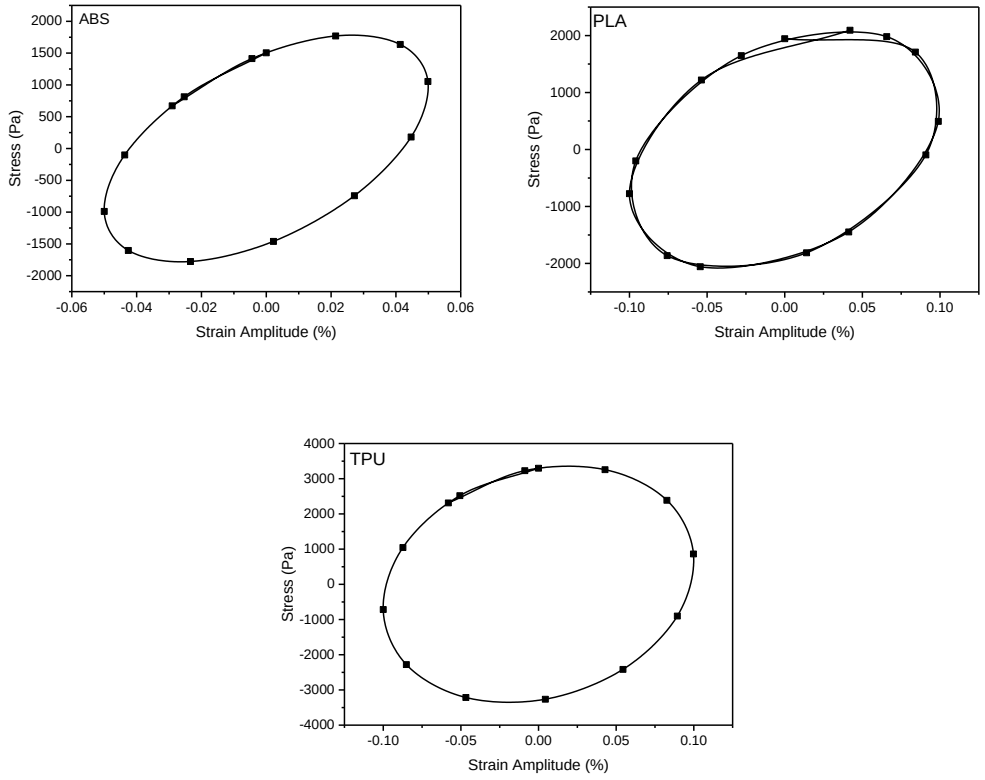

Figure 4-3. Lissajous diagrams generated for ABS, PLA and TPU at strains of 5, 10 and 0.1% respectively, which confirm measurements were taken within the LVE region.

4.2.1.2. Frequency Sweeps

For all polymers the complex viscosity (η^*), storage modulus (G') and loss modulus (G'') were measured over a range of angular frequencies (ω) at several fixed temperatures (Table 4-1). With respect to their viscosities, the standard materials show slightly different responses to one another (Figure 4-4). In all cases the polymer was less viscous at higher temperatures, an expected result as the chains become more mobile with increased thermal motion, and both ABS and the TPU demonstrated shear thinning behaviour at all temperatures. However, PLA when heated

above 190 °C appeared to show no dependence on ω, demonstrating Newtonian behaviour and indicating a plateau in the viscosity. This difference arises due to the relative flexibility of the PLA backbone compared with ABS and TPU, with the chain able to reach the minimum viscosity for a given temperature at lower deformation frequency than the stiffer, harder to deform, aromatic-containing polymers.

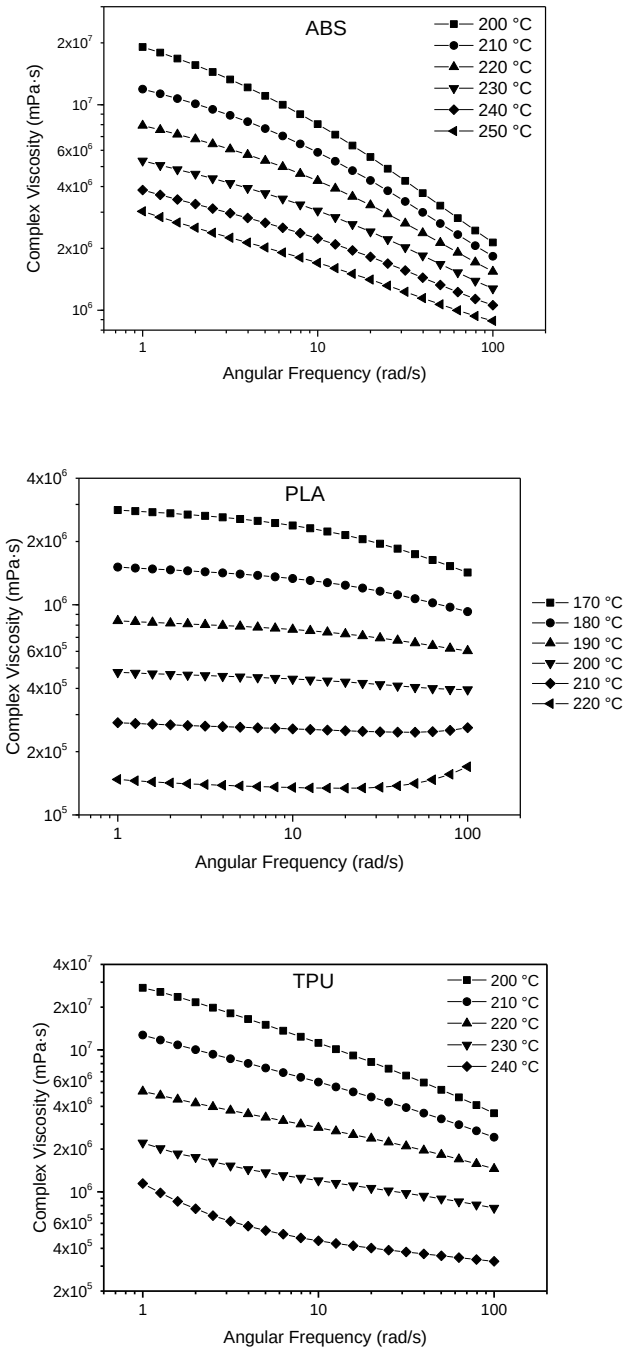

Figure 4-4. Frequency sweep results for the change in viscosity of ABS, PLA and TPU with increasing angular frequency.

Trends in the shear moduli as measured by the frequency sweep can be used to determine the physical properties of the polymers under increasing levels of shear stress by indicating the relative contribution from the elastic (G') and viscous (G'') part. For liquid-like viscoelastic polymer melts it is expected that at low frequency G'' will be greater than G' until some frequency is reached where a crossover occurs and the inverse relationship holds.[12]

For all three standard materials this trend is observed (Figure 4-5), including for the TPU which had G' greater than G'' in the amplitude sweep, confirming that this material formed the expected liquid-like melt under the conditions of the frequency sweep. The location of the crossover gives further information about the structure of each polymer as the transition from liquid to solid-like behaviour occurs when the motion of the polymer chains is slower than the timescale of the experiment, and so an increasingly elastic-like response is seen as the frequency of the oscillation is increased as less energy can be dissipated through transfer to neighbouring chains. The crossover is therefore dependent not only on the temperature, but also the nature of the polymer backbone. ABS and TPU are relatively stiff polymers due to the rigid polystyrene and diphenyl blocks respectively (Figure 4-1), and this is expressed by the lower frequencies required for crossover to elastic-dominated behaviour to occur with respect to the flexible PLA chain. For PLA the transition occurs at frequencies higher than those reached during the experiment and so crossover is only seen at the lowest temperature measured, when the chains are at their least mobile.

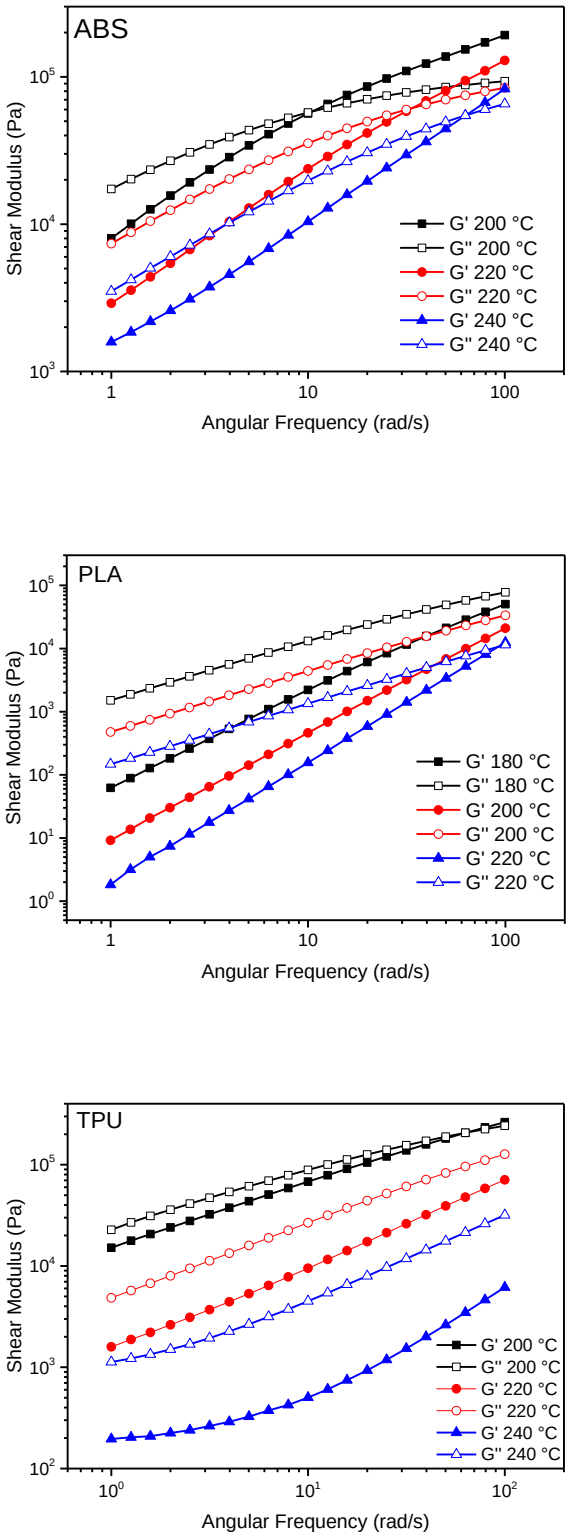

Figure 4-5. Frequency sweep results for the change in shear modulus of ABS, PLA and TPU with increasing angular frequency at selected temperatures.

These results for the standard materials give several examples of the properties required by the LCE in order to be suitable for melt extrusion under the experimental conditions chosen for this study. A broad range of viscosities was measured, however, the key feature that the standard materials have in common is that G'' is greater than G' over a wide range of ω at the recommended printing temperatures during the frequency sweep. The results also show the impact the flexibility of the polymer backbone has on the melt properties. The experimental triblock copolymers contain a relatively rigid polystyrene (PS) block and a relatively flexible poly(methylvinylsiloxane) (PMVS) block, and so it is unknown which will have the greater impact on the overall rheological properties.

4.2.2. Rheology of Thermoplastic Liquid Crystal Elastomers

From the materials synthesised in Chapter 2, SAOS experiments were first carried out on disks of **PS-*b*-PMVS-*b*-PS**, **P-3**, **P-3-M1(65)-COOH(35)** and **P-3-M2(80)-COOH(20)**. Temperature ranges for these experiments were determined from the results of the Differential Scanning Calorimetry (DSC) and Thermogravimetric Analysis (TGA) experiments described in Section 2.2.6. The starting temperature was chosen to be approximately 20 °C above the highest temperature transition measured by DSC, where the LC domain was expected to be isotropic and both the PS and PMVS domains above their glass transition temperature (T_g). The final temperature was fixed at 180 °C in order to minimise effects due to thermal degradation. This was especially important as whilst TGA and DSC measurements were taken under a nitrogen atmosphere, it was not possible to carry out the rheological measurements under an inert atmosphere with the equipment available. **P-3** and **P-3-M2(80)-COOH(20)** were shown to have higher transition temperatures and so experiments were carried out in the range 140-200 °C.

4.2.2.1. Amplitude Sweeps

Amplitude sweeps were carried out as described in Section 4.2.1.1 to determine the limiting strain value for the LVE region as the largest value of G' where no dependence on the applied strain was observed (Figure 4-6). The results are summarised in Table 4-2 along with the temperature range used for the subsequent frequency sweep experiments. For all four polymers the values for G' were greater than those for G'' in the LVE region which, when combined with the results for the

TPU, suggest that this is a characteristic feature for thermoplastic elastomers under these experimental conditions.

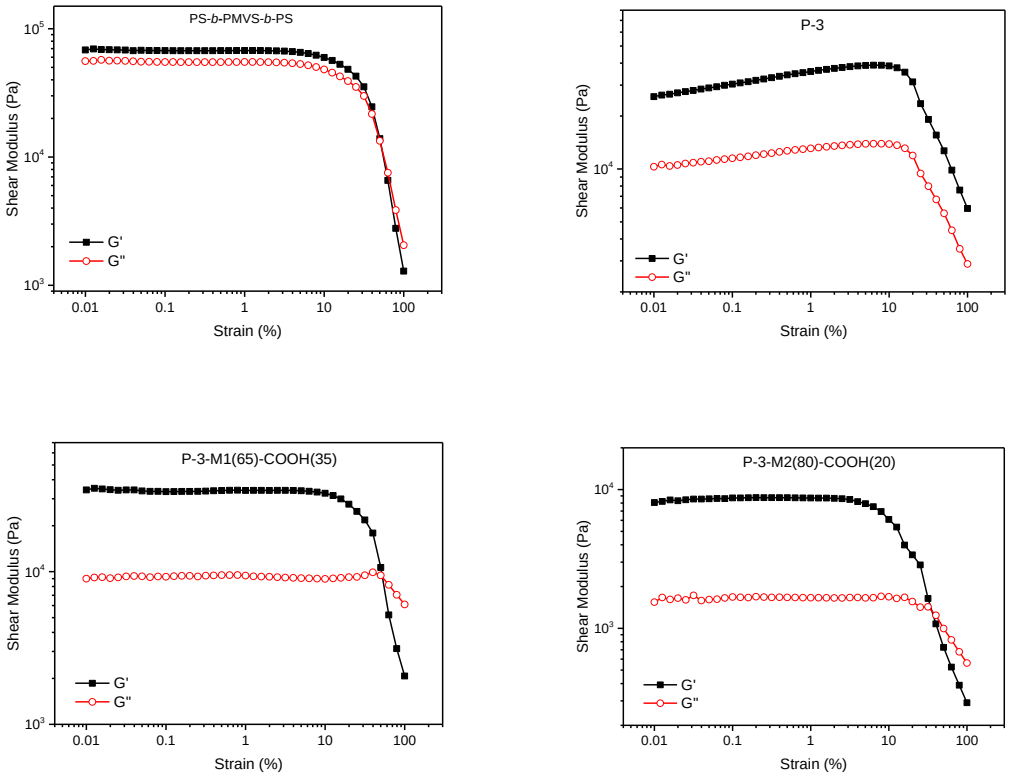

Figure 4-6. Results of amplitude sweeps for **PS-*b*-PMVS-*b*-PS**, **P-3**, **P-3-M1(65)-COOH(35)** and **P-3-M2(80)-COOH(20)**.

Table 4-2. Amplitude sweep results for LCE polymers and temperature ranges for frequency sweeps.

Polymer	Amplitude Sweep Temperature (°C)	Limiting LVE Region Strain (%)	Frequency Sweep Temperature Range (°C)
PS-*b*-PMVS-*b*-PS	120	3	120-180
P-3	140	10	140-200
P-3-M1(65)-COOH(35)	120	10	120-180
P-3-M2(80)-COOH(20)	140	10	140-200

Lissajous diagrams were again generated, and their elliptical shapes confirmed that the chosen strain values were within the LVE range (Figure 4-7). For all cases apart from **PS-*b*-PMVS-*b*-PS** the ellipses were narrow, indicating a strong contribution from the elastic component. This was different to the results seen for the three standard materials, including the TPU, and suggests that these materials will demonstrate a significantly different response to the frequency sweep experiment.

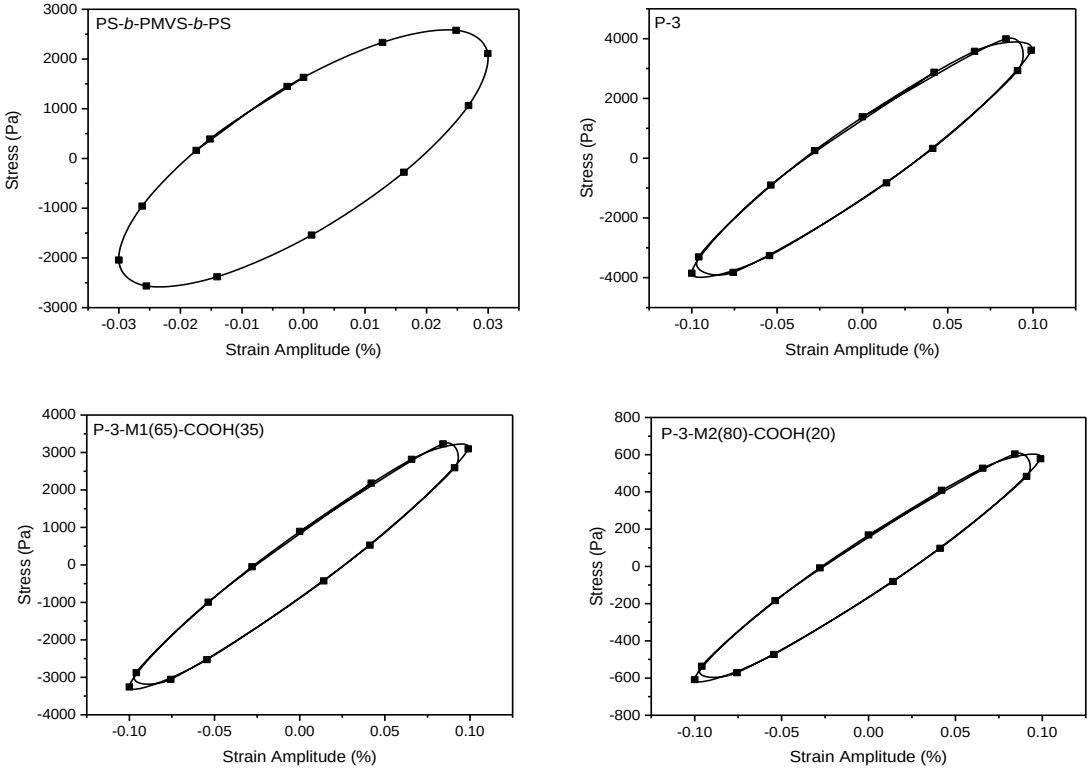

Figure 4-7. Lissajous diagrams for **PS-*b*-PMVS-*b*-PS**, **P-3**, **P-3-M1(65)-COOH(35)** and **P-3-M2(80)-COOH(20)** at 3, 10, 10 and 10% strain respectively.

4.2.2.2. Frequency Sweeps

Frequency sweeps were carried out for all samples in the temperature ranges given in Table 4-2. With respect to the viscosity, a clear distinction can be made between the results for the polymers with and without liquid crystal functionalisation. For **PS-*b*-PMVS-*b*-PS** and **P-3** a standard relationship was seen, whereby the viscosity of the material decreased with increasing temperature and shear (Figure 4-8 and Figure 4-9 respectively). For a given shear rate **PS-*b*-PMVS-*b*-PS** demonstrated a noticeable decrease in viscosity at all temperatures, whereas **P-3** had a much weaker temperature dependence, especially under high shear conditions.

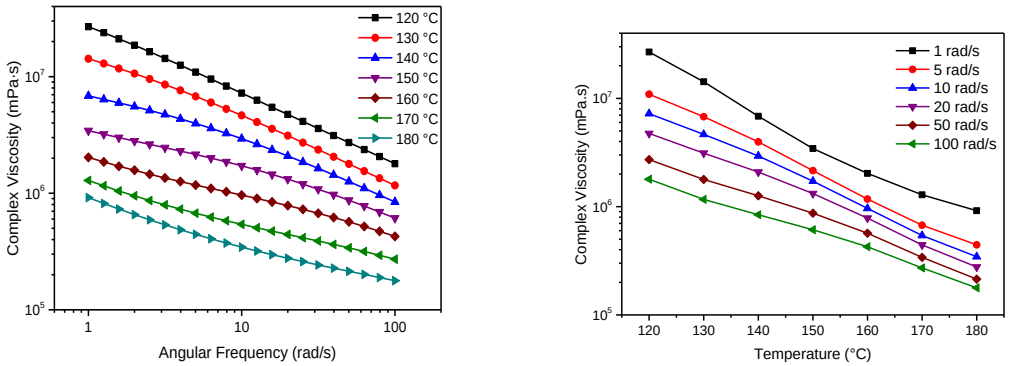

Figure 4-8. Variation in complex viscosity with angular frequency (left) and temperature (right) for **PS-*b*-PMVS-*b*-PS**.

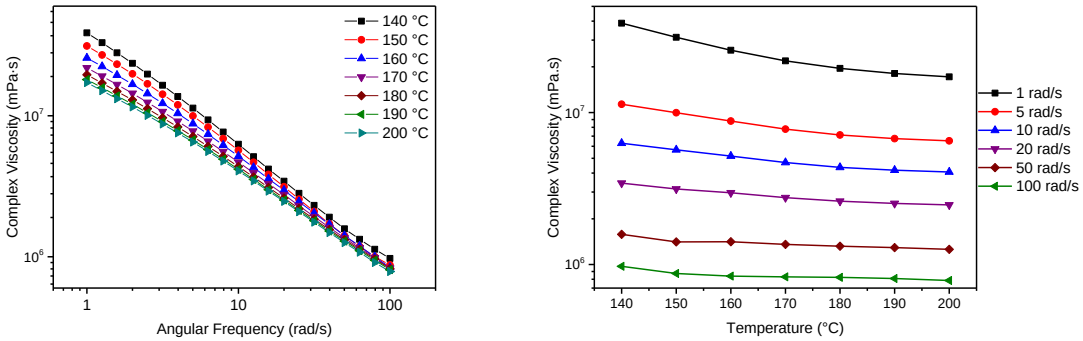

Figure 4-9. Variation in complex viscosity with angular frequency (left) and temperature (right) for **P-3**.

In contrast, for the two LC-functionalised polymers **P-3-M1(65)-COOH(35)** and **P-3-M2(80)-COOH(20)** the viscosity increased with increasing temperature (Figure 4-10 and Figure 4-11 respectively) . This is a characteristic feature of liquid crystalline polymers with a nematic mesophase present, and is due to the increased resistance to flow on transitioning from a state where the mesogen is well aligned (nematic) to one where there are more entanglements (isotropic).[13] Neither polymer demonstrated the considerable decrease in viscosity that could be interpreted as reaching the fully isotropic state, suggesting that they remained biphasic throughout the experiment.

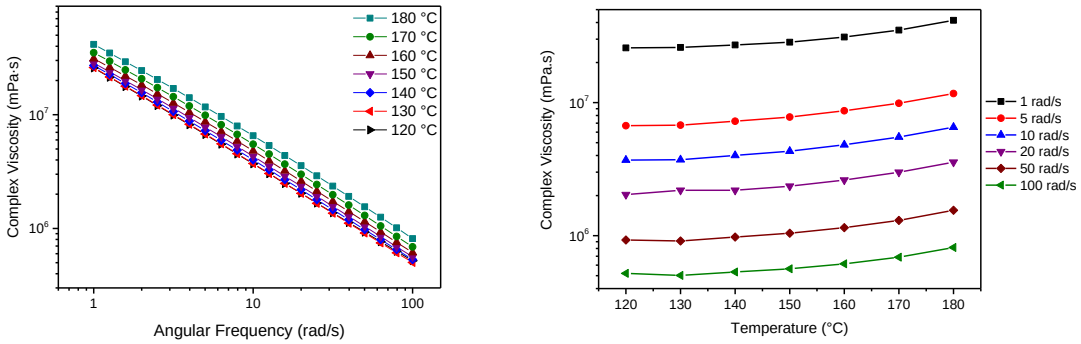

Figure 4-10. Variation in complex viscosity with angular frequency (left) and temperature (right) for **P-3-M1(65)-COOH(35)**.

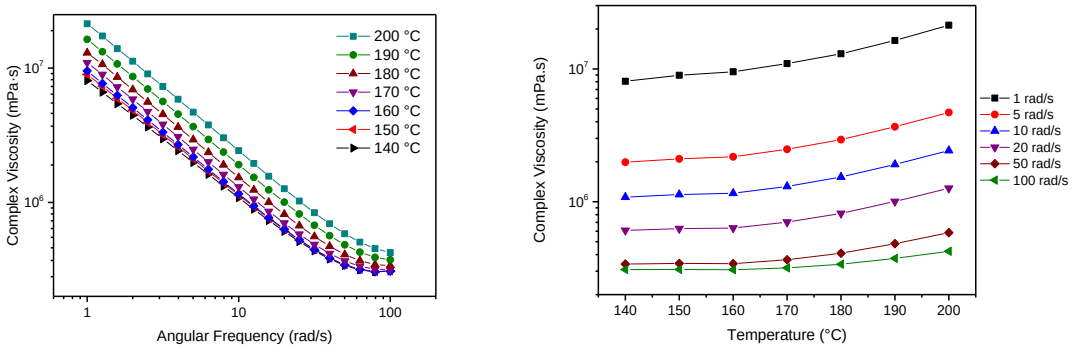

Figure 4-11. Variation in complex viscosity with angular frequency (left) and temperature (right) for **P-3-M2(80)-COOH(20)**.

Whilst this trend is to be expected for **P-3-M2(80)-COOH(20)**, where the T_{iso} was not detected below 200 °C by DSC, for **P-3-M1(65)-OH(35)** the result is surprising. The lowest temperature rheological measurements were taken at was 120 °C, which is above the T_{iso} of 99.4 °C, as measured by DSC, and it was therefore expected that the PMVS block would be isotropic at all temperatures investigated. This result suggests the presence of a shear-induced nematic mesophase, which is maintained due to the continued deformation experienced during the frequency sweep.

The formation of a shear-induced nematic mesophase was a positive result with respect to combining the alignment and processing stages of manufacturing responsive LCEs, however, the results for the shear moduli presented a significant problem. For **PS-*b*-PMVS-*b*-PS** the polymer formed a liquid-like melt with the expected crossover from viscous to elastic-dominated

behaviour observed at all temperatures, as shown in Figure 4-12. This crossover occurred at low frequency and shifted to higher frequencies as the temperature was increased, with the viscous component dominating from low to high frequency conditions between 150-180 °C. However, once the linking group was introduced in **P-3**, **P-3-M1(65)-COOH(35)** and **P-3-M2(80)-COOH(20)** the polymers demonstrated behaviour typical of a crosslinked or filled material. At all frequencies and at all temperatures investigated G' was greater than G'' (Figure 4-13) which means that none of the samples formed a homogeneous, liquid-like melt in the temperature range explored.

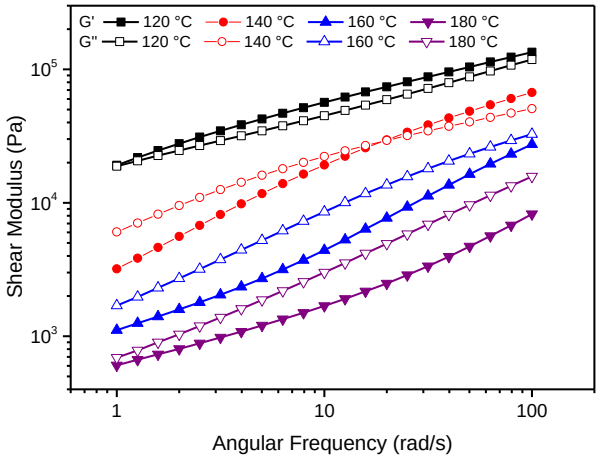

Figure 4-12. Frequency sweep results for the change in shear modulus of **PS-*b*-PMVS-*b*-PS** with increasing angular frequency at selected temperatures.

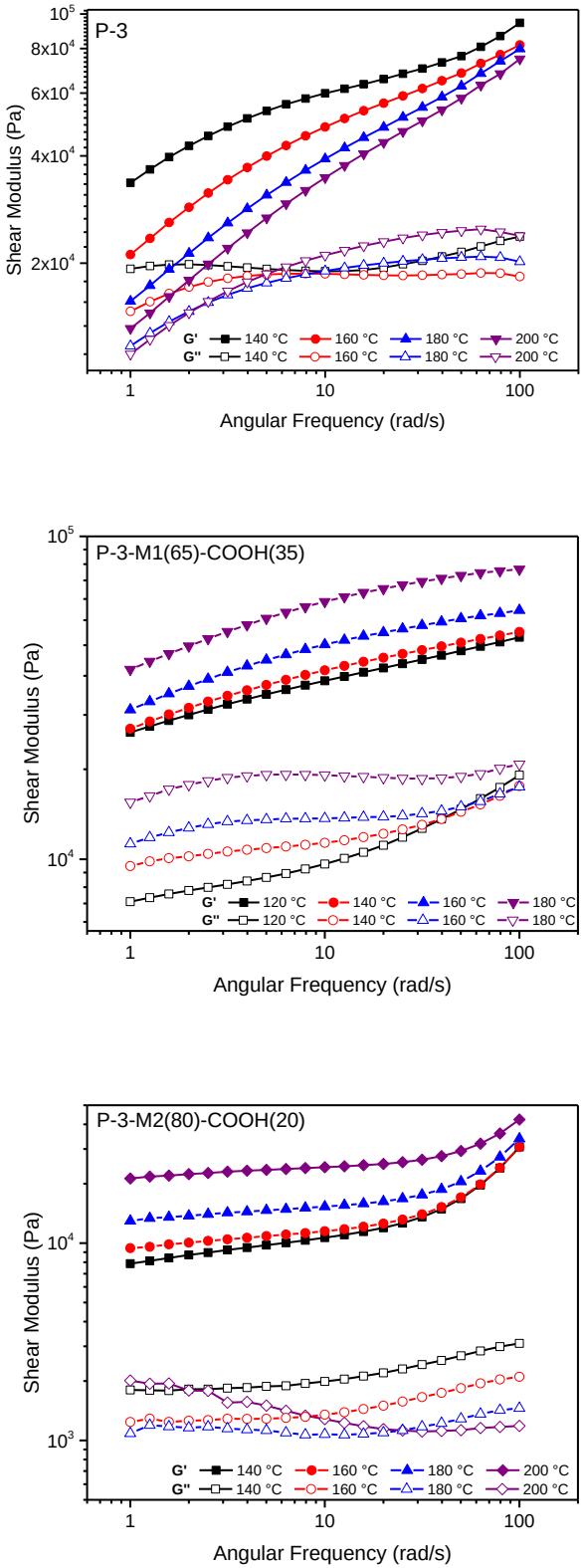

Figure 4-13. Frequency sweep results for the change in shear modulus of **P-3**, **P-3-M1(65)-COOH(35)** and **P-3-M2(80)-COOH(20)** with increasing angular frequency at selected temperatures.

For both LC-functionalised polymers this result is perhaps not surprising, as it was demonstrated that a nematic mesophase was present in both, which would act in a similar manner to a nanoscale filler particle by introducing heterogeneity to the polymer structure. However, **P-3** contains no liquid crystalline group and so its behaviour cannot be explained by this theory. It was shown by SAXS and TEM that **P-3** did not form an ordered microphase separated structure at room temperature, and so the elastic-like behaviour may be a result of the strongly repulsive interactions between the non-polar PS block and the polar carboxylic acid groups present in the PMVS block. This likely resulted in the T_{ODT} of the block copolymer shifting to a higher temperature, which can be confirmed by replotting the results of the frequency sweep using the method developed by Han and Kim,[2] as discussed in the following section.

4.2.2.3. Investigation of T_{ODT}

It has been shown that block copolymers below the T_{ODT} will behave as filled polymers, which would result in the trend observed for the shear moduli for **PS-*b*-PMVS-*b*-PS** functionalised with the linking group or mesogen (neglecting the contribution from the nematic mesophase). If the polymer's microstructure is homogeneous (i.e. above the T_{ODT}), values for G' and G'' will have no temperature dependence when plotted against each other, as is demonstrated for ABS in Figure 4-14.

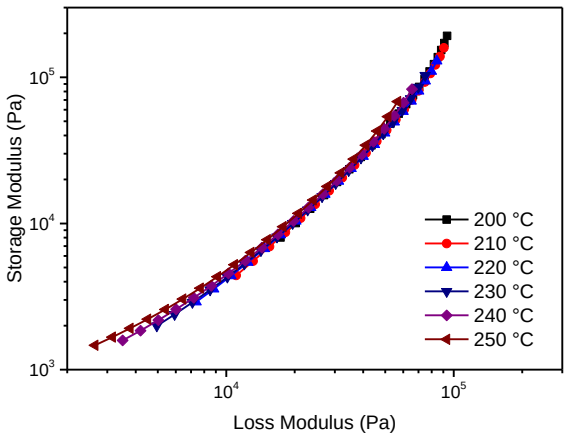

Figure 4-14. Plot of G' against G'' for ABS. The lack of temperature dependence indicates the polymer is above the T_{ODT}.

The triblock copolymer backbone was the only novel material to show liquid-like melt behaviour, and as expected a plot of *G'* against *G''* showed excellent overlap and no temperature dependence, suggesting that the T_{ODT} had been exceeded and that the PS and PMVS blocks were fully mixed at all temperatures and frequencies measured (Figure 4-15). However, the expected gradient of 2 in the terminal region was not seen for either ABS or **PS-*b*-PMVS-*b*-PS**. This may arise due to the relatively high molecular weights shifting the terminal region to a frequency too low to measure, or due to the polydispersity of the polymer samples.[14] Nonetheless, both materials displayed liquid-like behaviour in the temperature range measured and no temperature dependence was seen, and so it appears likely these materials were above the T_{ODT} despite the gradient of the terminal region.

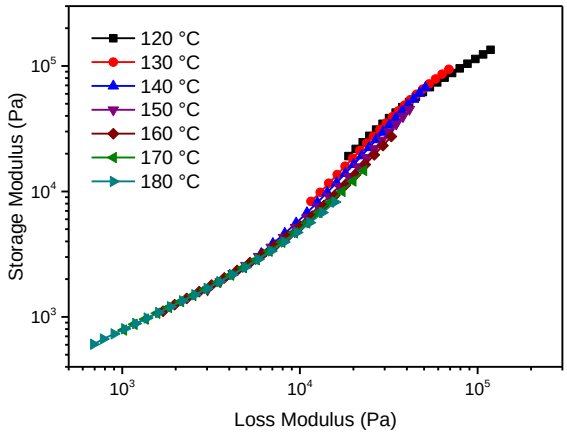

Figure 4-15. Plot of *G'* against *G"* for **PS-*b*-PMVS-*b*-PS**. The lack of temperature dependence indicates the polymer is above the T_{ODT}.

The origin of the elastic-like behaviour seen in the functionalised block copolymers becomes clear when plotting *G'* against *G''* for **P-3** and **P-3-M1(65)-COOH(35)** (Figure 4-16). A strong temperature dependence was seen for both samples, implying that the PS and PMVS blocks were unable to mix in either case at any temperature or frequency measured. For **P-3** some overlap was observed at low frequencies (low values of *G'* and *G''*), especially at temperatures between 150-180 °C, but was lost at high frequencies and above 180 °C. The plot of shear moduli against angular frequency for **P-3** (Figure 4-13) showed that the values for *G'* and *G''* approached each other with increasing temperature at low frequency, suggesting that if this experiment was continued to higher temperature a liquid-like melt might be obtained.

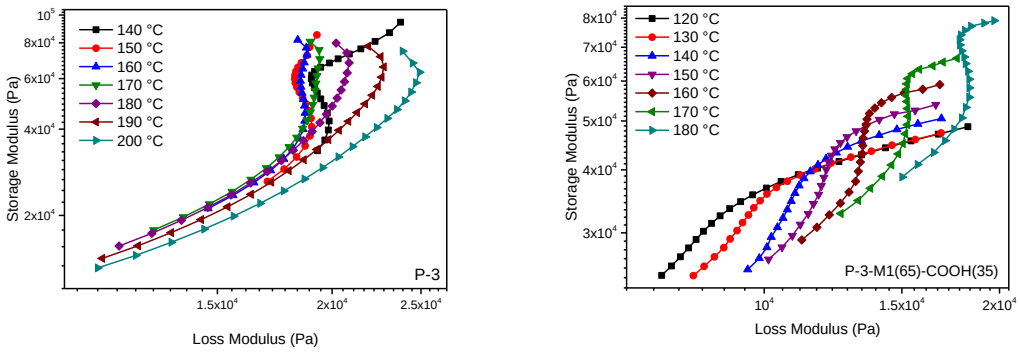

Figure 4-16. *G'* against *G"* for **P-3** and **P-3-M1(65)-COOH(35)**. Both polymers displayed a strong temperature dependence, and so are below the T_{ODT} at all temperatures measured.

In the case of **P-3-M1(65)-COOH(35)** there was no overlap seen at any temperature or frequency measured, suggesting that the microphase segregation of the PS and PMVS blocks persisted despite the shear deformation which would be expected to disrupt any internal structure.[2] This is most likely driven by the presence of the nematic mesophase, which is stabilised by spherical interfaces,[7] but which would be expected to eventually become isotropic under high temperature and shear conditions.[6]

The microphase structure of an AB diblock copolymer is strongly dependent on the interactions between the A and B blocks (as characterised by the Flory-Huggins interaction parameter, χ), and the molecular weight and volume fraction of each. The addition of the linking group therefore increased the repulsion between the PS and PMVS blocks, most likely due to hydrogen bonding interactions between the carboxylic acid groups present which has been shown to decrease χ,[15] which in turn raised the T_{ODT} of the triblock copolymer from below 120 °C to above 200 °C. For the LCEs this is the temperature where thermal degradation was first detected by TGA (Section 2.2.6.), and so it was not possible to simply increase the temperature of the experiments in order to try and obtain a liquid-like melt. Therefore, in order to try and increase the compatibility between the PS and PMVS blocks (and so lower the T_{ODT}) the polymers **P-3** and **P-3-M1(65)-COOH(35)** were modified to convert the carboxylic acid groups to methyl esters and so remove any effect due to hydrogen bonding interactions. This afforded polymers **P-3-COOMe** and **P-3-M1(65)-COOMe(35)** (Section 2.2.5). To isolate the role of the stabilisation of the nematic mesophase by the spherical PS domains on the microphase segregated morphology behaviour of the LCE, a PMVS homopolymer was synthesised and functionalised with **M1** to yield **PMVS-3-M1(84)-COOH(16)** (Section 2.2.4.3.). A final potential contributor to the elastic-like behaviour would be undesired cross-linking occurring during the thiol-ene click reaction. This was investigated by functionalising the PMVS block of the triblock copolymer with the thermally

activated initiator 2,2′-azobis(2-methylpropionitrile) (AIBN) rather than using a UV-activated initiator, to obtain **P*-3(AIBN)**, which was further functionalised to give **P*-3(AIBN)-COOMe** and **P*-3(AIBN)-M1-COOMe**.

4.2.3. Impact of Polymer Modifications on Melt Behaviour

From the materials synthesised in Chapter 2, SAOS experiments were carried out on disks of **P*-3(AIBN)**, **P-3-COOMe**, **P*-3(AIBN)-COOMe**, **P-3-M1(65)-COOMe(35)**, **P*-3(AIBN)-M1-COOMe** and **PMVS-3-M1(84)-COOH(16)**. Disks with a diameter of 15 mm and approximate thickness of 1 mm (0.1 mm for **PMVS-3-M1(86)-COOH(14)**) were cast from toluene in a PDMS mould. For all materials, the LVE region was first established by an amplitude sweep from 0.01-100% strain, before frequency sweeps were carried out between 1-100 radians per second in a material appropriate temperature range. The starting temperature was chosen as being approximately 20 °C above the highest temperature transition seen by DSC (where the LC domains are expected to be isotropic and both the PS and PMVS are above their T_g) and the final temperature fixed at 180 °C to minimise the effects of thermal degradation.

4.2.3.1. Amplitude Sweeps

Amplitude sweeps were carried out on each of the modified polymers to determine the limiting strain value of the LVE region. The results are given in Table 4-3, as well as the temperature ranges used for the subsequent frequency sweep experiments. In each case G' was greater than G'' and Lissajous diagrams were elliptical (see Appendix C).

Table 4-3. Amplitude sweep results for modified polymers.

Polymer	Amplitude Sweep Temperature (°C)	Limiting LVE Region Strain (%)	Frequency Sweep Temperature Range (°C)
P-3-COOMe	120	0.2	120-180
P-3-M1(65)-COOMe(35)	120	1	120-180
P*-3(AIBN)	120	5	120-180
P*-3(AIBN)-COOMe	120	5	120-180
P*-3(AIBN)-M1-COOMe	120	3	120-180
PMVS-3-M1(84)-COOH(16)	130	5	130-180

In order to simplify the identification of the effect of each structural change on the viscoelastic properties of the polymers, the results for the frequency sweeps will first be discussed for the polymers with no LC functionalisation followed by the triblock copolymers with **M1** attached and finally for the PMVS homopolymer with **M1** attached.

4.2.3.2. Thermally Initiated Thiol-Ene Click Reaction

For **P*-3(AIBN)** the values of *G'* and *G''* at a given temperature were much closer at low angular frequency than was seen for **P-3**, with the viscous component greater than the elastic from 150-180 °C (Figure 4-18). This trend was only seen over a small angular frequency range (1-2 radians per second), with *G'* dominating again for the majority of the frequency sweep. This suggests that the side-chain functionalised polymer is relatively conformationally inflexible compared with the linear polymers given as standard materials, an effect which would arise due to hydrogen bonding between chains preventing the motion necessary for dissipation of deformation energy.

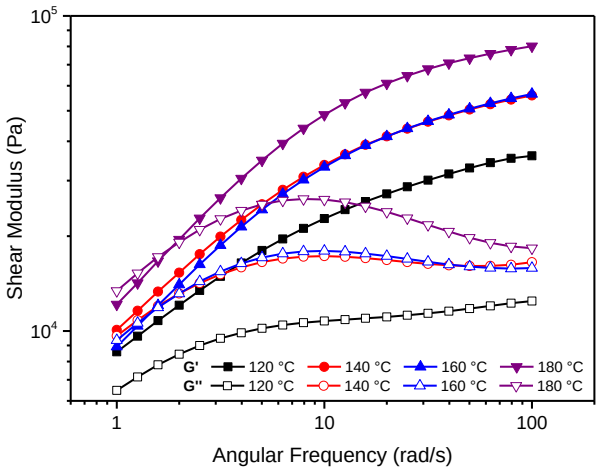

Figure 4-17. Frequency sweep results for the change in shear modulus of **P*-3(AIBN)** with increasing angular frequency at selected temperatures.

The crossover from liquid to elastic-like behaviour was not observed for **P-3**, where at low angular frequency it appeared that a crossover might occur at temperatures greater than 180 °C (Figure 4-13). It cannot be concluded that this difference in behaviour arises solely from the change in synthesis method however, as **P*-3(AIBN)** was synthesised from a triblock copolymer backbone with a lower number average molecular weight than that used for **P-3**, and so it would be expected that transitions dependent on the conformational flexibility of the polymer chains would shift towards lower temperatures for this material.

To determine whether the T_{ODT} was exceeded for **P*-3(AIBN)**, G' was plotted against G'' (Figure 4-18). A strong temperature dependence was apparent at temperatures between 120-140 °C, before overlap occurred between 140-160 °C. This coincided with the transition from solid-like to liquid-like behaviour seen in the plot of the shear moduli against angular frequency and suggests that the T_{ODT} had been exceeded. Above 160 °C, however, the plot of G' against G'' again demonstrated a temperature dependence. At these temperatures liquid-like behaviour was seen in the low frequency region, which suggests that some further structural change had occurred. It is expected that the carboxylic acid functionality will have a significant effect on the properties of this polymer, and so it may be that the formation and disruption of hydrogen bonding interactions and the resulting impact this had on the microphase segregation resulted in complex rheological behaviour. In order to remove this effect, and to ascertain whether a significant difference in properties is seen by utilising a thermally activated rather than UV activated thiol-ene click reaction, experiments were repeated for samples of **P-3** and **P*-3(AIBN)** where the carboxylic acid groups were converted to methyl esters.

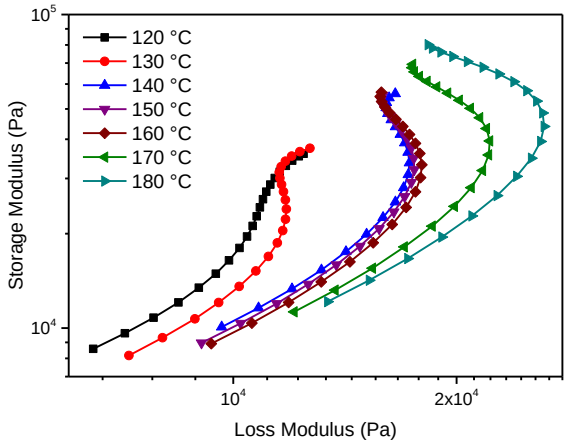

Figure 4-18. Plot of G' against G'' for **P*-3(AIBN)**. The strong temperature dependence indicates the polymer is above the T_{ODT} between 120-150 °C, before temperature independence is observed from 150-160 °C suggesting that the PS and PMVS blocks are mixing. Above 160 °C the curve is strongly temperature dependent again, suggesting that the structure is heterogeneous.

4.2.3.3. Conversion of Carboxylic Acid Groups to Methyl Esters

The plot of viscosity with increasing temperature at constant frequency for **P-3** (Figure 4-9) showed no temperature dependence, suggesting that the polymer structure was constant across the temperature range measured. This is consistent with the results presented in Chapter 3, where it was shown that at room temperature this polymer did not form a microphase segregated

morphology. The viscosity of **P-3-COOMe** on the other hand demonstrated a clear temperature dependence, decreasing with increasing temperature at all frequencies tested (Figure 4-19). This result suggests that on conversion of the carboxylic acid groups to the non-hydrogen bond forming methyl ester group it was possible for microphase segregation of the PS and PMVS blocks to occur, with the blocks becoming increasingly mixed with increasing temperature, resulting in the decrease in viscosity.

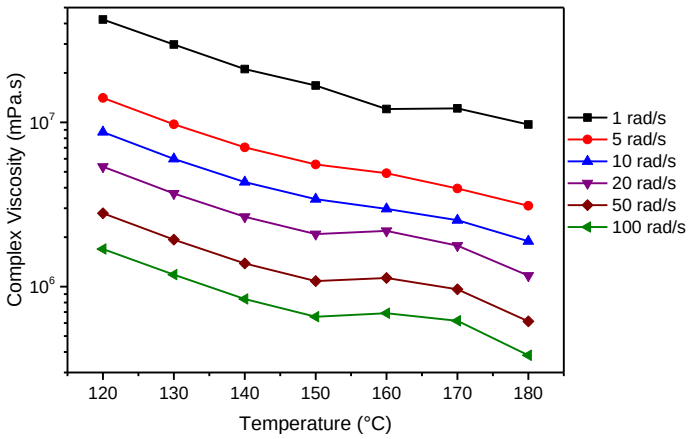

Figure 4-19. Variation in complex viscosity with temperature for **P-3-COOMe**.

This trend was also apparent for **P*-3(AIBN)** and **P*-3(AIBN)-COOMe** (Figure 4-20). Converting the carboxylic acid groups to methyl esters lead to a clear decrease in viscosity with increasing temperature and confirms that hydrogen bonding has a strong influence on the microphase structure of this polymer, even under the highest shear stress and at temperatures far above the T_g for both the PMVS and PS blocks.

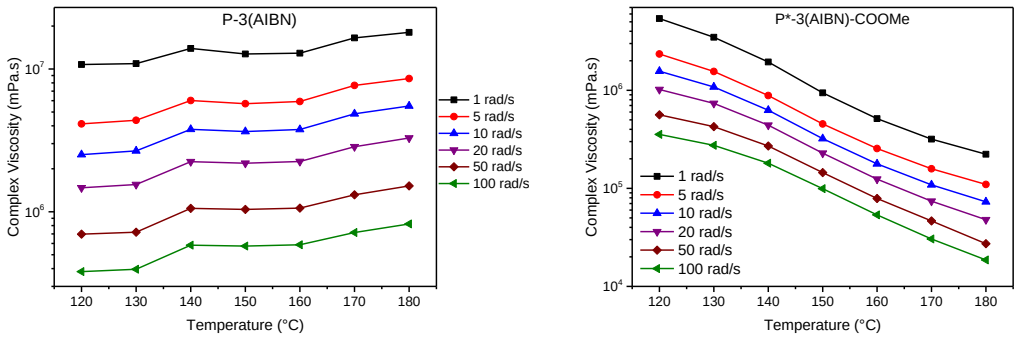

Figure 4-20. Variation in complex viscosity with temperature for **P*-3(AIBN)** and **P*-3(AIBN)-COOMe**.

The effect of conversion of the carboxylic acid groups to methyl esters was also apparent from plots of G' against G'' for both **P-3-COOMe** and **P*-3(AIBN)-COOMe**. From Figure 4-21 it is clear that no temperature dependence was observed for **P-3-COOMe**, with some deviations from the trend observed at higher temperatures which may be due to the onset of thermal degradation of the sample. For **P*-3(AIBN)-COOMe** good overlap was again seen between curves at all temperatures until 170 °C, where a deviation occurred. This temperature coincides with the transition from temperature independent to dependent behaviour observed in the same plot for **P*-3(AIBN)** (Figure 4-18). The overlap was stronger in this case but suggests that at high temperature this material undergoes some change in structure, which rules out hydrogen bonding as the origin of this transition.

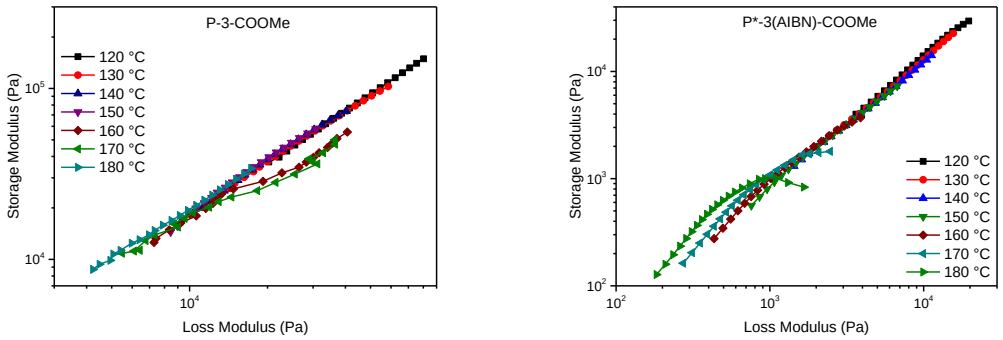

Figure 4-21. Plot of G' against G'' for **P-3-COOMe** (left) and **P*-3(AIBN)-COOMe** (right). Both polymers give temperature independent results suggesting that they are above the T_{ODT}. However, **P*-3(AIBN)-COOMe** appears to return to temperature dependent behaviour from 170 °C.

The results of the frequency sweeps for **P-3-COOMe** and **P*-3(AIBN)-COOMe** confirm that the removal of hydrogen bond forming groups from the triblock copolymer can be used to lower the T_{ODT}, a result which may prove useful in obtaining an LCE with the desired melt properties for extrusion. However, plots of the shear moduli against angular frequency indicated that mixing of the PS and PMVS blocks was not sufficient for **P-3-COOMe** to form a liquid-like melt. The elastic component dominated the viscous component at all temperatures and frequencies measured with the curves approximately parallel to each other, indicating that any crossover would occur at very low frequencies, outside the range of the rheometer (Figure 4-22).

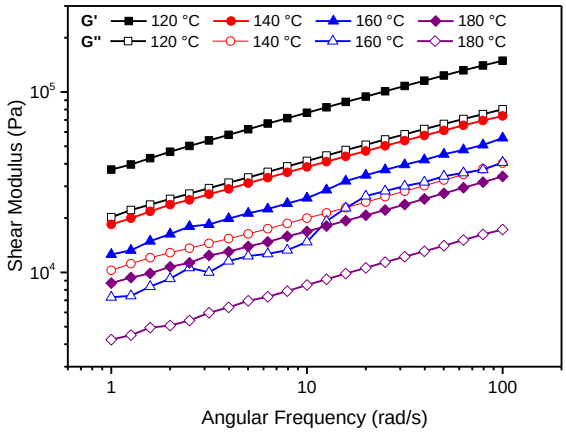

Figure 4-22. Frequency sweep results for the change in shear modulus of **P-3-COOMe** with increasing angular frequency at selected temperatures.

For triblock copolymers such as **P-3-COOMe**, it is expected that heating above the T_{ODT} should be sufficient for a liquid-like state to be achieved. For this to not be the case, it would suggest that either the polymer backbone is sufficiently conformationally inflexible that elastic-like behaviour is observed from very low frequencies, or that some level of crosslinking or inter-chain interaction is present in the PMVS block. The latter could have arisen during the thiol-ene click reaction if bonds were formed between radical-initiated vinyl groups. For this reason, **P*-3(AIBN)** was synthesised to determine whether using a slower attachment reaction had any effect on the melt properties. From the plots of the shear moduli against angular frequency given in Figure 4-18 and Figure 4-23 for both **P*-3(AIBN)** and **P*-3(AIBN)-COOMe** respectively, it would appear that this could be the case, although the effect of the reduced molecular weight of **P*-3(AIBN)** should not be ignored.

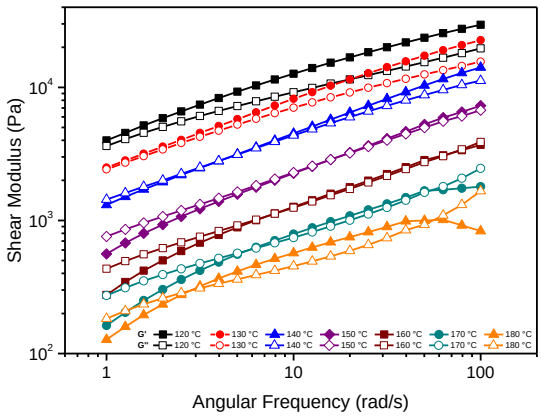

Figure 4-23. Frequency sweep results for the change in shear modulus of **P*-3(AIBN)-COOMe** with increasing angular frequency.

In Figure 4-23, *G''* was greater than *G'* at low frequencies from 160 °C, until a crossover to elastic-like behaviour was observed. This crossover occurred between 2-5 radians per second, depending on the temperature of the experiment, and so the viscous state persisted to higher frequencies than those measured for **P*-3(AIBN)** (Figure 4-17). It was expected that on conversion of the carboxylic acid groups to yield **P*-3(AIBN)-COOMe** a more flexible polymer network would form than observed for **P*-3(AIBN)** due to the removal of hydrogen bonding interactions, and so this result confirms that the relatively high molecular weight and inflexible architecture of these polymers contribute to the solid-like response.

From 170-180 °C a second crossover was also observed. This is the temperature range where plots of *G'* against *G''* for both **P*-3(AIBN)** and **P*-3(AIBN)-COOMe** demonstrated a return to temperature dependent behaviour. There is no clear separation between *G'* and *G''* for any of the measurements in Figure 4-23, and so it appears that under these experimental conditions the polymer was close to a transition, and that the structure fluctuated between the homogeneous and heterogeneous states.

From the results obtained for the polymers before and after conversion of the carboxylic acid groups to methyl esters it can concluded that the hydrogen bonding present in **P-3** and **P*-3(AIBN)** acts to prevent mixing of the PS and PMVS blocks, raising the T_{ODT} to temperatures significantly higher than that seen for **PS-*b*-PMVS-*b*-PS**. The resulting block copolymers displayed behaviour typical of cross-linked or filled polymers at temperatures below the T_{ODT}, which explains the origin of the elastic behaviour seen previously for **P-3**. Converting the carboxylic acid groups to methyl esters acted to lower T_{ODT} back to below 120 °C for **P-3-COOMe** and **P*-3(AIBN)-COOMe**, allowing the PS and PMVS block microstructure to become disordered. This mixing was

not sufficient for liquid-like melt behaviour to be seen in the desired frequency range for **P-3-COOMe**, however, suggesting that the stiffness of this polymer chain favours elastic behaviour under these shear conditions. **P*-3(AIBN)-COOMe** appeared to demonstrate viscous like behaviour at high ω, but neither the elastic nor the viscous response clearly dominated the other over the full frequency range measured. Nevertheless, it was demonstrated that with the correct functionality it was possible to exceed the T_{ODT} under some shear conditions and form a liquid-like melt, although only at relatively low shear.

4.2.3.4. Conversion of Residual Carboxylic Acid Groups to Methyl Esters for Liquid Crystal Elastomers

The influence of hydrogen bonding on the microphase segregation of the PS and PMVS blocks of the LC-functionalised triblock copolymers was apparent from comparison of the plots of G' against G'' for **P-3-M1(65)-COOH(35)** (Figure 4-16) and **P-3-M1(65)-COOMe(35)** (Figure 4-24). No temperature dependence was observed between 120-160 °C for the methyl ester polymer, suggesting that in this temperature range the triblock copolymer was above the T_{ODT}. From 160-180 °C, however, the ratio of the two moduli became temperature dependent again. This suggests a change in the microstructure of the polymer occurred, where the microphase separation transition (MST) resulted in a structure where the PS and PMVS domains were segregated.

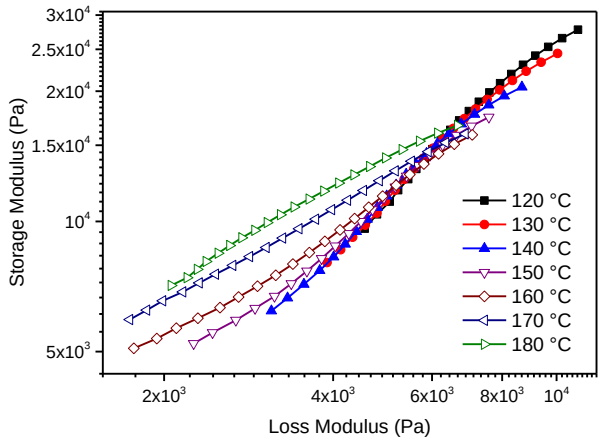

Figure 4-24. Plot of G' against G'' for **P-3-M1(65)-COOMe(35)**. From 120-140 °C the curves are independent of temperature. However, from 150 °C they become temperature dependent which suggests that a change in the polymer microstructure has occurred, raising the T_{ODT}. Filled symbols indicate an isotropic state whereas unfilled symbols indicate a nematic state.

The origin of the change in trend became apparent on inspection of the variation in the viscosity with angular frequency and temperature (Figure 4-25). For both plots a change in gradient was detected at 160 °C. The viscosity initially decreased with temperature, until reaching 160 °C where it started to increase, which was especially apparent at low frequencies. No T_{iso} was detected by DSC for this polymer, suggesting that the LC-containing PMVS block was isotropic in the as-cast polymer disk. Therefore, it appears that at 160 °C a shear-induced nematic mesophase was formed, which would explain the increase in viscosity seen from this temperature forward and also the apparent MST seen in Figure 4-24. It has been shown that for asymmetric block copolymers that form spheres in a matrix of the LC block, as in this case, the nematic mesophase acts to stabilise the microphase segregated state, with the microstructure observed at temperatures considerably higher than the T_{iso}.[7] This work however did not demonstrate a switching of behaviour between the two states occurring due to applied shear and elevated temperatures.

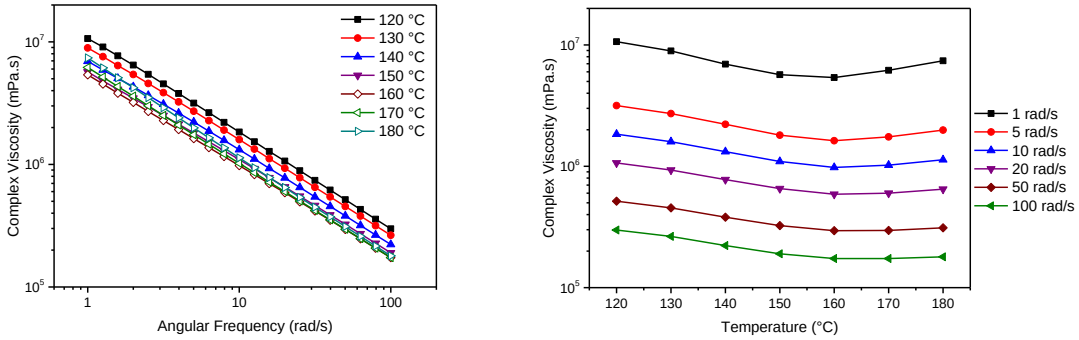

Figure 4-25. Variation in complex viscosity with angular frequency (left) and temperature (right) for **P-3-M1(65)-COOMe(35)**. Filled symbols indicate an isotropic state whereas unfilled symbols indicate a nematic state.

The plot of G' and G'' against angular frequency demonstrated no obvious difference between these two states (Figure 4-26). An elastic-like response was seen at all temperatures and frequencies, both before and after the nematic behaviour was evident. By calculating the difference between the values for G' and G'' at ω=1 and ω=100 at fixed temperatures, it was seen that in the isotropic state the two curves were converging with increasing temperature, then started to diverge once the transition occurred. This suggests that liquid-like behaviour might be possible for this polymer before formation of the nematic mesophase, but at very low values of ω or at temperatures outside the thermally stable range of the polymer. This is similar to the results seen for **P-3-COOMe** and suggests that the relatively high molecular weight of the polymer and

the stiffness imparted by the PS blocks may be detrimental to achieving the desired liquid-like melt properties.

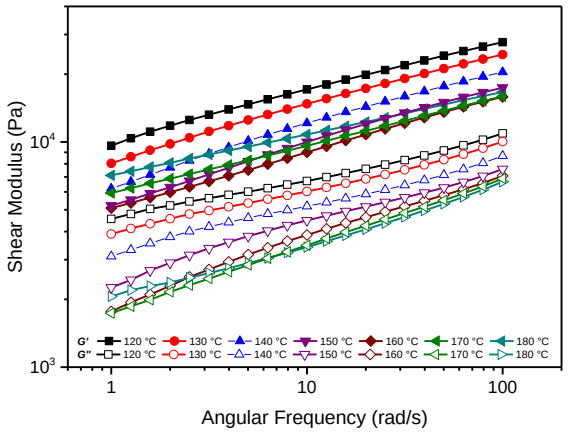

Figure 4-26. Frequency sweep results for the change in shear modulus of **P-3-M1(65)-COOMe(35)** with increasing angular frequency.

Considering that viscous behaviour was measured for **P*-3(AIBN)**, a portion of this polymer was functionalised with **M1** before converting the carboxylic acid functionality to methyl esters to give **P*-3(AIBN)-M1-COOMe**. This polymer also did not have a T_{iso} detectable by DSC in the as-cast state, which suggests that on conversion of the carboxylic acid to a methyl ester the resulting reduction in the T_g of the PMVS block to temperatures significantly lower than room temperature prevented the highly mobile PMVS chains from supporting an ordered nematic state.

The results for the viscosity obtained from the frequency sweep on this polymer again suggest the formation of a shear-induced nematic mesophase, albeit one that formed at lower temperatures than observed for **P-3-M1(65)-COOH(35)**. In this case the onset of nematic-like behaviour could be detected from 140 °C (Figure 4-27), which is likely due to **P*-3(AIBN)** having a lower T_g than **P-3** and so the polymer chains being more deformable (and so easier to align by applied shear) at lower temperatures.

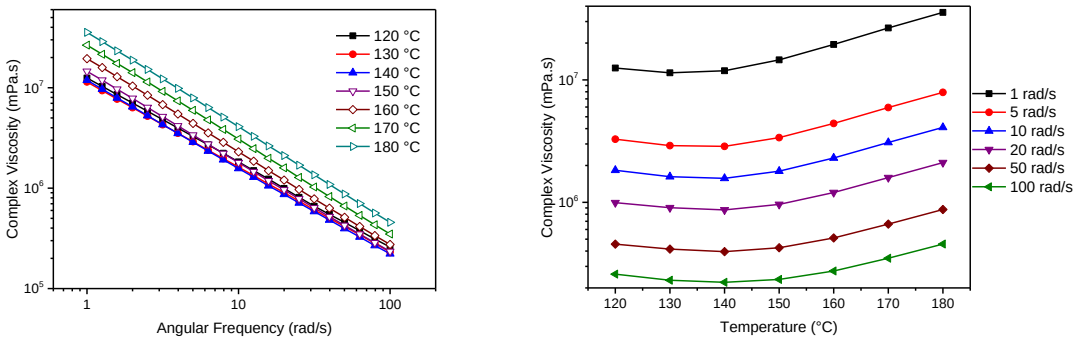

Figure 4-27. Variation in complex viscosity with angular frequency (left) and temperature (right) for **P*-3(AIBN)-M1-COOMe**. Filled symbols indicate an isotropic state whereas unfilled symbols indicate a nematic state.

The overlap between curves in the plot of G' against G'' was much weaker for **P*-3(AIBN)-M1-COOMe** than for **P-3-M1(65)-COOMe(35)** at low temperature (Figure 4-28), which suggests that in this temperature range there was sufficient nematic character that the blocks were unable to mix. At 180 °C the material was clearly still below the T_{ODT}, again suggesting that the induced nematic mesophase prevented the formation of a homogeneous melt.

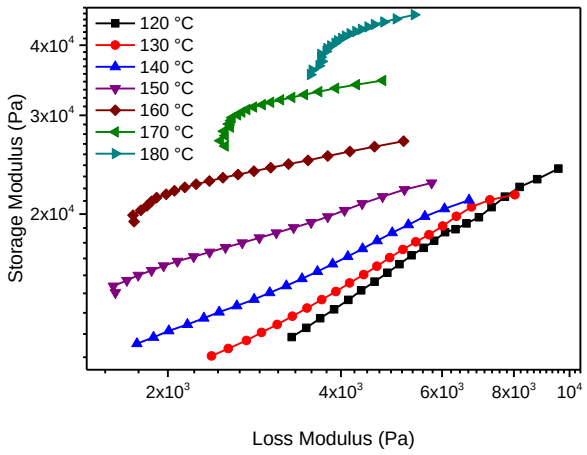

Figure 4-28. Plot of G' against G'' for **P*-3(AIBN)-M1-COOMe**. The strong temperature dependence suggests that the polymer is above T_{ODT} at all temperatures measured.

The plot of the shear moduli against angular frequency demonstrated elastic-like behaviour at all temperatures and angular frequencies measured. This result suggests that the nature of the linking group attachment step is not the limiting factor in forming a liquid-like melt, with both the photoinitiator and AIBN resulting in LCEs that demonstrate elastic properties. The apparent phase transition from an isotropic to nematic state appears to have a greater influence on the

microstructure, with the nematic mesophase acting to stabilise microphase segregation of the PS and PMVS blocks due to the energy penalty associated with mixing the highly aligned nematic with the disordered PS block, therefore acting like a nanoscale filler. It would appear that this effect, combined with the relatively stiff and high molecular weight triblock copolymer backbone, acted to maintain microphase segregation of the blocks in the stable temperature range of the LCEs and under the shear conditions accessible by the rheometer.

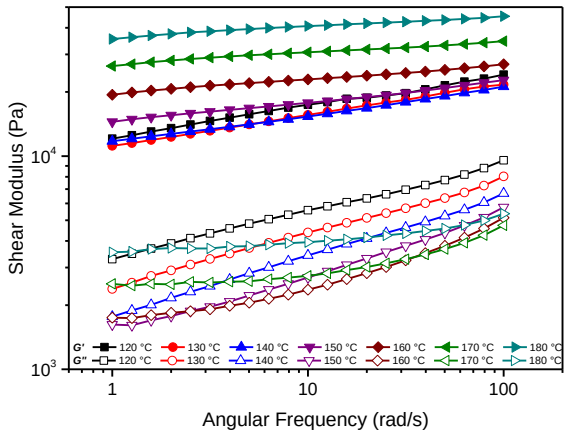

Figure 4-29. Frequency sweep results for the change in shear modulus of **P*-3(AIBN)-M1-COOMe** with increasing angular frequency.

To confirm that a shear-induced nematic mesophase was formed in **P*-3(AIBN)-M1-COOMe**, which then induced the MST to occur from a homogeneous state, DSC experiments were carried out for a piece of the disk used in the rheology experiment. Three cyclic measurements were carried out, with the first heating cycle expected to erase the thermal history of the sample and reproducible data collected on the second and third cycles. Two features were observed in the resulting thermogram: a second order transition that corresponded to the T_g of the PMVS block at -13.2 °C and a first order transition at 95 °C, which was taken as being the nematic to isotropic transition (Figure 4-30). The persistence of this peak after heating above T_{iso} suggests that the shear-induced structure of the polymer was maintained under these experimental conditions and confirms that once the mesophase is induced in the polymer, it is stabilised by the microphase segregation of the PS and PMVS blocks.

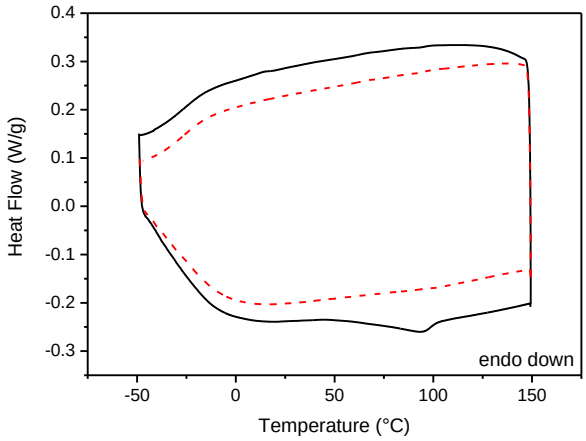

Figure 4-30. DSC results for **P-3-M1(65)-COOMe(35)** taken on heating (lower) and cooling (upper). Samples were obtained before (dashed) and after (solid) rheological measurements. Only the sheared rheology sample gave a peak corresponding to the nematic-isotropic transition at 95 °C.

These results for **P-3-M1(65)-COOMe(35)** and **P*-3(AIBN)-M1-COOMe** therefore suggest that the presence of the nematic mesophase acts to prevent mixing of the PS and PMVS blocks by stabilising the spherical microphase segregated structure and so inhibits the formation of a homogeneous, liquid-like melt. Literature examples of side-chain LCPs have demonstrated that liquid-like properties can be obtained at high enough shear,[8] and so in order to understand the effect of the LC block without considering interactions with the PS blocks, a PMVS homopolymer was synthesised and functionalised with **M1**.

4.2.3.5. Comparison of Liquid-Crystal Functionalised PMVS Homopolymer with Triblock Copolymer

Further insight into the mechanism preventing liquid-like flow of the LCE was be obtained by studying the shear response of **PMVS-3-M1(86)-COOH(14)**. Results were limited to three temperatures as during the experiment the sheared melt flowed from beneath the top plate of the rheometer, meaning that the higher temperature measurements were taken on an unevenly filled bottom plate. This is also the source of the deviation from trend seen for all results at 150 °C.

Results for G' and G'' with increasing angular frequency are given in Figure 4-31. The polymer displays significantly different properties to those seen for the LCEs based on the triblock copolymer backbone, with an elastic response observed at low frequencies and a liquid-like response at high frequencies. This confirms that without the PS domains it is possible for the LC-functionalised PMVS block to form a liquid-like melt. Unlike the standard response observed for ABS, PLA and TPU, however, the plot of G' and G'' against increasing ω initially demonstrated a decrease in modulus.

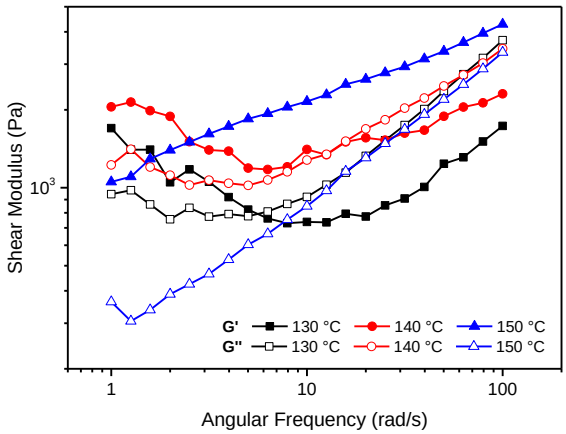

Figure 4-31. Frequency sweep results for the change in shear modulus of **PMVS-3-M1(84)-COOH(16)** with increasing angular frequency at selected temperatures.

The low shear measurements were taken at a temperature above the T_{iso} where it was expected that the LC would exist in an isotropic state with no nematic domains present. If this was the case, the LCP would behave as an uncrosslinked, random-coil polymer, with liquid-like behaviour seen much like that for the standard materials and **PS-*b*-PMVS-*b*-PS**. However, from the results for the viscosity given in Figure 4-32 it would appear that even at low shear the deformation was sufficient to form a shear-induced nematic mesophase in the highly flexible PMVS homopolymer. This resulted in a continuous decrease in viscosity and shear modulus as the polymer chains become more aligned, and so less entangled.

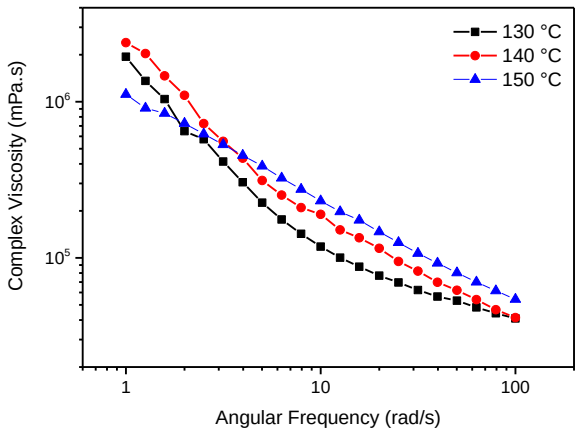

Figure 4-32. Variation in complex viscosity with temperature for **PMVS-3-M1(84)-COOH(16)**.

A sharp decrease in viscosity and G' was seen for values of ω between 1-3 rad s^{-1}, and then from 3-11 rad s^{-1} the rate of the decrease in viscosity appeared to slow and G' was approximately constant. This elastic-like behaviour at low shear when heated above the T_{iso} (and so in a region where the material is expected to show liquid-like behaviour) has been reported for other side-chain liquid crystal polymers (SCLCPs).[16–18]

In these literature examples it was claimed that the alignment of mesogenic groups lead to the formation of a shear-induced nematic mesophase, although some disagreement existed as to whether this resulted in solid-like[18] or gel-like[19,20] behaviour. In either case, G' was greater than G'' under low strain and low angular frequency conditions, such as those encountered for measurements on **PMVS-3-M1(86)-COOH(14)**. This low-shear elastic-like behaviour was shown to be dependent on interactions with the rheometer plates and the gap distance,[21] with the measurements for **PMVS-3-M1(86)-COOH(14)** taken on a disk with thickness around 0.1 mm, well within the sub-millimetre range where this effect has been observed.[21] The explanation for the elastic-like behaviour above the T_{iso} was proposed to be the polymer architecture, with the side-chain mesogen acting as interconnects between chains and the level of elastic behaviour dependent on the amount of interdigitation possible.[18] It can therefore be proposed that for **PMVS-3-M1(86)-COOH(14)** between ω = 3-11 rad s^{-1} the nematic mesophase was sufficiently aligned that interdigitation of the side chains could occur, resulting in the elastic-like behaviour and a change in gradient of the decrease in viscosity with time, until the shear reached a value between 11-100 rad s^{-1} where the ordered state was disrupted and so became increasingly isotropic. At high shear the viscosity started to converge for all temperatures measured and the material displayed more typical viscoelastic behaviour.

In literature examples with polyacrylates the effect persisted to temperatures 100 °C higher than the measured T_g, and up to 14 °C higher than the T_{iso}, although no measurements were taken at higher temperatures in this case due to potential thermal degradation of the polymer.[18] Due to the breakdown of the sample it is not known to what temperature this effect could be detected for **PMVS-3-M1(86)-COOH(14)**, but a clear plateau was apparent for the measurement taken at 140 °C, which is 117 °C above the T_g and 11 °C above the T_{iso} as measured by DSC.

These results confirm that without the PS block a PMVS homopolymer functionalised with **M1** and carboxylic acid groups is capable of forming a liquid-like melt in its stable temperature range through the disruption of an induced nematic mesophase. The dual effect of stabilising the ordered nematic mesophase and increasing the molecular weight (and so the rigidity) of the triblock copolymer seen on introduction of the PS blocks therefore explain the elastic-like response seen for **P-3-M1(65)-COOH(35)** and **P-3-M1(65)-COOMe(35)** (as well as the AIBN equivalents).

4.2.3.6. Elastic Behaviour in P-3-M1(65)-COOMe(35) Above T_{ODT}

Whilst it was shown that the nematic mesophase appears to prevent mixing of the PS and PMVS blocks in the LCEs by stabilisation of the spherical morphology, this does not explain the elastic behaviour seen for **P-3-M1(65)-COOMe(35)** above the T_{ODT} and before the nematic mesophase was induced. In this case the elastic-like behaviour was likely due to the relatively high molecular weight and stiffness of the polymer chain, as suggested for **P-3-COOMe**, with the low-shear elastic-like behaviour reported for the homopolymer potentially offering a further explanation. Whilst low-shear elastic behaviour has not been investigated for side-chain triblock copolymers or at temperatures so far above the T_{iso}, it may be that interdigitation of the bulky side chains and the resulting intermolecular interactions produced a physical network which contributed to the elastic-like properties.

A further explanation could be found in work which demonstrated that on heating highly asymmetric block copolymers which adopt a body centred cubic (bcc) spherical morphology to temperatures around the T_{ODT}, a disordered micellar morphology can be accessed between the ordered bcc and homogeneous state.[3,4,8] This phase adopts a liquid-like structure, with no long-range order, and was identified both on heating and cooling through a decrease in the G' and viscosity due to softening of the sphere-forming lattice. The aggregates acted as filler particles and so resulted in elastic-like behaviour. In the case of **P-3-M1(65)-COOMe(35)** a similar microstructure could be obtained but would not result in an obvious change in G' or η due to the disordered nature of the undeformed lattice occupied by the spherical PS domains.

4.3. Conclusions

The rheological behaviour of the side-chain liquid crystal triblock copolymer was shown to be complex, and to have a strong dependence on the temperature and functionality present on the PMVS block, and so the microphase structure adopted by the triblock copolymer. The functionalisation of the triblock copolymer with a linking group and then either **M1** or **M2** resulted in block copolymers that were not suited for processing by melt extrusion.

It was likely that carboxylic acid functionality prevented mixing of the PS and PMVS domains in the stable temperature range of the LCEs. Conversion of the carboxylic acid to a methyl ester acted to lower the T_{ODT} back to a temperature where the LC-functionalised polymers were stable and SAOS experiments on these samples confirmed that initially the PS and PMVS blocks were able to mix. However, elastic behaviour was still observed – potentially due to the high molecular weight of the polymer and interactions between side-chains. On formation of a shear-induced nematic mesophase the T_{ODT} was raised back above the thermally stable range of the polymer. This shear induced nematic mesophase was shown to persist for multiple cycles of heating above the T_{iso} by DSC and so it appears that the resulting segregated microstructure was stable and had a high barrier to mixing once formed.

The stabilising effect of the nematic mesophase was confirmed by results obtained for the PMVS homopolymer functionalised with **M1**. At low shear elastic-like behaviour was seen, potentially due to interdigitation of the aligned side-chains, but at angular frequencies above 11 rad s^{-1} the polymer became increasingly isotropic and viscous behaviour was observed. This suggests the stabilisation of the nematic mesophase by the microphase segregation in the triblock copolymer prevents liquid-like melt formation which, combined with the increased molecular weight with PS blocks present, prevents melt extrusion of the LCEs.

In order for extrusion to be a viable processing for these materials, further studies should be carried out to identify whether reduction of the molecular weight of the **PS-*b*-PMVS-*b*-PS** block copolymer backbone results in a LCE with sufficient conformational flexibility that liquid-like behaviour can be observed. The LC-functionalised PMVS homopolymer demonstrated suitable rheological behaviour under shear and should therefore be suitable for extrusion, however, the lack of PS blocks will limit the mechanical properties of the polymer and may result in undesired thermal creep due to the relatively low T_g.

4.4. Experimental

Samples of the experimental polymers were prepared as 15 mm diameter disks by casting from toluene in a PDMS mould, with a target thickness of approximately 1 mm. Standard material samples were prepared using commercially available filaments of polylactic acid (PLA) (Natureworks 4043D, natural colour), acrylonitrile butadiene styrene (ABS) (Reprapper Tech. Ltd., natural colour) and a thermoplastic polyurethane (TPU) (Ninjaflex by Ninjatek, clear colour). Disks were printed with a diameter of 15 mm and a thickness of 1 mm.

4.4.1. Rheology

Rheology was carried out on an Anton Paar MCR302 rotational rheometer with a 15 mm diameter parallel plate geometry and heated using an electric Peltier in air. Temperatures were measured with an accuracy of ±0.2 °C.

4.4.1.1. Procedure

The sample was located centrally on the bottom plate of the rheometer and aligned with the top geometry before decreasing the gap size manually and heating to the test temperature. The sample was held for five minutes to ensure equilibration and then the experimental gap size was set automatically by bringing the plates together until a normal force of 0.25 N was measured to ensure contact between the sample and upper geometry before starting the experiment (amplitude or frequency sweep). This normal force control was maintained throughout the experiments, with the gap size automatically adjusted where necessary.

4.4.1.2. Amplitude Sweep

For each sample an amplitude sweep was first carried out at a constant frequency of 10 rad s^{-1} and a fixed temperature (sample dependent). The strain amplitude was varied on a logarithmic scale from 0.01-100% with 10 measurements made per decade to give 41 data points in total. The strain to be used for the frequency measurement was identified as the largest strain within the linear viscoelastic region where G' was independent of the applied strain.

4.4.1.3. Frequency Sweep

Each frequency sweep was carried out at a fixed temperature and strain. Measurements were taken after the amplitude sweep with an oscillating frequency on a logarithmic scale from 1-100 rad/s with 10 measurements made per decade to give 21 data points in total at each temperature. When measurements were taken for multiple temperatures the sample was heated after each experiment to the next target temperature at a rate of 2 °C per minute and held for 5 minutes to ensure equilibration of the structure before performing the next frequency sweep measurement.

4.4.2. Differential Scanning Calorimetry

DSC experiments were carried out with a TA Instruments Q100. Samples were weighed into an aluminium pan and cycled three times between -50 and 150 °C under a nitrogen atmosphere, with measurements taken on both the heating and cooling cycles using a heating/cooling rate of 10 °C per minute.

4.5. References

1 S. V. Ahir, A. R. Tajbakhsh and E. M. Terentjev, Self-Assembled Shape-Memory Fibers of Triblock Liquid-Crystal Polymers, *Adv. Funct. Mater.*, 2006, **16**, 556–560.

2 C. D. A. E. Han and J. Kim, Rheological Technique for Determining the Order-Disorder Transition Of, *Polymer*, 1987, **25**, 1741–1764.

3 N. Sakamoto, T. Hashimoto, C. D. Han, D. Kim and N. Y. Vaidya, Order−Order and Order−Disorder Transitions in a Polystyrene- Block -Polyisoprene- Block -Polystyrene Copolymer, *Macromolecules*, 1997, **30**, 1621–1632.

4 C. D. Han, N. Y. Vaidya, D. Kim, G. Shin, D. Yamaguchi and T. Hashimoto, Lattice Disordering/Ordering and Demicellization/Micellization Transitions in Highly Asymmetric Polystyrene-Block-Polyisoprene Copolymers, *Macromolecules*, 2000, **33**, 3767–3780.

5 X. Wang, E. E. Dormidontova and T. P. Lodge, The Order−Disorder Transition and the Disordered Micelle Regime for Poly(Ethylenepropylene-b-Dimethylsiloxane) Spheres, *Macromolecules*, 2002, **35**, 9687–9697.

6 S. S. Kim and C. D. Han, Oscillatory Shear Behaviour of a Thermotropic Liquid-Crystalline Polymer, *Polymer*, 1994, **35**, 93–103.

7 M. Anthamatten and P. T. Hammond, A SAXS Study of Microstructure Ordering Transitions in Liquid Crystalline Side-Chain Diblock Copolymers, *Macromolecules*, 1999, **32**, 8066–8076.

8 K. M. Lee and C. D. Han, Microphase Separation Transition and Rheology of Side-Chain Liquid-Crystalline Block Copolymers, *Macromolecules*, 2002, **35**, 3145–3156.

9 PLA Data Sheet, https://www.natureworksllc.com/~/media/Files/NatureWorks/Technical-Documents/Technical-Data-Sheets/TechnicalDataSheet_4043D_3D-monofilament_pdf.pdf?la=en, (accessed 28 March 2018).

10 ABS Data Sheet, https://shop.3dfilaprint.com/filaprint-abs-x-natural-175mm-3d-printer-filament-10518-p.asp, (accessed 28 March 2018).

11 TPU Data Sheet, https://ninjatek.com/products/filaments/ninjaflex/, (accessed 28 March 2018).

12 T. G. Mezger, *The Rheology Handbook*, Vincentz Network, Hanover, 4th edn., 2014.

13 F. N. Cogswell and K. F. Wissbrun, *Rheology and Processing of Liquid Crystal Polymer Melts*, Chapman & Hall, London, 1996.

14 C. D. Han, J. Kim and J. K. Kim, Determination of the Order-Disorder Transition Temperature of Block Copolymers., *Macromolecules*, 1989, **22**, 383.

15 F. S. Bates, Polymer-Polymer Phase Behavior, *Science*, 1991, **251**, 898–905.

16 C. Pujolle-Robic and L. Noirez, Observation of Shear-Induced Nematic-Isotropic Transition in Side-Chain Liquid Crystal Polymers, *Nature*, 2001, **409**, 167–171.

17 H. Mendil, P. Baroni and L. Noirez, Unexpected Giant Elasticity in Side-Chain Liquid-Crystal Polymer Melts: A New Approach for the Understanding of Shear-Induced Phase Transitions, *Europhys. Lett.*, 2005, **72**, 983–989.

18 H. Mendil, P. Noirez, P. Baroni and I. Grillo, The Frozen State in the Liquid Phase of Side-

Chain Liquid-Crystal Polymers, *Phys. Rev. Lett.*, 2006, **96**, 077801.

19 D. Collin, P. Martinoty, P. Collin and P. Martinoty, Comment on 'the Frozen State in the Liquid Phase of Side-Chain Liquid-Crystal Polymers', *Phys. Rev. Lett.*, 2007, **98**, 249801.

20 O. Pozo, D. Collin, H. Finkelmann, D. Rogez and P. Martinoty, Gel-like Elasticity in Glass-Forming Side-Chain Liquid-Crystal Polymers, *Phys. Rev. E*, 2009, **80**, 031801.

21 L. Noirez, P. Baroni and H. Mendil-Jakani, The Missing Parameter in Rheology: Hidden Solid-like Correlations in Viscous Liquids, Polymer Melts and Glass Formers, *Polym. Int.*, 2009, **58**, 962–968.

Chapter 5: Suitability of P-3-M1(65)-COOH(35) for Processing by Electrospinning

5.1. Introduction

It was shown in Chapter 4 that the thermoplastic liquid crystal elastomers (LCEs), including **P-3-M1(65)-COOH(35)**, were not suitable for melt processing due to a combination of the stabilising effect of the nematic mesophase on the microphase separation of the polystyrene (PS) and poly(methylvinylsiloxane) (PMVS) blocks and the high molecular weight. These resulted in elastic-like behaviour throughout the stable temperature range. However, the high molecular weight (and so viscosity) is beneficial for processing from solution and makes this polymer a viable candidate for electrospinning. Solution processing methods are well suited for the formation of polymeric fibres, where the action of drawing a fibre is expected to align the LC mesophase along the long axis, with the resulting fibres having a high surface area to volume ratio. This property makes fibres obtained by electrospinning attractive for applications as stimuli-responsive actuators.[1]

Responsive fibres of liquid crystal polymers (LCPs) and LCEs have previously been produced from polymer solutions. For LCPs both a custom microfluidic setup[2] and electrospinning[3,4] have been shown to result in smooth fibres with small diameters (30-33 μm for the microfluidic setup and 0.5-2.0 μm by electrospinning).[2–4] It was demonstrated that the level of LC alignment was dependent on the diameter of the fibres, with smaller diameters resulting in stronger mesophases,[3] and so it is expected that electrospinning of LCEs should result in well-aligned fibres that could be used as mats or bundles for actuation.

To obtain continuous, defect free fibres rather than droplets it is important to consider the balance between the surface tension (which will act to reduce surface area through the formation of droplets) and of the surface charge (where repulsion of electrostatic charges will act to elongate the jet and so form fibres). Therefore, the viscosity, charge density and surface tension of the polymer solution all have a strong effect on the fibre morphology. Smooth fibres can also be achieved by the incorporation of additives to the spinning solution, for example, through the addition of salts it is possible to modify the charge density and the addition of high molecular weight polymers such as polyethylene oxide (PEO) increase interactions between the polymer and the solvent, and so increase the viscosity of the solution favouring smooth fibre formation.[7]

The diameter of the fibre can be controlled by adjustment of experimental parameters such as the feed rate, electric field and the gap between the spinneret and the collector, as well as by the

solution concentration.[7] The concentration has been shown to have a large effect on the diameter of the fibres, with increasing concentration resulting in more chain entanglements and so a polymer structure which is better able to resist the stretching applied as the jet travels towards the collector.[8] The effect of the electric field is smaller, but will act to control the shape of the solution drop at the nozzle and the velocity at which the jet travels. The voltage will also determine the stability of the jet, with a threshold value required for a fibre to form but too high a voltage resulting in droplet formation.[8,9]

Only one example of electrospinning a pure main-chain LCE has been reported to date, with crosslinking introduced during the spinning processes by irradiation of the jet with UV light.[5] For electrospinning to be successful the polymer must have a high enough molecular weight, and so viscoelastic character, that entanglements can form between chains and the fibre can extend with the jet during the spinning process and overcome the competing effect of forming beads due to Rayleigh instabilties.[6] Electrospinning has been shown to be possible for LCEs with a molecular weight of 44,000 g mol^{-1},[5] and so **P-3-M1(65)-COOH(35)** with a molecular weight of 150,000 g mol^{-1} was expected to form continuous fibres.

Therefore, the aim of the work reported herein was to determine the suitability of **P-3-M1(65)-COOH(35)** for electrospinning and to attempt to produce the first example of an electrospun side-chain thermoplastic LCE fibre. This was achieved by first manually drawing fibres from a viscous solution, with their morphology and level of order identified by Small Angle X-Ray Scattering (SAXS). Electrospinning experiments were then carried out, with the solution concentration and solvent surface tension varied in order to obtain continuous fibres. It was also attempted to obtain aligned arrays of fibres through the choice of fibre collector. The successful formation of LC monodomains was confirmed by Polarised Optical Microscopy (POM) on the fibres, and their response to applied UV irradiation or heating through the isotropic transition temperature (T_{iso}) investigated.

5.2. Results and Discussion

5.2.1. Microphase Segregated Morphology of Hand-Drawn Fibres

To test the suitability of **P-3-M1(65)-COOH(35)** for electrospinning a 40 wt% solution in CH_2Cl_2 was prepared, from which fibres with diameters between 0.13-0.20 mm were obtained by drawing the viscous solution with a glass capillary. Two of the fibres were annealed at 120 °C for 2 hours, using the procedure described in Chapter 3 for the polymer films, in order to promote formation of the microphase segregated morphology. One of these fibres was then stretched along

its length whilst heated at 120 °C in order to induce stronger alignment of the mesophase. Room temperature SAXS experiments were carried out to determine the level of alignment present in both cases, with the fibres mounted vertically.

It was shown in Section 3.2. that **P-3-M1(65)-COOH(35)** adopts a microphase segregated morphology at room temperature, with spherical PS domains occupying a disordered lattice within a continuous PMVS phase. The results of the azimuthal integration for both stretched and unstretched fibres are given in Figure 5-1, from which it was apparent that the spherical morphology was present in both. The location of the structure factor (q^*) peak was shifted to lower values in reciprocal space for the stretched fibre, suggesting an increase in the inter-sphere spacing occurred with respect to the undeformed fibre.

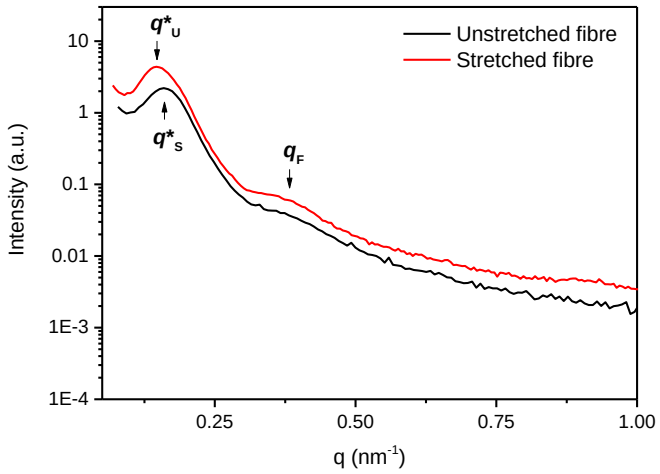

Figure 5-1. Background subtracted room temperature SAXS data for fibres of **P-3-M1(65)-COOH(35)** before and after stretching. The q^* peaks at 0.146 and 0.159 nm^{-1} correspond to an average spacing between PS domains of 39.5 and 43.0 nm for the unstretched and stretched fibre respectively. The broad q_F peak at 0.39 nm^{-1} indicates an average PS domain radius of 16 nm.

It was not possible to unambiguously identify the peak value for the broad, low-intensity spherical form factor (q_F) peak and therefore the value of the average radius of the spheres was calculated to two significant figures. This gave a result of 16 nm, smaller than the 20 nm measured for films of the same polymer. Values of the average centre-to-centre spacing of the PS domains were obtained by identification of the maximum in the q^* peak for each fibre and quoted to 3 significant figures. The undeformed fibre had a q^* peak which corresponded to a spacing of 39.5 nm between PS domains, which is comparable to the value of 39.8 nm measured in Section 3.2.2.3. for a film of **P-3-M1(65)-COOH(35)**. The stretched fibre had a q^* peak indicative of a spacing of 43.0 nm between spheres, which suggests deformation of the lattice occupied by the spheres into an

anisotropic arrangement. A good fit was obtained between the experimental data and that generated from the model described in Section 3.2.2.4. for the affine deformation of the PMVS domain with hard, undeformed particles (the PS domains) present. As before, the fit obtained by the model was in good agreement with the experimental data (Figure 5-2), with an increase in the calculated draw ratio and d-spacing observed for the stretched fibre compared with the unstretched fibre (Table 5-1).

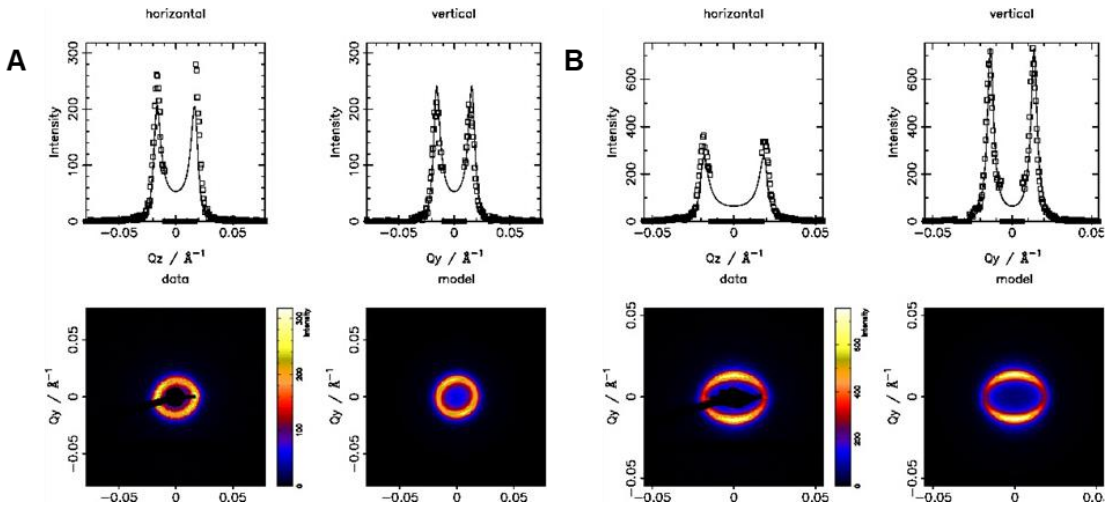

Figure 5-2. Comparison of model results with experimental data for (A) unstretched and (B) stretched fibres of **P-3-M1(65)-COOH(35)**.

Table 5-1. Results for model fit and experimental SAXS results for comparison.

Sample	PS Radius (nm)	d-spacing (nm)	Draw Ratio
Unstretched P-3-M1(65)-COOH(35)	13.40 ± 0.02	33.84 ± 0.03	1.06
SAXS	*16*	*39.5*	
Stretched P-3-M1(65)-COOH(35)	13.73 ± 0.01	34.83 ± 0.02	1.24
SAXS	*16*	*43.0*	

With the SAXS data suggesting anisotropy in the stretched fibre, integrations were carried out around the 0° and 90° directions only for both the stretched and unstretched fibres, with the directions relative to the 2D scattering result given in Figure 5-3. The fibres were mounted such that the direction of stretch was along the 90° direction.

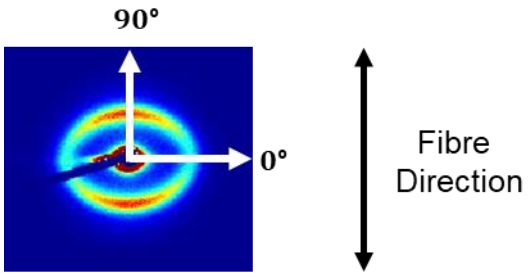

Figure 5-3. Definition of 0° and 90° directions used for anisotropic integrations of SAXS results and fibre direction.

The results of the perpendicular integrations for the unstretched fibre are given in Figure 5-4, where a small separation was seen between the q^* peaks, demonstrating that the elongational strain encountered whilst drawing the fibre from solution was sufficient for a minority of the PS domains to align along the fibre axis. The q^* peaks were located at values corresponding to an inter-sphere spacing of 36.1 and 41.3 nm in the 0° and 90° directions respectively. This was a larger difference between peaks in reciprocal space than observed for the stretched film of **P-3-M1(65)-COOH(35)** (0.022 nm^{-1} for the fibre compared with 0.015 nm^{-1} for the film) and suggests that the action of drawing the fibre induced stronger alignment of the PS domains in this case.

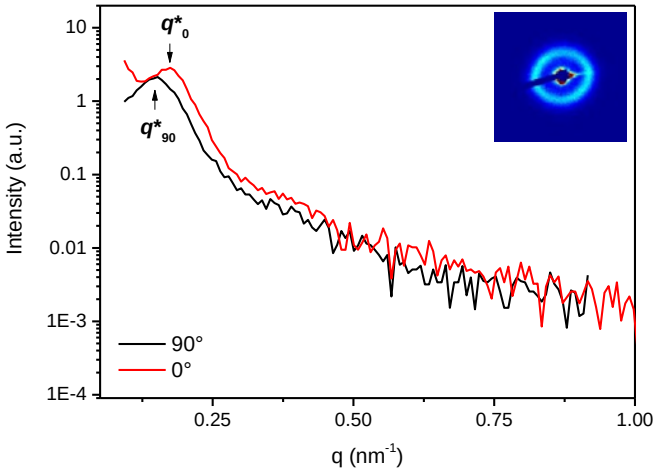

Figure 5-4. Background subtracted room temperature SAXS data for undeformed fibre of **P-3-M1(65)-COOH(35)**. The q^* peaks at 0.152 and 0.174 nm^{-1} correspond to an average spacing between PS domains of 36.1 and 41.3 nm respectively. Inset – 2D SAXS pattern showing weakly elliptical response.

The analysis was repeated for the stretched fibre. From the plot obtained in Figure 5-5 it was clear that increased alignment of the PS domains was obtained when compared with the undeformed fibre. The q^* peak was located at a value of q which corresponded to an inter-sphere spacing of 34.1 nm in the 0° direction and to 45.9 nm in the 90° direction. The curve obtained by integration in the direction of the stretch featured a weakly resolved shoulder which was located around 0.24 nm^{-1}, equivalent to $\sqrt{3}q^*$, a result that was seen in Section 3.2.2.4. for the aligned film of **P-3-M1(82)-COOH(18)**. No further peaks were apparent at values close to $\sqrt{2}q^*$ or $2q^*$, suggesting that rather than a body-centred cubic structure, a weakly aligned hexagonal close packed structure developed. The increased order in the 90° direction allowed for the calculation of an order parameter using Equation 3.7, with a value of 0.12 obtained for the spherical PS domains. This is relatively low, but comparable with the figure of 0.11 measured for the aligned film of **P-3-M1(82)-COOH(18)**. This polymer was shown to respond to UV irradiation in Section 2.2.7., and so it is expected that the aligned fibres of **P-3-M1(65)-COOH(35)** would also demonstrate responsive behaviour.

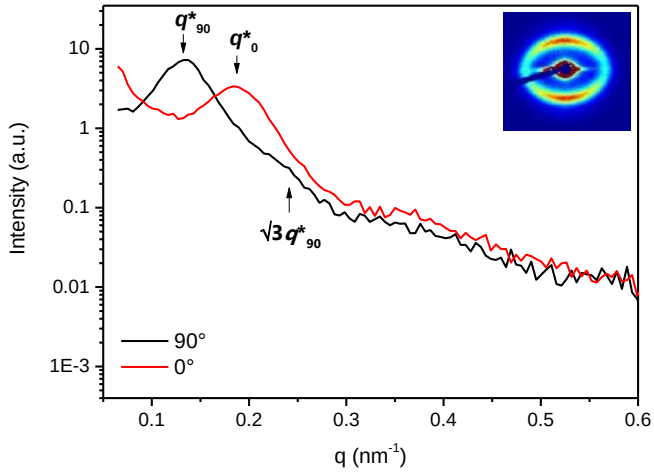

Figure 5-5. Background subtracted room temperature SAXS data for stretched fibre of **P-3-M1(65)-COOH(35)**. The q^* peaks at 0.137 and 0.184 nm^{-1} correspond to an average spacing between PS domains of 45.9 and 34.1 nm respectively. Inset – 2D SAXS pattern showing elliptical, anisotropic response.

It was evident from the 2D SAXS data that the alignment of PS domains occurred along the length of the fibre, with a contraction observed in reciprocal space in the 90° direction. The elliptical scattering pattern with increased intensity in the fibre direction indicated that the deformation occurred in the PMVS block, with the lattice occupied by the PS domains reordering, but the domains themselves retaining their original size and shape.[10] The broad reflections in the alignment direction suggest that the lattice occupied by the PS domains was relatively disordered, as was the case for the aligned film of **P-3-M1(82)-COOH(18)**.

From these results it was shown that an aligned fibre of **P-3-M1(65)-COOH(35)** could be drawn from a viscous solution of CH_2Cl_2, suggesting that the polymer had a molecular weight sufficient for forming fibres by electrospinning. It was also shown that the polymer adopted the spherical morphology required for thermoplastic elastomeric behaviour, and so retained the potential for actuation. Applying a tensile force to the fibre whilst heating above the T_{iso} acted to improve the alignment when compared with a fibre that underwent no deformation other than that encountered when drawing from solution. It is expected that significant extensional forces will be experienced by the fibre during electrospinning, and so an aligned LC mesophase is expected.

5.2.2. Electrospinning Fibres of P-3-M1(65)-COOH(35)

Many factors contribute to the ability to create smooth fibres from a polymer solution by electrospinning, including the molecular weight, PDI and T_g of the polymer itself. Whilst these values are fixed for **P-3-M1(65)-COOH(35)**, other contributors such as the solution and experimental conditions can be varied to favour forming smooth fibres or to control the diameter. To identify appropriate conditions for spinning of **P-3-M1(65)-COOH(35)**, the solvent system with surface tension suitable for electrospinning of fibres rather than electrospray of droplets was first identified, before finding a concentration of **P-3-M1(65)-COOH(35)** that gave a solution with a suitable viscosity for the formation of continuous fibres. Finally, the nature of the collector was varied in order to increase the alignment of the fibres. The distance between the needle and the collector was maintained at approximately 12 cm in order to fix another variable and all experiments were carried out at room temperature and humidity. In all cases, the positive voltage was applied to the needle, and the negative voltage to the collector.

5.2.2.1. Determination of Conditions for Electrospinning

In order for electrospinning to occur (rather than electrospray of droplets) it is necessary to obtain a solution where the repulsion between electrostatic forces on the Taylor cone (which favour extension of the jet to form a fibre) overcomes the surface tension of the solvent (which favours the formation of droplets). An initial solution of 40 wt% **P-3-M1(65)-COOH(35)** in *N*,*N*-dimethylformamide (DMF) was prepared and stirred for 16 hours in order to ensure a homogeneous solution was obtained. Electrospinning was then attempted using several voltages and feed rates, with the fibres collected on a flat collector covered in aluminium foil. Initially, short fibres were obtained, with an example image given in Figure 5-6. It was expected that the molecular weight of 150,000 g mol^{-1} calculated for **P-3-M1(65)-COOH(35)** is high enough for continuous fibre formation, therefore, the surface tension of the solution was reduced by mixing DMF with THF in a ratio of 9:1 and the polymer concentration reduced to 32.5 wt%. DMF has a surface tension of 34.4 mN m^{-1} at 25 °C, compared with a value of 26.7 mN m^{-1} for THF,[11] therefore, by mixing the two it is expected that the electrostatic repulsion should start to dominate and allow for the formation of continuous fibres.

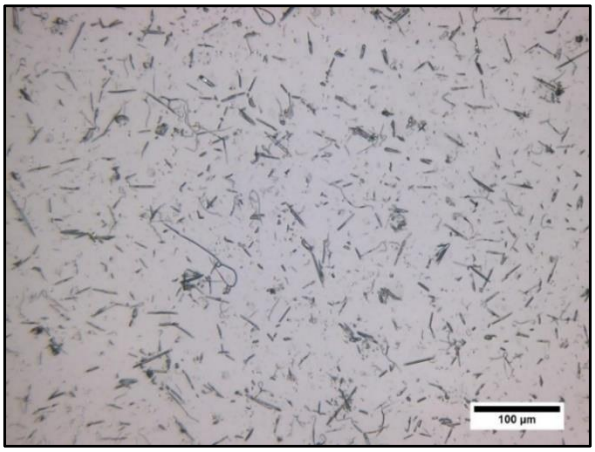

Figure 5-6. Short fibres obtained with 40 wt% solution of **P-3-M1(65)-COOH(35)** in DMF.

The modification of the solvent system was sufficient to reduce the surface tension such that long, continuous fibres could be collected. However, large droplets were still present on the fibres and some shorter, smaller diameter fibres were also present as shown in Figure 5-7. The continuous fibres were relatively large in diameter, with values measured from the microscopy images using ImageJ found to be between 2.8-4.6 µm, whereas the smaller fibres had diameters around 1.6 µm. The droplets were also large, with diameters up to 38.4 µm measured. It was expected that through adjustment of the experimental conditions it should be possible to reduce the number of beads. However, insufficient polymer was available to carry out a systematic investigation into the effect of these additives and so instead it was next confirmed that electrospinning formed an ordered nematic mesophase in the fibres, before increasing the level of alignment within the fibre array by replacing the flat collector with one that promoted ordered deposition of fibres.

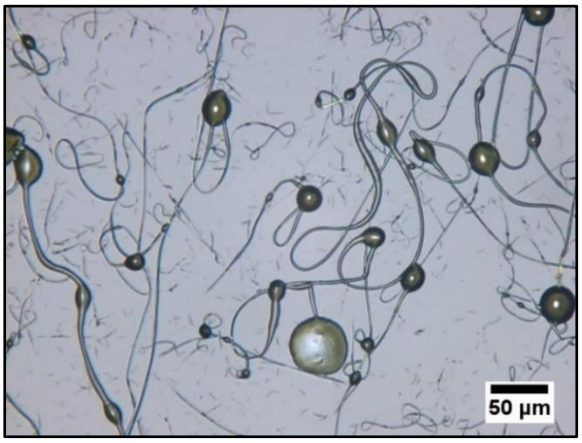

Figure 5-7. Longer fibres obtained from a 32.5 wt% solution of **P-3-M1(65)-COOH(35)** in DMF/THF.

5.2.2.2. Confirmation of Ordered Nematic Mesophase in Fibres

With experimental conditions for fibre spinning determined, the ability of the electrospinning process to form a nematic mesophase was next investigated. This was achieved using POM, where areas containing an ordered LC mesophase are expected to rotate the polarised light such that fibres oriented away from the direction of either polariser will appear bright, with the most intense response seen when oriented at 45° to the crossed polarisers. Areas with no aligned mesophase present remain dark. The formation of a nematic mesophase was first confirmed for fibres collected on a glass slide with applied voltages of -6.0 kV and +19.0 kV and a feed rate of 0.5 mL per hour. As before, predominantly continuous fibres were observed with large droplets and a small number of short fibres (Figure 5-8). Diameters of the fibres were measured to be between 1.7-4.6 μm, with the short fibres being thinner than the continuous fibres, whilst the droplets were measured to have diameters between 11.8-38.4 μm.

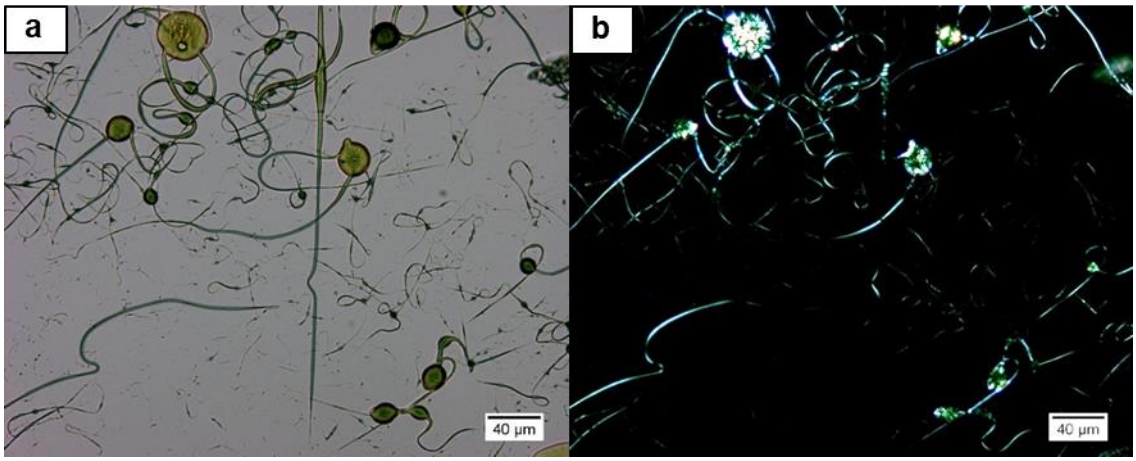

Figure 5-8. Images of fibres taken under (a) normal light and (b) crossed polarisers. Bright regions in (b) correspond to areas with LC mesophase present.

Under crossed polarisers it was apparent that alignment of the LC mesophase had occured (Figure 5-8), with bright regions observed in areas where the fibres lay at approximately 45° to the polarisers. Droplets also demonstrated birefringence, but it is expected that a more complex LC arrangement occurs in these regions. Areas where the fibres were oriented along the direction of one of the polarisers remained dark, for example the large, vertical fibre in the centre of Figure 5-8, suggesting that birefringence resulted in the bright areas as opposed to refraction.

In order to reduce the number of short fibres the solution was heated at 40 °C for 1 hour and then left to stir for 60 hours. When spun at applied voltages of -1.0 kV and +16.0 kV and a feed rate of 0.75 mL per hour continuous fibres were obtained as demonstrated in Figure 5-9. The fibres were measured to have diameters between 1.6-2.6 μm, with the droplets having diameters between 3.2 and 15.8 μm. No preferred orientation of the fibres was observed, as expected when using a flat collector, and under crossed polarisers it was apparent that an ordered LC mesophase was present, although the birefringence was relatively weak. Few short fibres were observed, and the droplets were considerably smaller than those seen previously, which suggested that the short period of heating and long stirring time improved the solubility of the polymer, resulting in a more viscous solution with improved spinnability.

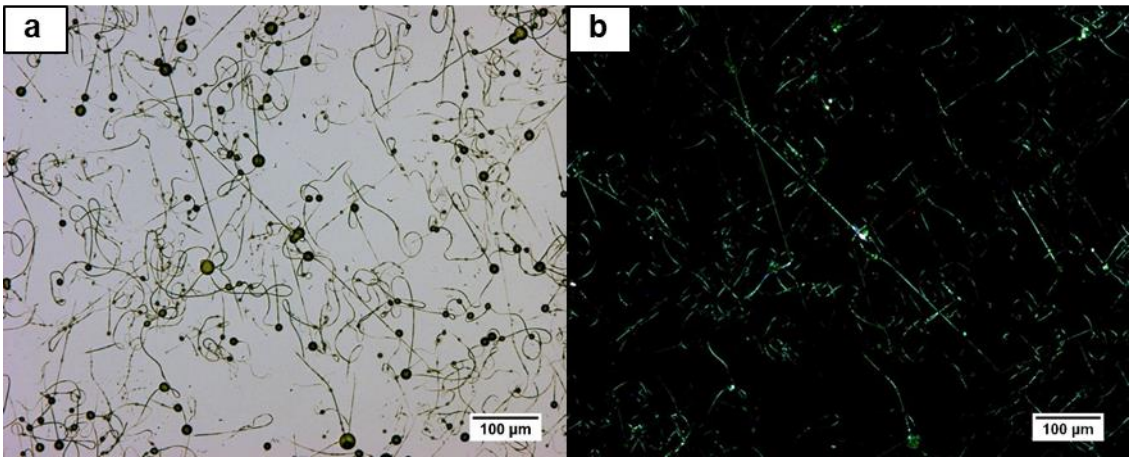

Figure 5-9. Images of fibres taken under (a) normal light and (b) crossed polarisers. Bright regions in (b) correspond to areas with LC mesophase present.

It is not possible to obtain an aligned, well-ordered array of fibres using a flat collector due to the whipping motion of the jet during fibre formation,[12] therefore, with conditions that give continuous fibres identified, the collector was varied to see if increased alignment of both the fibres and the LC mesophase could be achieved.

5.2.2.3. Improving Fibre Alignment

For applications that rely on actuation it is imperative that a highly aligned LC monodomain is obtained and that the angle of this alignment can be controlled. The ability to collect aligned mats, either with all fibres oriented in one direction or at 90° to one another, would also be useful for

the construction of actuating structures from the micrometre-scale fibres. For this reason, the flat collector was replaced with first parallel electrodes, which have been shown to result in highly aligned free-standing mats,[13] and secondly with wheel-shaped collectors which can also be used to obtain arrays of aligned fibres.[12]

It was not possible to obtain any characterisable fibres from the parallel electrode, which is most likely due to the high number of droplets present on the fibres. With this collector configuration fibres are deposited such that they bridge the gap between the two electrodes, which is reliant on the fibres being strong enough to support their own weight. Droplets act as defect points in the fibre, and so as points of fracture, which reduces the overall strength. It has been shown that droplets in fibres of LCPs can be reduced or removed by increasing the concentration of the solution, although initial experiments on solutions above 32.5 wt% **P-3-M1(65)-COOH(35)** did not form fibres as seen in Section 5.2.2.1.

The parallel electrode was therefore replaced with a rotating wheel (see Experimental section). In this configuration a supporting surface is provided for the fibres, and so is not reliant on their strength in order to produce an aligned array. However, it is not possible to obtain free-standing arrays for mechanical characterisation or SAXS by this method. As for the flat collector samples were collected on glass slides which were affixed to the rotating wheel, which was first coated in aluminium foil in order to create the counter-electrode. The level of alignment can be varied by changing the rate of rotation of the collector, where it was expected that increasing the speed of the rotation would impart a stronger elongational force on the fibres as they form and therefore improve the alignment. Three rotation speeds were investigated – 800, 950 and 1100 rpm, with two wheel-shaped collectors. Both had a diameter around 200 mm but with a collection surface width of either 25 or 15 mm. The effect of reducing the space available for fibre deposition was investigated, with the expectation that the narrower wheel would result in stronger alignment of fibres relative to one another due to increased confinement.

800 rpm

Fibres were spun with applied voltages of -1 kV and +18 kV and a feed rate of 1 mL per hour. Relatively uniform fibres with diameters between 1.4-1.9 μm were produced (Figure 5-10). Droplets were still present, with diameters between 3.5-15.2 μm. A clear preferred direction could be seen, although not all fibres were deposited parallel to this. Under crossed polarisers strong birefringence was observed in the fibres when oriented at 45° to the polarisers, and if the stage was rotated such that the fibres lay parallel with either of the polarisers the birefringence was lost and the fibre became dark (Figure 5-10). It was therefore shown that the electrospinning process had acted to align the mesophase as well as the fibres themselves.

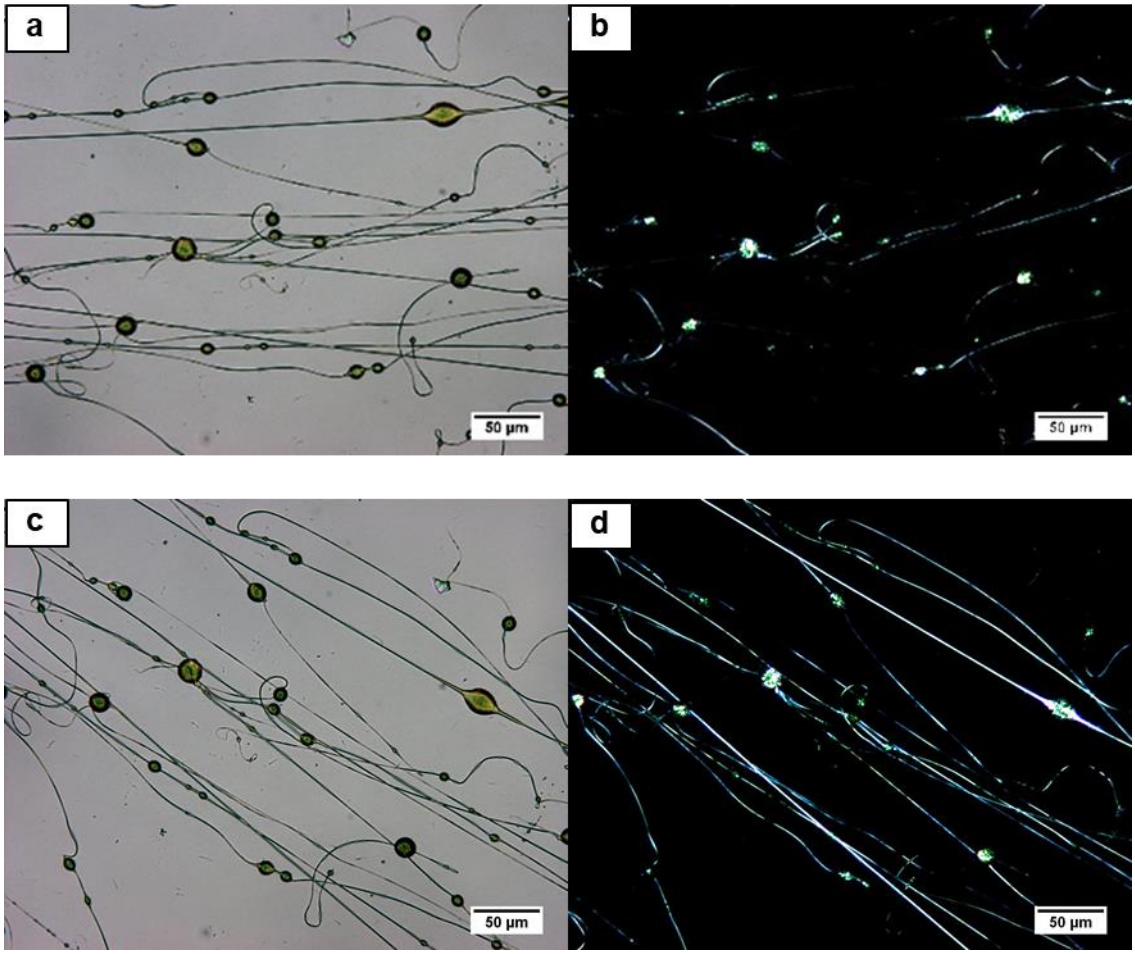

Figure 5-10. Images of fibres obtained at a rotation speed of 800 rpm taken under: (a) and (c) normal light and (b) and (d) crossed polarisers. Bright regions in (b) and (d) correspond to areas with LC mesophase present. Images (c) and (d) were obtained by rotating (a) and (b) through 45°.

950 rpm

Fibres were spun with applied voltages of -2 kV and +19 kV and a feed rate 1 mL per hour. Again, alignment was seen along a common direction, however, a number of short, randomly oriented fibres could also be observed (Figure 5-11). These fibres may have arisen due to properties of the solution or may be due to the increased strain placed on the fibre as it forms from the rotation of the collector. From the parallel electrodes it was shown that the fibres of **P-3-M1(65)-COOH(35)** were weak, and so the increased elongational force may break the fibres as they form. Under crossed polarisers only weak birefringence was observed, suggesting poor alignment in the LC domains. Fibres had diameters between 2.0-3.4 µm, larger than seen at 800 rpm, which again suggests that the fibres fractured before they could be extended further.

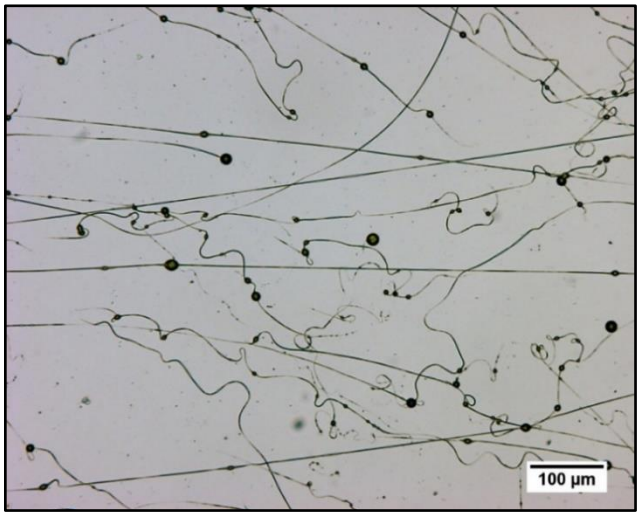

Figure 5-11. Images of fibres obtained at a rotation speed of 950 rpm under normal light.

1100 rpm

Electrospinning was carried out with applied voltages of -2 kV and +19 kV and a feed rate of 1 mL per hour. Fibres collected at 1100 rpm showed much weaker directional alignment relative to one another, as can be seen in Figure 5-12. Again, birefringence was apparent under crossed polarisers which suggests order was present within the LC mesophase, but the fibres themselves were oriented in all directions. This suggests that if the rotation of the collector is too fast, the fibres are not able to be deposited in an ordered fashion. Fibres were measured with diameters between 2.2-3.0 µm, similar to those obtained at 950 rpm. The fact that alignment did not appear to increase with increasing speed of the rotation suggests that the fibres did not precipitate fast enough to be aligned, or else fractured on evaporation of the solvent due to the increased elongational force, before depositing in a random manner on the collector.

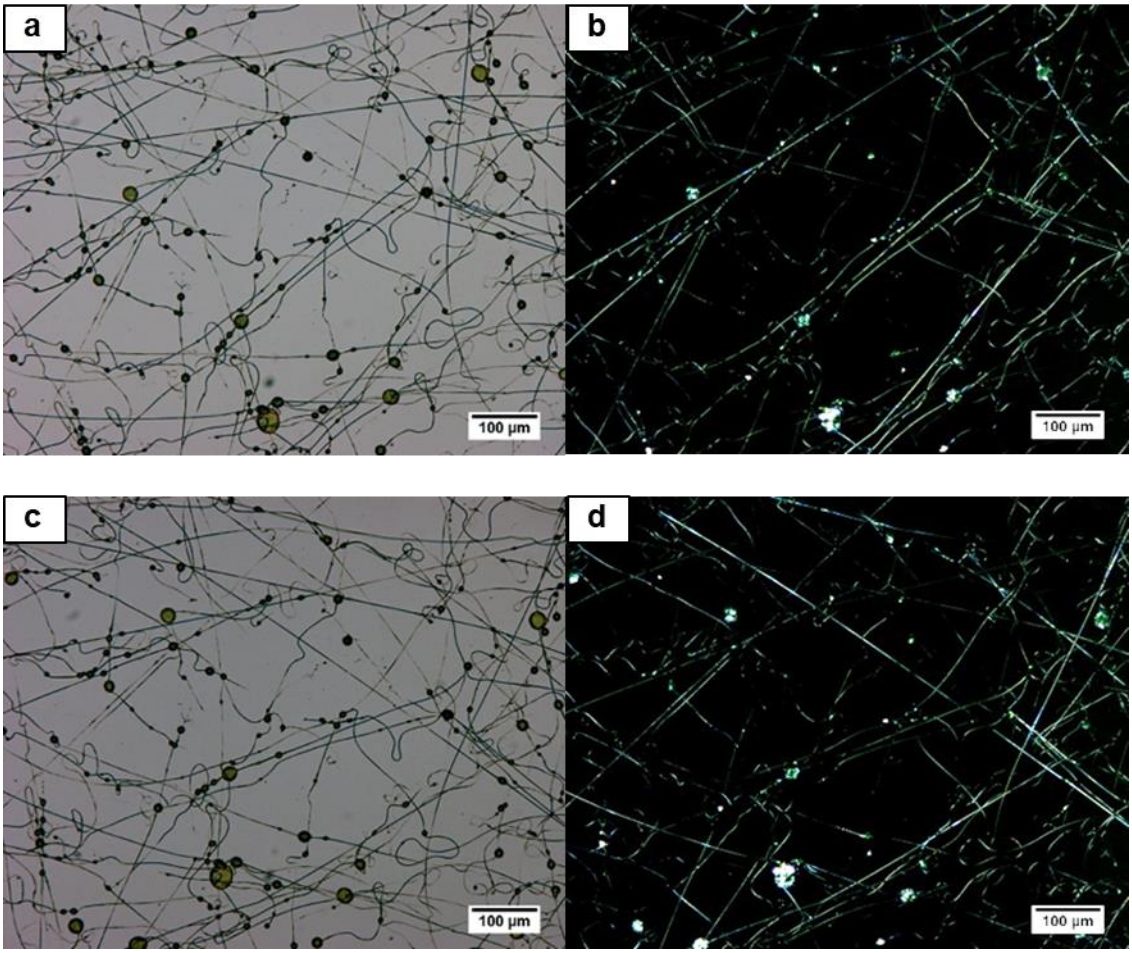

Figure 5-12. Images of fibres obtained at a rotation speed of 1100 rpm taken under: (a) and (c) normal light and (b) and (d) crossed polarisers. Bright regions in (b) and (d) correspond to areas with LC mesophase present. Images (c) and (d) were obtained by rotating (a) and (b) through 45°.

Considering that increasing the rotation did not improve the alignment of the fibres, a wheel with a narrower rim was utilised as a collector. It was expected that by reducing the surface area for the fibres to deposit on the level of alignment would increase. All experiments were carried out at 800 rpm with the 32.5 wt% solution in DMF/THF. The results of a short collection time, carried out to obtain a clear image of the level of alignment, with applied voltages of -1 kV and +18 kV and a feed rate of 1 mL per hour are given in Figure 5-13.

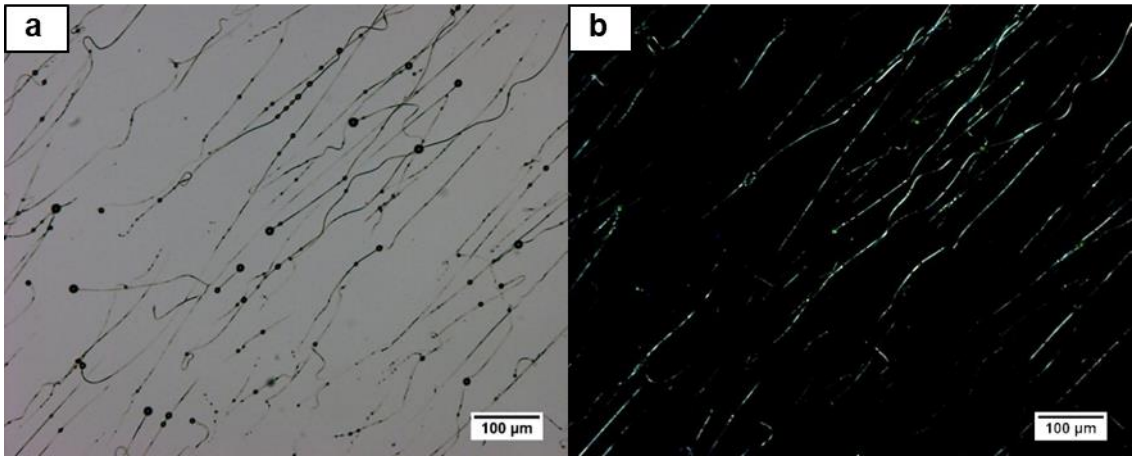

Figure 5-13. Images of fibres taken under (a) normal light and (b) crossed polarisers. Bright regions in (b) correspond to areas with LC mesophase present.

A narrow distribution of diameters was measured, with values for fibres found to be between 2.2-2.9 µm. However, a number of the fibres did not appear to be continuous, which may be due to the short collection time. It takes a certain amount of time for the jet to stabilise once electrospinning starts, and it may be that the short collection time was not long enough for continuous fibres to form, therefore, the experiment was repeated with a longer collection time. This resulted in a denser array of fibres, with representative images given in Figure 5-14. Again, a clear alignment direction was evident, but some fibres were present which were aligned perpendicular to this direction. The fibres collected under these conditions appeared continuous, confirming that the fibres in Figure 5-13 were collected before stabilisation of the jet. Large droplets which were not part of a fibre were also present in this sample. These likely were a result of the syringe emptying during the experiment, and so were formed by electrospray rather than electrospinning as there was insufficient solution to maintain constant fibre formation.

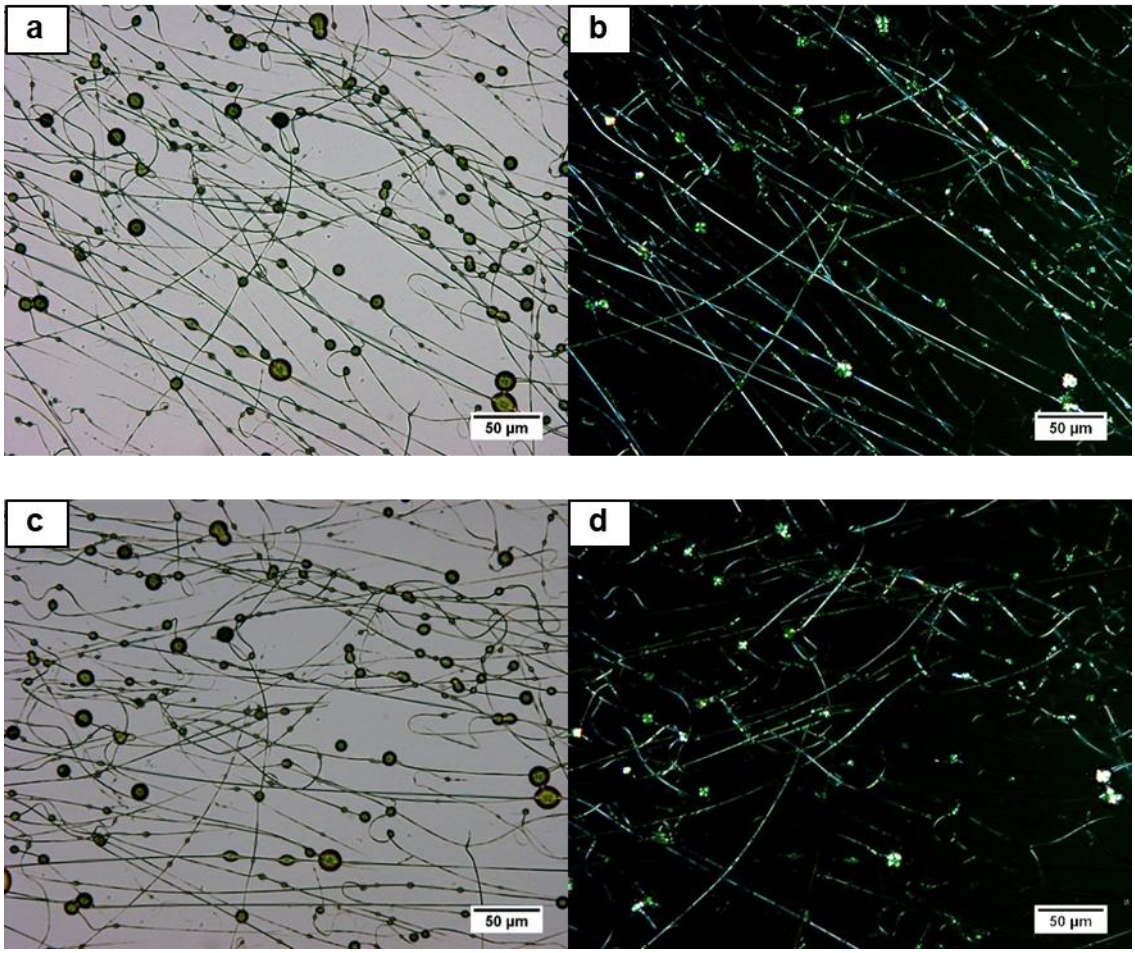

Figure 5-14. Images of fibres obtained at a rotation speed of 800 rpm taken under: (a) and (c) normal light and (b) and (d) crossed polarisers. Bright regions in (b) and (d) correspond to areas with LC mesophase present. Images (c) and (d) were obtained by rotating (a) and (b) through 45°.

Fibres were measured with diameters between 1.2-2.5 µm, with beads on fibres having diameters between 1.9-11.5 µm. From POM it was clear that ordered LC mesophases were present along the length of the fibres, with rotation of the microscope stage reducing or increasing the brightness of fibres depending on their orientation relative to the crossed polarisers.

It was therefore demonstrated that a rotating collector could be used to obtain an ordered array of LCE fibres, with a speed of 800 rpm showing a good balance between the level of alignment and the level of force applied to the fibres. The alignment achieved by the rotating collectors was good, but not as strong as examples in the literature utilising the parallel electrode setup. The large numbers of droplets are also problematic, therefore, whilst this work is the first example of electrospinning a side-chain thermoplastic LCE, there are still considerable improvements that could be made to the fibre morphology.

5.2.3. Responsive Behaviour of Aligned Fibres

The images shown in the previous sections show that aligned mesophases were formed within the electrospun fibres. To confirm this, and to demonstrate that **P-3-M1(65)-COOH(35)** retains its responsive properties after processing, the fibres were exposed to either UV light or heating above the isotropic transition temperature (T_{iso}).

5.2.3.1. Response to UV Irradiation

Light with a wavelength of 365 nm triggers the isomerization of the azobenzene group in the mesogen from the linear *trans*-conformation to the bent *cis*-conformation. This acts to disrupt the ordered packing and so results in a transition to the disordered isotropic phase. Fibres were used for these experiments that were deposited on a flat collector (Figure 5-15) and on the thinner wheel (Figure 5-16). Images under parallel and crossed polarisers were taken before and after irradiating *in situ* for 5 minutes with a UV light source.

For the randomly oriented sample there was a clear decrease in intensity observed for fibres oriented at 45° to the polarisers after irradiation (Figure 5-15). Bright spots were still apparent, which were located in regions where droplets were visible. No clear difference in diameter was observed for the fibre oriented along the diagonal (top left to bottom right) before and after irradiation, with diameters between 1.6-1.8 μm measured along its length. It is expected that on transitioning from the nematic mesophase to the isotropic state a contraction would occur in the direction of the director, and an expansion perpendicular to it. However, these fibres were collected on glass slides which may act to prevent significant distortions, and any such change in diameter may have been below the resolution limit of the microscope.

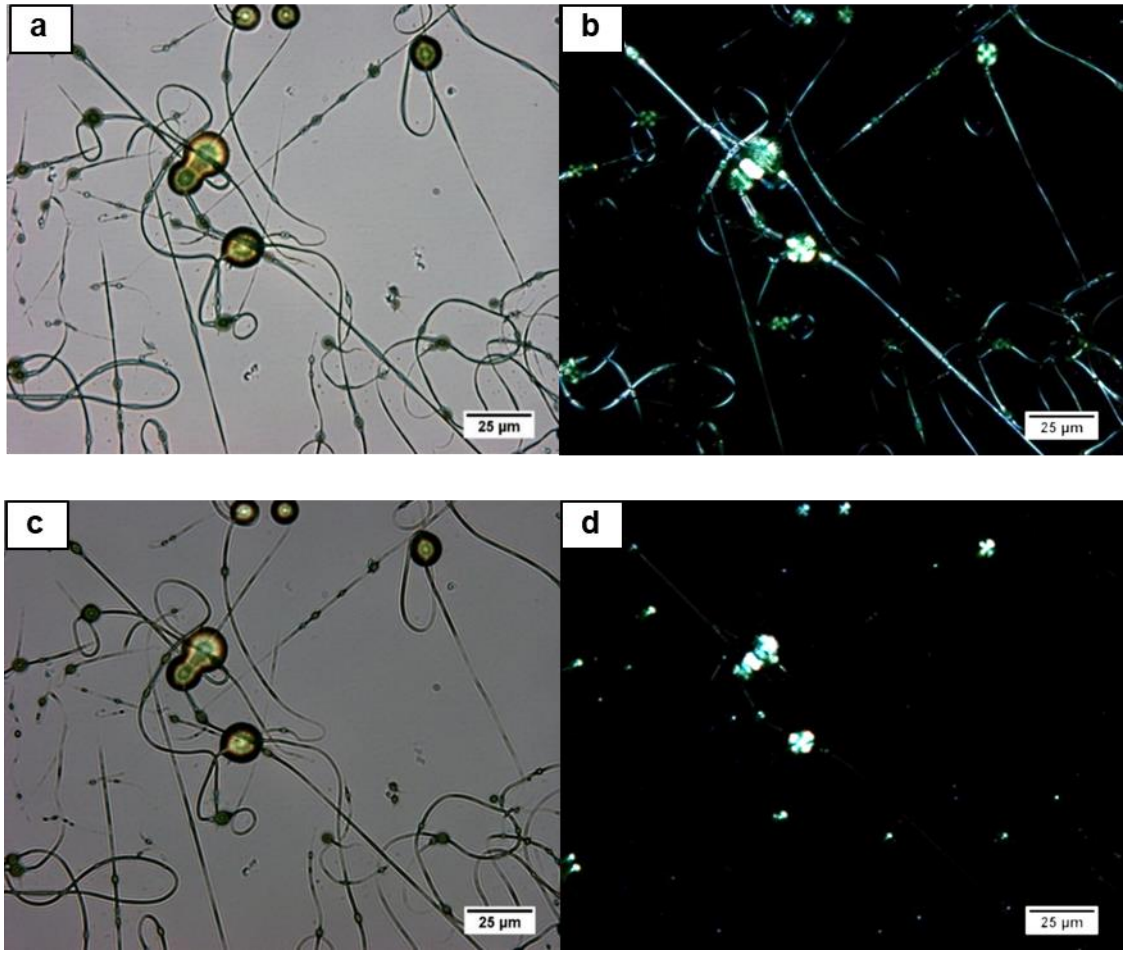

Figure 5-15. Images of fibres collected on a flat surface taken before (a and b) and after (c and d) irradiation with UV light. Images (a) and (c) are taken under normal light, and (b) and (d) taken under crossed polarisers. The level of birefringence observed in the fibre was greatly reduced after irradiation, confirming disruption of the nematic mesophase.

Similar results were obtained for fibres collected on the thin wheel at 800 rpm (Figure 5-16). Initially, birefringence was clearly apparent for fibres oriented at 45° to the crossed polarisers, but after irradiation with UV the bright areas become dark, suggesting that the fibres are isotropic. Before irradiation, diameters between 2.5-2.9 µm were measured for the diagonal, continuous fibres to the left of the images. Similar values were obtained after irradiation, which again may be due to the fibres being constrained by the glass slide or due to any change in dimension being too small to detect at the resolution of the microscope images. From these results it can therefore be concluded that irradiation with UV induced a nematic-isotropic transition in the polymer, which resulted in a loss of birefringence under crossed polarisers.

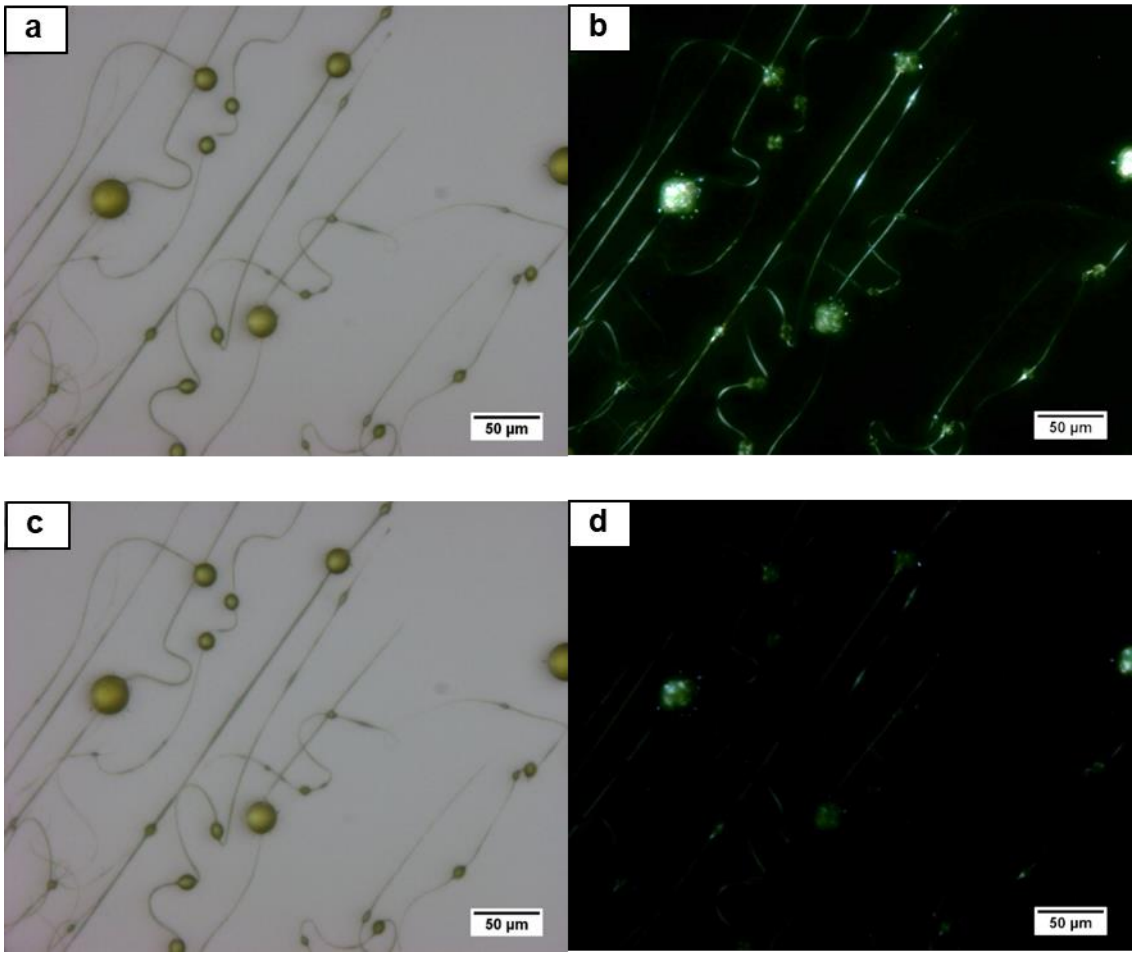

Figure 5-16. Images of fibres collected on a rotating wheel taken before (a and b) and after (c and d) irradiation with UV light. Images (a) and (c) are taken under normal light, and (b) and (d) taken under crossed polarisers. The level of birefringence observed in the fibre was greatly reduced after irradiation, confirming disruption of the nematic mesophase.

5.2.3.2. Response to Heating Above T_{iso}

Previously characterised films of **P-3-M1(65)-COOH(35)** were not suitable for POM due to their thickness. The micrometre-scale fibres collected by electrospinning, however, were suitable for POM, and so were imaged on a heating stage on heating through the T_{iso} to track the transition from a nematic mesophase to the isotropic state through the loss of birefringence. Unfortunately, between collecting the fibres and carrying out the POM experiment the level of LC order within the fibres appeared to have degraded. This may be due to relaxation of the PMVS block over time or from damage incurred during the transportation of the fibres, which were shown to be mechanically weak. Nevertheless, a region of increased intensity was located and its response to heating was recorded.

The T_{iso} of **P-3-M1(65)-COOH(35)** was measured as 99 °C by DSC, therefore, the slide was heated from 80 °C to 120 °C at a rate of 5 °C per minute and video recorded continuously. Stills were extracted from the video at time points that corresponded to approximately 5 °C increments. From these stills it was evident that the LC mesophase started to be disrupted at 100 °C, with a clear reduction in size occurring from 105-110 °C (Figure 5-17). At 120 °C a slight birefringence was still apparent, but this may be due to the presence of droplets and was considerably weaker than observed at the start of the experiment. It was therefore demonstrated that the ordered LC mesophase could also be disrupted by heating through the T_{iso}.

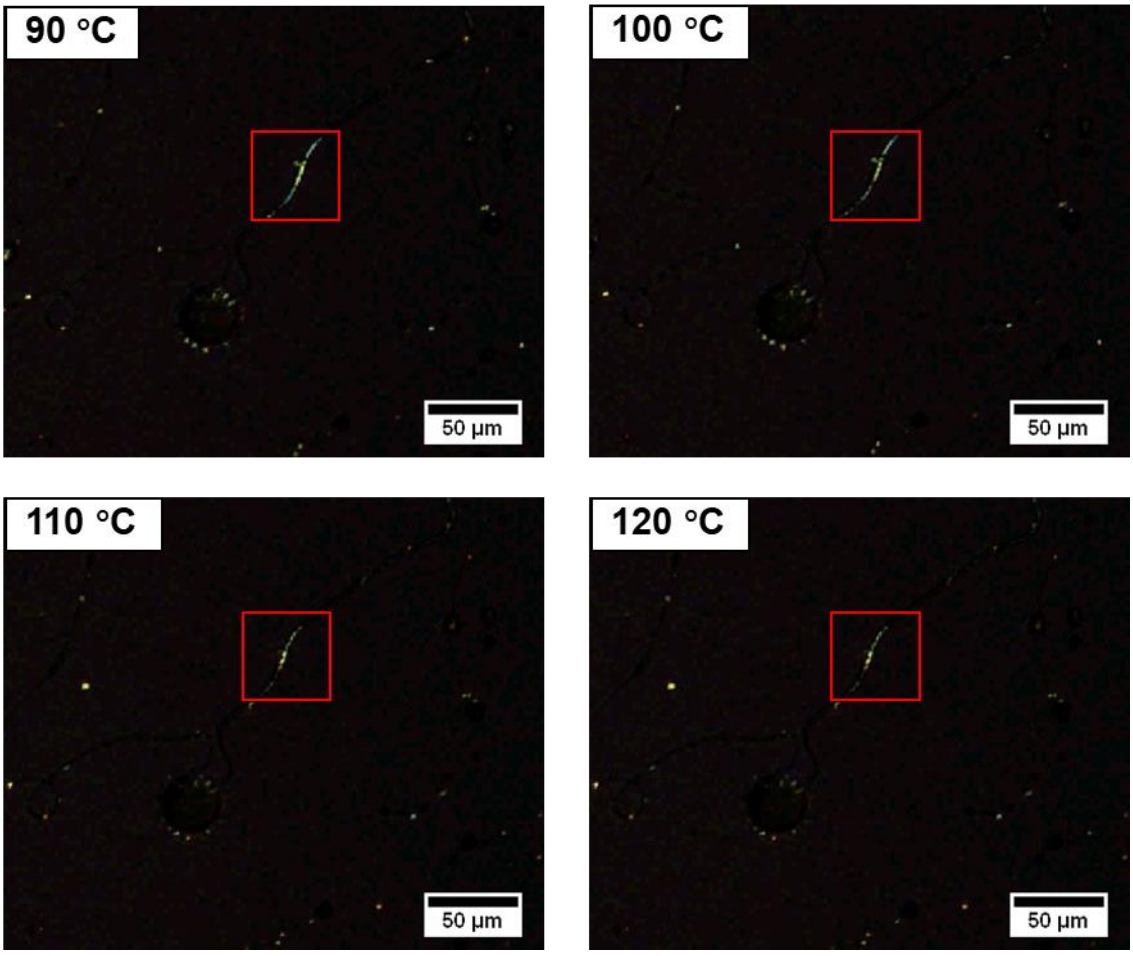

Figure 5-17. Images taken at 90, 100, 110 and 120 °C under crossed polarisers. Red frames are the same size in each image to help visualise decrease in size of the ordered domain.

5.3. Conclusions

It was shown that electrospinning can be used to generate fibres of the thermoplastic LCE **P-3-M1(65)-COOH(35)**, with diameters measured to be between 1-3 μm. The fibres were not smooth, with significant numbers of droplets present which acted to reduce the mechanical strength and so prevented the formation of free-standing mats, but with further optimisation of the spinning solution it should be possible to reduce the number of droplets. It was not possible to quantify the level of alignment present within the electrospun fibres as a sample suitable for SAXS was not obtained, however, it was shown using hand-drawn fibres that alignment occurs along the long axis of the fibre and that through the application of a uniaxial elongation, such as that encountered during electrospinning, it was possible to obtain a measurable level of alignment. POM confirmed that ordered mesophases were present within the electrospun fibres, with alignment disrupted both by irradiation with UV light and by heating through the T_{iso}. Electrospinning therefore imparts sufficient alignment in the fibres that responsive structures should be obtainable with improvements to the spinning solution, presenting a viable method for the production of hierarchical LCE structures based on layers of uniaxially aligned fibres.

5.4. Experimental

5.4.1. Hand-Drawn Fibres

Fibres were drawn from concentrated solution of **P-3-M1(65)-COOH(35)** in CH_2Cl_2 (approximately 40 wt%) using a glass capillary. Fibres with diameters between 0.13-0.20 mm were obtained, with dimensions measured using a Vernier Calliper. For SAXS measurements the fibres were then dried under vacuum at 40 °C before annealing for 2 hours at 120 °C. One fibre was also stretched along its length whilst heated to 120 °C in order to increase the level of alignment, which resulted in a diameter of 0.20 mm.

5.4.2. SAXS

SAXS experiments were carried out at room temperature using a Ganesha SAXS/WAXS instrument (Xenocs) at room temperature, using a Cu Kα source (1.5406Å) over a Q-range of $0.001 < Q < 0.7$ $Å^{-1}$ and an exposure time of 1800 seconds. Data were visualized and reduced using SAXSGUI. Scattering patterns were normalised against the transmitted beam intensity and corrected for background scattering. Peak values in reciprocal space were calculated to four decimal places

from the reduced data as local maxima using Origin 9.1 and rounded to 3 significant figures. For broad form factor peaks with no clear maximum the value was quoted to 2 significant figures. Peak values in reciprocal space were converted to give the average inter-sphere spacing, *d*, by the relationship:

$$d = \frac{2\pi}{q} \qquad 5.1$$

Data were fit to a model describing affine deformation with hard particles by Professor Robert Richardson at the University of Bristol. Data was fitted with Porod constant = 0 and an interface thickness of 1, with further parameters given in Table 5-2.

Table 5-2. Parameters obtained from fitting of SAXS data for stretched and unstretched fibres of **P-3-M1(65)-COOH(35)**.

Sample	Number of points	Standard Deviation (nm^{-1})	PDI of Radius	Tilt Direction (°)	Reduced χ^2
P-3-M1(65)-COOH(35) Stretch	47,696	8.4	1.03	91.3	1.90
P-3-M1(65)-COOH(35) No stretch	48,120	6.7	1.03	114.2	0.76

5.4.3. Electrospinning

Electrospinning of polymer solutions and determination of voltage and feed rate was carried out by Martin Pretscher at the University of Bayreuth.

Concentrated solutions of **P-3-M1(65)-COOH(35)** were made up by dissolving the polymer in the given solvent mixture (DMF or DMF/THF) and stirred for 16 hours to ensure full dissolution. Solutions were then used to fill a 1 mL syringe with a 20G needle (0.6 mm inner diameter). This was then placed in the electrospinning setup (Figure 5-18) and connected to the power supply. The feed rate was controlled by a syringe pump. The fibres were collected on aluminium foil on either a flat collector or spinning wheel at a distance of approximately 12 cm from the tip of the syringe, and the rate of rotation controlled.

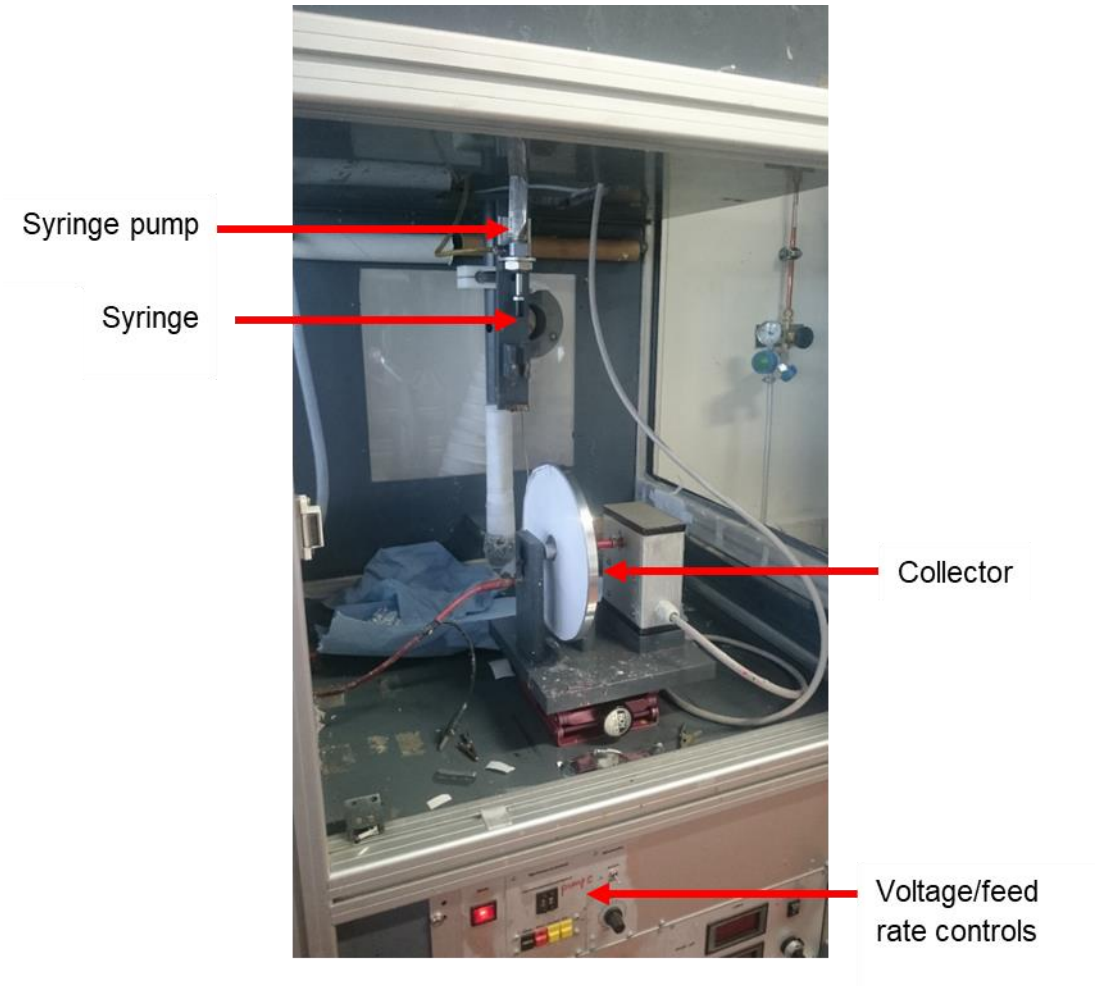

Figure 5-18. Electrospinning setup with narrow wheel collector.

5.4.4. Polarised Optical Microscopy

Fibres were imaged using optical microscopy. Polarised optical microscopy (POM) was carried out using a Leica DM6000 microscope equipped with a Leica DFC450 digital camera. Images were taken with transmitted light and with either parallel or crossed polarisers. The visible light source was replaced with a UV light source (100W) for irradiation experiments. Fibres were exposed to UV for five minutes before returning to the visible light source and taking images under both parallel and crossed polarisers.

Heating stage experiments were taken on an Olympus BX53 polarising microscope equipped with a Linkam THM 600 heating stage, with the heating profile set by a Linkam TMS 91 system controller. The sample was heated to 80 °C at a rate of 10 °C per minute before heating to 120 °C at a rate of 5 °C per minute.

For all microscopy images dimensions of the fibres were measured using ImageJ.

5.5. References

1 C. Huang, S. J. Soenen, J. Rejman, B. Lucas, K. Braeckmans, J. Demeester and S. C. De Smedt, Stimuli-Responsive Electrospun Fibers and Their Applications, *Chem. Soc. Rev.*, 2011, **40**, 2417–2434.

2 C. Ohm, M. Morys, F. R. Forst, L. Braun, A. Eremin, C. Serra, R. Stannarius and R. Zentel, Preparation of Actuating Fibres of Oriented Main-Chain Liquid Crystalline Elastomers by a Wetspinning Process, *Soft Matter*, 2011, **7**, 3730.

3 K. Nakashima, K. Tsuboi, H. Matsumoto, R. Ishige, M. Tokita, J. Watanabe and A. Tanioka, Control over Internal Structure of Liquid Crystal Polymer Nanofibers by Electrospinning, *Macromol. Rapid Commun.*, 2010, **31**, 1641–1645.

4 Y. Wu, Q. An, J. Yin, T. Hua, H. Xie, G. Li and H. Tang, Liquid Crystal Fibers Produced by Using Electrospinning Technique, *Colloid. Polym. Sci.*, 2008, **286**, 897–905.

5 S. Krause, R. Dersch, J. H. Wendorff and H. Finkelmann, Photocrosslinkable Liquid Crystal Main-Chain Polymers: Thin Films and Electrospinning, *Macromol. Rapid Commun.*, 2007, **28**, 2062–2068.

6 S. L. Shenoy, W. D. Bates, H. L. Frisch and G. E. Wnek, Role of Chain Entanglements on Fiber Formation during Electrospinning of Polymer Solutions: Good Solvent, Non-Specific Polymer-Polymer Interaction Limit, *Polymer*, 2005, **46**, 3372–3384.

7 D. Li and Y. Xia, Electrospinning of Nanofibers: Reinventing the Wheel?, *Adv. Mater.*, 2004, **16**, 1151–1170.

8 V. Jacobs, R. D. Anandjiwala and M. Maaza, The Influence of Electrospinning Parameters on the Structural Morphology and Diameter of Electrospun Nanofibers, *J. Appl. Polym. Sci.*, 2010, **115**, 3130–3136.

9 J. M. Deitzel, J. Kleinmeyer, D. Harris and N. C. Beck Tan, The Effect of Processing Variables on the Morphology of Electrospun Nanofibers and Textiles, *Polymer*, 2001, **42**, 261–272.

10 D. J. Blundell, G. Eeckhaut, W. Fuller, A. Mahendrasingam and C. Martin, Real Time SAXS / Stress – Strain Studies of Thermoplastic Polyurethanes at Large Strains, *Polymer*, 2002, **43**, 5197–5207.

11 C. L. Yaws, Ed., *Thermophysical Properties of Chemicals and Hydrocarbons*, William Andrew, Norwich, 2008.

12 W. E. Teo and S. Ramakrishna, A Review on Electrospinning Design and Nanofibre Assemblies, *Nanotechnology*, 2006, **17**, R89–R106.

13 D. Li, Y. Wang and Y. Xia, Electrospinning of Polymeric and Ceramic Nanofibers as Uniaxially Aligned Arrays, *Nano Lett.*, 2003, **3**, 1167–1171.

Chapter 6: Conclusions and Future Work

6.1. Conclusions

The aim of the work reported in this thesis was to develop UV-responsive thermoplastic liquid crystal elastomers (LCEs) for processing using common thermoplastic techniques, which would allow for the production of geometries beyond thin films. In order to achieve this, three main objectives were identified: to develop a high yielding synthetic route to a responsive thermoplastic LCE, and to investigate the suitability of these materials for processing from the melt and from solution.

6.1.1. Synthesis of a Thermoplastic Liquid Crystal Elastomer

In order to produce sufficient material for processing, an alternative and higher yielding synthetic pathway to the LC functionalised thermoplastic LCE to the hydrosilylation method reported in the literature was desired.[1] This was achieved through a mild, post-polymerisation modification of the poly(methylvinylsiloxane) (PMVS) block of an ABA triblock copolymer, where the hard A block consisted of polystyrene (PS). In the first step, a carboxylic acid-terminated linking group was attached to the vinyl group on PMVS *via* a high-yielding (>86%) thiol-ene click reaction. This method allowed for modification of the number of alkyl units in the linking group through the choice of thiol, with 3-mercaptopropionic acid shown to provide a good balance between yield, ease of synthesis and thermal properties. In the second step, the mesogen was coupled to the carboxylic acid functionality on the linking group using a carbodiimide (DCC) mediated esterification reaction. This reaction had a yield of 78-85%, which was a significant improvement on the yield of 30% for the equivalent step in the literature method.[2] The DCC-mediated coupling could also form an amide link, and so a modified synthetic route to the amine functionalised mesogen **M2** was reported. It was shown that the increased hydrogen bonding interactions raised both the glass transition temperature (T_g) and isotropic transition temperature (T_{iso}) to temperatures that were not suited for room temperature actuation. The ester linked LCEs **P-3-M1(82)-COOH(18)** and **P-3-M1(65)-COOH(35)** were identified as being the best suited for processing experiments, with values for the T_g of 16-20 °C and for the T_{iso} of 99-118 °C.

In order for the polymer to behave as a thermoplastic elastomer it was necessary that the PS blocks self-assembled to form spheres in a matrix of the LC-functionalised PMVS. This was demonstrated to be the case through a combination of Small Angle X-ray Scattering (SAXS) and Transmission Electron Microscopy (TEM). Stretching the polymer films whilst heated above the

T_{iso} acted to distort the PMVS domains and realign the hard PS spheres relative to one another, with no other deformation of the spheres occurring. The increased anisotropy of the microphase structure suggested the formation of a LC monodomain, with the order parameter calculated from variable temperature SAXS experiments confirming that the PS spheres aligned along the direction of stretch. In order to confirm this, a film of **P-3-M1(82)-COOH(18)** was aligned by stretching along its length whilst heated above the T_{iso}, and was demonstrated to contract against an applied tension on irradiation with UV light.

6.1.2. Suitability of Thermoplastic Liquid Crystal Elastomers for Melt Processing

Processing by extrusion from the melt is desirable for thermoplastic polymers due to the simplicity of the process, and the high throughout possible. However, from rheological experiments it was demonstrated that liquid-like melts were not obtained at any temperature, which was attributed to the stabilisation of the nematic mesophase by the spherical morphology (raising the order-disorder transition temperature, T_{ODT}). This was problematic for melt processing as the microphase separated morphology prevents the formation of a liquid-like melt, making these materials unsuitable for processing by extrusion. Removing hydrogen bonding interactions by converting carboxylic acid groups to methyl esters, to yield **P-3-M1(65)-COOMe(35)** and **P*-3(AIBN)-M1-COOMe**, acted to lower the T_{ODT} to a more useful temperature range, however, no liquid-like melt behaviour was observed. For these polymers (whilst above the T_{ODT}) it appears that the high molecular weight and entanglements due to the side-on linking group architecture act to reduce the conformational flexibility of the polymer backbone, to the extent that viscous-dominated behaviour is restricted to low frequency shear, which would be exceeded during extrusion.

6.1.3. Suitability of Thermoplastic Liquid Crystal Elastomers for Processing from Solution

Processing of thermoplastic polymers from solution is another industrially important method utilised to produce fibres. The high molecular weight and side-on architecture of the LCEs are beneficial in this case, as a high level of entanglement is required for fibres to form from an elongated jet of polymer solution. The electrospinning of thermoplastic LCEs had not been previously reported, and so preliminary experiments were carried out using **P-3-M1(65)-COOH(35)** to assess their suitability. Fibres of the polymer were obtained; however, the large numbers of droplets present reduced the mechanical strength such that free-standing samples

could not be produced. Fibres were shown to contain ordered LC mesophases by Polarised Optical Microscopy, with bright regions coinciding with the location of fibres being extinguished after inducing the isotropic transition by either heating or irradiation with UV light.

6.2. Future Work

6.2.1. Extrusion of Thermoplastic Liquid Crystal Elastomers

For the thermoplastic LCEs to be processable by melt extrusion, it would be beneficial to reduce the overall molecular weight, and so increase the conformational flexibility of the backbone. This would be aided by conversion of any carboxylic acid groups to methyl esters to remove hydrogen bonding interactions between chains. This could be achieved by only partially functionalising the PMVS block with linking groups during the thiol-ene click synthetic step. Reducing the number of side-chains would also act to reduce interdigitation, and so an investigation into the ability to control the percentage of attachment during the thiol-ene click reaction would prove useful.

Another interesting result which arose from rheological measurements was that LCEs with carboxylic acid groups converted to methyl esters (**P-3-M1(65)-COOMe(35)** and **P*-3-M1-COOMe**) did not have a nematic mesophase present at room temperature, instead it appeared to be induced under shear at elevated temperatures. This coincided with a transition from temperature independent to dependent behaviour, suggesting a sudden change in the microphase separated morphology and a subsequent increase in T_{ODT}. In order to better understand the structural origin of this transition, which is potentially due to stabilisation of the nematic mesophase once it forms by the spherical microphase structure, VT-SAXS experiments would be useful, especially if *in situ* shear could be applied.

6.2.2. Electrospinning of Thermoplastic Liquid Crystal Elastomers

A systematic study into the effect of additives such as salts or polyethylene oxide on the ability to obtain smooth fibres by electrospinning should be carried out. If defect-free fibres cannot be obtained from a pure solution, coaxial electrospinning of the LCE with a polymer known to be readily electrospun could also be attempted.[3]

Once smooth fibres can be obtained, mats of fibres should be attainable. The level of order within the fibre could then be assessed by SAXS and mechanical experiments carried out. Whilst the level of contraction expected for a single fibre is small, it should be possible to amplify the actuation through either combing several fibres to form one strand or by incorporating aligned mats into

composite structures. This would then allow for fabrication of flat sheets that can be programmed to bend and twist through the laminate stacking sequence, utilising Classical Laminate Theory.

The high surface area of the micron-scale fibres obtained by this method makes them particularly well suited for use as UV-triggered actuators, as the amount of non-active material is minimised compared with the surface exposed to the light source. LCEs have been proposed to be materials with great potential in soft robotics. If electrospinning could be used to increase the scale of LCE structures by removing the need for more complex alignment steps, then these mats or fibres could find applications as light-triggered valves,[4] tactile displays[5] or as artificial muscles.[6]

6.2.3. PMVS Homopolymer

It was demonstrated that the PMVS homopolymer functionalised with **M1** (**PMVS-3-M1(86)-COOH(14)**) was obtained as a soft and deformable solid, with a T_g of 23 °C. A literature example of this polymer was reported by Petr and Hammond, consisting of a PMVS homopolymer where every Si atom was functionalised with a linking group and the mesogen, **M1**. However, this polymer had a T_g of -7 °C, and existed as a liquid unless sheared, when a metastable crystalline phase was observed.[2] The significantly different physical properties between these two polymers arise due to the additional hydrogen bonding interactions in **PMVS-3-M1(86)-COOH(14)**, and make this material potentially interesting as an actuator in its own right.

LCEs which demonstrate responsive and self-healing properties due to hydrogen bonding have been reported.[7,8] Whilst it would not benefit from the mechanical advantage offered by the PS block, it was shown that **PMVS-3-M1(86)-COOH(14)** formed a liquid-like melt under shear and so would be potentially suitable for processing by extrusion to give a highly aligned, photoresponsive fibre. It would therefore be pertinent to attempt to process **PMVS-3-M1(86)-COOH(14)** by extrusion and to investigate if responsive behaviour is observed on irradiation of the resulting fibre with UV light. Thermoplastic LCEs crosslinked by exchangeable bonds such as hydrogen bonds or disulfide linkages offer a promising alternative to their chemically crosslinked analogues.[8–10] To date, however, despite the ability to mould shapes from these materials, literature examples have been limited to films or hand-drawn fibres. The development of a responsive LCP that could be processed by extrusion would therefore be novel, with further potential for more complex structures through extrusion in fused filament fabrication 3D printing.

6.3. References

1 M. Petr, B. A. Katzman, W. Dinatale and P. T. Hammond, Synthesis of a New, Low-Tg Siloxane Thermoplastic Elastomer with a Functionalizable Backbone and Its Use as a Rapid, Room Temperature Photoactuator, *Macromolecules*, 2013, **46**, 2823–2832.

2 M. Petr and P. T. Hammond, Room Temperature Rapid Photoresponsive Azobenzene Side Chain Liquid Crystal Polymer, *Macromolecules*, 2011, **44**, 8880–8885.

3 J. P. F. Lagerwall, J. T. McCann, E. Formo, G. Scalia and Y. Xia, Coaxial Electrospinning of Microfibres with Liquid Crystal in the Core, *Chem. Commun.*, 2008, 5420–5422.

4 A. Sánchez-Ferrer, T. Fischl, M. Stubenrauch, A. Albrecht, H. Wurmus, M. Hoffmann and H. Finkelmann, Liquid-Crystalline Elastomer Microvalve for Microfluidics, *Adv. Mater.*, 2011, **23**, 4526–4530.

5 C. J. Camargo, H. Campanella, J. E. Marshall, N. Torras, K. Zinoviev, E. M. Terentjev and J. Esteve, Batch Fabrication of Optical Actuators Using Nanotube–elastomer Composites: Towards Refreshable Braille Displays, *J. Micromechanics Microengineering*, 2012, **22**, 75009.

6 M. Li and Keller P., Artificial Muscles Based on Liquid Crystal Elastomers., *Philos. Trans. Ser. A, Math. Phys. Eng. Sci.*, 2006, **364**, 2763–2777.

7 M. Yan, J. Tang, H.-L. Xie, B. Ni, H.-L. Zhang and E.-Q. Chen, Self-Healing and Phase Behavior of Liquid Crystalline Elastomer Based on a Block Copolymer Constituted of a Side-Chain Liquid Crystalline Polymer and a Hydrogen Bonding Block, *J. Mater. Chem. C*, 2015, **3**, 8526–8534.

8 B. Ni, H. Lou Xie, J. Tang, H. L. Zhang and E. Q. Chen, A Self-Healing Photoinduced-Deformable Material Fabricated by Liquid Crystalline Elastomers Using Multivalent Hydrogen Bonds as Cross-Linkers, *Chem. Commun.*, 2016, **52**, 10257–10260.

9 Z. Pei, Y. Yang, Q. Chen, E. M. Terentjev, Y. Wei and Y. Ji, Mouldable Liquid-Crystalline Elastomer Actuators with Exchangeable Covalent Bonds, *Nat. Mater.*, 2014, **13**, 36–41.

10 L. Chen, M. Wang, L.-X. Guo, B.-P. Lin and H. Yang, A Cut-and-Paste Strategy towards Liquid Crystal Elastomers with Complex Shape Morphing, *J. Mater. Chem. C*, 2018, **6**, 8251–8257.

Appendix A: Supporting Information for Chapter 2

A.1. Mesogen Synthesis

M1 Synthetic Scheme

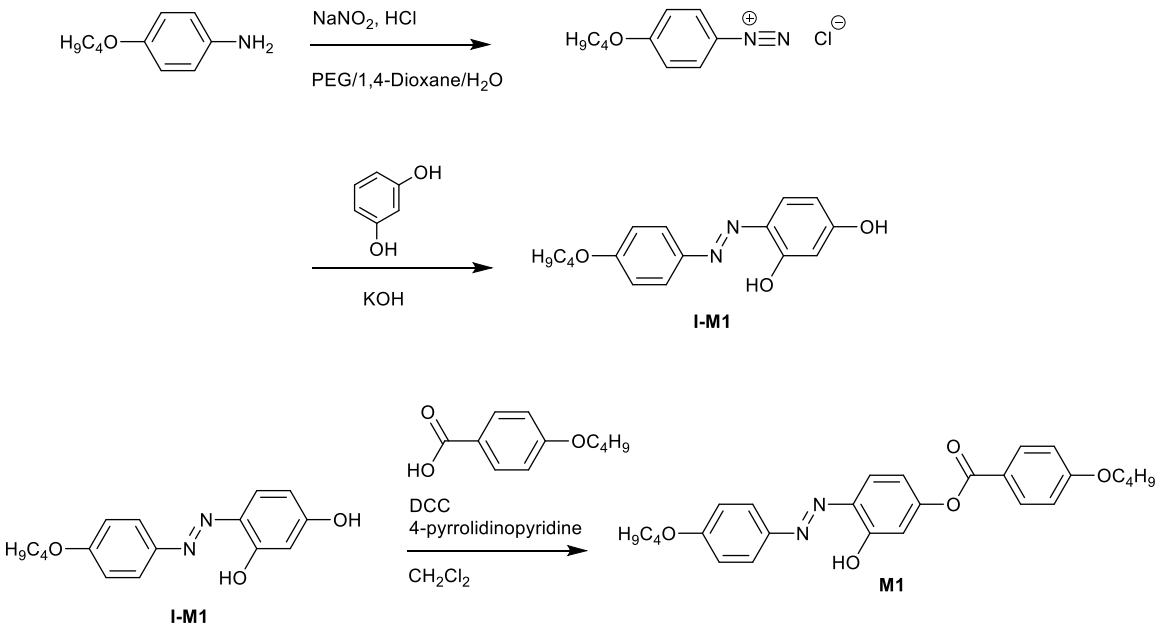

Figure A-1. Synthetic route to **M1**. PEG = Poly(ethylene glycol) average mol. wt. 200 g mol^{-1}, DCC = *N,N'*-dicyclohexylcarbodiimide.

I-M1

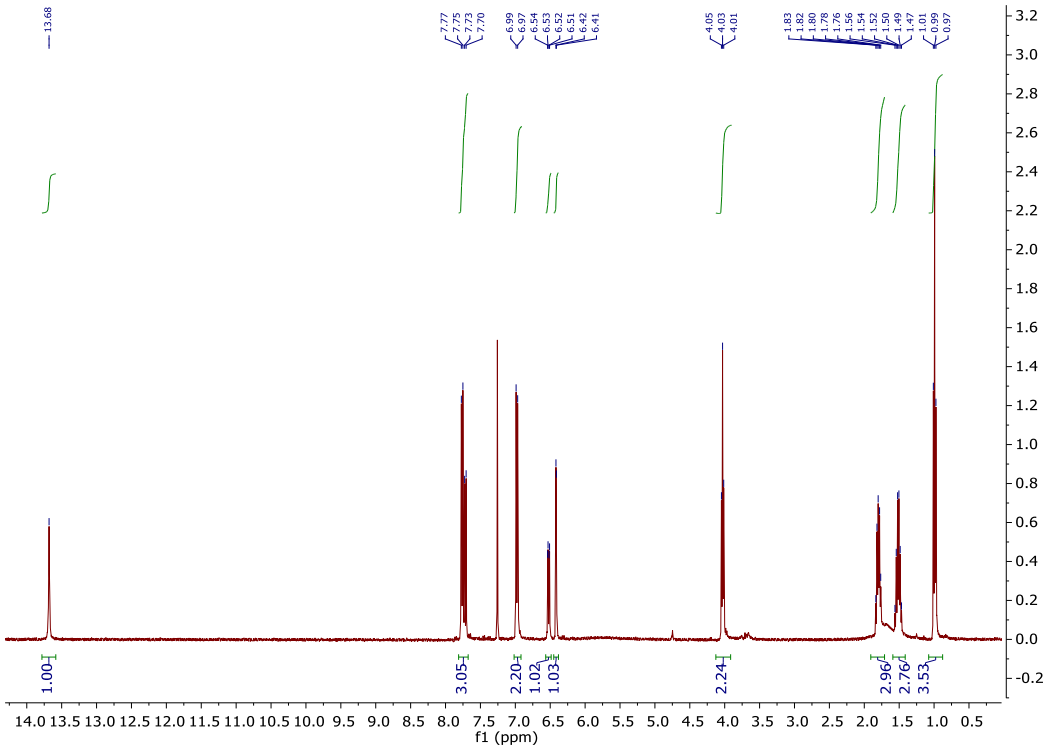

Figure A-2. ^{1}H NMR spectrum for **I-M1** in $CDCl_3$.

M1

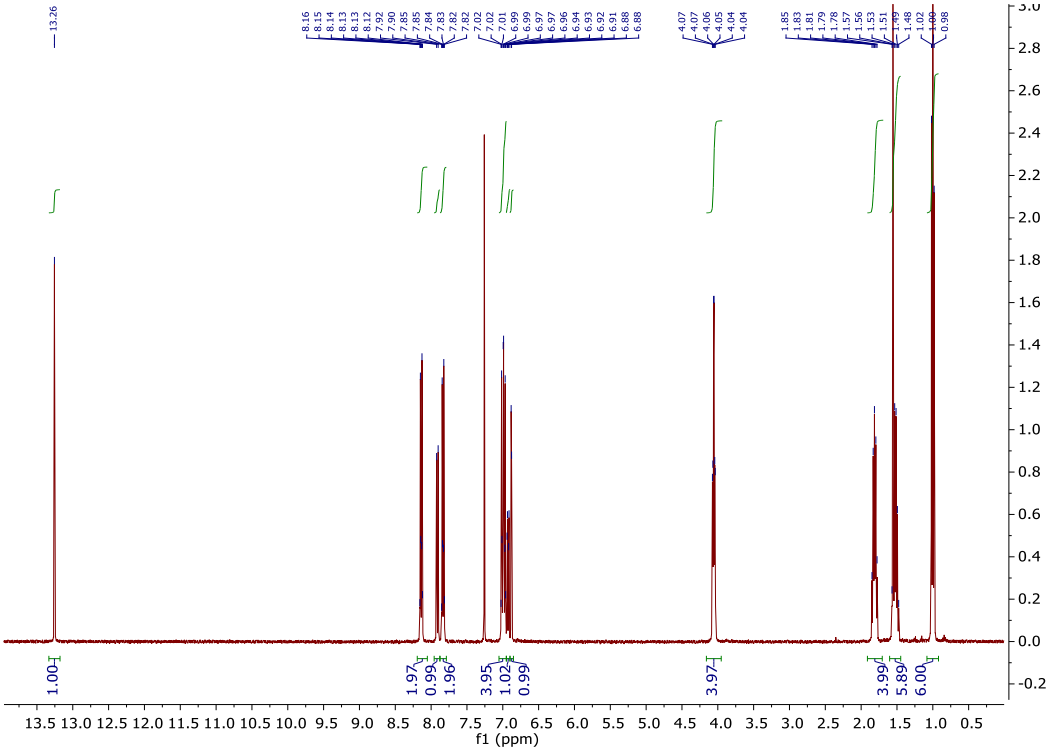

Figure A-3. ^{1}H NMR spectrum for **M1** in $CDCl_3$.

M1-Allyl

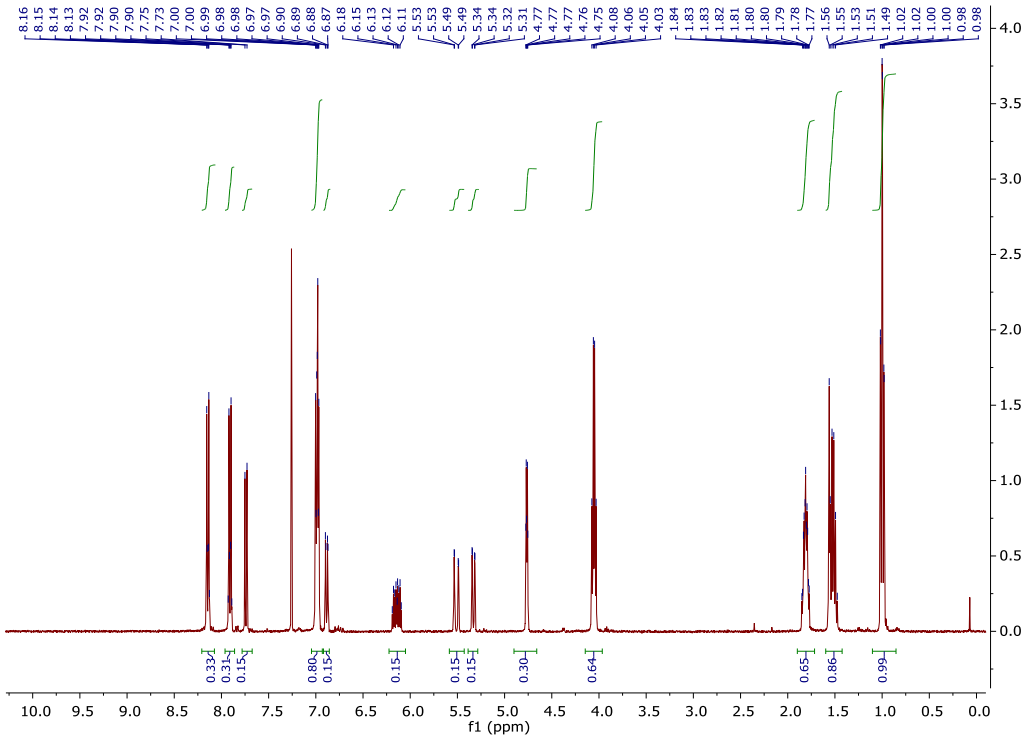

Figure A-4. ^{1}H NMR spectrum for **M1-Allyl** in $CDCl_3$.

M1-Thiol

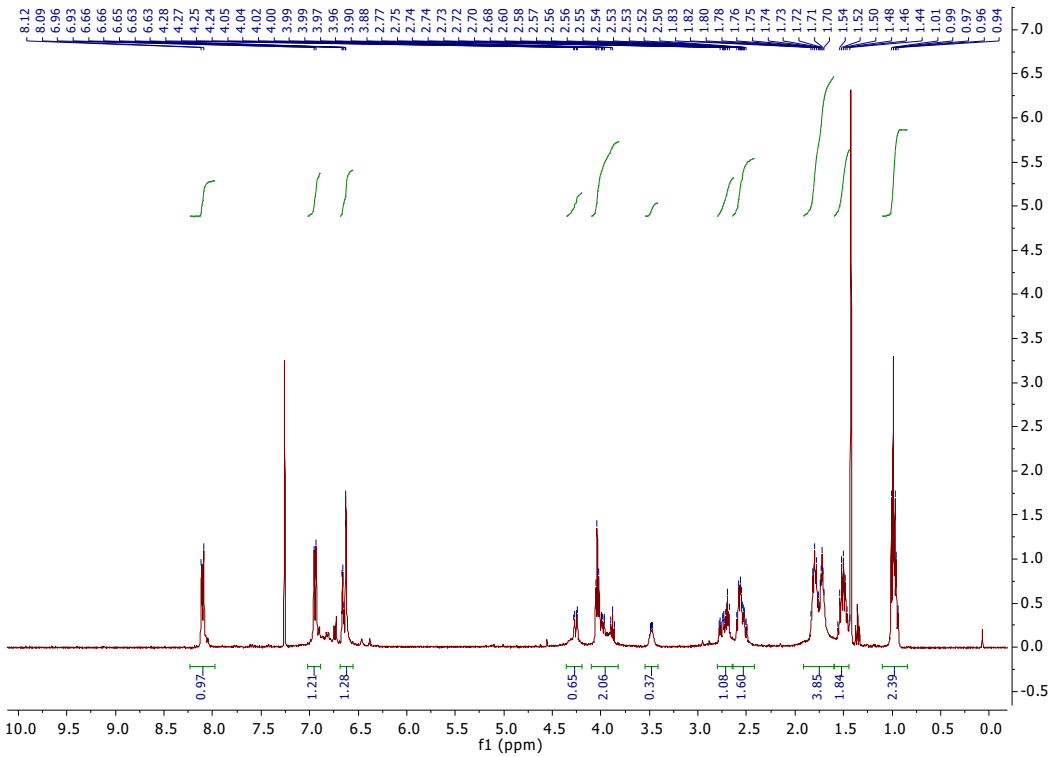

Figure A-5. ^{1}H NMR spectrum for **M1-Thiol** in $CDCl_3$.

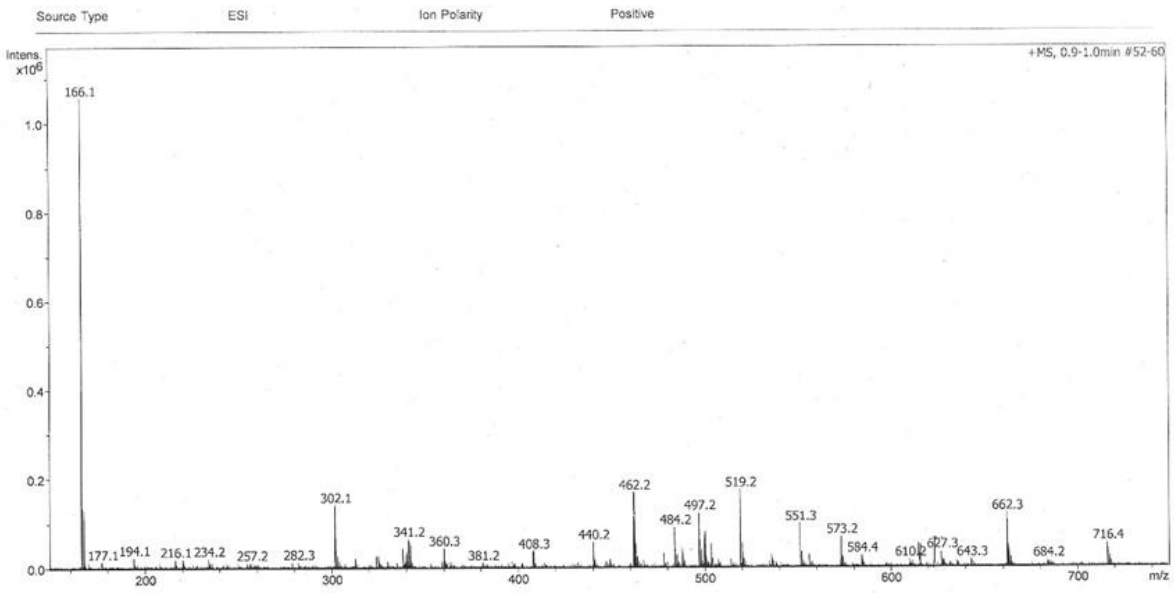

Figure A-6. ESI mass spectrum for **M1-Thiol**.

3-aminophenol-Boc

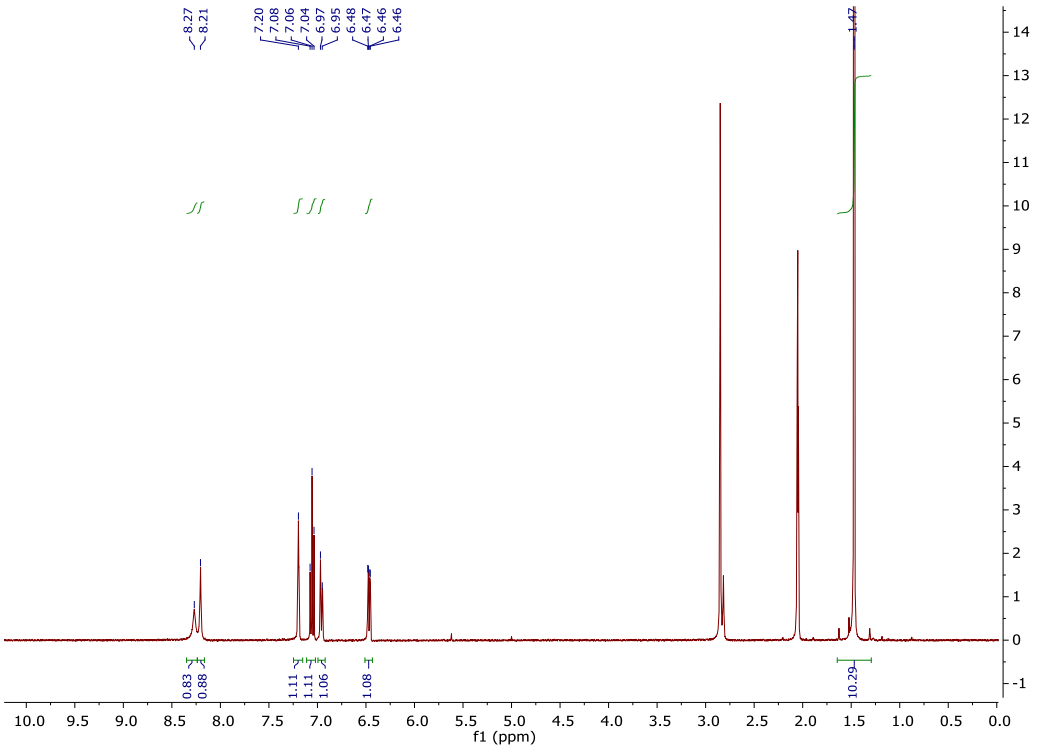

Figure A-7. ^{1}H NMR spectrum for **3-aminophenol-Boc** in $CDCl_3$.

I-M2-Boc

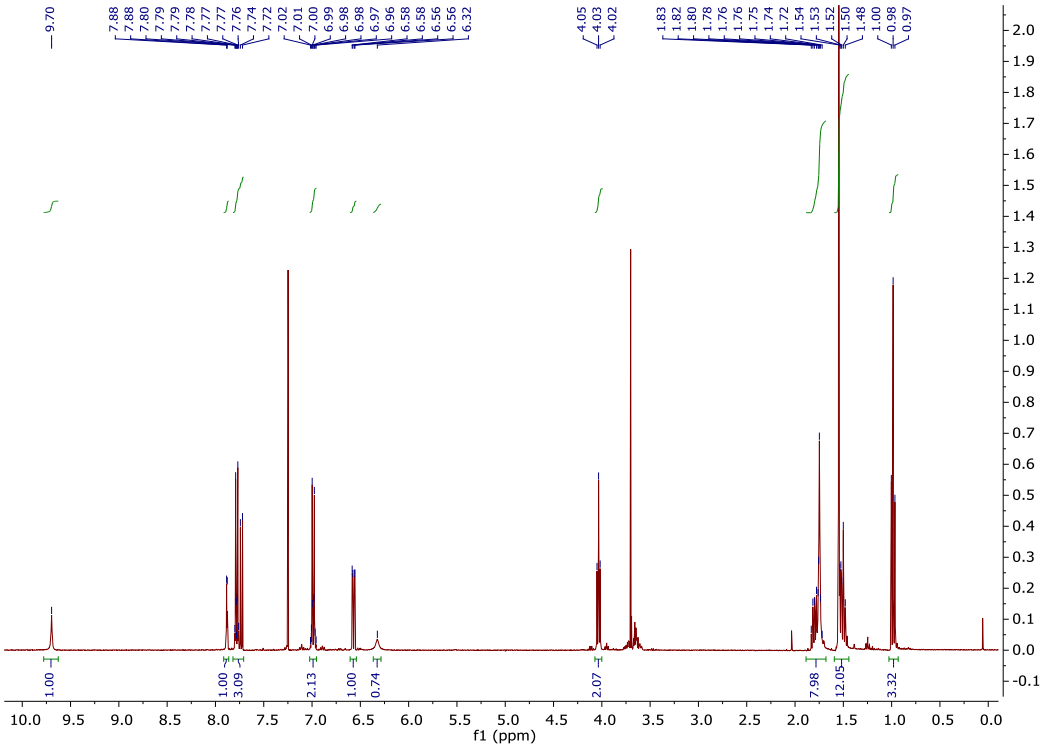

Figure A-8. ^{1}H NMR spectrum for **I-M2-Boc** in $CDCl_3$.

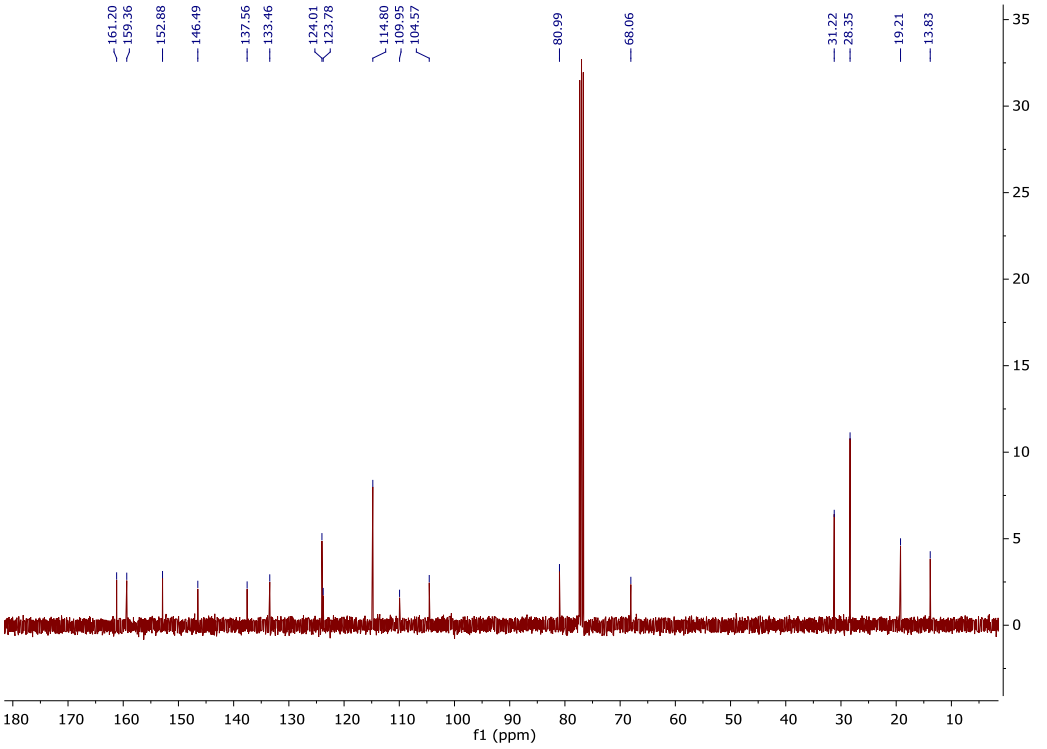

Figure A-9. Decoupled ^{13}C NMR spectrum for **I-M2-Boc** in $CDCl_3$.

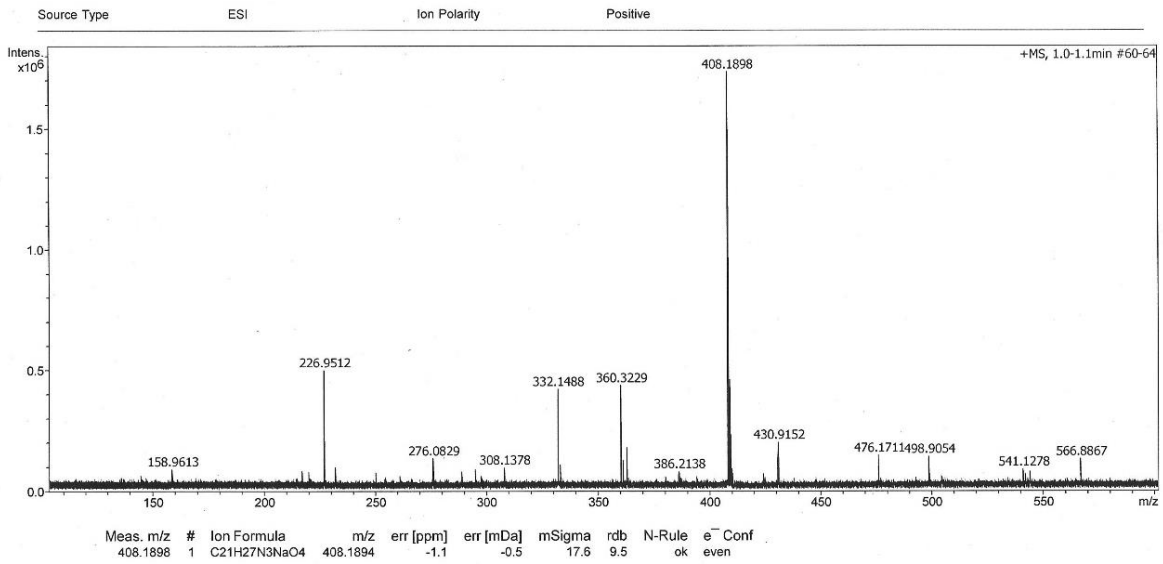

Figure A-10. ESI mass spectrum for **I-M2-Boc**.

M2-Boc

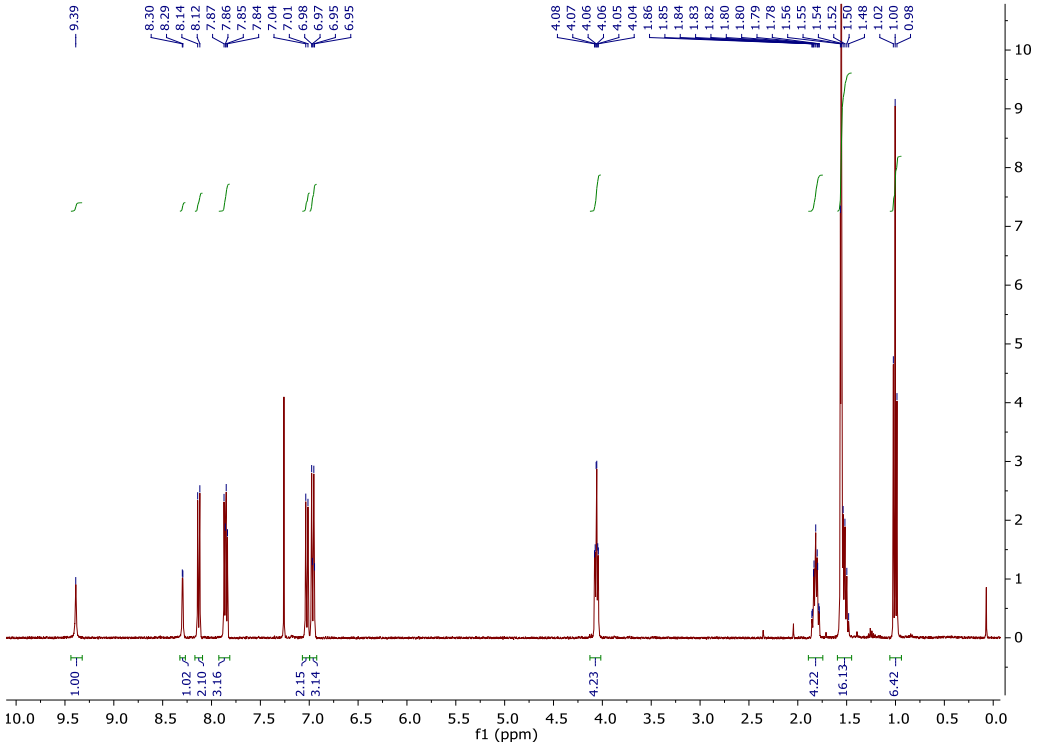

Figure A-11. ^{1}H NMR spectrum for **M2-Boc** in $CDCl_3$.

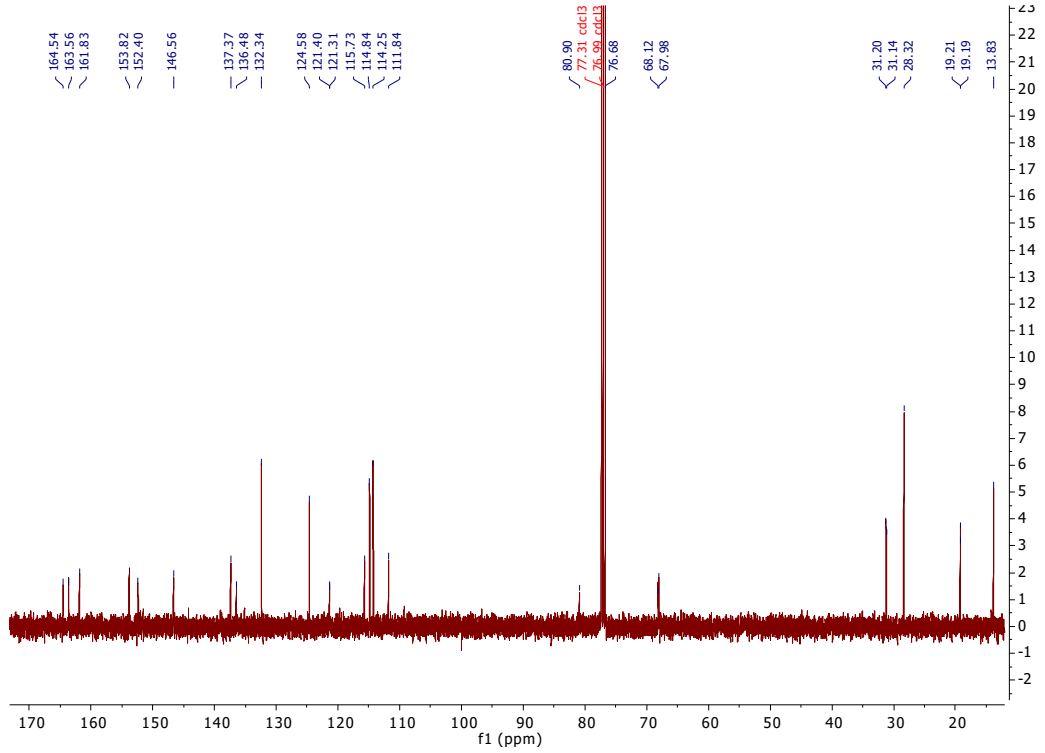

Figure A-12. Decoupled ^{13}C NMR spectrum for **M2-Boc** in $CDCl_3$.

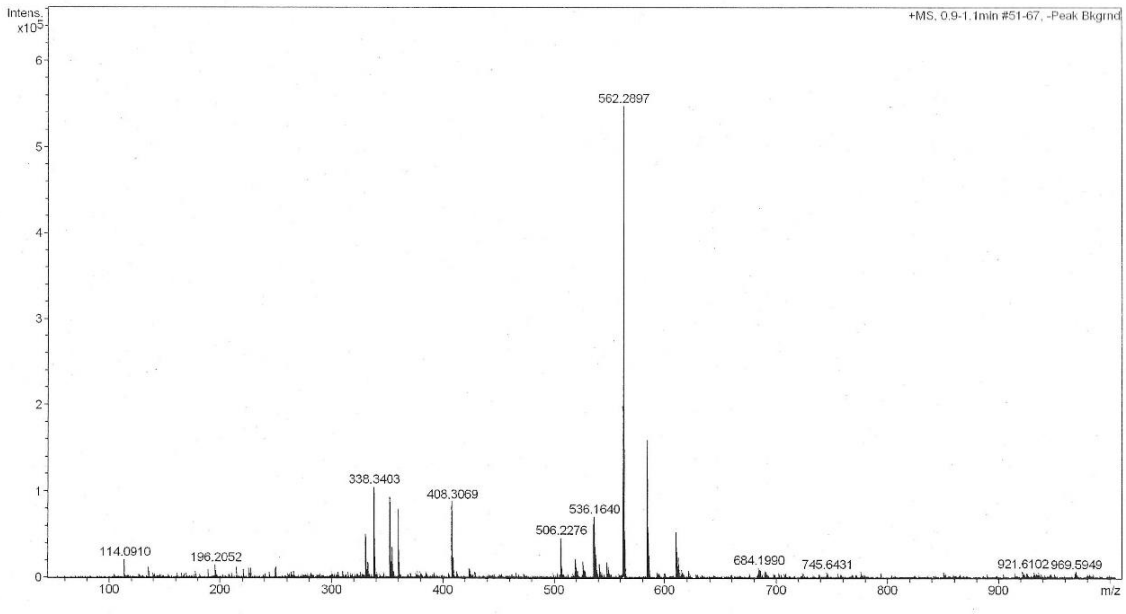

Figure A-13. ESI mass spectrum for **M2-Boc**.

M2

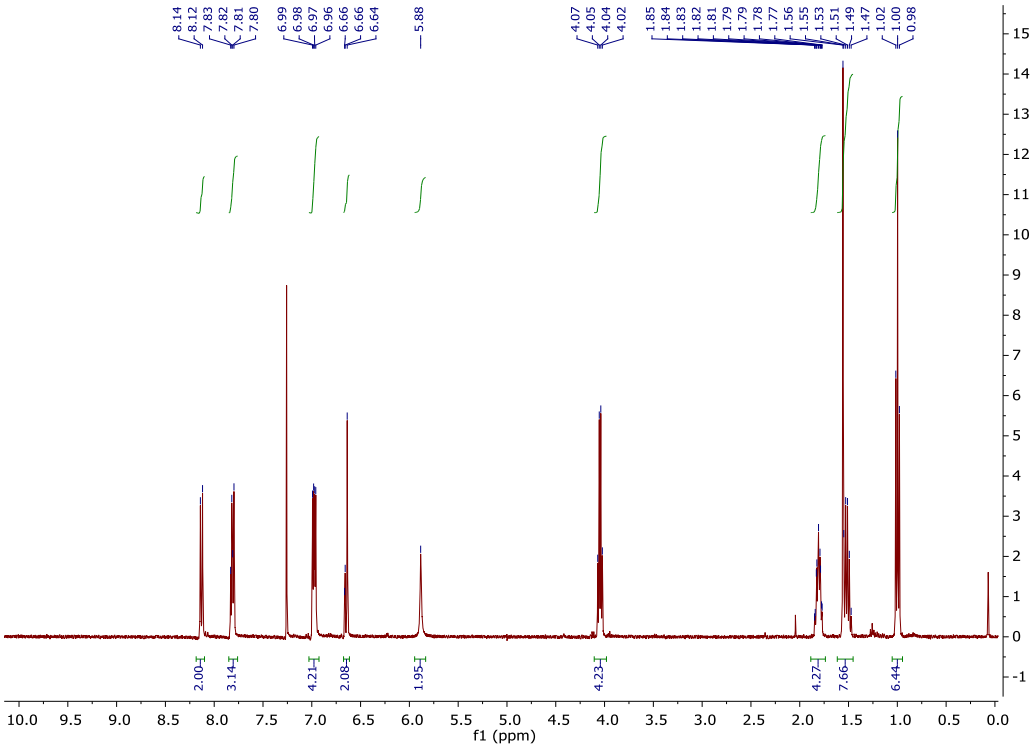

Figure A-14. ^{1}H NMR spectrum for **M2** in $CDCl_3$.

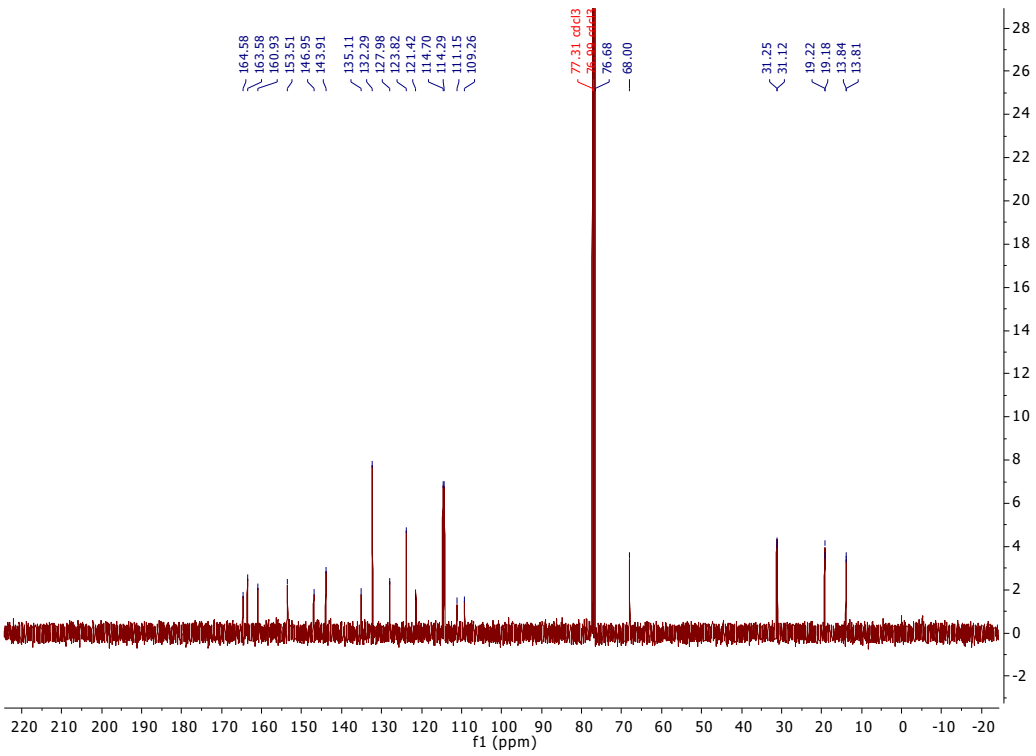

Figure A-15. Decoupled ^{13}C NMR spectrum for **M2** in $CDCl_3$.

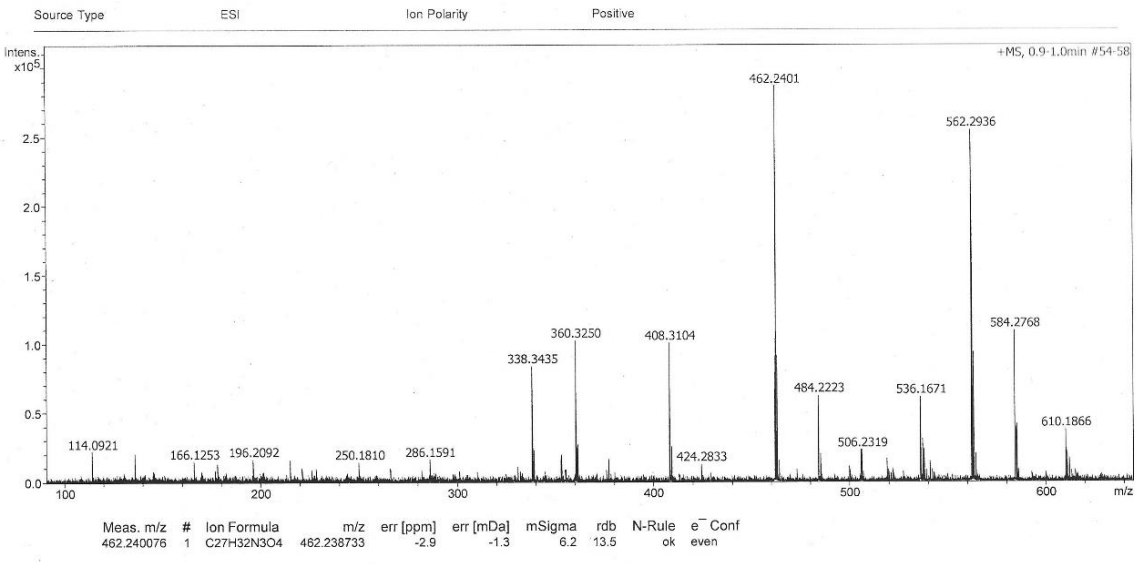

Figure A-16. ESI mass spectrum for **M2**.

A.2. Polymer Backbone Synthesis

Aliquot 1, PS

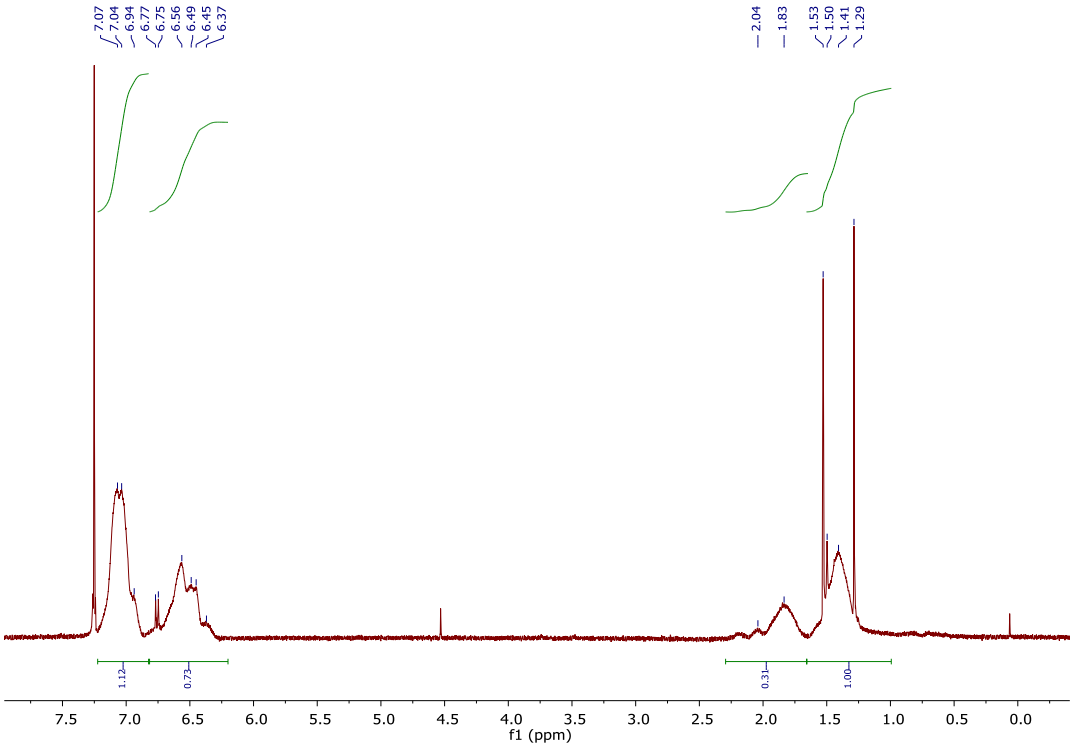

Figure A-17. ^{1}H NMR spectrum for Aliquot 1 in $CDCl_3$.

Aliquot 2, PS-*b*-PDMS

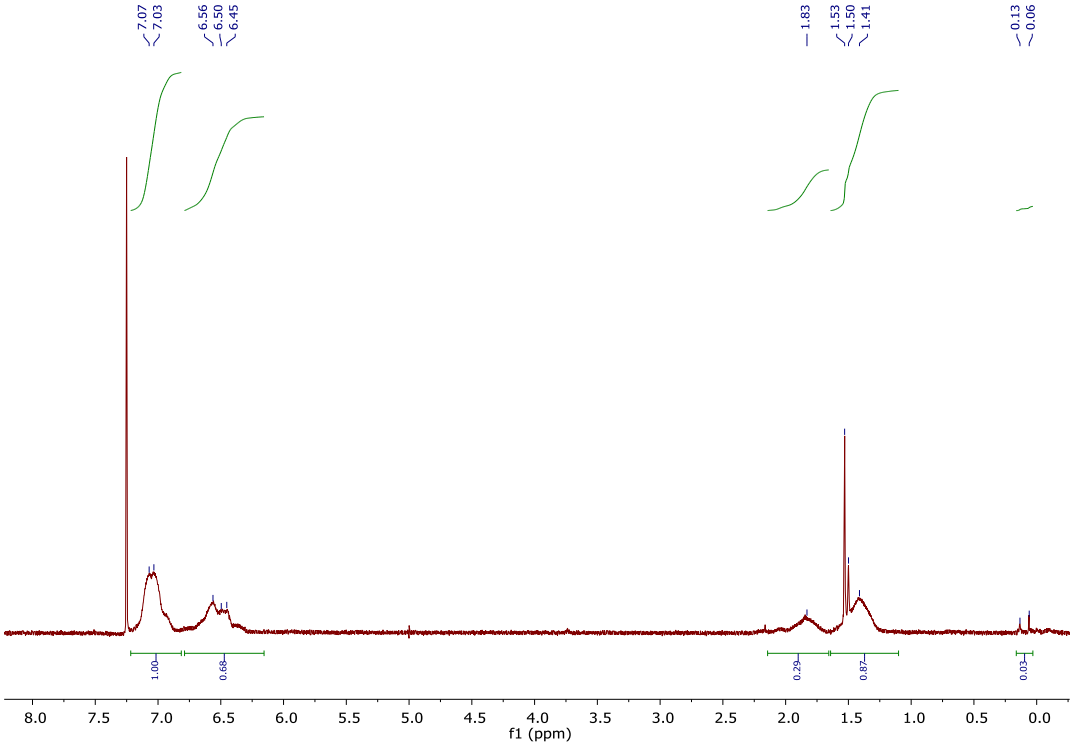

Figure A-18. ^{1}H NMR spectrum for Aliquot 2 in $CDCl_3$.

Aliquot 3, PS-*b*-PDMS-*b*-PMVS

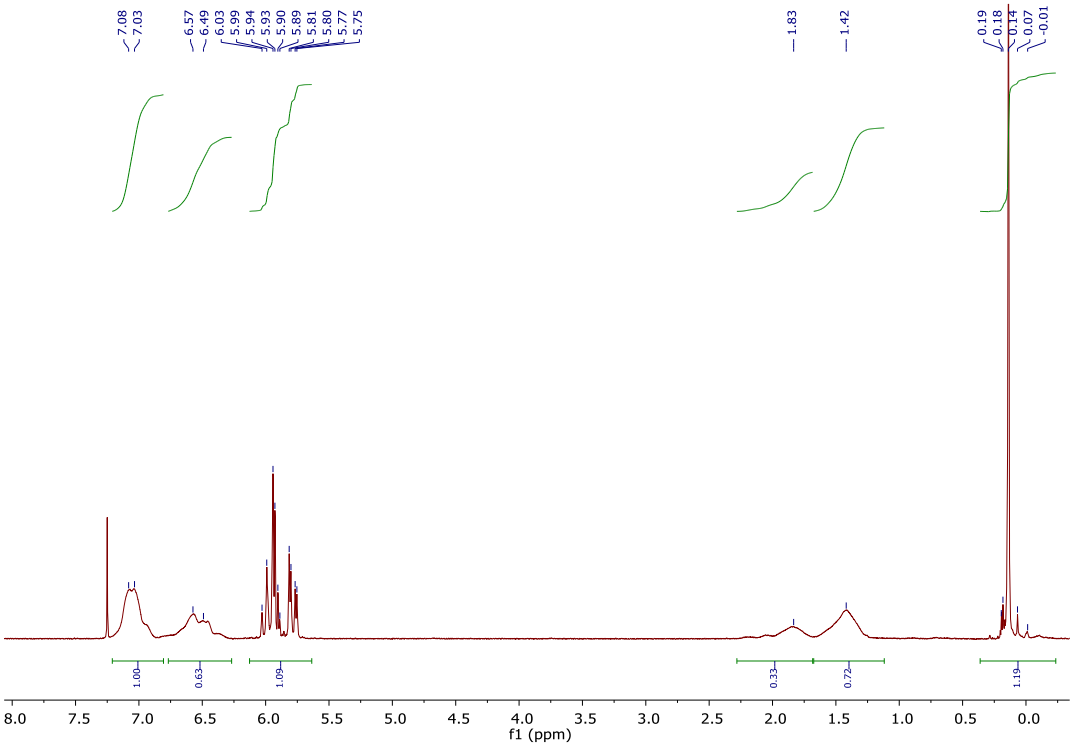

Figure A-19. ^{1}H NMR spectrum for Aliquot 3 in $CDCl_3$.

Aliquot 4, PS-*b*-PMVS-*b*-PS

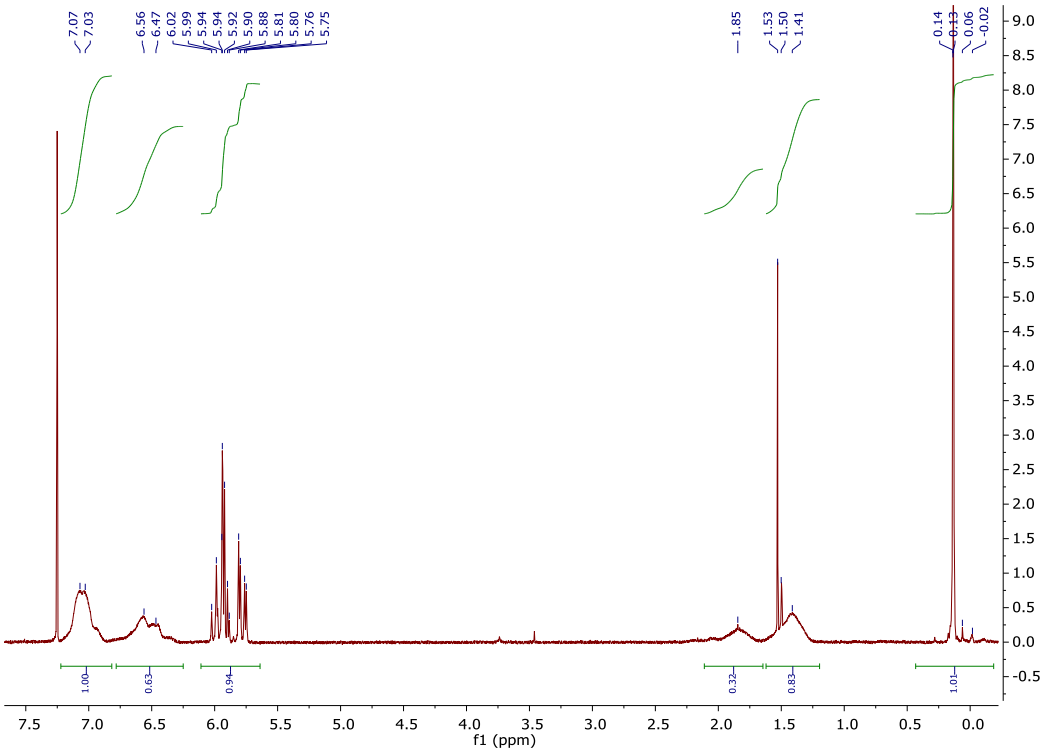

Figure A-20. ^{1}H NMR spectrum for **PS-*b*-PMVS-*b*-PS** in $CDCl_3$.

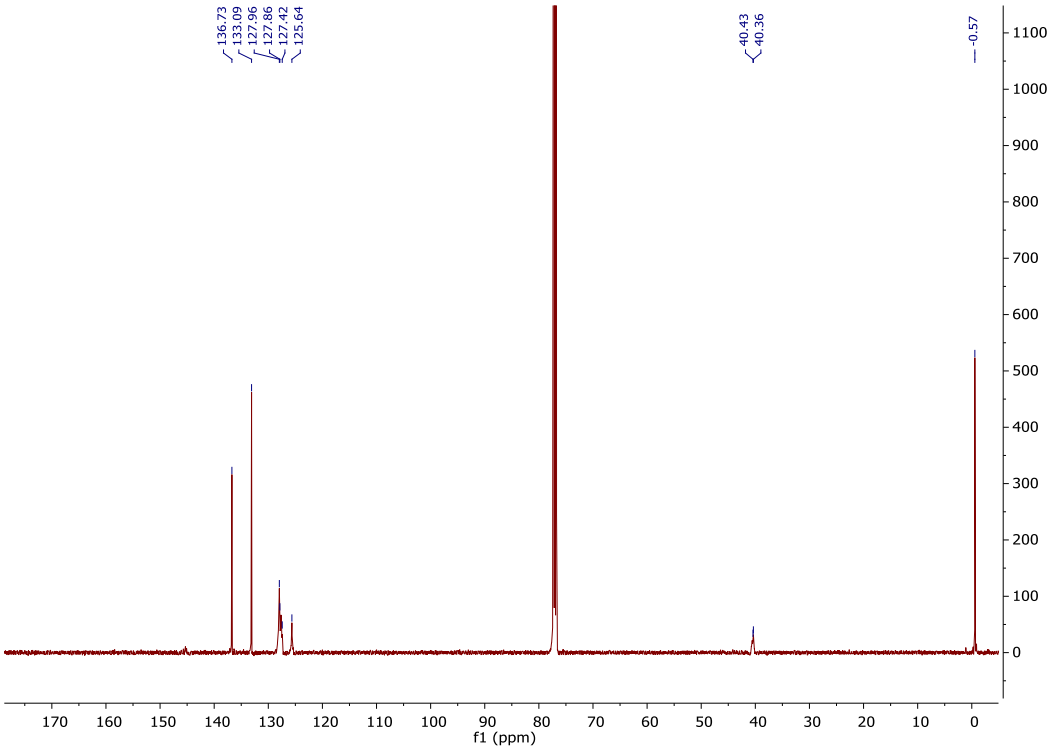

Figure A-21. Decoupled ^{13}C NMR spectrum for **PS-*b*-PMVS-*b*-PS** in $CDCl_3$.

PMVS

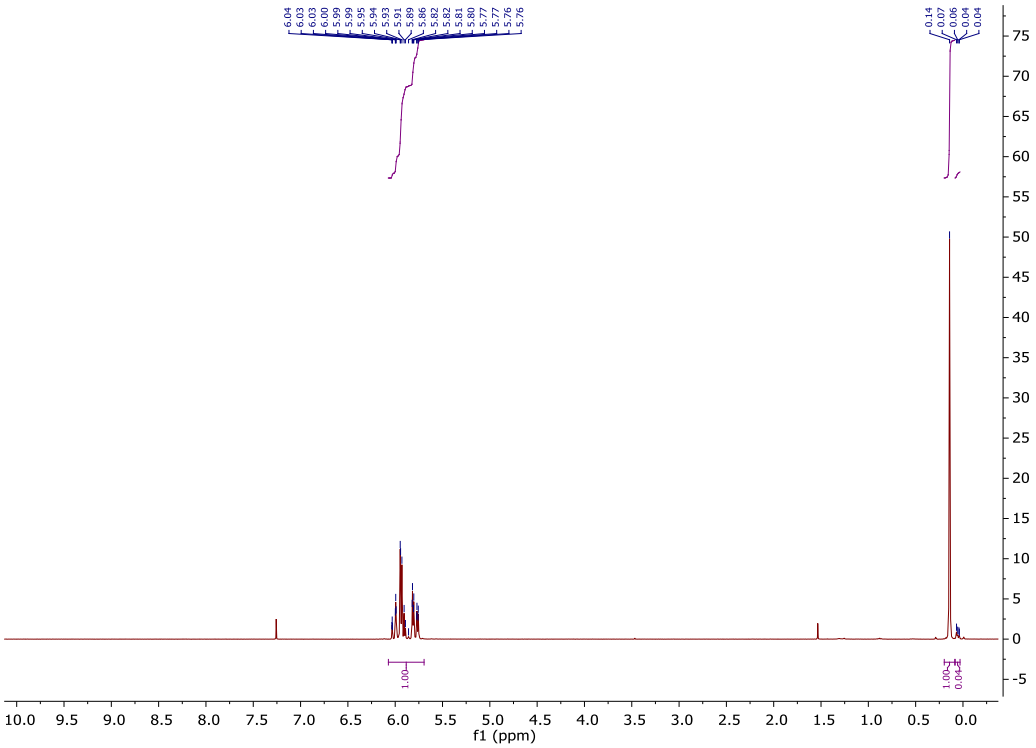

Figure A-22. ^{1}H NMR spectrum for **PMVS** in $CDCl_3$.

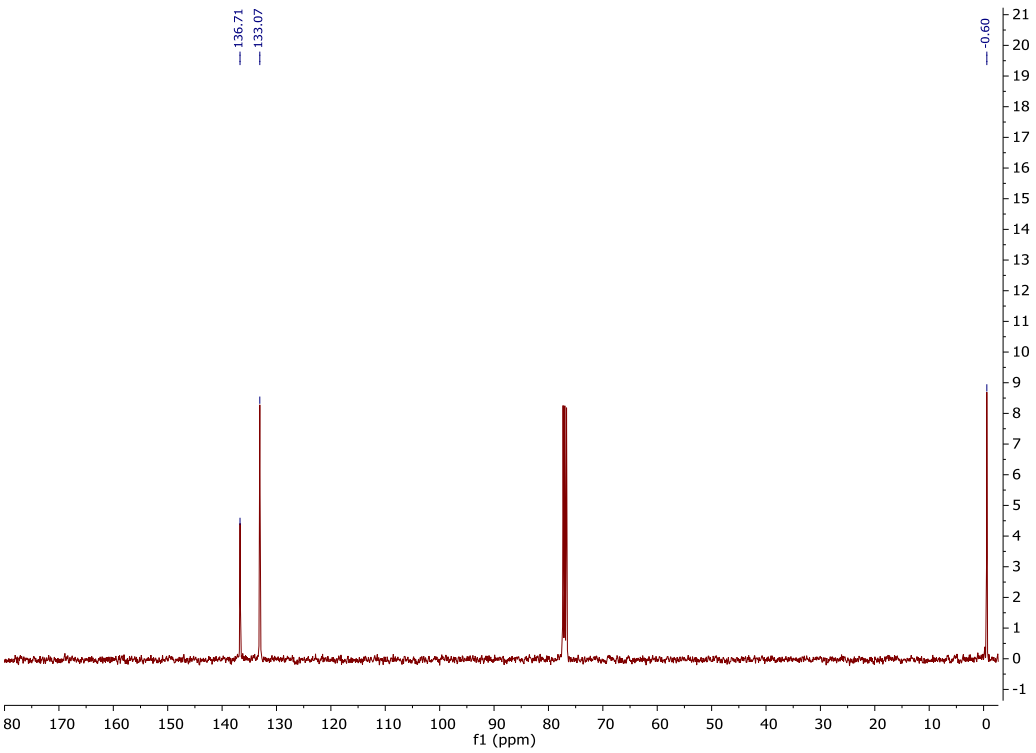

Figure A-23. Decoupled ^{13}C NMR spectrum for **PMVS** in $CDCl_3$.

A.3. Linking Group Attachment

P-3

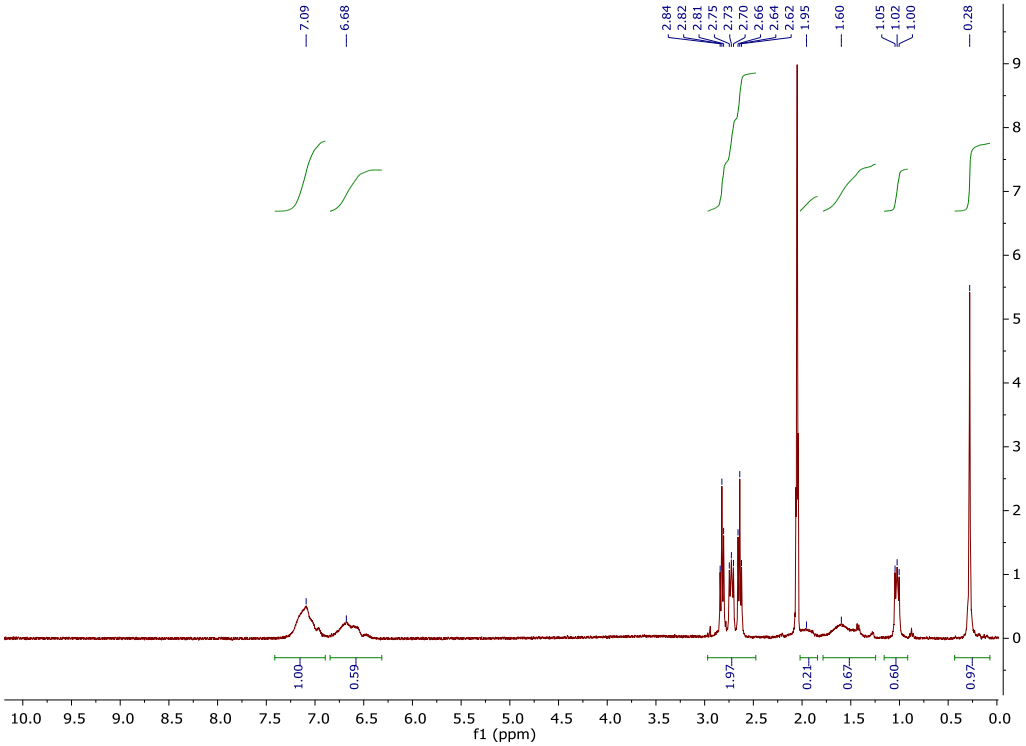

Figure A-24. ^{1}H NMR spectrum for **P-3** in acetone-d_6.

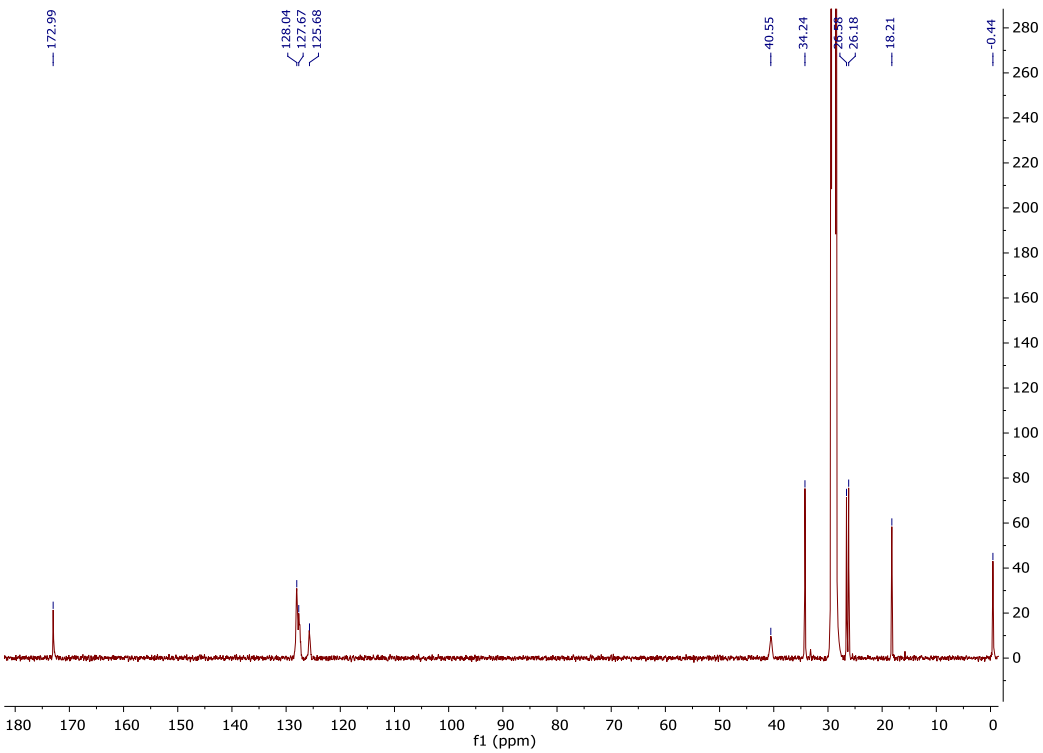

Figure A-25. Decoupled ^{13}C NMR spectrum for **P-3** in acetone-d_6.

5-mercaptopentanoic acid

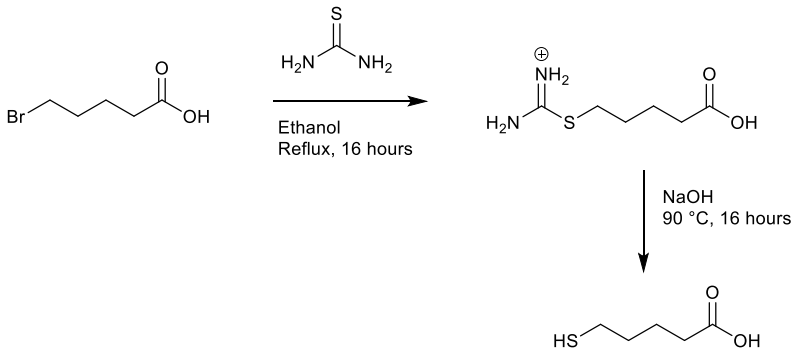

Figure A-26. Synthetic scheme for conversion of 5-bromovaleric acid to 5-mercaptopentanoic acid.

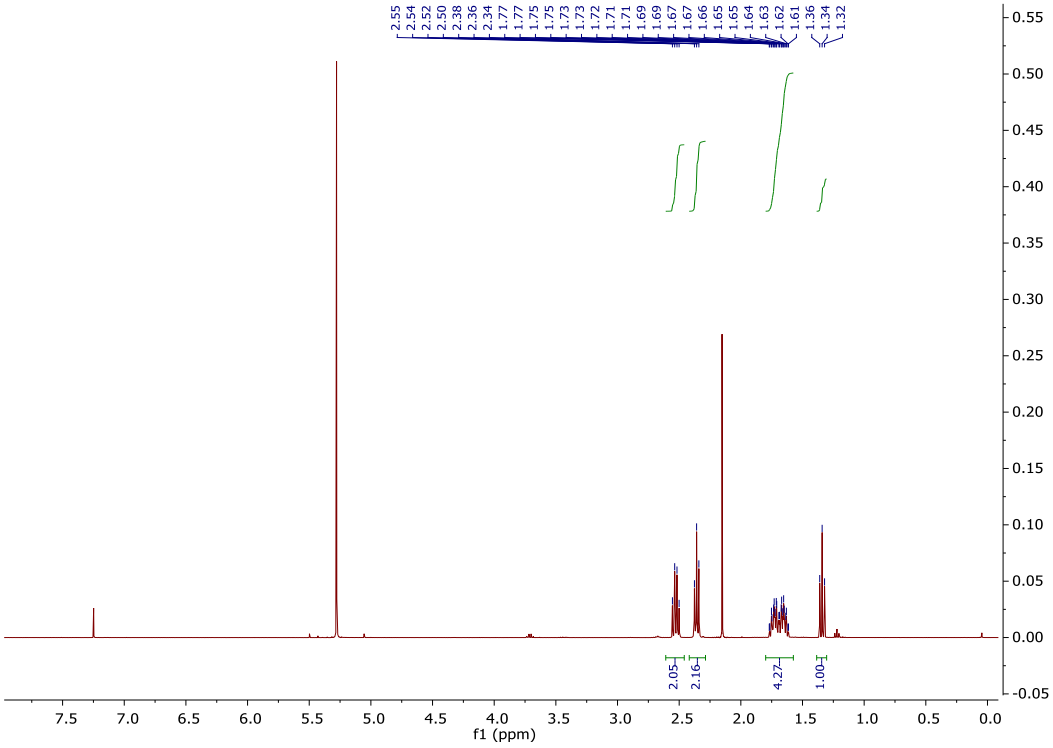

Figure A-27. ^{1}H NMR spectrum for 5-mercaptopentanoic acid in $CDCl_3$.

P-5

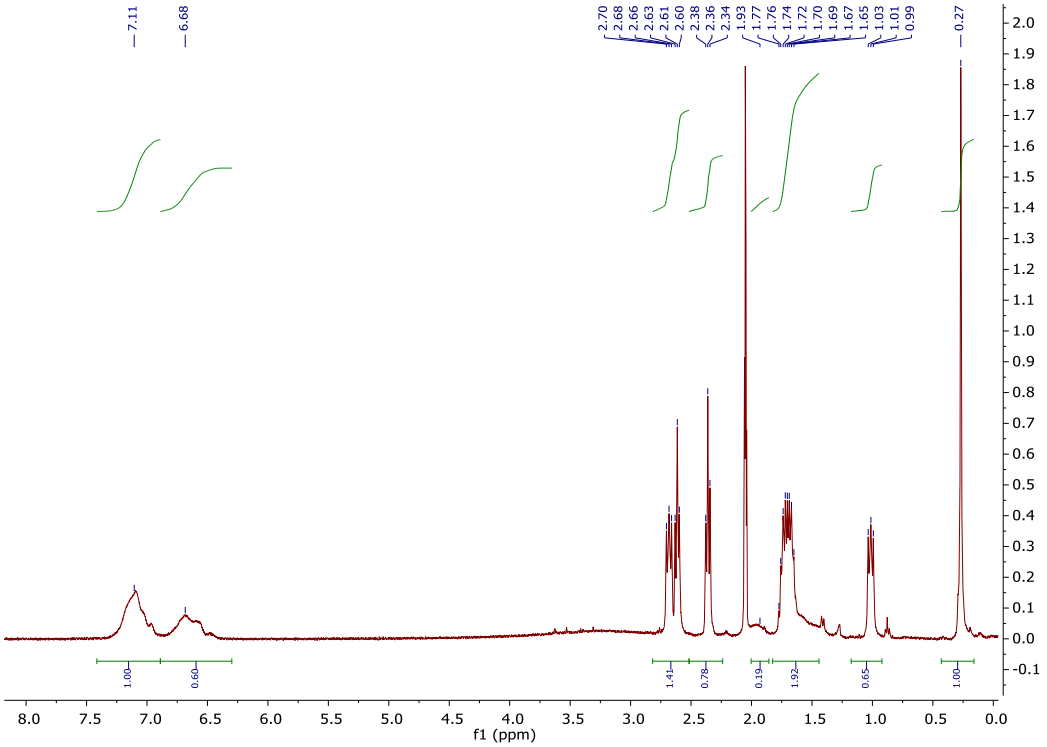

Figure A-28. ^{1}H NMR spectrum for **P-5** in acetone-d_6.

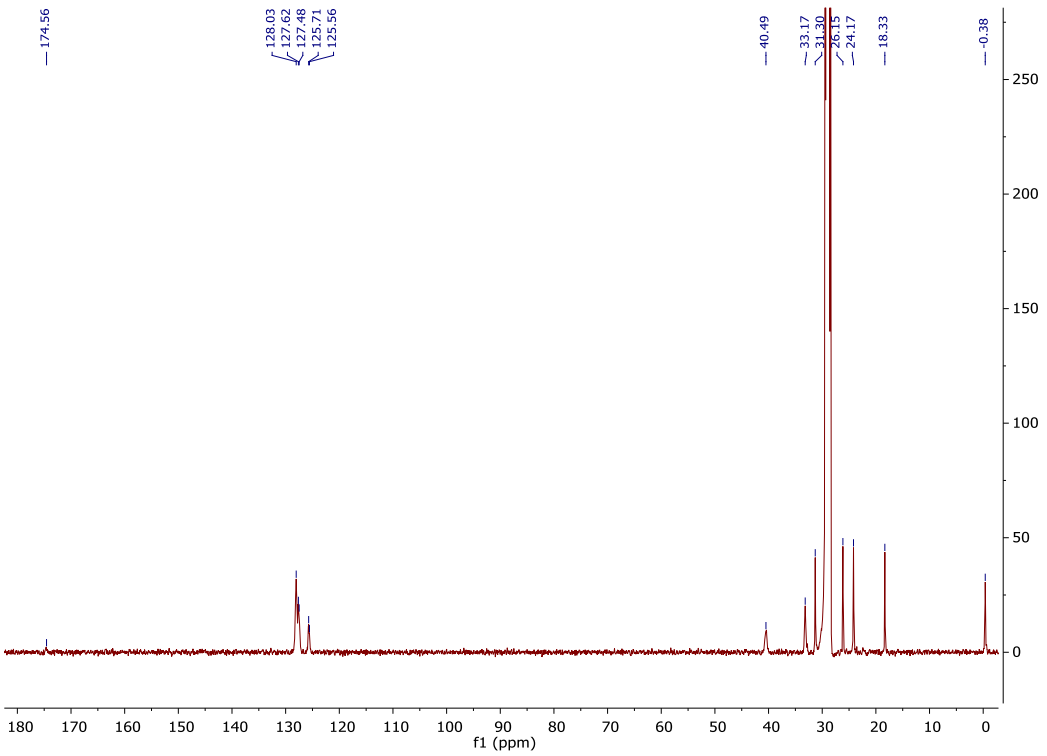

Figure A-29. Decoupled ^{13}C NMR spectrum for **P-5** in acetone-d_6.

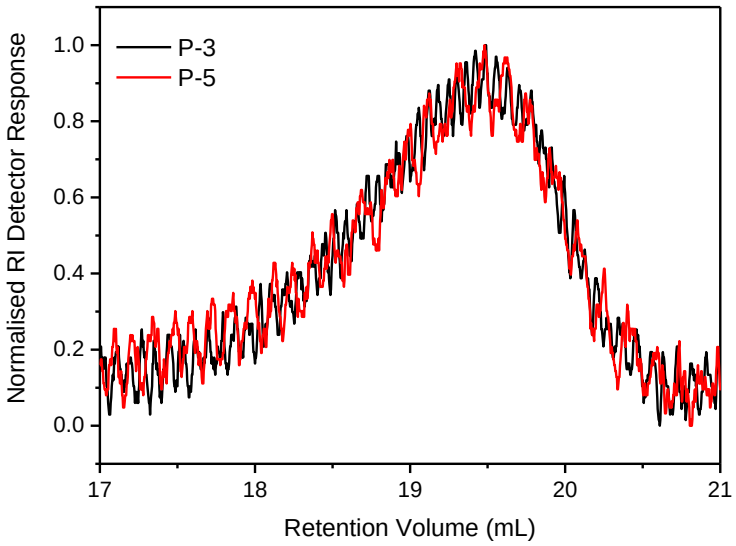

Figure A-30. GPC data for **P-3** and **P-5**.

PMVS-3

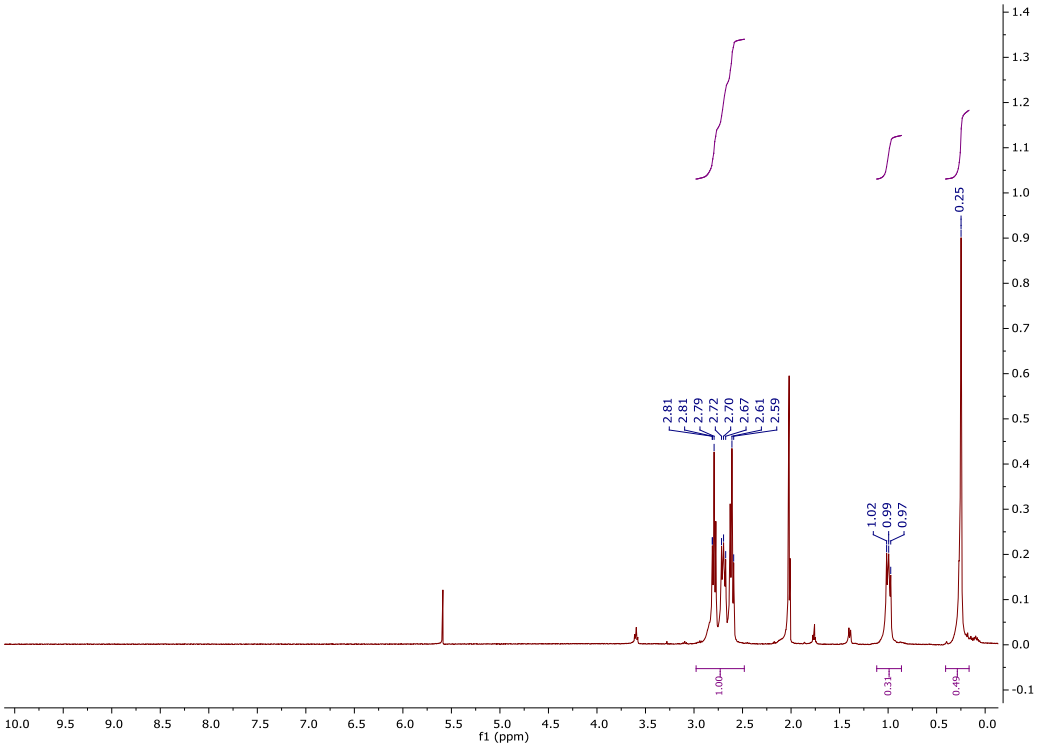

Figure A-31. ^{1}H NMR spectrum for **PMVS-3** in acetone-d_6.

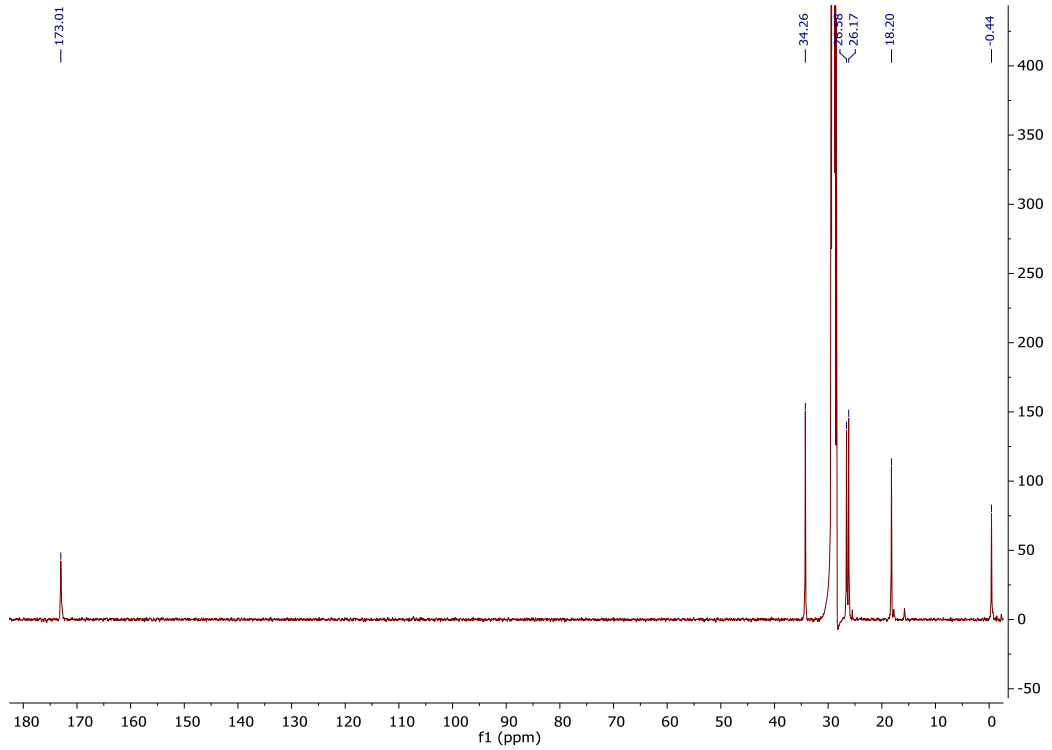

Figure A-32. Decoupled ^{13}C NMR spectrum for **PMVS-3** in acetone-d_6.

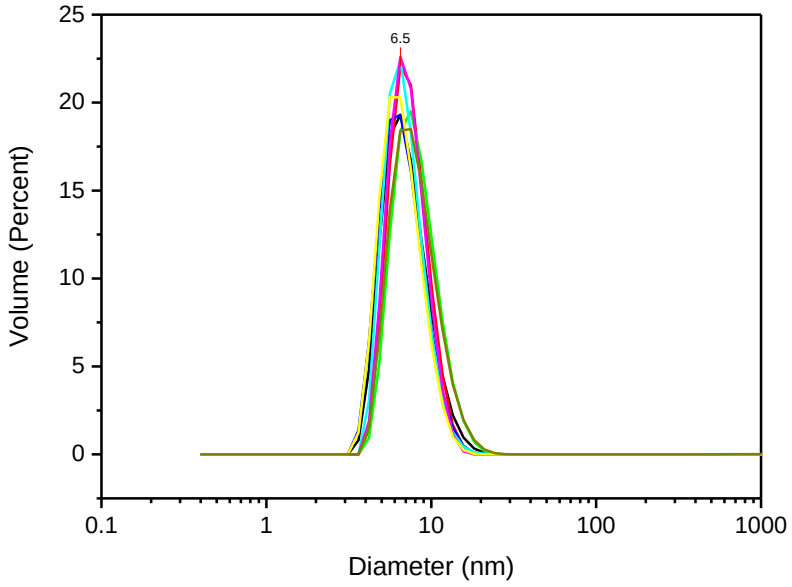

Figure A-33. DLS of **PMVS-3** in THF, 8 repeats.

P*-3(AIBN)

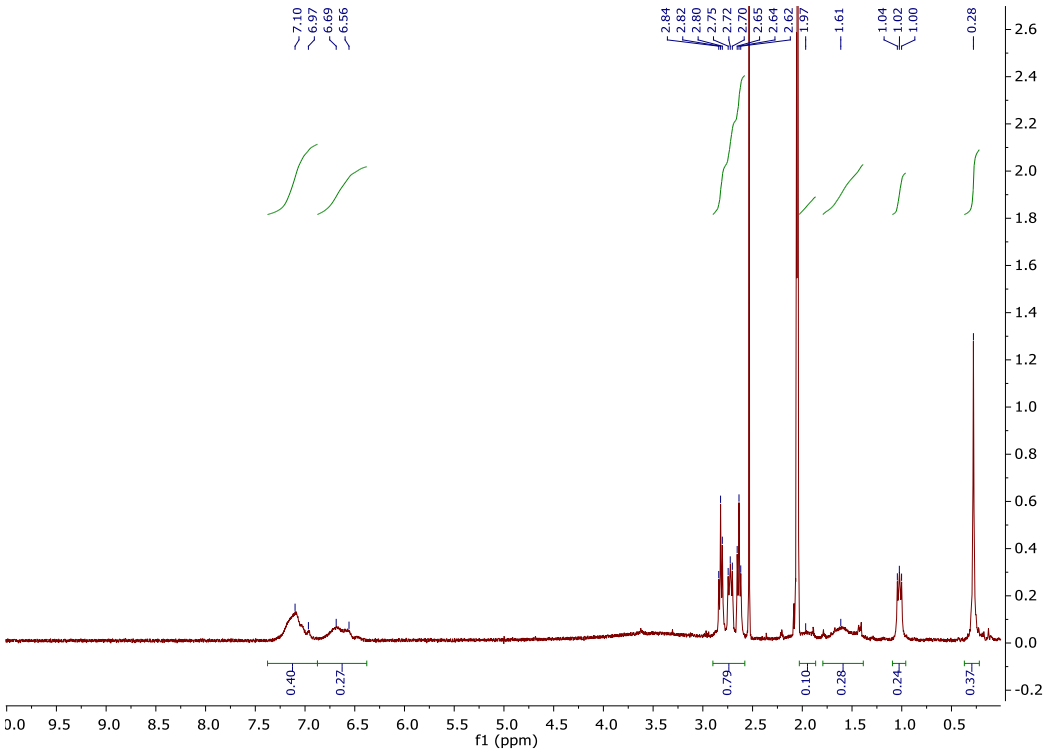

Figure A-34. ^{1}H NMR spectrum for **P*-3(AIBN)** in acetone-d_6.

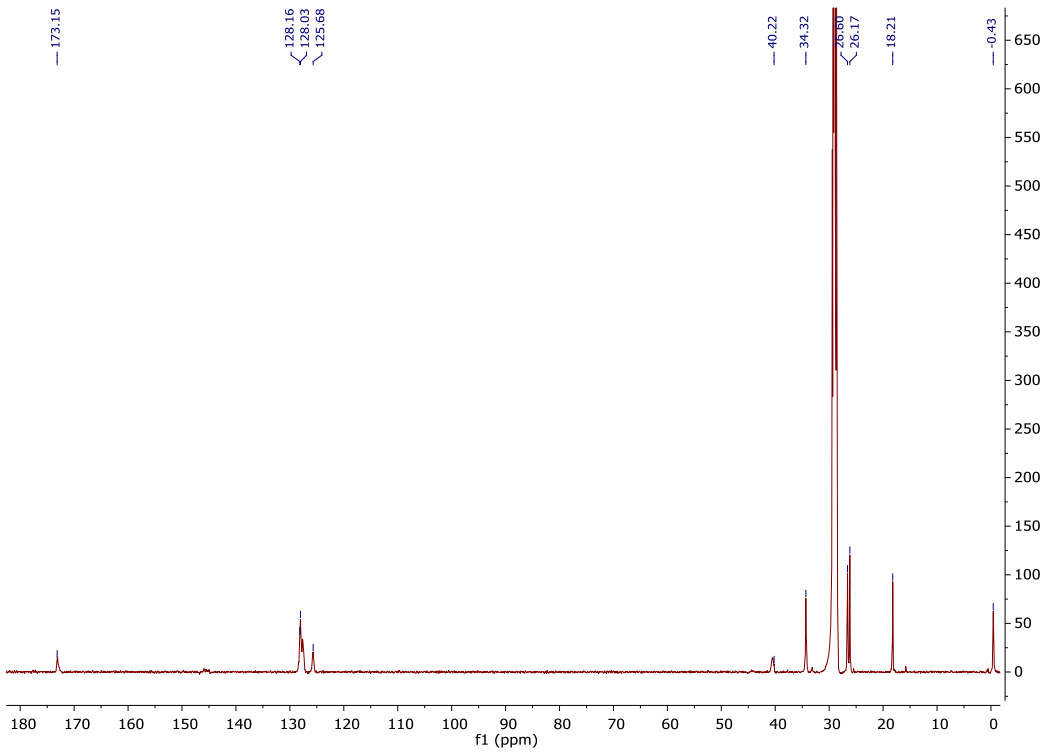

Figure A-35. Decoupled ^{13}C NMR spectrum for **P*-3(AIBN)** in acetone-d_6.

P-3-NHS

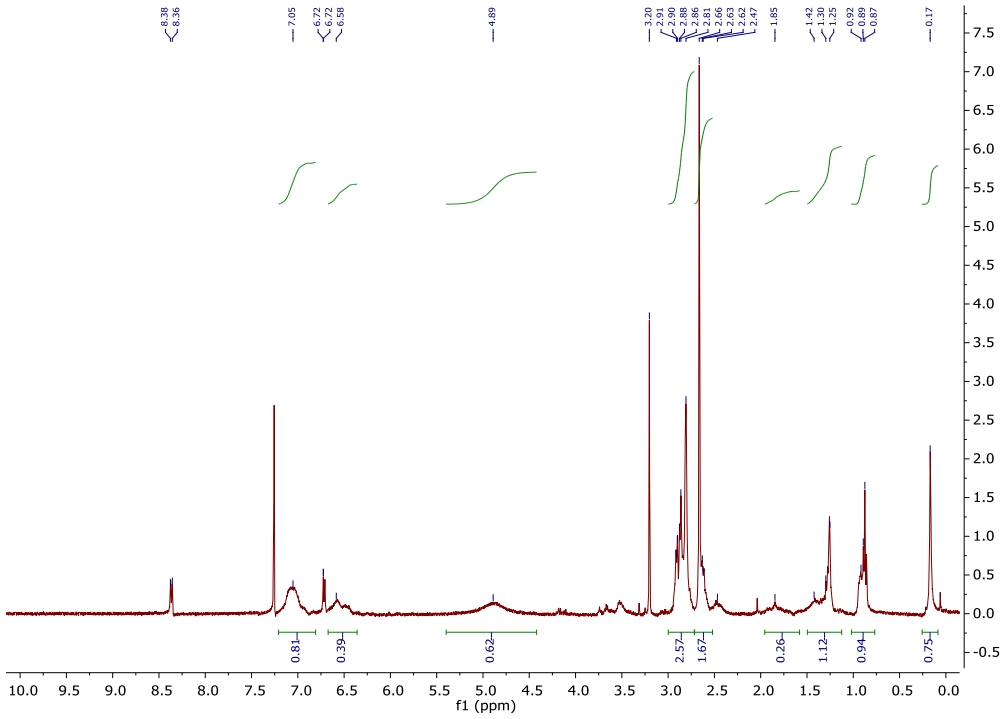

Figure A-36. ^{1}H NMR spectrum for **P-3-NHS** in $CDCl_3$.

A.4. Mesogen Attachment

Displacement of NHS ester with M2

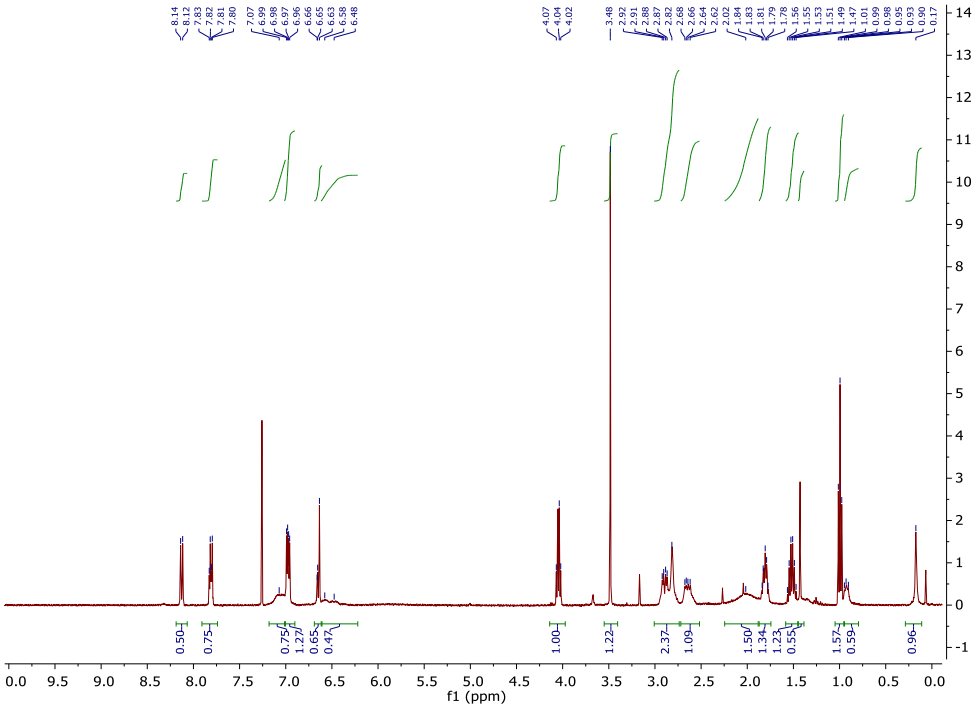

Figure A-37. ^{1}H NMR spectrum for product of NHS ester coupling reaction in $CDCl_3$.

P-5 with M2

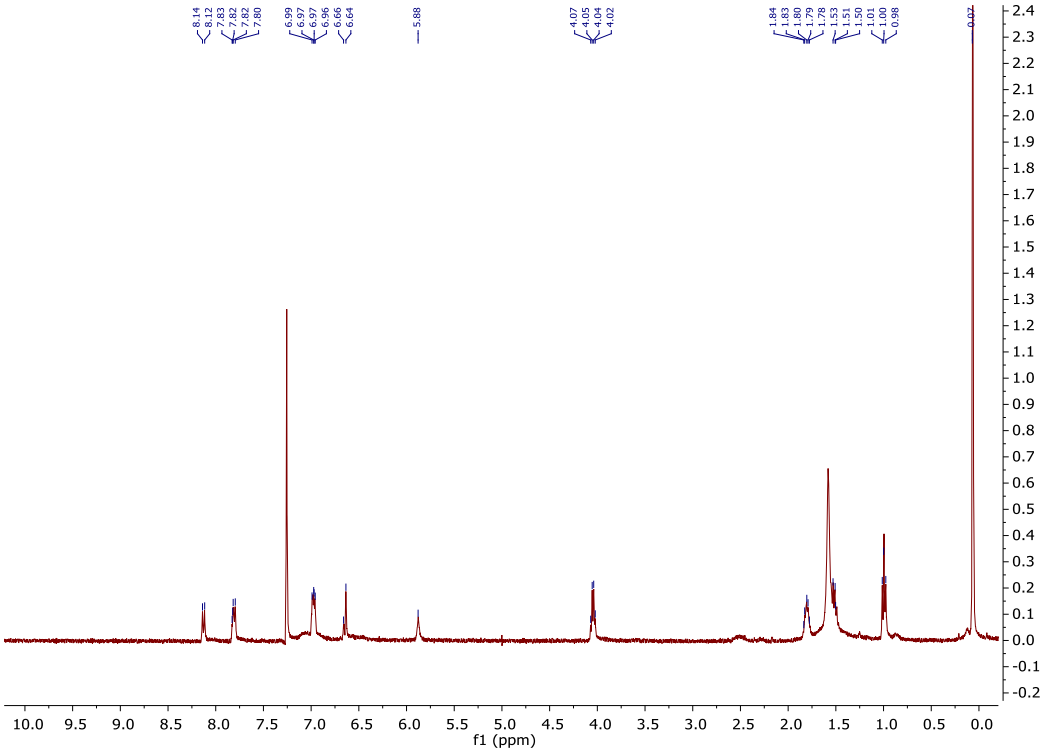

Figure A-38. ^{1}H NMR spectrum for product of reaction of **P-5** with **M2** in $CDCl_3$.

P-3-M1(82)-COOH(18)

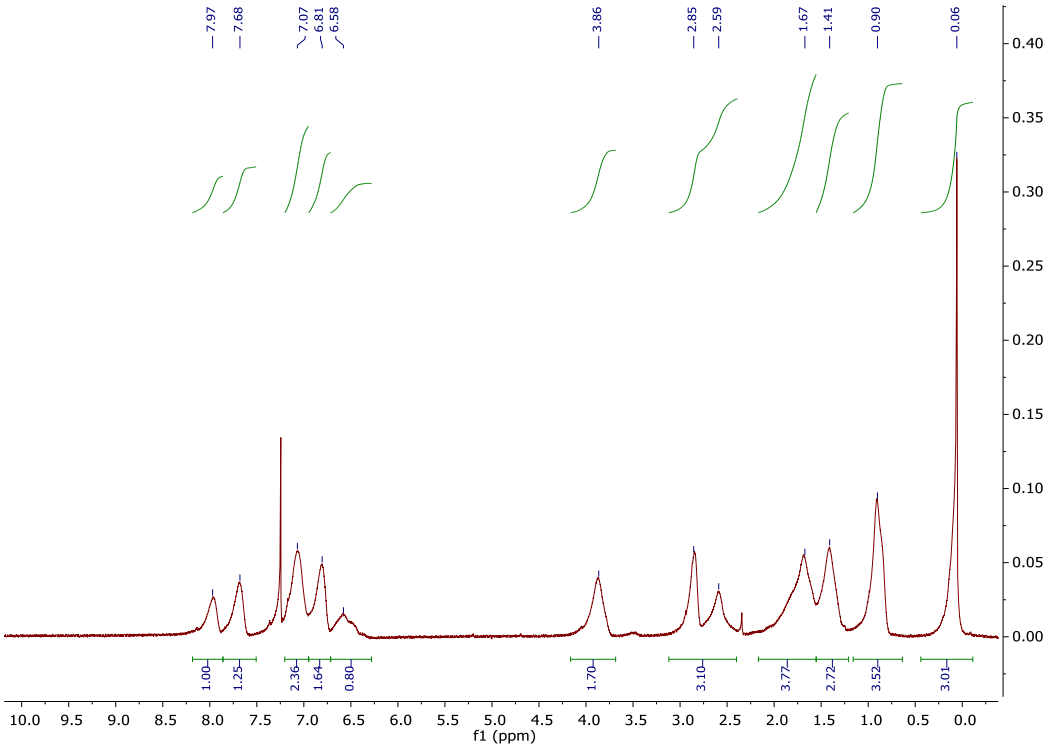

Figure A-39. ^{1}H NMR spectrum for **P-3-M1(82)-COOH(18)** in $CDCl_3$.

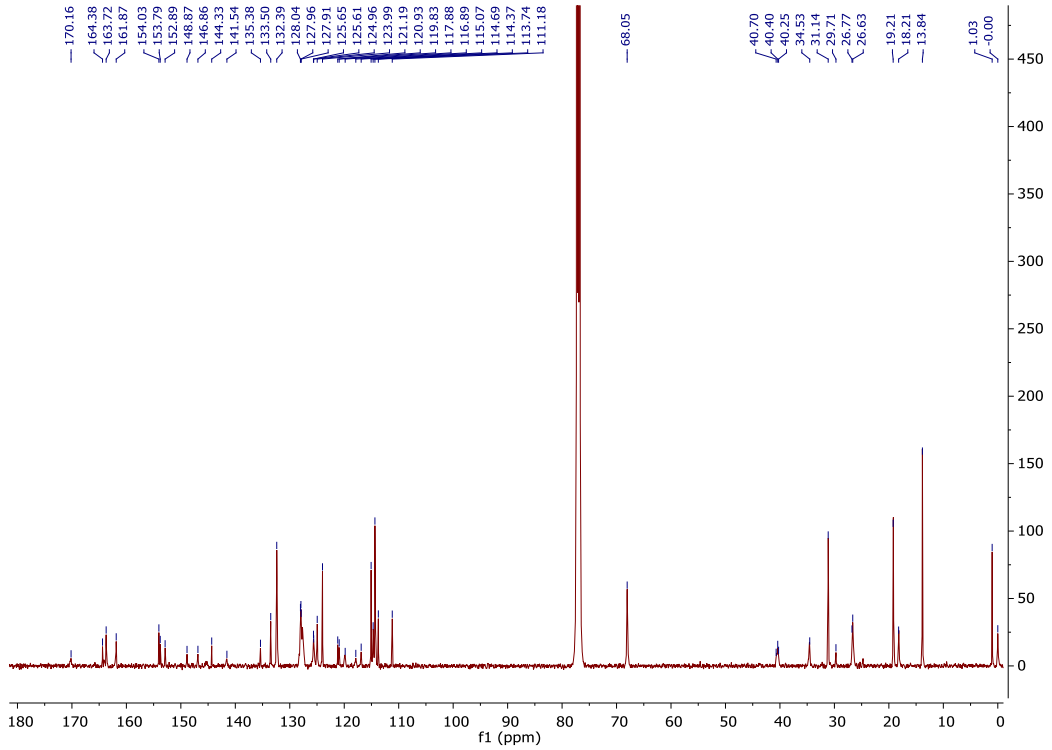

Figure A-40. Decoupled ^{13}C NMR spectrum for **P-3-M1(82)-COOH(18)** in $CDCl_3$.

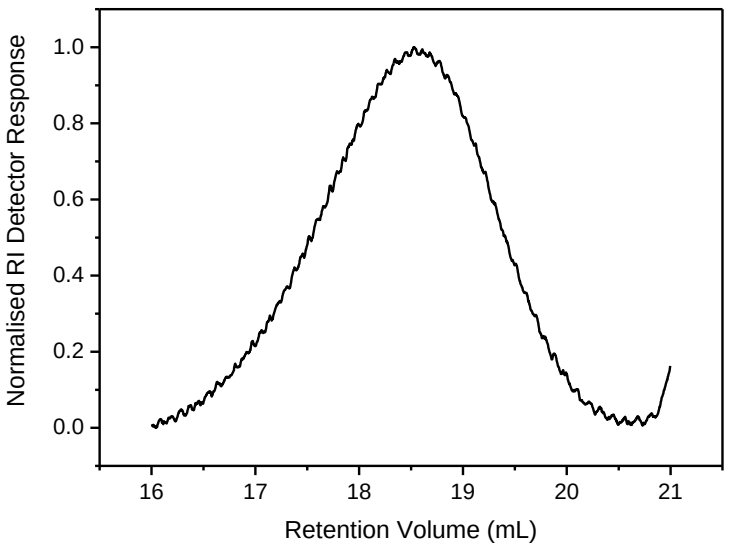

Figure A-41. GPC data for **P-3-M1(82)-COOH(18)**.

P-3-M2(80)-COOH(20)

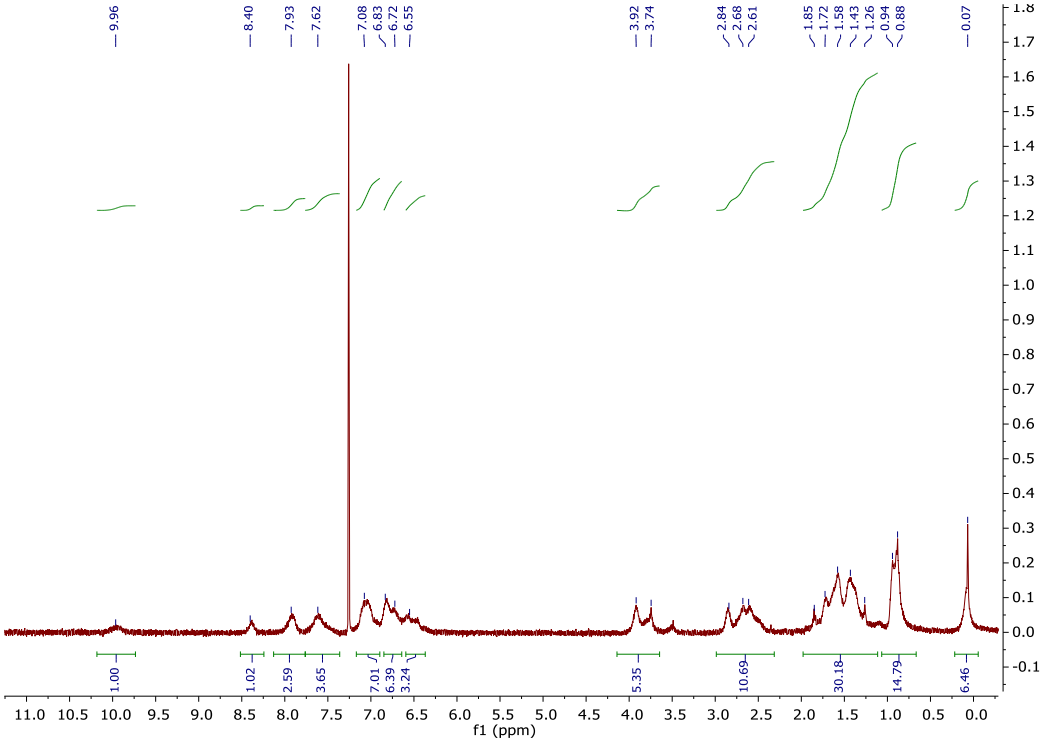

Figure A-42. ^{1}H NMR spectrum for **P-3-M2(80)-COOH(20)** in $CDCl_3$.

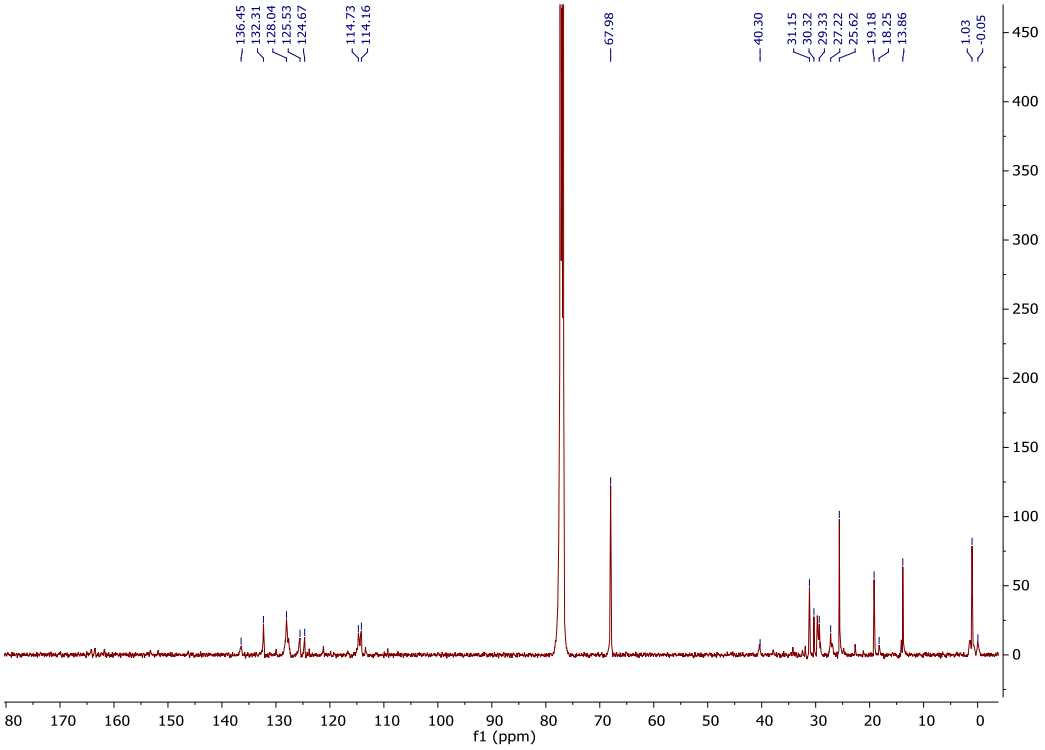

Figure A-43. Decoupled ^{13}C NMR spectrum for **P-3-M2(80)-COOH(20)** in $CDCl_3$.

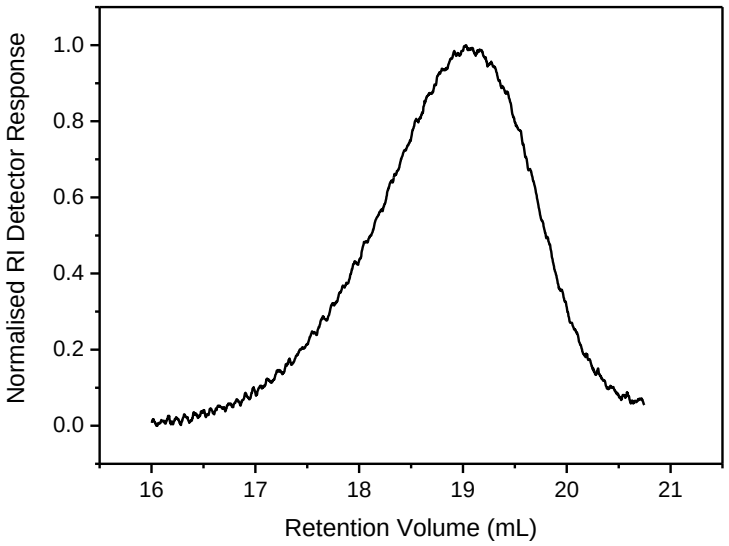

Figure A-44. GPC data for **P-3-M2(80)-COOH(20)**.

P-5-M1(86)-COOH(14)

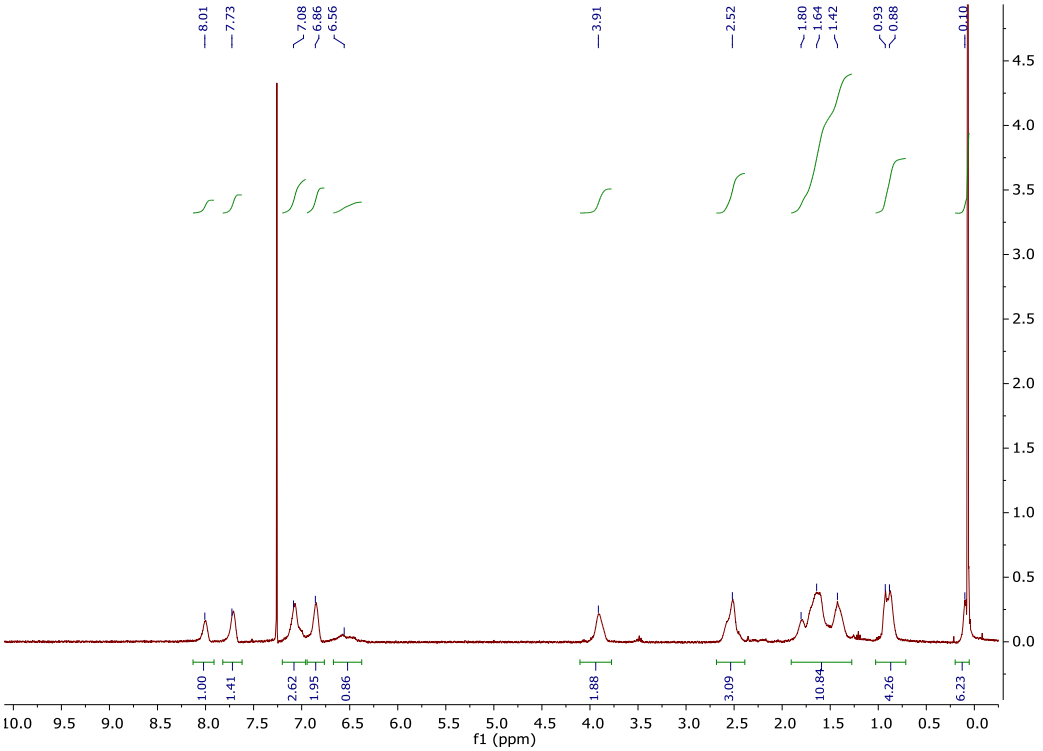

Figure A-45. ^{1}H NMR spectrum for **P-5-M1(86)-COOH(14)** in $CDCl_3$.

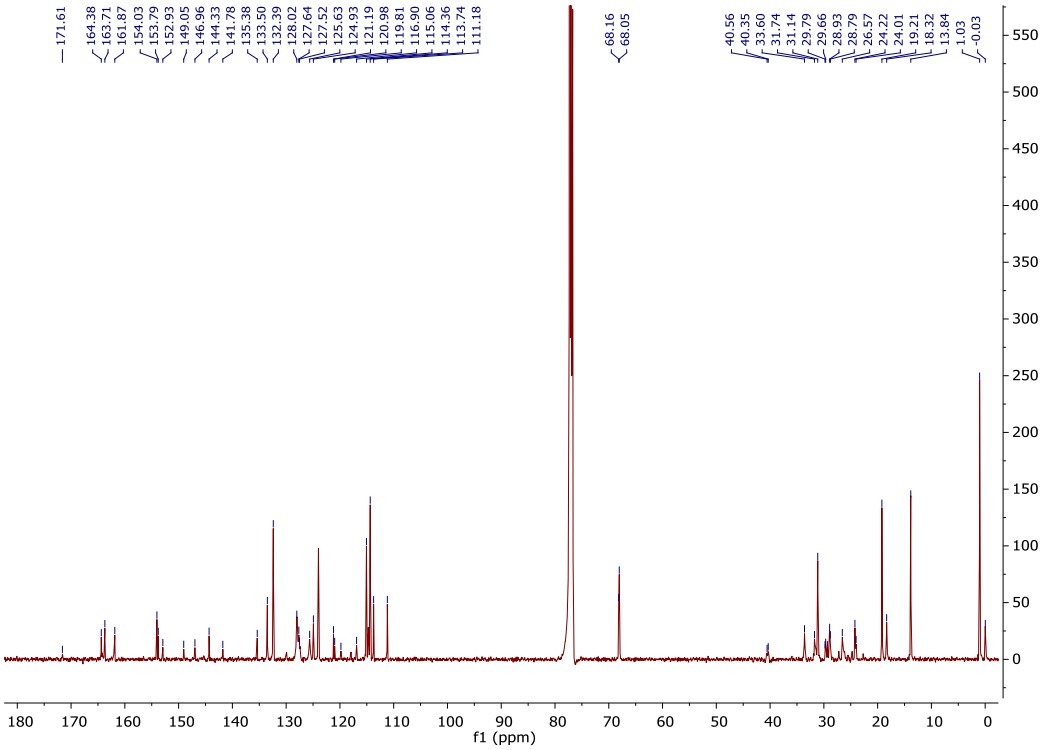

Figure A-46. Decoupled ^{13}C NMR spectrum for **P-5-M1(86)-COOH(14)** in $CDCl_3$.

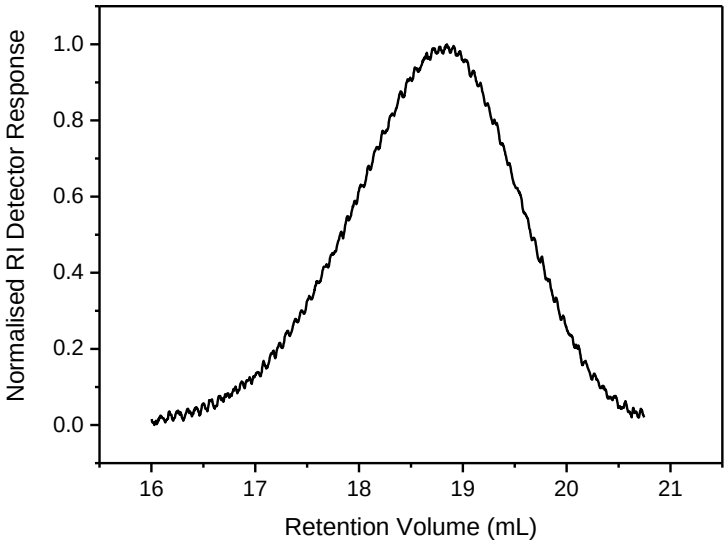

Figure A-47. GPC data for **P-5-M1(86)-COOH(14)**.

P-3-M1(65)-COOH(35)

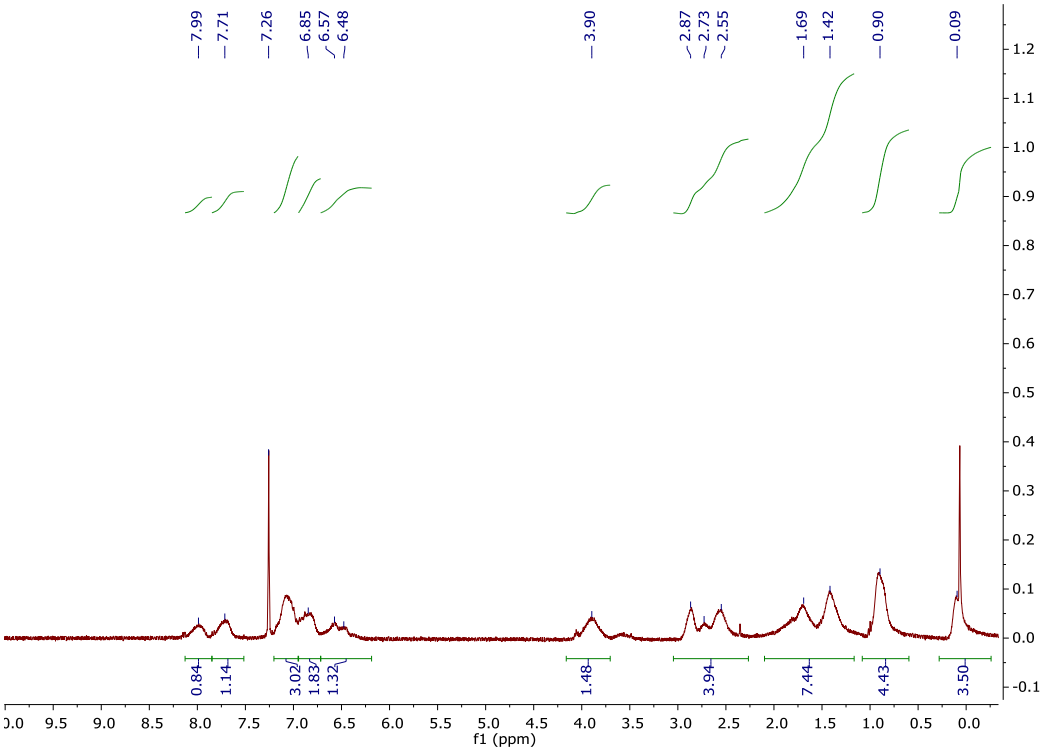

Figure A-48. ^{1}H NMR spectrum for **P-3-M1(65)-COOH(35)** in $CDCl_3$.

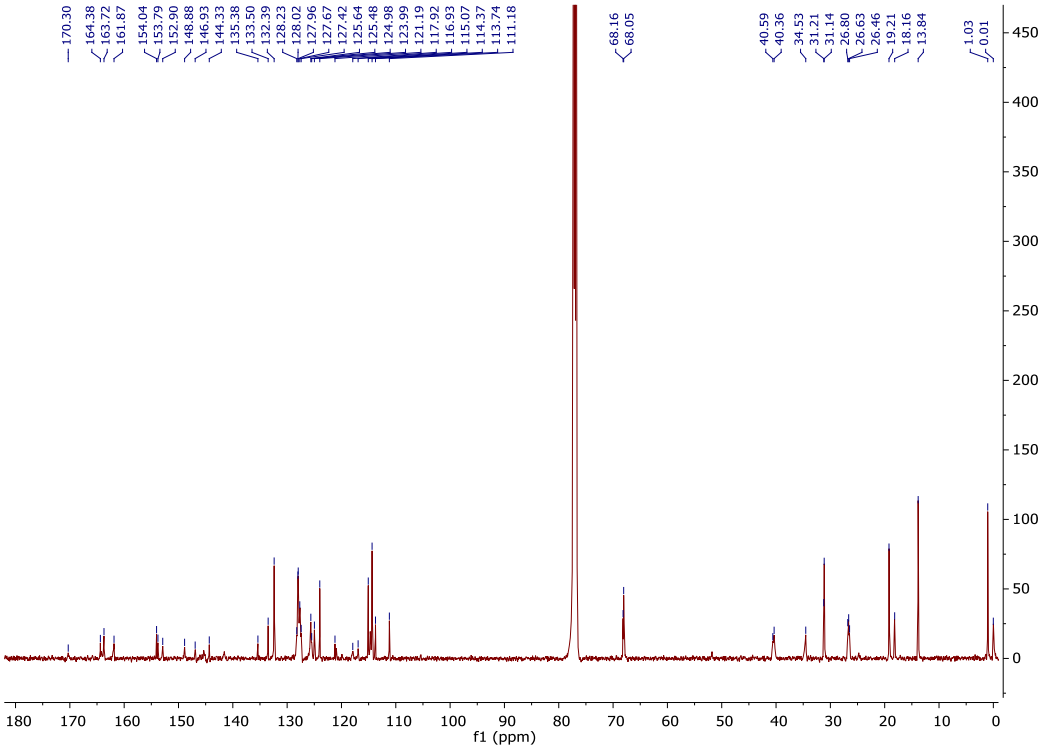

Figure A-49. Decoupled ^{13}C NMR spectrum for **P-3-M1(65)-COOH(35)** in $CDCl_3$.

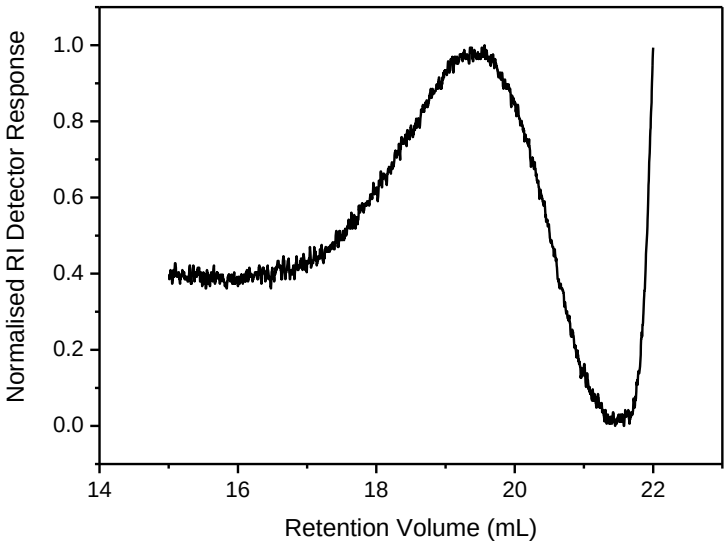

Figure A-50. GPC data for **P-3-M1(65)-COOH(35)**.

PMVS-M1(84)-COOH(16)

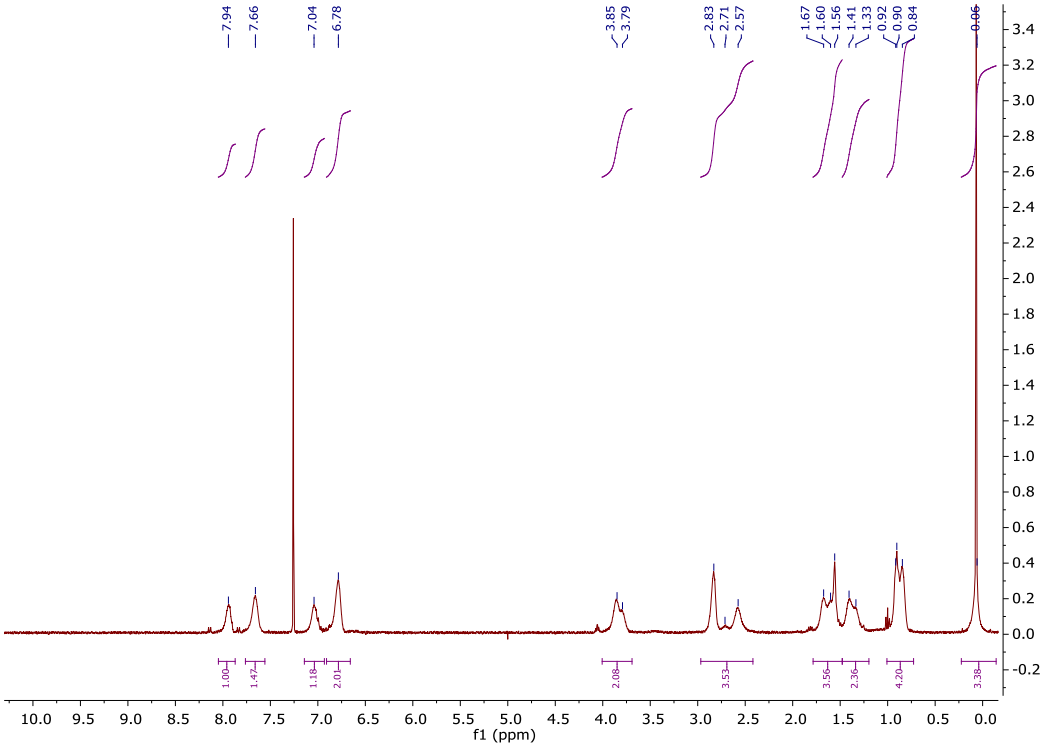

Figure A-51. ^{1}H NMR spectrum for **PMVS-M1(84)-COOH(16)** in $CDCl_3$.

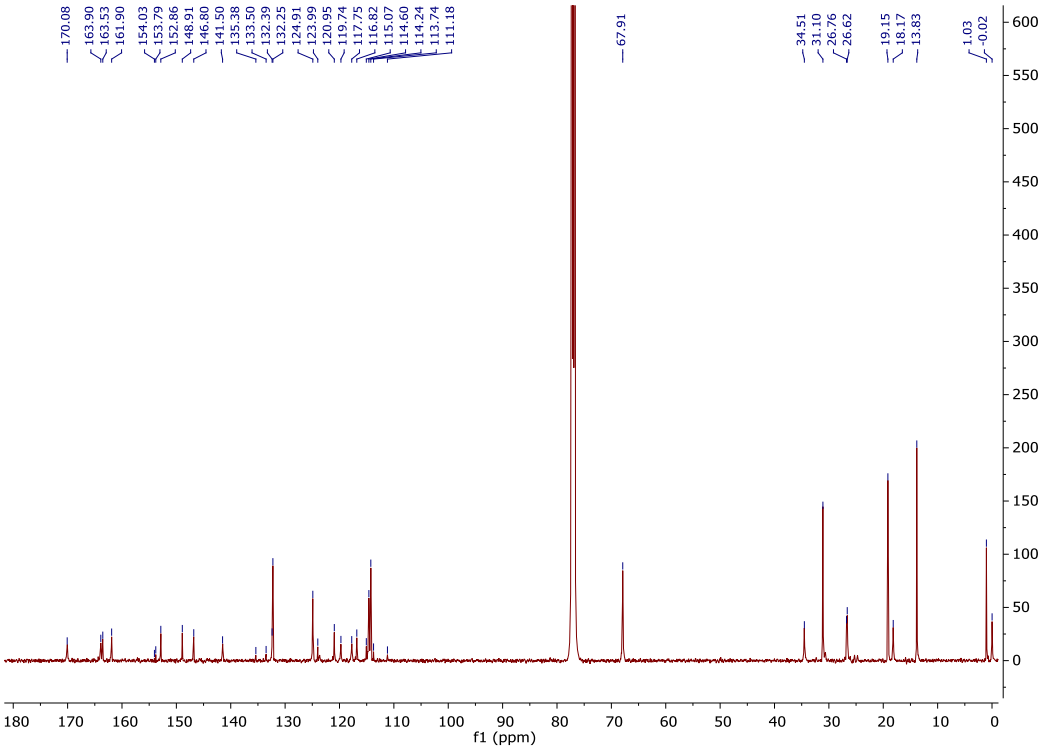

Figure A-52. Decoupled ^{13}C NMR spectrum for **PMVS-M1(84)-COOH(16)** in $CDCl_3$.

A.5. Conversion of Carboxylic Acid Groups to Methyl Esters

P-3-COOMe

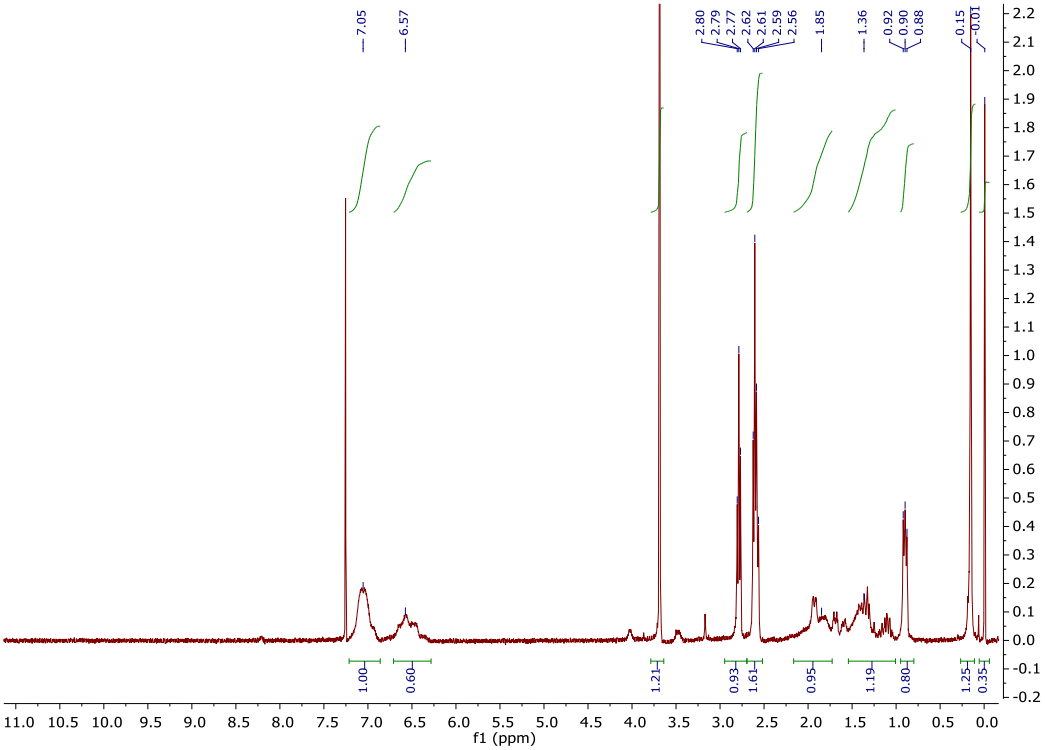

Figure A-53. ^{1}H NMR spectrum for **P-3-COOMe** in $CDCl_3$.

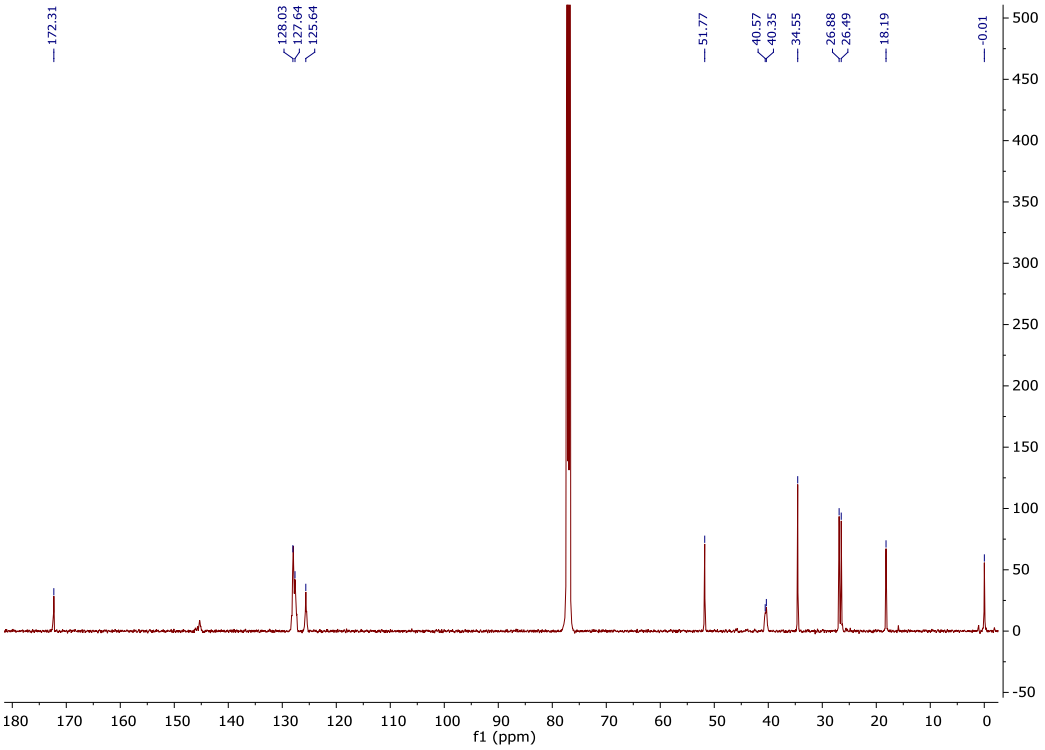

Figure A-54. Decoupled ^{13}C NMR spectrum for **P-3-COOMe** in $CDCl_3$.

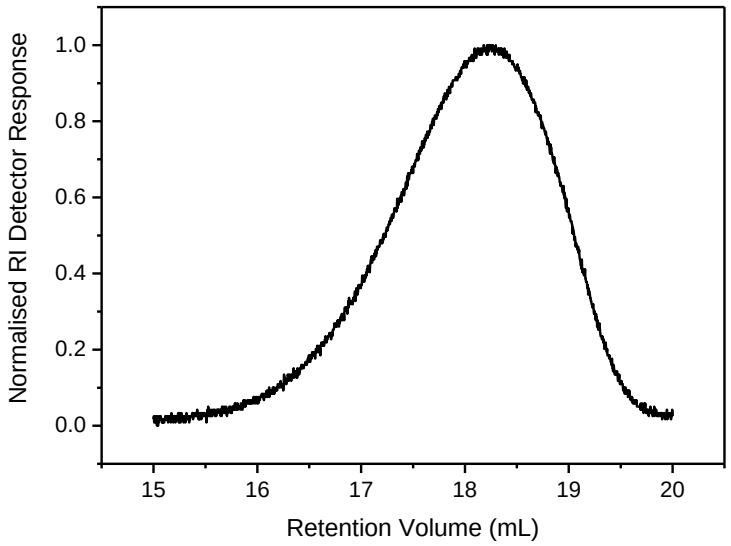

Figure A-55. GPC data for **P-3-COOMe**.

P*-3(AIBN)-COOMe

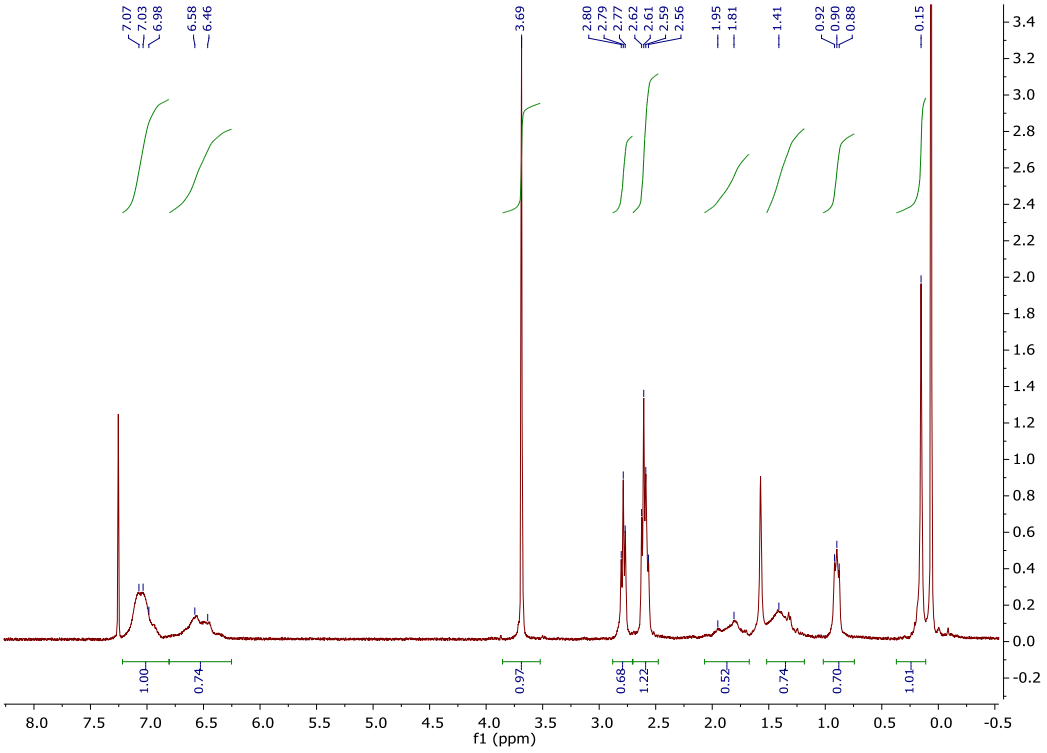

Figure A-56. ^{1}H NMR spectrum for **P*-3(AIBN)-COOMe** in $CDCl_3$.

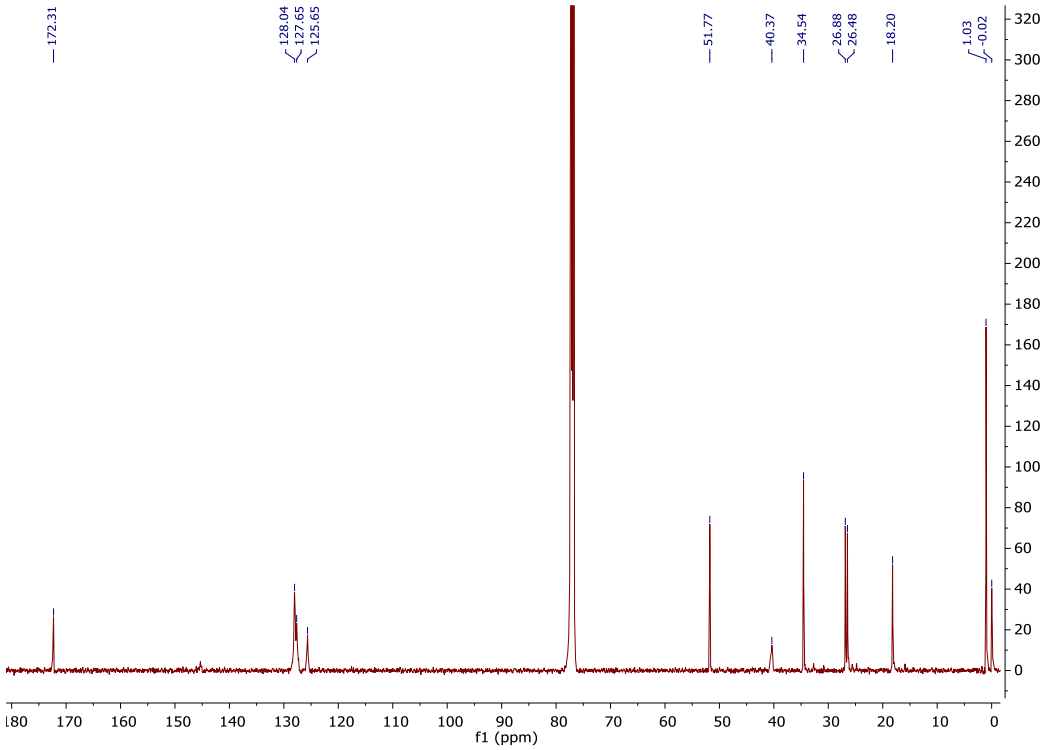

Figure A-57. Decoupled ^{13}C NMR spectrum for **P*-3(AIBN)-COOMe** in $CDCl_3$.

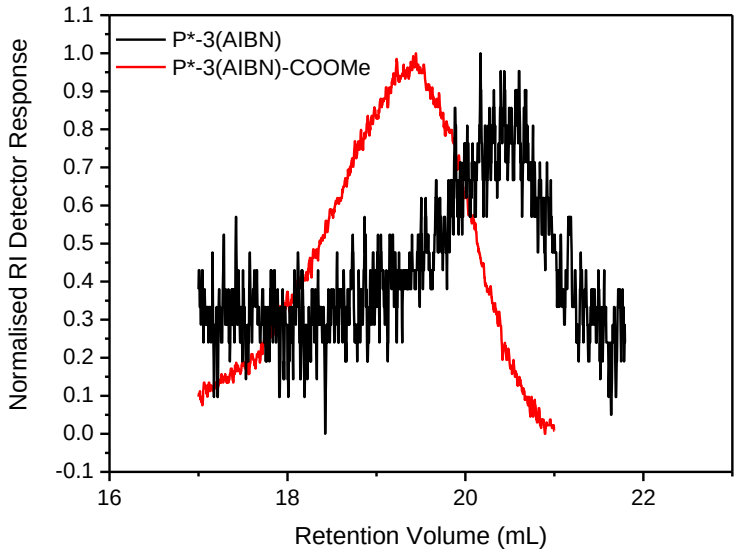

Figure A-58. GPC data for **P*-3(AIBN)** and **P*-3(AIBN)-COOMe.**

P-3-M1(65)-COOMe(35)

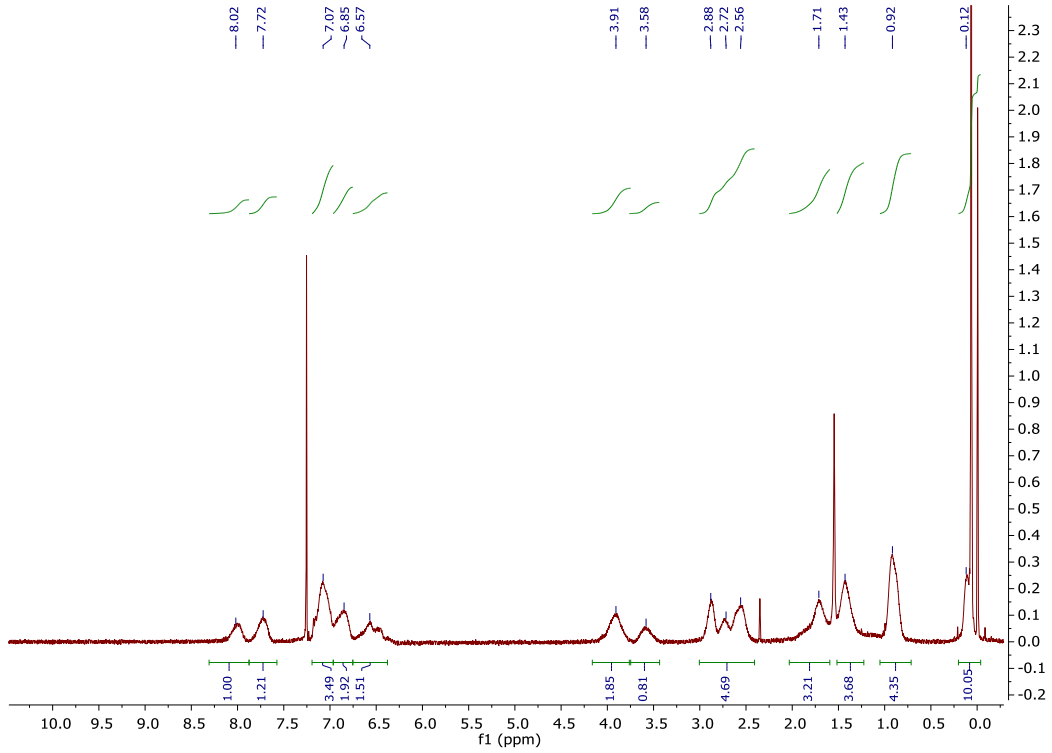

Figure A-59. ^{1}H NMR spectrum for **P-3-M1(65)-COOMe(35)** in $CDCl_3$.

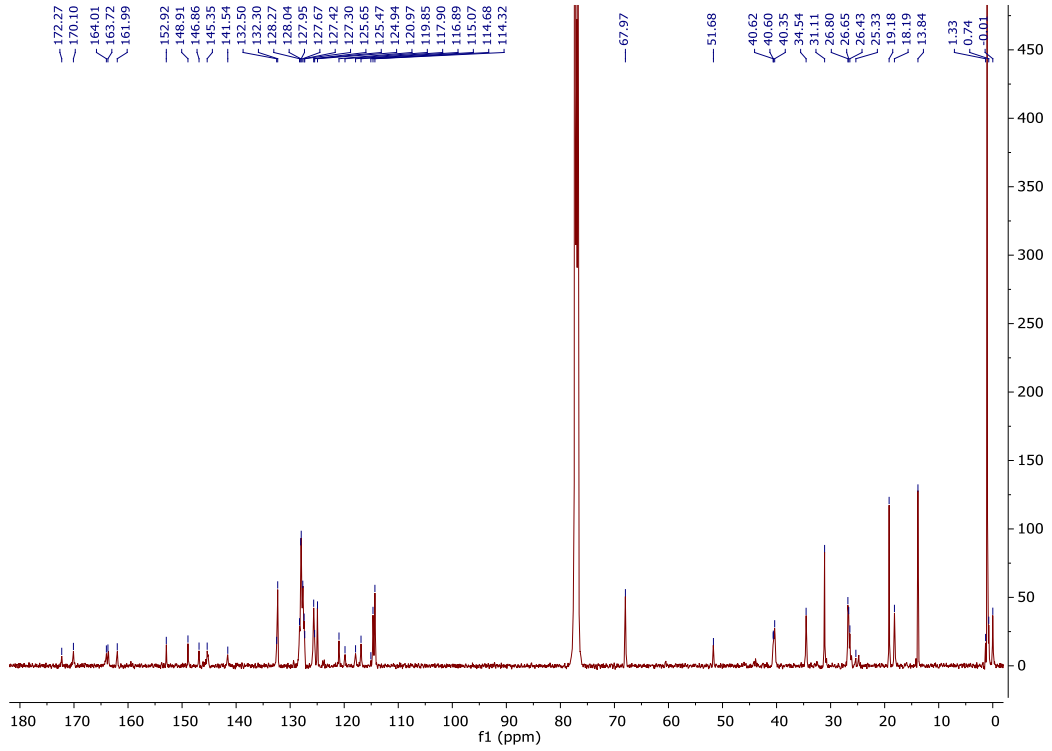

Figure A-60. Decoupled ^{13}C NMR spectrum for **P-3-M1(65)-COOMe(35)** in $CDCl_3$.

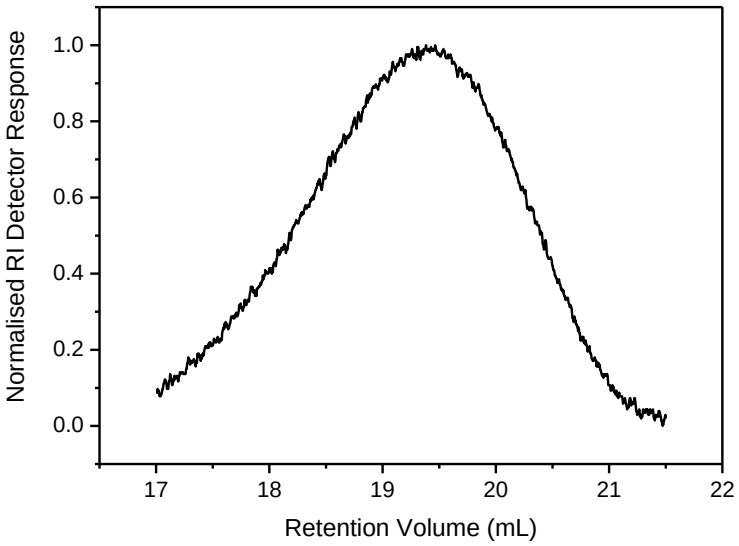

Figure A-61. GPC data for **P-3-M1(65)-COOMe(35)**.

P*-3(AIBN)-M1-COOMe

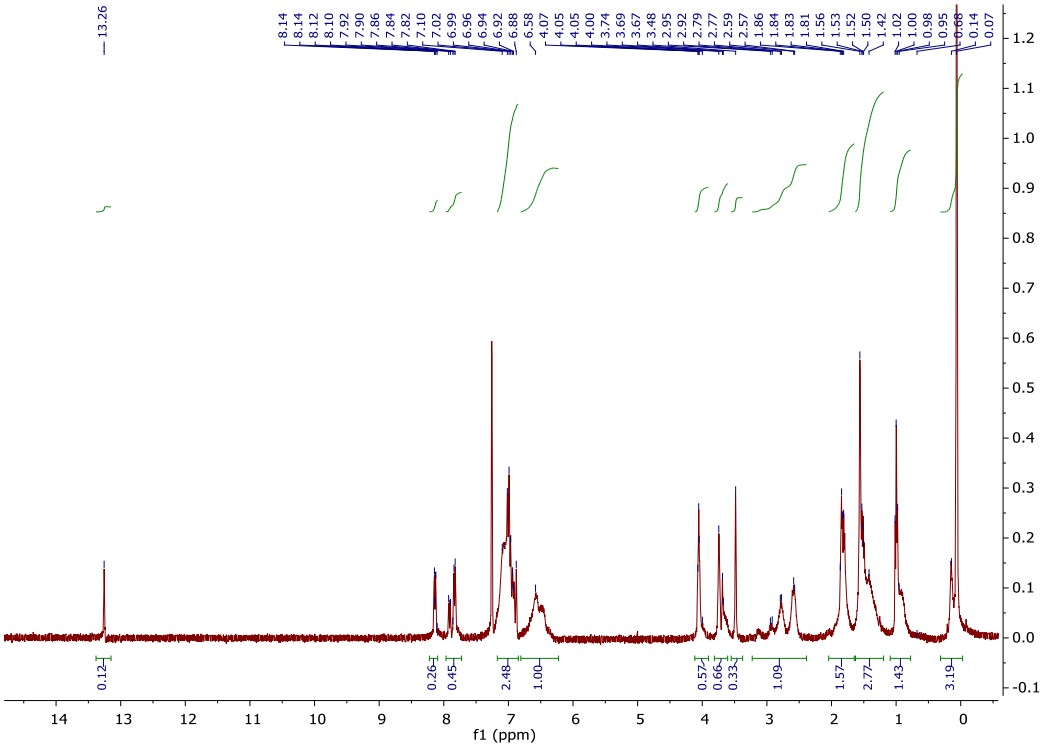

Figure A-62. ^{1}H NMR spectrum for **P*-3(AIBN)-M1-COOMe** in $CDCl_3$.

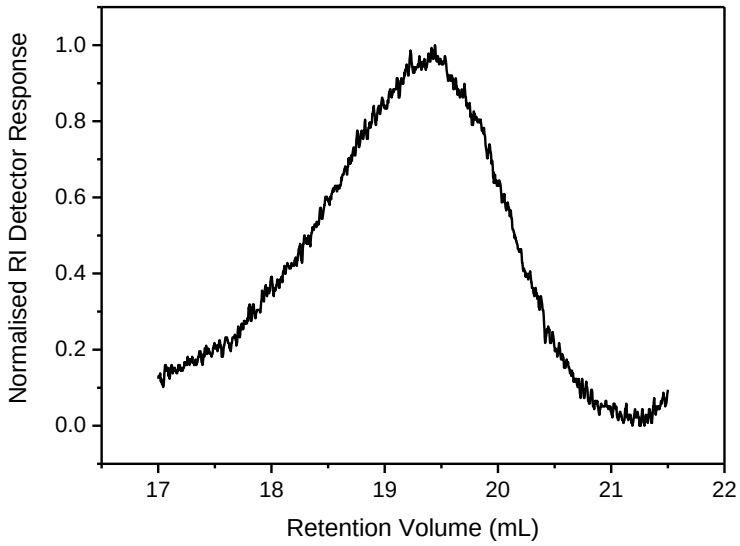

Figure A-63. GPC data for **P*-3(AIBN)-M1-COOMe**.

A.6. Thermal Analysis

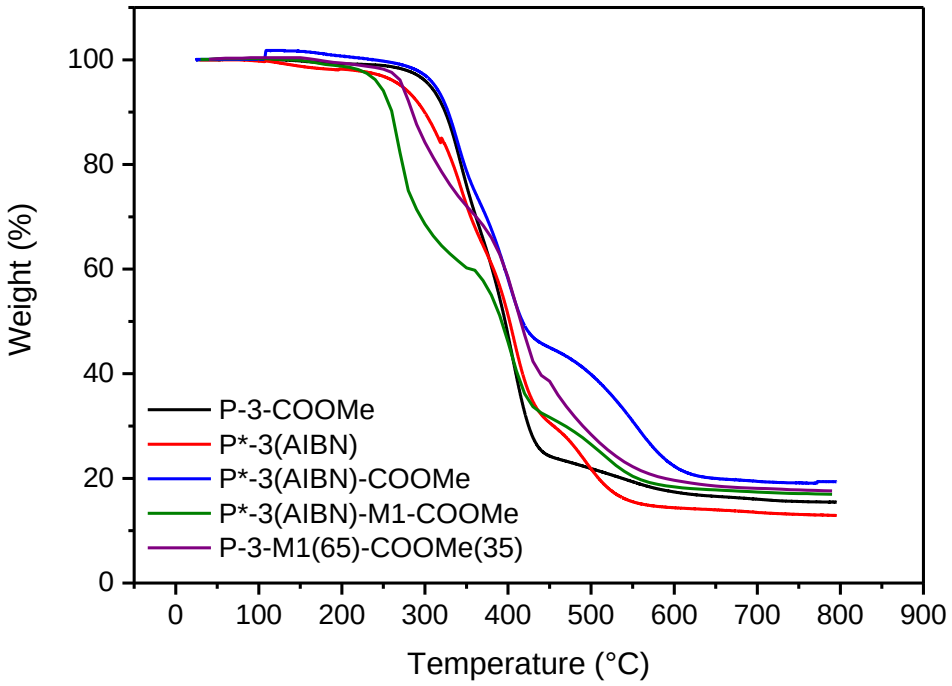

Figure A-64. TGA thermograms for **P-3-COOMe**, **P*-3(AIBN)**, **P*-3(AIBN)-COOMe**, **P*-3(AIBN)-M1-COOMe** and **P-3-M1(65)-COOMe(35)**.

Appendix B: Supporting Information for Chapter 3

Molar volume group contributions for PMVS homopolymer, all individual contributions taken from D. W. van Krevelen, *Properties of Polymers*, Elsevier, Amsterdam, 3rd edn., 1997.

Table B-1. Volume contributions for PMVS repeat unit.

Group	V_M (cm^3/mol)	Number	Total V_M (cm^3/mol)
-CH$_3$*	21.87	1	65.61
Si (Tetravalent)*	26.56	1	26.56
-O-	8.5	1	8.5
-CH=CH-	27.0	1	27.0
		Total	**127.7**

*Calculated from V_w using V_M=1.6 V_W

Table B-2. Volume contributions for LC end-functionalised PMVS repeat unit.

Group	V_M (cm^3/mol)	Number	Total V_M (cm^3/mol)
-CH$_3$*	21.87	3	65.61
-CH$_2$-	16.37	10	163.7
Aromatics (Divalent)	65.5	2	131.0
Aromatic (Trivalent)*	61.28	1	61.28
-COO-	23	2	46
-N≡N-†	25	1	25
-S-	17.3	1	17.3
-O-	8.5	3	17
Si (Tetravalent)*	26.56	1	26.56
		Total	**570.5**

*Calculated from V_w using V_M=1.6 V_W

† Using data for -C≡C-

Table B-3. Volume contributions for COOH end-functionalised PMVS repeat unit.

Group	V_M (cm^3/mol)	Number	Total V_M (cm^3/mol)
-CH_3*	21.87	1	21.87
-CH_2-	16.37	4	65.48
-COO-	23	1	23
-S-	17.3	1	17.3
-O-	8.5	1	8.5
Si (Tetravalent)*	26.56	1	26.56
		Total	**162.7**

*Calculated from V_w using V_M=1.6 V_W

Appendix C: Supporting Information for Chapter 4

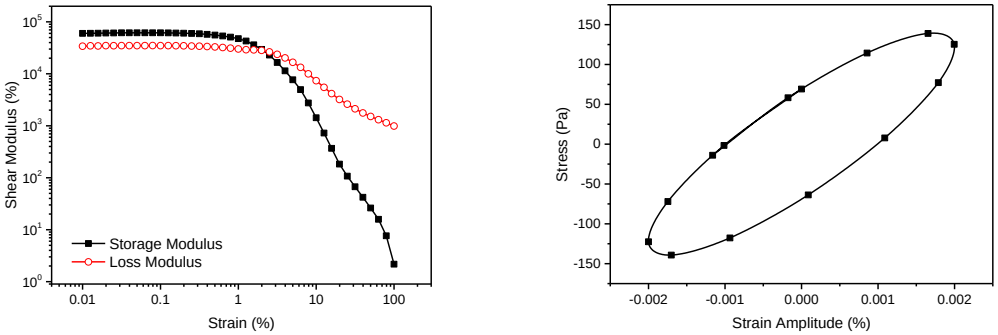

Figure C-1. Amplitude sweep results (left) and corresponding Lissajous diagram (right) at 0.2% strain for **P-3-COOMe**.

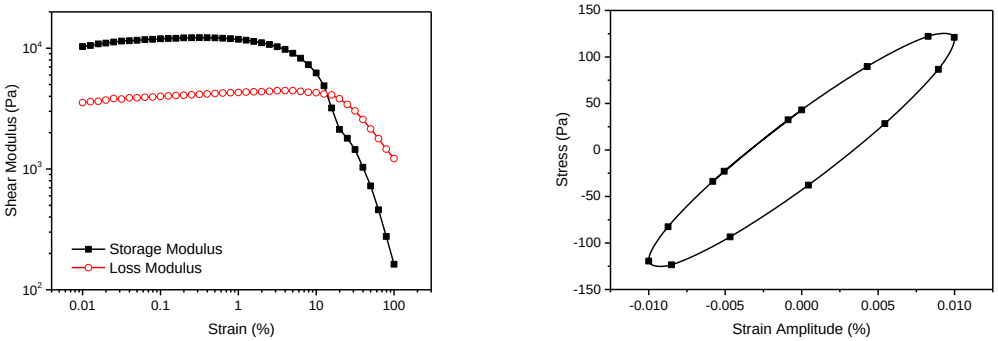

Figure C-2. Amplitude sweep results (left) and corresponding Lissajous diagram (right) at 1% strain for **P-3-M1(65)-COOMe(35)**.

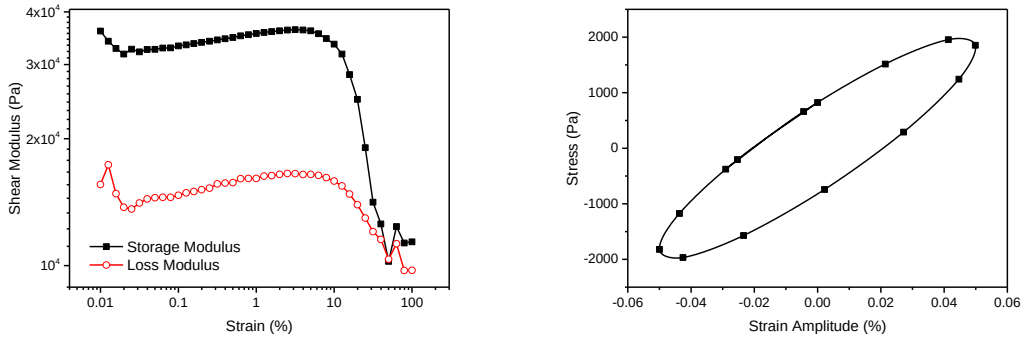

Figure C-3. Amplitude sweep results (left) and corresponding Lissajous diagram (right) at 5% strain for **P*-3(AIBN)**.

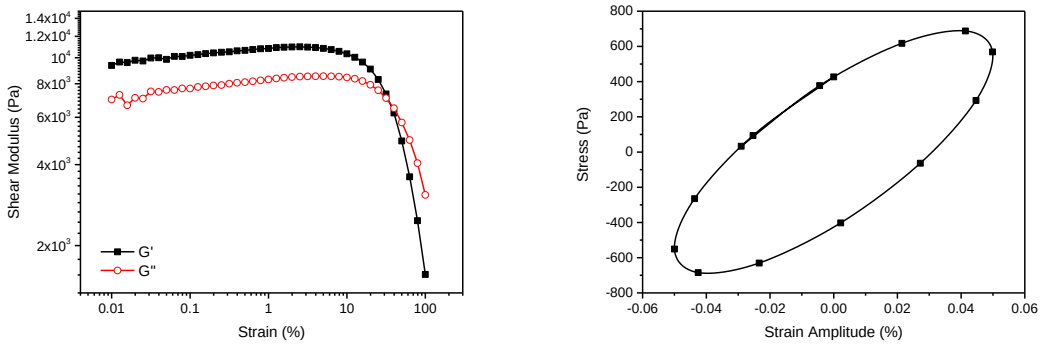

Figure C-4. Amplitude sweep results (left) and corresponding Lissajous diagram (right) at 5% strain for **P*-3(AIBN)-COOMe**.

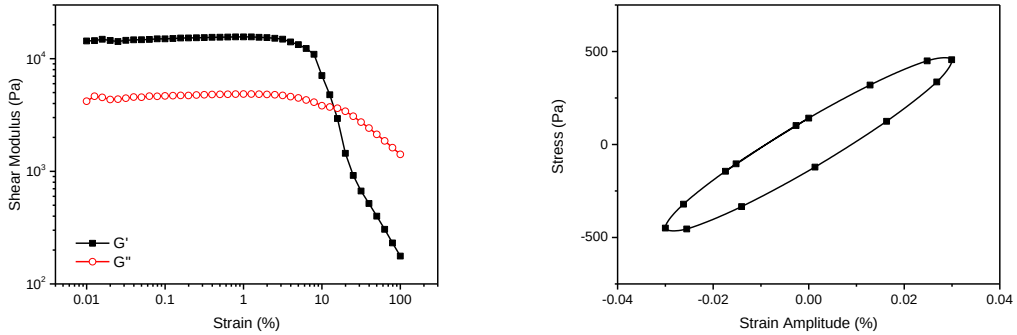

Figure C-5. Amplitude sweep results (left) and corresponding Lissajous diagram (right) at 3% strain for **P*-3(AIBN)-M1-COOMe**.

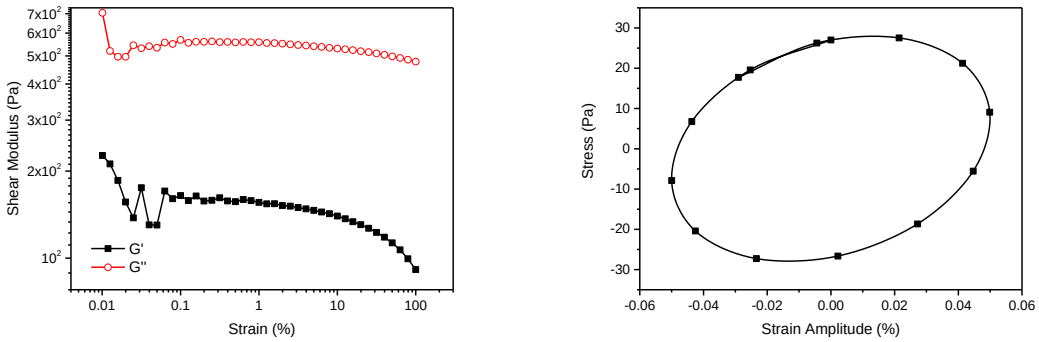

Figure C-6. Amplitude sweep results (left) and corresponding Lissajous diagram (right) at 5% strain for **PMVS-3-M1(86)-COOH(14)**.